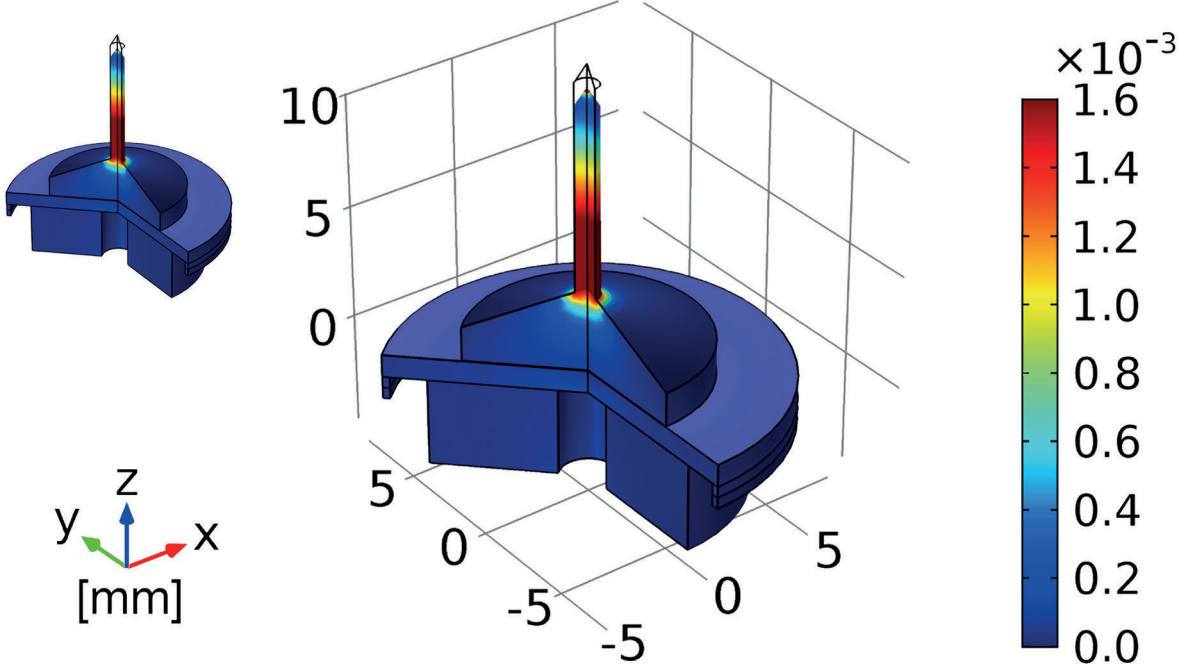

FAU Forschungen, Reihe B, Medizin, Naturwissenschaft, Technik 33

Marianne Unterreitmeier

Contact related Failure Detection of Semiconductor Layer Stacks using an Acoustic Emission Test Method

FAU UNIVERSITY PRESS

Marianne Unterreitmeier

Contact related Failure Detection of Semiconductor Layer Stacks using an Acoustic Emission Test Method

FAU Forschungen, Reihe B
Medizin, Naturwissenschaft, Technik
Band 33

Herausgeber der Reihe:
Wissenschaftlicher Beirat der FAU University Press

Marianne Unterreitmeier

Contact related Failure Detection of Semiconductor Layer Stacks using an Acoustic Emission Test Method

Erlangen
FAU University Press
2020

Bibliografische Information der Deutschen Nationalbibliothek:
Die Deutsche Nationalbibliothek verzeichnet diese Publikation in der Deutschen Nationalbibliografie; detaillierte bibliografische Daten sind im Internet über http://dnb.d-nb.de abrufbar.

Bitte zitieren als
Unterreitmeier, Marianne. 2020. *Contact related Failure Detection of Semiconductor Layer Stacks using an Acoustic Emission Test Method*. FAU Forschungen, Reihe B, Medizin, Naturwissenschaft, Technik Band 33. Erlangen: FAU University Press.
DOI: 10.25593/978-3-96147-306-9.

Verlag und Auslieferung:
FAU University Press, Universitätsstraße 4, 91054 Erlangen

Druck: docupoint GmbH

ISBN: 978-3-96147-305-2 (Druckausgabe)
eISBN: 978-3-96147-306-9 (Online-Ausgabe)
ISSN: 2198-8102
DOI: 10.25593/978-3-96147-306-9

Contact related Failure Detection of Semiconductor Layer Stacks using an Acoustic Emission Test Method

Detektion von kontaktinduzierten Beschädigungen an Halbleiterschichten unter Anwendung der Schallemissionsprüfung

Der Technischen Fakultät
der Friedrich-Alexander-Universität
Erlangen-Nürnberg
zur
Erlangung des Doktorgrades

Doktor-Ingenieurin

vorgelegt von

Marianne Unterreitmeier
aus Erding

Als Dissertation genehmigt
von der Technischen Fakultät
der Friedrich-Alexander-Universität Erlangen-Nürnberg

Tag der mündlichen Prüfung: 05.11.2019

Vorsitzender des Promotionsorgans: Prof. Dr.-Ing. habil. Andreas Paul Fröba

Gutachter: Prof. Dr.-Ing. Dr.-Ing. habil. Robert Weigel
Prof. Dr.-Ing. Lothar Pfitzner
Prof. Dr.-Ing. Rainer Holmer

„Ich habe gelernt,
dass der Weg des Fortschritts
weder kurz noch unbeschwerlich ist.“

Marie Curie

Acknowledgement / Danksagung

Vielen Dank an alle Personen, die diese Arbeit ermöglicht und durch ihre vielfältige Unterstützung zu ihrem Gelingen beigetragen haben!

Die vorliegende Arbeit entstand während meiner Tätigkeit als Doktorandin bei der Firma Infineon Technologies AG in der Abteilung für „Test Technology and Innovation“ in Neubiberg. Darüber hinaus leistete diese einen wichtigen Beitrag in dem vom BMBF geförderten Verbundprojekt ACME4.0-Chip (Akustisches Condition Monitoring für den Halbleiter-Wafertest, Förderkennzeichen 16ES0470). Die Durchführung der Promotion erfolgte in Kooperation mit der Friedrich-Alexander-Universität in Erlangen-Nürnberg und der Ostbayerischen Technischen Hochschule in Regensburg.

Mein besonderer Dank gilt:

… Herrn ***Prof. Dr. Dr. Robert Weigel***, Herrn ***Prof. Dr. Lothar Pfitzner*** und Herrn ***Prof. Dr. Rainer Holmer***, für die eingeräumte Möglichkeit zur kooperativen Promotion sowie die gewährten wissenschaftlichen Freiräume, die maßgeblich zum Gelingen dieser Arbeit beigetragen haben.

> Des Weiteren bedanke ich mich bei Herrn ***Prof. Dr. Dr. Robert Weigel***, für die Unterstützung bei der Fertigstellung dieser Arbeit, die wertvollen Hinweise zu meiner Disputation und die Übernahme des Erstgutachtens.
>
> Herrn ***Prof. Dr. Lothar Pfitzner*** danke ich zudem für die wertvollen Anregungen und Hinweise zu meiner Arbeit sowie die Übernahme des Zweitgutachtens.
>
> Herrn ***Prof. Dr. Rainer Holmer*** gilt mein besonderer Dank, für das rege Interesse an meinem Thema sowie die Begleitung meiner Arbeit durch wertvolle Diskussionen und Ratschläge und nicht zuletzt die Übernahme des Drittgutachtens.

… Herrn ***Prof. Dr. Bernhard Schmauß*** und Herrn ***Prof. Dr. Wolfgang Heiß***, für die wohlwollende Beteiligung als weitere Mitglieder des Prüfungskollegiums.

... meinem Betreuer von Seiten der Infineon Technologies AG ***Dr. Oliver Nagler***, der mir eine Industriepromotion zu diesem interessanten Thema ermöglichte, durch seine vielen Ideen und wohlwollenden Hinweise einen großen Beitrag zu meiner Arbeit leistete und nicht zuletzt mich bei der Korrektur der Arbeit unterstützte.

... my team leader ***Dr. Eric Chee Hong Liau***, who gave me the chance to continue working on my topic after finishing my PhD thesis in a permanent position at the Infineon Technologies AG in Munich.

... Herrn ***Georg Georgakos***, für die wertvollen Hinweise und Ratschläge während und bei der Fertigstellung dieser Arbeit.

... meinen Studenten ***Florian Rettenmeier*** und ***Florian Tremmel***, die mit ihrer Hilfe einen wesentlichen Beitrag zu meiner Arbeit beigetragen haben. Ich wünsche ihnen viel Glück und Erfolg für die Zukunft!

... den Kollegen und Kolleginnen von der Fehleranalyse der Infineon Technologies AG in München, für die Ermöglichung von und Unterstützung bei experimentellen Versuchen. Insbesondere gilt mein Dank Herrn ***Dr. Stephan Schömann***, für die Anfertigung der FIB-Schliffe, Frau ***Melanie Riedl***, für die Möglichkeit einige Mikroskope in der Fehleranalyse zu nutzen, Herrn ***Günter Grützmann***, für das Sägen der Wafer und Frau ***Dr. Anja Dübotzky***, für das Training zur chemisch-optischen Rissinspektion.

... den Kollegen der Abteilung „Automation and Equipment Technology" der Infineon Technologies AG in Regensburg, für die spannenden Diskussionen und die gute Zusammenarbeit.

... Herrn ***Dr. Christoph Bernd Angelkort***, für die guten Diskussionen und die zeitnahe Prozessierung der Teststrukturen.

... Herrn ***Matthias Vobl***, für die Möglichkeit, gemeinsam Messungen am Laservibrometer durchzuführen.

... der Firma ***Vallen Systeme GmbH***, mit deren Messgeräte ich die akustischen Messungen durchgeführt habe. Mein besonderer Dank gilt Herrn ***Dr. Herbert Karzel***, für die gute Betreuung und die hilfreichen Ratschläge.

... der Firma ***Synton-MDP AG***. Ein großes Dankeschön gilt Herrn ***Simon Hostettler***, für die hervorragende Zusammenarbeit bei der Anfertigung des neu entwickelten Indenters, der entscheidend zum Gelingen dieser Arbeit beigtragen hat.

... meinen Eltern ***Gertraud*** & ***Georg***. Vielen Dank für Eure Förderung und Unterstützung bei all meinen Aktivitäten! Ohne ihren Rückhalt wären viele Dinge nicht möglich gewesen.

~ Ihnen sei diese Arbeit gewidmet. ~

... meinem Freund ***Niklas***, der mir durch seine positive und verständnisvolle Art, seine vielfältige Unterstützung und seine große Geduld stets eine große Stütze war.

... meiner Schwester ***Anja*** und meinen ***Freunden***, die immer für mich da waren, gleichzeitig jedoch, vor allem im letzten Jahr, häufig auf mich verzichten mussten.

Abstract

Complex semiconductor circuits must be electrically tested after manufacturing at wafer level due to process variations and design defects to separate functional from defective chips prior to further processing. Therefore, the chip is mechanically contacted on its connection pads with tiny spring probes and electrically connected to external test instruments. The induced mechanical stresses can partially exceed the permissible yield and fracture stresses in the thin layers and lead to their plastic deformation or cracking. These pre-damages can later in operation again lead to an electrical disfunction or complete failure of the ***I***ntegrated ***C***ircuit (IC). Until now, there are only destructive methods to optically detect cracks in deeper-lying brittle insulation layers. However, these are always applicable after the wafer test, time consuming, and sometimes inaccurate. In addition, since the crack rate is usually very low, a very high number of samples for the optical inspection is necessary to make reliable predictions regarding the quality of the tested chips.

In this work, a novel method is presented to reliably and efficiently detect mechanical damage during contacting of sensitive semiconductor structures by thin needles. This non-destructive method is based on the ***A***coustic ***E***mission (AE) testing. In this measuring principle, the stored elastic energy, which becomes impulsively released during the crack initiation, leads to an acoustic shockwave in the material. By suitable sensors, which are attached to the surface of the sample, the signal can be measured, electrically amplified, and processed. Using an advanced system model and a modified measurement setup, it was possible to explain and experimentally validate the crack mechanism and excitation of the sensor-indenter system by means of an acoustic wave.

To use this measurement principle for crack detection in thin layers during wafer test, some fundamental investigations and adjustments were necessary. First, an analytical model of a rigid, pointed needle (indenter) that presses vertically on a flat surface was created. In this case, mechanical stresses occur inside and outside the contact area, which can lead to deformations and cracks depending on the material parameters and the tip geometry. In order to calculate stresses in complex multi-layer structures, additional computer-aided ***F***inite ***E***lement ***M***ethod (FEM) simulations were performed. Due to the pulse-like excitation during the cracking, the sensor-indenter system gets into a harmonic oscillation, which is measured electrically. The measuring sensitivity could be significantly increased by an

improved coupling and tuning of the resonance frequencies of the sensor and indenter.

With the optimized measuring setup, it was now possible to experimentally carry out parameter studies on suitable test structures for the determination of crack probability during contact by thin needles. The accuracy of the AE test method was correlated by conventional failure analysis methods. It could be shown that the structure, the thickness, and the material behavior of the layers significantly influence the *Weibull*-distributed crack frequency and the results of the simulation and the experiments agree very well. Finally, the validation of the crack detection could also be performed on processed ***C***omplementary ***M***etal ***O***xide ***S***emiconductor (CMOS) chips with metallized surfaces, which allows the use for industrial purposes, too.

The effort and duration of the ***P***ad-***O***ver-***A***ctive-***A***rea (POAA) qualification can be significantly reduced with the help of the novel AE test method, which was developed and validated within the scope of this thesis. The accuracy is much higher compared to conventional detection methods. In addition, it is now much easier to determine the robustness of increasingly complex and sensitive semiconductors and to optimize them by design changes. Beside the innovative AE test method for crack detection during wafer test, there are a number of other potential applications and research areas, which, however, will not be further examined within this thesis.

Kurzfassung

Komplexe Halbleiterschaltungen müssen aufgrund von Prozessschwankungen und Designfehlern nach der Herstellung elektrisch auf Scheibenebene getestet werden, um funktionale von defekten Chips vor der weiteren Verarbeitung zu separieren. Dabei wird der Chip über seine Anschlusspads mit kleinsten Federkontakten mechanisch kontaktiert und elektrisch mit externen Messinstrumenten verbunden. Die dabei induzierten mechanischen Spannungen können teilweise die zulässigen Fließ- und Bruchspannungen in den dünnen Schichten überschreiten und zu deren plastischer Deformation oder Bruch führen. Diese Vorschädigungen können später im Betrieb wiederum zu einer elektrischen Fehlfunktion oder zum Ausfall der integrierten Schaltung (engl. ***I***ntegrated ***C***ircuit (IC)) führen. Es gibt bisher nur zerstörende Verfahren, um Risse in tieferliegenden spröden Isolationsschichten optisch zu detektieren. Diese sind jedoch immer erst nach dem Scheibentest anwendbar, außerdem zeitaufwendig und teilweise ungenau. Da die Risshäufigkeit üblicherweise sehr niedrig liegt, ist außerdem eine sehr hohe Stichprobenanzahl für die optische Inspektion notwendig, um zuverlässige Vorhersagen bzgl. der Qualität der getesten Chips zu treffen.

In dieser Arbeit wird eine neuartige Methode vorgestellt, um mechanische Beschädigungen von empfindlichen Halbleiterstrukturen, die während der Kontaktierung durch dünne Nadeln auftreten können, zuverlässig und effizient zu detektieren. Diese zerstörungsfreie Methode basiert auf der ***S***chall***e***missions (SE)-Prüfung. Bei diesem Messprinzip führt die gespeicherte elastische Energie, die bei der Rissentstehung impulsartig frei wird, zu einer akustischen Stoßwelle im Material. Durch geeignete Sensoren, die an der Oberfläche der Probe angebracht sind, kann das Signal gemessen, elektrisch verstärkt und verarbeitet werden. Mit Hilfe eines weiterentwickelten Modells und eines modifizierten Messaufbaus wurde es möglich, den Riss-Mechanismus und die Anregung des Sensor-Indenter-Systems durch eine akustische Welle zu erklären und experimentell zu validieren.

Um dieses Messprinzip für die Rissdetektion in dünnen Schichten beim Wafertest zu nutzen, waren jedoch einige grundlegende Untersuchungen und Anpassungen notwendig. Zunächst wurde ein analytisches Modell einer starren, spitzen Nadel (Indenter), die vertikal auf eine ebene Fläche drückt, erstellt. Dabei treten innerhalb und außerhalb der Kontaktfläche mechanische Spannungen auf, die, abhängig von den Materialparametern und der Spitzengeometrie, zu Verformungen und Rissen führen können.

Um auch Spannungen in komplexeren Mehrschicht-Strukturen berechnen zu können, wurden zusätzliche computergestütze Simulationen nach der ***F***inite-***E***lemente-***M***ethode (FEM) durchgeführt. Durch die impulsartige Anregung bei der Rissentstehung gerät das Sensor-Indenter-System in eine harmonische Schwingung, die elektrisch gemessen wird. Die Messempfindlichkeit konnte durch eine verbesserte Kopplung und Abstimmung der Resonanzfrequenzen des Sensors und des Indenters wesentlich gesteigert werden.

Mit dem optimierten Messaufbau war es nun möglich, an geeigneten Teststrukturen Parameterstudien zur Bestimmung der Risswahrscheinlichkeit beim Kontaktieren durch dünne Nadeln experimentell durchzuführen. Die Genauigkeit der SE-Prüfmethode wurde jeweils mit konventionellen Fehleranalyseverfahren verglichen. Es konnte gezeigt werden, dass der Aufbau, die Dicken und das Materialverhalten der Schichten die *Weibull*-verteilte Risshäufigkeit wesentlich beeinflussen und die Ergebnisse der Simulation und der Experimente dabei sehr gut übereinstimmen. Die Verwendbarkeit der Rissdetektion konnte schließlich auch an prozessierten ***C***omplementary ***M***etal ***O***xide ***S***emiconductors (engl. CMOS; „komplementärer Metall-Oxid-Halbleiter“) mit metallisierten Kontakt-Oberflächen nachgewiesen werden, was den Einsatz für industrielle Zwecke ermöglicht.

Der Aufwand und die Dauer der Qualifikation für ***P***ad-***O***ver-***A***ctive-***A***rea (engl. POAA; „Kontaktanschluss über aktiven Schaltungsbereich“) können mit Hilfe der neuartigen akustischen SE-Prüfmethode, die im Rahmen dieser Arbeit entwickelt und validiert wurde, entscheidend reduziert werden. Die Genauigkeit ist im Vergleich mit konventionellen Detektionsmethoden wesentlich höher. Außerdem ist es nun deutlich einfacher, die Robustheit von immer komplexeren und empfindlicheren Halbleitern zu bestimmen und durch Designänderungen zu optimieren. Neben der in dieser Arbeit entwickelten Methode zur Rissdetektion anhand der SE-Prüfung für den Einsatz beim Scheibentest, gibt es eine Reihe von weiteren potentiellen Anwendungen und Forschungsbereichen, die hier jedoch nicht weiter erörtert werden.

Contents

Nomenclature

List of Abbreviations

AE	***A***coustic ***E***mission
AET	***A***coustic ***E***mission ***T***echnique
ADC	***A***nalog-to-***D***igital ***C***onverter
BE	***B***ack ***E***nd
BEOL	***B***ack-***E***nd-***O***f-***L***ine
BPSG	***B***oro-***P***hospho-***S***ilicate ***G***lass
C	2-***C***omponent indenter (namining of indenters)
CCFF	***C****haracteristic* ***C****ontact* ***F****orce* ***F****unction*
CMOS	***C***omplementary ***M***etal ***O***xide ***S***emiconductor
CMP	***C***onfocal ***M***ulti ***P***inhole
CVD	***C***hemical ***V***acuum ***D***eposition
DB	***D***ata***b***ase
DDT	***D***uration ***D***iscrimination ***T***ime
DIC	***D***ifferential ***I***nterference ***C***ontrast
DIN	***D***eutsches ***I***nstitut für ***N***ormung
DUT	***D***evice-***U***nder-***T***est
EMC	***E***lectro***m***agnetic ***C***ompatibility
FE	***F***ront ***E***nd
FEM	***F***inite ***E***lement ***M***ethod
FIB	***F***ocused ***I***on ***B***eam
FP	***F***lat ***P***unch (naming of indenters)
FSG	***F***luorinated-***S***ilicate ***G***lass
FTEOS	***F***luorinated ***T***etra***e***thyl ***O***rtho***s***ilicate
IC	***I***ntegrated ***C***ircuit
IMD	***I***nter-***M***etal layer ***D***ielectric

I/O	***I***nput / ***O***utput
LEFM	***L***inear-***E***lastic ***F***racture ***M***echanics
LC01 - 09	***L***oad ***C***ases 01 - 09
LSL	***L***ower ***S***pecification ***L***imit
M1 - 7	***M***etal layer 1 - 7
M	***M***onolithic indenter (naming of indenters)
MEMS	***M***icro ***E***lectro-***M***echanical ***S***ystem
MOSFET	***M***etal-***O***xide-***S***emiconductor ***F***ield-***E***ffect-***T***ransistor
MSA	***M***easurement ***S***ystem ***A***nalysis
MTF	***M***edian ***T***ime to ***F***ailure
NDT	***N***on-***D***estructive ***T***esting
NSH	***N***ormal ***S***tress ***H***ypothesis
PCB	***P***rinted ***C***ircuit ***B***oard
PCM	***P***rocess ***C***ontrol ***M***easurement
POAA	***P***ad-***O***ver-***A***ctive-***A***rea
PROFIT	***Pro***be ***F***orce ***I***nvestigation ***T***ool
PSG	***P***hospho-***S***ilicate ***G***lass
PZT	Lead ***Z***irconate ***T***itanate
RIE	***R***eactive ***I***on ***E***tching
SAM	***S***canning ***A***coustic ***M***icroscopy
SE	***S***chall***e***mission
SEM	***S***canning ***E***lectron ***M***icroscope
SNR	***S***ignal-to-***N***oise ***R***atio
TD	***T***ouch***d***own
TEOS	***T***etra***e***thyl ***O***rtho***s***ilicate
TR	***T***ransient ***R***ecorder
USL	***U***pper ***S***pecification ***L***imit
W01 - 06	***W***afer 01 - 06

List of Chemical Elements and Formulas

Al	Aluminum
Al-Cu	Aluminum-copper metallization
Al_2O_3	Aluminum oxide
Al-Si-Cu	Aluminum-copper metallization with silicon
Ag	Silver
Au	Gold
C	Carbon
Cu	Copper
Cu-Be	Copper-beryllium alloy
HNO_3	Nitric acid
H_3PO_4	Phosphoric acid
Ni-Pd	Nickel-palladium alloy
W-Rh	Tungsten-rhodium alloy
Si	Silicon
SiC	Silicon carbide
SiCN	Silicon carbon nitride
Si_3N_4	Silicon nitride
SiO_2	Silicon dioxide
SiO_x	Silicon oxide
Sn-Ag	Tin-silver alloy
Ta	Tantalum
Ti	Titanium
Ti_3N_4	Titanium nitride
W	Tungsten

List of Symbols

a	Radius of contact area
A	Area / Amplitude
B	Amplitude / constant
B_1, B_2	Coefficients of *CCFF*
A_o	Initial cross-section area
A_b	Load bearing area
A_c	Contact area
A_{peak}	Bust signal peak amplitude
A_{tip}	Indenter tip area
CNTS	Ring down counts
c_l	Longitudinal sound velocity of the material
c_s	Spring constant
D	Lehr attenuation / damping factor
d_{os}	Degree of damping of the oscillator
d_{base}	Diameter of the indenter base
d_f	Film thickness
d_{rod}	Diameter of the indenter rod
d_{tip}	Diameter of the indenter tip
E	*Young's* or elastic modulus
E_a	Activation energy
E_{burst}	Burst signal energy
E_{el}	Electrical field
F	Force / load
F_o	Characteristic contact force
F_c	Contact force
F_{crit}	Critical contact force
F_d	Damping force

F_{el}	Electrostatic force
F_f	Frictional force
F_i	Inertia force
F_k	Spring force
F_{max}	Maximal force
F_p	Force from the exchange of momentum
F_t	Tensile load
F_z	Normal load
f	Frequency
f_k	Undamped resonance frequencies
f_s	Sampling frequency
$f_{\Delta Fo}$	Increase factor of characteristic contact force F_o
H	Hardness
h_{base}	Height of the indenter base
h_{cone}	Height of the indenter cone
I	Current flow
ΔI	Normalized unit pulse
J	Current density
K	Stress intensity factor
K_I	Stress intensity factor for mode I
K_{Ic}	Critical stress intensity factor / fracture toughness
K_m	Material constant of the conductor
k	Order of natural frequency
k_{os}	Spring rate of the oscillator
k_B	*Boltzmann's* constant
L	Length of tensile specimen
L_o	Initial length of tensile specimen
ΔL	Change in length of tensile specimen

l	Length of one-sided fixed rod
l_b	Length of electric conductor
l_c	Crack length
l_{rod}	Length of indenter rod
m_{os}	Mass of oscillator
m	*Weibull* modulus
$\boldsymbol{n}$	Unit vector normal to the surface
P_f	Cumulative crack probability
P_i	Individual crack probabilities
p	Pressure
p_m	Mean contact pressure
R_b	Bulk resistance
R_{co}	Constriction resistance
R_{ct}	Contact resistance
R_f	Film resistance
R_t	Electrical resistance at transition points
r_b	Radius of load bearing area
r_e	Indenter tip edge radius
r_{tip}	Indenter tip radius
Δr	Radial distance
S	Sensitivity of AE sensor
S_b	Cross-section of electric conductor
S_{ref}	Reference value of AE sensor sensitivity
$\boldsymbol{s}$	Unit vector parallel to the surface
T_K	Temperature
T	Oscillation time or period
T_s	Sampling time
t	Time

$\boldsymbol{t}$	Vector of traction
t_{arr}	Arrival time
t_{dur}	Burst signal duration
t_{rise}	Burst signal rise time
U	Voltage
U_o	Reference Voltage
U_i	Voltage samples
U_{th}	Detection threshold
ΔU	Voltage drop
u	Displacement
V	Magnification function
v	Velocity
v_o	Initial velocity
Δz	Overdrive
Δz_{el}	Penetration depth
α_i	Constriction radius
γ_s	Elastic strain energy
Δ	Decay factor
ε	Strain
ε_L	*Lüders* elongation
ε_r	Relative static permittivity
ε_u	Uniform elongation
ε_{ut}	Total elongation
ε_f	Fracture elongation
ε_{ft}	Total elongation at fracture
ε_u	Uniform elongation
ε_{ut}	Total elongation

$\varepsilon_{\perp}$	Lateral contraction
ε_{II}	Longitudinal extension
λ	Eigenvalue of differential equation
μ_r	Friction coefficient
ν	*Poisson's* ratio
ρ	Density
ρ_f	Specific film resistivity
ρ_m	Electrical resistivity of contact material
σ	Normal (tensile or compressive) stress / strength
σ_o	Characteristic strength
$\sigma_{1,2,3}$	Principle stresses
σ_f	Fracture stress / strength
σ_t	External tensile stress
σ_u	Ultimate tensile strength
σ_{yh}	Upper yield strength
σ_{yl}	Lower yield strength
τ	Shear stress
φ	Phase shift
ω	Circular / angular frequency
ω_o	Natural angular frequency of undamped oscillator
ω_d	Natural angular frequency of damped oscillator

1 Introduction

1.1 Motivation and Problem Description

Today, semiconductor circuits are used in almost all technical devices with a wide range of application areas. The number of chips continues to grow due to digital trends such as the ***I***nternet ***o***f ***T***hings (IoT), autonomous driving, or ***A***rtificial ***I***ntelligence (AI). The ***I***ntegrated ***C***ircuits (ICs) must survive at high reliability partly in extreme environmental conditions with electrical and mechanical loads. At the same time, chip performance and integration density are increasing, requiring further miniaturization of feature sizes for ***C***omplementary ***M***etal ***O***xide ***S***emiconductor (CMOS) and power semiconductor technologies. In addition to the technological challenges, the semiconductor industry is under enormous cost pressure from volatile and globalized markets. Therefore, the manufacturing processes have to be constantly optimized and shortened in time and new, innovative processes are required [1,2]. This thesis contributes to improve the quality and reliability of the chips while reducing manufacturing costs through shorter qualification times.

Both during production and operation of semiconductors mechanical forces occur, which act directly or indirectly on the IC structure and can lead to damage or even destruction of the chip. Depending on the type and amount of external load, which acts on the body of the chip, in some cases high mechanical stresses are induced. There are different kinds of external load, like inertial forces, vibrations, pressure, or impacts causing shear, tensile, or compressive stresses. If the occurring stresses exceed the permissible elastic stress, plastic deformation or breakage of thin layers occurs, which represents a reliability risk or leads to an electrical failure of the circuit. In addition, when considering the type of load, it must be distinguished whether the external forces act on the structure in a punctiform (1-dimensional), planar (2-dimensional), or volumetric (3-dimensional) manner and whether the load is static or dynamic.

During semiconductor wafer test, high mechanical stresses caused by external point-shaped, dynamic forces may occur, for instance. The chips are electrically tested for functionality within the specification limits, in order to sort out functional chips for further processing. Therefore, the ***I***nput / ***O***utput (I/O) pads of the chips are contacted by pointed elastic needles (probes), which are assembled on a probe card, to ensure an electrical connection between the device and a test system. To achieve a low

electrical contact resistance between the probe and the pad a sufficiently high contact stress is required, but exceeding allowed stress limits leads to an increased fracture probability of brittle insulating layers below the pad (see Fig. 1.1). This can cause a failure of the device due to short circuits or leakage [1,3].

Particularly problematic are hidden cracks in deeper isolation layers, which initially do not cause an electrical failure or a violation of the test specification and are hence not recognized in the wafer test. However, these damages can lead to a later failure in the field and should be avoided in any case. Hence, appropriate quality assurance procedures need to be developed and applied to ensure that cracks do not occur at all or only in an extremely small number during wafer tests [1].

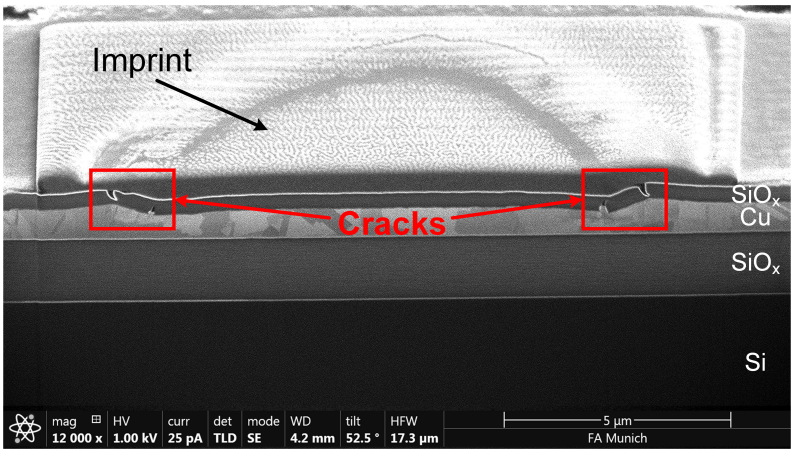

Fig. 1.1. Mechanical failure in upper oxide layer below pad.

To guarantee a stable and reliable wafer test, the process window of minimum required and maximum allowed contact stress limits must be determined in advance during a probing technology qualification. While the ***L***ower ***S***pecification ***L***imit (LSL) of the contact stress is given by electrical contact fails, the ***U***pper ***S***pecification ***L***imit (USL) is given by brittle layer cracks. The range between LSL and USL can result in a smaller or wider process window depending on the combination of pad stack and probing technology.

Probe cards for operational wafer test are assembled with hundreds or thousands of individual probes. The maximum contact stress of each probe is scattering as a function of the contact force and tip diameter caused by

manufacturing tolerances. As the smallest / largest tip applies the highest / lowest stress to the pad, it is important to consider every probe into the risk assessment. The blue curves in Fig. 1.2 show exemplary for three different frequency distributions how a robust process window should look like. The LSL and USL must not be violated by the distribution function of the contact stress.

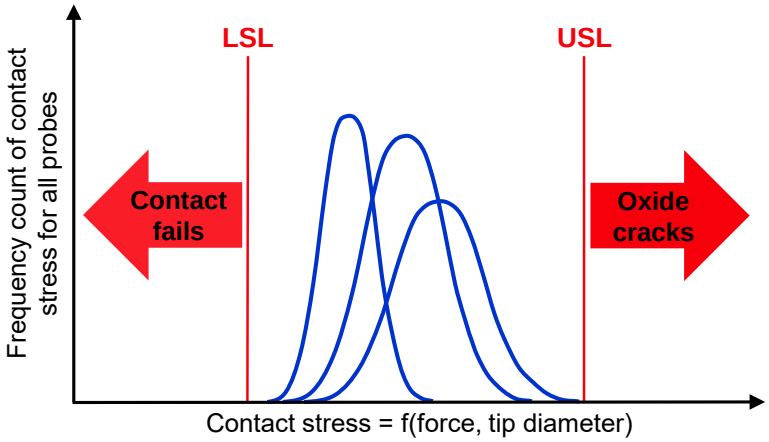

Fig. 1.2. Schematic explanation of the process window used for wafer probing.

In the past, many investigations (e.g. [4], [5], or [6]) were done to define and optimize the probing process regarding electrical contact stability, i.e. to avoid contact fails if the stress is below the LSL. This thesis contributes an important part to a more accurate and faster determination of the USL regarding cracks for existing and upcoming semiconductor technologies at wafer test. This is intensified by technology trends like introduction of more sensitive ***I***nter-***M***etal layer ***D***ielectric (IMD) layers (low / high-k dielectrics), a higher number of metal routing layers in more complex CMOS IC's, or ultra-thin wafers for power semiconductors. For this, it is important to know the true forces and needle geometries to be able to predict the critical contact stress causing crack initiation. In addition, an advanced knowledge of contact physics and material science must be present and a model of the contact process must be developed.

As already mentioned above, the cracks are usually not detectable by electrical or optical inspection methods during or immediately after the wafer test. Until today, there are only destructive methods available to visualize cracks. Current methods for crack detection are the chemical-optical

inspection, which is used in particular for CMOS technologies [1], and the more elaborate preparation of ***S***canning ***E***lectron ***M***icroscope (SEM) cross-section images after ***F***ocused ***I***on ***B***eam (FIB)-milling. Both methods are destructive, time-consuming, and thus cost-intensive. Moreover, compared to CMOS technology devices with evenly spaced oxide-metal layers, the chemical etching method does not work for complex and vertical integrated structures, which are typical for power semiconductor technology devices [3].

So far, considerations have been made how to replace inefficient optical analyzes with alternative crack detection methods that are faster and more reliable. A new way of detecting cracks is acoustic event monitoring, which has been used successfully in other applications for some time [7,8]. In crack initiation and propagation, the stored potential strain energy suddenly releases and creates an acoustic, harmonic wave that can be measured with suitable sensors. Although the released energy is very low for layers in the sub-micrometer range in the present case, it should theoretically be possible to measure this energy at the same time when it is released. The aim of this work is hence, to develop a crack detection method based on ***A***coustic ***E***mission (AE) testing and to validate it experimentally, in order to acoustically monitor the contact process and to detect brittle oxide cracks as soon as they arise.

In contrast to the optical methods, the AE test method is a non-destructive method. Furthermore, with this method a wide variety of crack categories can be detected directly on any semiconductor technology with higher accuracy and reproducibility. Real-time acoustic detection significantly reduces or eliminates costly downstream optical and electrical quality checks. This will make it possible in the future to determine the permissible load due to contact probes on highly sensitive IC structures during the functional test at wafer level much faster and more accurately than before.

1.2 Structure of Thesis

This work has been structured into several chapters, in order to elaborate and validate the AE testing for thin layer characterization. The following topics are covered:

- Semiconductor and probing technology for ***P***ad-***O***ver-***A***ctive-***A***rea (POAA)
- Existing crack analysis methods
- Theory and simulation of contact physics with a flat punch

- Stress modeling and crack probability function
- AE testing concept and sensor-indenter system optimization
- Experimental verification of crack detection by AE testing
- Application of AE testing for POAA qualifications

First, an overview of the manufacturing chain and technology of CMOS and power semiconductors related to wafer test and probe card technologies used is given. The contact forces that occur during probing can lead to damage of sensitive structures of the IC under the connection pad. For this purpose, different conventional crack inspection methods and microscopy techniques to detect hidden cracks are explained.

Based on simplified and stepwise more complex contact models, the resulting stresses are calculated analytically using the theory of continuum and fracture mechanics supported by computer-aided simulations in compliance with material properties of brittle and ductile layers. From this, the crack probability for a *Weibull* distribution can be determined. All this is mandatory for a fundamental understanding of crack occurrence during POAA, which is influenced by material, design, geometry, and mechanical loads of both, the probe tip and crack-sensitive test structure.

The next step is to explain the principle of AE testing in general and more specifically in relation to the application presented here. For this purpose, the concept and development of a measuring station and its components as well as the applied AE test method for the contacting of test structures with rigid needles will be elaborated. The acoustic crack detection mechanism is simulated by a suitable model and experimentally confirmed. So the sensor-indenter system can be modified in a way to improve the sensitivity of the test setup.

In the experimental part, the accuracy and reproducibility of the AE test method are first verified using different test structures based on CMOS technology, which were specially made for the evaluation of the AE test method. By setting a suitable threshold voltage and optimized adjustments of the instrument, the hits for the respective “first acoustic crack” event can be identified. The results of the acoustic measurements are validated afterwards with conventional optical analysis methods. This ensures that the AE test method is capable for determining and predicting the crack probability when contacting multi-layer structures.

Subsequently, in further experiments on unstructured ***B***ack-***E***nd-***O***f-***L***ine (BEOL) stacks and processed test chips, parameter studies are carried out

to determine the influence of the design and structure of the contact pairs (tip diameter, layer thickness, routing of metal layers, etc.) and to establish a functional relationship between applied stress and crack probability. In addition, computer-aided ***F***inite ***E***lement ***M***ethod (FEM) simulations were performed to understand the stress concentration and propagation of cracks with correlation data of optical analysis.

In the last chapter of this thesis, the major achievements will be summarized together with a new process flow to enable faster POAA qualifications and guidelines for more robust designs of complex BEOL stacks. Finally, an outlook on future work and advanced research fields will be given.

2 Failure Mechanisms during Wafer Probing

In order to understand the failure mechanisms of sensitive layers during wafer test, one must get an overview of the semiconductor manufacturing process including wafer test, probing technologies, and test system components. Highly relevant for the problem description is also the pad stack layout of most common CMOS and power semiconductor technology devices, which are affected by potential damages. In this chapter the processes and technologies are described and the challenge due to probing-induced contact stress on typical pad layer stacks is explained.

2.1 Semiconductor Manufacturing Process

The semiconductor manufacturing process can be categorized into four process groups, which can be further divided into several sub-process steps (see Fig. 2.1).

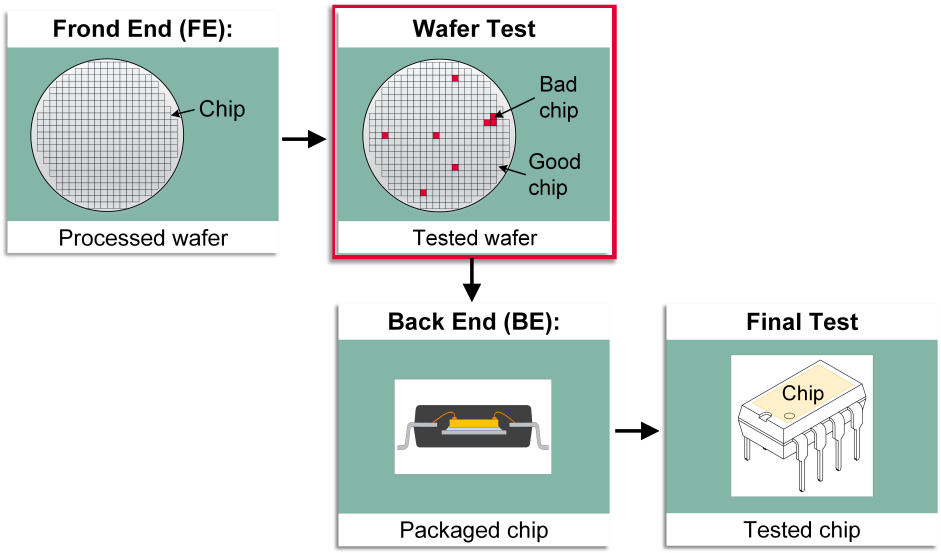

Fig. 2.1. Semiconductor manufacturing process chain.

It starts with the so-called ***F***ront ***E***nd (FE) process group where the electrical components (e.g. transistors, diodes, resistors, etc.) of the IC are manufactured. Here multiple layers are deposited on the surface of a high-purity, monocrystalline silicon (Si) wafer of different diameters (e.g. 150mm,

200mm, or 300mm). This requires multiple process steps such as epitaxy, lithography, and various vapor deposition (e.g. sputtering, ***C***hemical ***V***acuum ***D***eposition (CVD)) and etch (e.g. wet-chemically, ***R***eactive ***I***on ***E***tching (RIE)) processes. The second process group is the semiconductor wafer test, which consists of multiple sub-process steps like wafer handling, wafer probing, and inking. During IC testing on wafer level, called wafer probing, the functionality and specification limits of the dies are tested, in order to detect malfunctioning dies caused by contaminating particles, design, or manufacturing faults before further processing. Based on the test results a wafer map to separate "good" from "bad" chips is created. Subsequent to the wafer test, the assembly and packaging of the IC is done during the ***B***ack ***E***nd (BE) process group. Here the wafers are diced into separated dies and attached on a substrate, interconnects (I/O pads) of the chip are connected with bond wires on external pins of a lead frame or substrate, and the assembled chips are molded to protect them to the environment. In the final process group, the packaged dies are tested once more (Final Test), in order to sort out failing devices before marking and shipping to the customer [9].

For this work mainly the second process group, the semiconductor wafer test, is most relevant and therefore explained in more detail.

2.2 Semiconductor Wafer Test

The wafer test is mandatory for the semiconductor production for two main reasons. Firstly, wafer test is required to separate non-functional (bad) from functional (good) dies at an early stage of the manufacturing process chain. As the package and assembly processes are time consuming, it is more effective to assemble only good dies to save cost during IC manufacturing. Secondly, the generated functional data during wafer test also provide information regarding the process stability and yield (typically ≥ 80% for newly released and ≥ 95% for longer established technologies) of the semiconductor manufacturing process. This helps to optimize and speed up the IC production and so reduce costs significantly. To enable this, multiple tests are performed during the IC testing on wafer level. It usually starts with a parameter test, in which different electrical parameters (resistances, capacities, leakage, etc.) of active and passive components as well as conductive connections of the circuits are measured, and proceeds with a first functional test of the dies (e.g. test of reading and writing operations) [1,9,10].

During semiconductor manufacturing the dies are tested at different development levels. The main categories for IC testing are [1]:

1. *Validation of IC-design:* to ensure, that the IC fulfills all logical functions correctly
2. *Device characterization:* to qualify a new IC design before production ramp
3. *Wafer test or "wafer sort":* to sort out bad dies before further processing
4. *Package test or final test:* to verify the design specification after assembly
5. *Test for quality assurance:* to test packaged chips randomly
6. *Burn-in test:* to verify the drift of physical parameters after an artificial aging process
7. *Failure analysis:* to locate the cause of failure to increase device reliability

In order to supply power from the external test equipment and to transmit and receive electrical signals in and out to the die, the IC must be connected through small contact pins. The following sections will give the reader a deeper understanding of the wafer test process, its most important test system components, and the challenges during probing on wafer level.

2.2.1 Wafer Prober and Tester

A schematic view of a wafer test cell is shown in Fig. 2.2. The processed wafer is manipulated by a wafer prober, which main tasks are to load, hold, move, and unload the wafer on the chuck and to regulate its test temperature. The probe card is the interface between the semiconductor device and the electronic test system, called tester. Its purpose is to provide an electrical connection between the tester and the IC of the die. The tester applies the power to the chips and runs the specified test patterns of the IC controlled by a test program. To establish an electrical contact between the IC and the test system, the wafer chuck, which holds the wafer vacuum-sealed, is moved vertically up and down and laterally sideward to the mounted probe card. Thereon several elastic contact pins, which are microscopic in size, are assembled underneath. Depending on the number of pins and available tester channels, multiple dies can be tested simultaneously to

speed up the test time. This test method is called multi-DUT[1] or parallel testing [1,9,10].

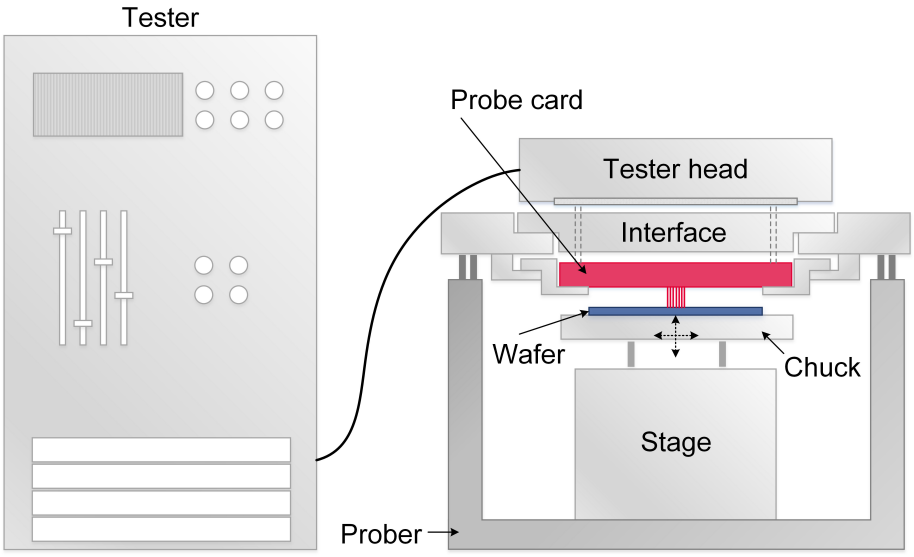

Fig. 2.2. Test cell with wafer prober and probe card.

2.2.2 Probe Card Technologies

Basically, probe cards consist of various main components. These are a multi-layer ***P***rinted ***C***ircuit ***B***oard (PCB), which acts as an interface between the contact pins (called probes) and the tester, a probe head (or needle ring) holding several probes, which are contacting the pads of a chip and are assembled in the upper and lower guide plate (or fixed in an epoxy ring) of the probe head. Fig. 2.3 shows a schematic view of a *vertical* probe card.

To ensure a reliable IC testing, despite of shrinking die size and hence more sensitive structures, the probes must fulfil probing specific demands such as small probe size, high electrical conductivity, and low contact force to avoid excessive pad damage. Table 2.1 gives an overview to this and some further important parameters characterizing a typical probe card [1].

[1] DUT: ***D***evice-***U***nder-***T***est

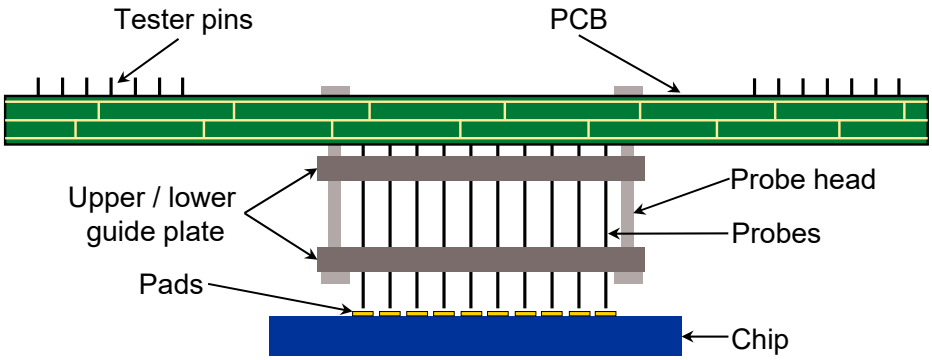

Fig. 2.3. Schematic view of a *vertical* probe card contacting a chip.

Table 2.1. Typical probe card parameters.

Parameter	**Value**
Max. pin count	>> 1000
Min. probe-to-probe distance	30µm - 60µm
Max. *xy*-alignment error	±10µm
Contact force per probe	30mN – 150mN
Contact resistance per probe	100mΩ – 500mΩ
Max. allowed current (DC)	200mA - 5A
Max. leakage	10nA
Probe life time	> 10^6 touchdowns
Probe material	Tungsten (W), Tungsten-rhodium alloy (W-Rh), Nickel-palladium alloy (Ni-Pd), Copper-beryllium alloy (Cu-Be)
Tip geometry	Flat, round, semi-round
Tip diameter	5µm – 50µm

There are three different state-of-the art probe card types, named according its needle technology as *cantilever*, *vertical*, and *MEMS* (***M***icro ***E***lectro-***M***echanical ***S***ystem) technology (see Fig. 2.4) [11]. *Cantilever* probes are widely used in production since a long time because of their short lead time and lower manufacturing costs compared to other probe card technologies [1,12]. Increasing performance and complexity of ICs, however, has driven continuously the number of I/O's and narrowing pad pitch (min. distance between two pads). Furthermore, increasing the test parallelism and thus decreasing test time is of high priority in the semiconductor production [9].

Because of its technical performance limitations a conventional *cantilever* probe card, which consist of an epoxy ring with manually mounted tens to hundreds of *cantilever* probes, would not be adaptable for the next-generation IC testing [12,13].

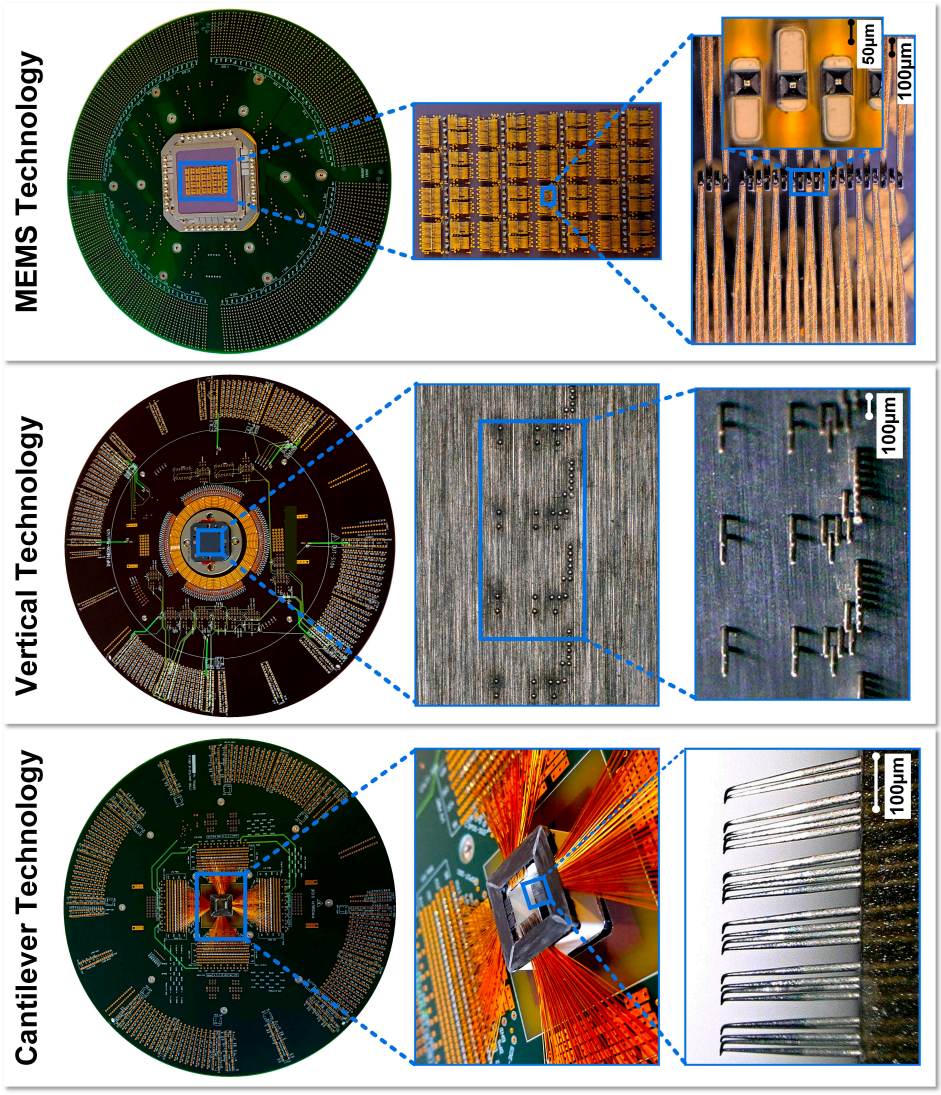

Fig. 2.4. *Cantilever*, *vertical*, and *MEMS* probe cards with close-up view to the probes.

Vertical probe cards offer a more effective alternative to this at acceptable cost. A more advanced version of probe card is based on *MEMS* technologies. Because of their great advantages over conventional probe cards, such as higher pin count, parallelism capability, and lower probe force, they have been accepted as a promising candidate for next-generation IC testing but with longer manufacturing times at relatively high costs. Therefore, *MEMS* probe cards are mainly used for high volume products, where parallel testing is required to reduce the test time [13,14].

To provide a physical contact between the probes and the metal pads of the dies on the wafer, all probing technologies use nearly the same principle. The wafer chuck, that holds the processed wafer, moves vertically towards the probes, which are mounted on the probe card and electrical connected to the tester. A relevant parameter thereby is the overdrive $\Delta z = z_1 - z_0$. It is defined as the vertical distance starting from the contact position ($z = z_0$) at which the first probe tip makes contact with the pad surface (contact force $F_z = F_c = 0$) to the final travel distance ($z = z_1$) of the wafer chuck. The probe, acting as an elastic spring, is deflected in a vertical direction by the same amount of overdrive causing a contact force between the pad and probe tip (see Fig. 2.5). A big enough amount of contact force, which is proportional to the applied overdrive Δz and the spring constant c_s (see Eq. (2.1)), is required to form a good electrical contact on the metal pad and hence guarantee a low and stable contact resistance (see Sect. 2.2.3) [1,10,11].

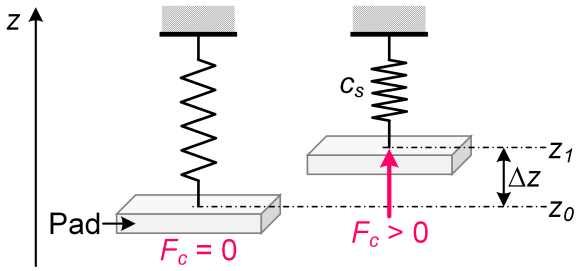

Fig. 2.5. Probe deflection mechanism.

As illustrated in Fig. 2.6, *cantilever* probes are mounted horizontally and bent downwards at the free end, which comes in contact with the metal pad during probing. Because of their design, *cantilever* probes exhibit mechanical deflection upon pad contact in vertical *z* and lateral *x* direction.

Cantilever probes linearly increase the contact force, F_z or F_c, with the applied overdrive (see Eq. (2.1) and Fig. 2.8).

$$F_c = c_s \Delta z \tag{2.1}$$

Their simultaneous lateral movement causes the probe tips to slide along the pad surface generating a scrub mark. Here a frictional force, F_x or F_f, depending on the coefficient of friction at the probe-pad interface, is applied to the probe tip [1,15].

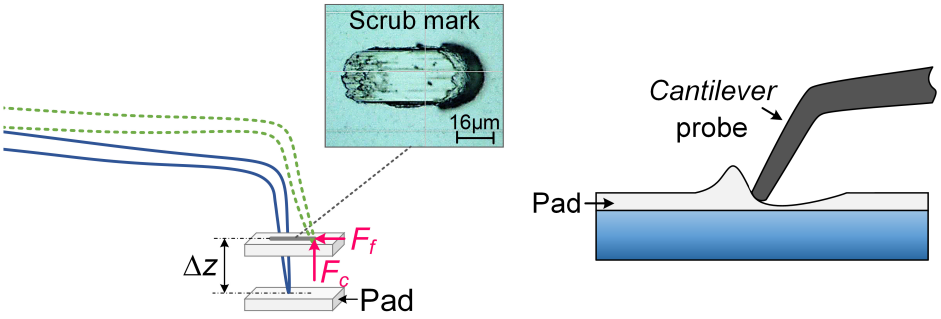

Fig. 2.6. Concept of a *cantilever* probe (l.) with scrub motion on the pad during probing (r.).

Vertical probes with a *buckling beam* concept are named according to the mechanical and respectively geometrical design of the probe (see Fig. 2.7). Because of the probe design and mounting configuration, *vertical* probes only cause a low, or even no, lateral scrub of the probe tips on the pad metallization [15].

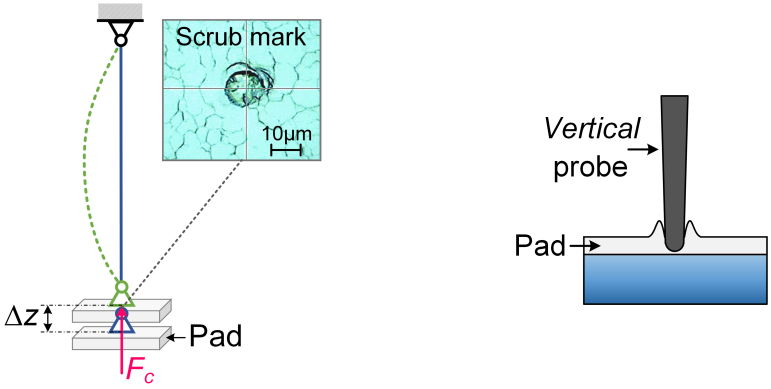

Fig. 2.7. Concept of a *vertical* probe (l.) without scrub motion on the pad during probing (r.).

Probes of *buckling beam* style are designed with mechanical properties for a saturation of contact force in terms of *Euler's* buckling load (see Fig. 2.8). *MEMS* probes can have both contact force characteristics of *cantilever* or *vertical* probes depending on their design. The major difference is caused by the lithographic manufacturing process of *MEMS* probes compared to conventional probes made of thin metallic wires [15].

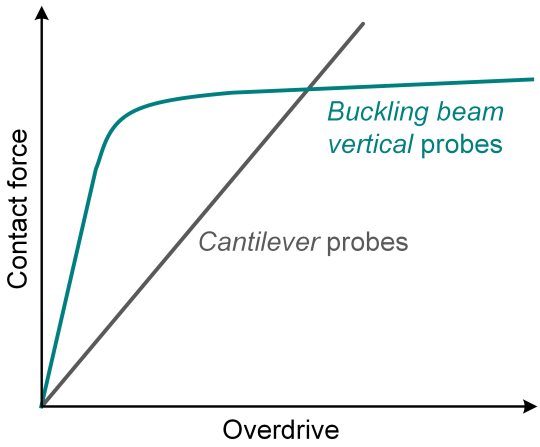

Fig. 2.8. Force displacement curve of *cantilever* probes vs. *buckling beam vertical* probes.

2.2.3 Electrical Contact Resistance during Probing

As explained in the previous section, a sufficient high contact force is required to achieve a low (< 1Ω) and stable electrical contact resistance between the probe and the contact pad [16]. In this section an analytical model of the electrical contact resistance is given, which is strongly dependent on the contact force and material parameters of the contact pairs pad and probe.

The Swedish scientist *Ragnar Holm* (1879 – 1970) developed the theory of electrical contact resistance. According to this, an electric contact is defined as a releasable junction between two conductors, or "contact pairs", which is apt to carry electric current [17]. In case of a current flow I, a voltage drop ΔU occurs between the interfaces of the contact pairs (see Fig. 2.9). The arising electrical resistance R_t at the transition points is defined by Ohm`s law and consists of two resistors in serial connection: bulk resistance R_b and contact resistance R_{ct} [1,18].

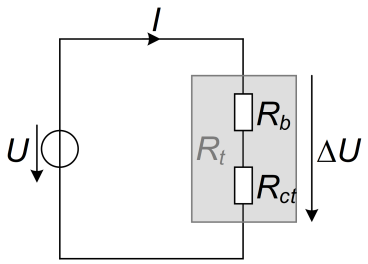

$$R_t = \frac{\Delta U}{I} = R_b + R_{ct} \tag{2.2}$$

Fig. 2.9. Electrical equivalent circuit diagram of transmission resistance.

The bulk resistance R_b is a constant value and depends on the electrical resistivity of the contact material ρ_m and the geometry of the electric conductor (length l_b and cross-section S_b) along the electrical signal's path [1,18].

$$R_b = \rho_m \frac{l_b}{S_b} = \text{const.} \tag{2.3}$$

In contrast, the value of contact resistance R_{ct} is the unknown variable of an electrical contact. The resistance appears at the transition point of the contact pairs and is made up of constriction resistance R_{co} and film resistance R_f of alien isolating layers [18–20].

$$R_{ct} = R_{co} + R_f \tag{2.4}$$

Since all real solid surfaces are rough on the microscale, the touching surfaces, which are pressed together by the mechanical load F_c, make contact at the surface spots and not on the whole contact area (see Fig. 2.10). This mechanical contact area is typically a small fraction of the nominal contact area, even for high contact loads. Due to oxidation films and other isolating films on top of the metal surface, only a part of the so-called load bearing area is electrically conductive [17,19,21].

The film resistance is given by the ratio between its material properties, like the specific resistivity ρ_f and thickness d_f of the insulating film, and the load bearing area A_b [19–21].

$$R_f = \rho_f \frac{d_f}{A_b} \tag{2.5}$$

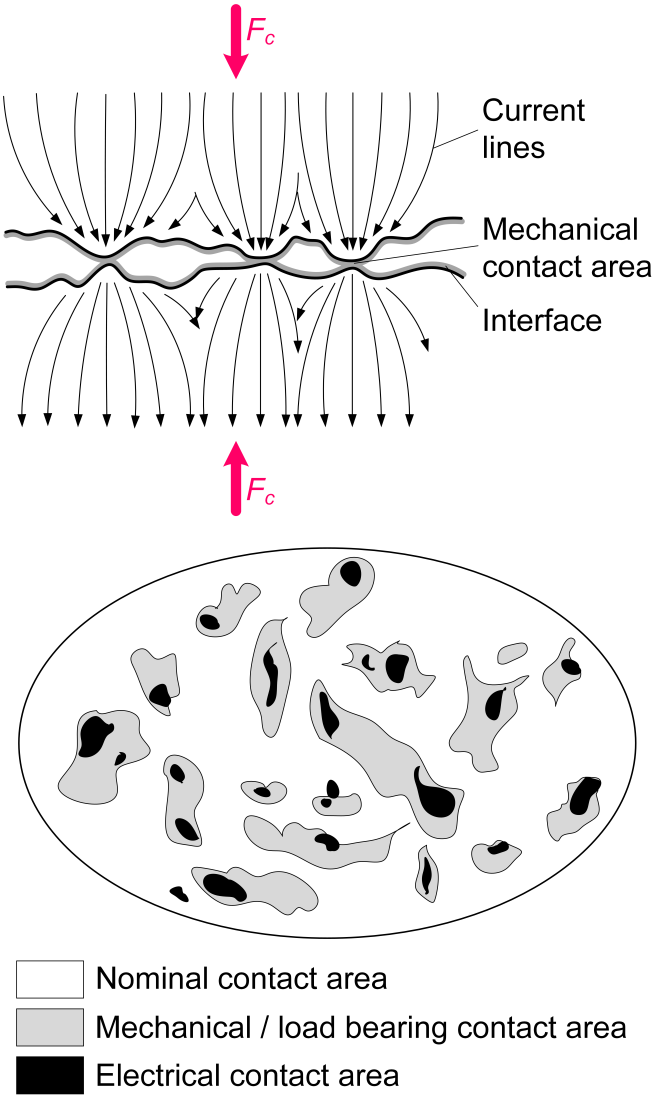

Fig. 2.10. Schematic of current constriction and subdivision of contact area (modified by [19]).

As shown in Fig. 2.10, left, the current flow is constricted through small conducting spots, the so-called α-spots, to cross the interface, which results in the emerging electrical constriction resistance R_{co} [21]. According to

Holm [17], its value for a single circular α-spot $R_{co,i}$ with the constriction radius a_i is given by:

$$R_{co,i} = \frac{\rho_m}{2a_i}, \tag{2.6}$$

where ρ_m is the effective specific electrical resistivity of the contact pairs. In practice an electrical connection comprises a multitude of n contact α-spots [21]. Its value can be found as a summation of α-spots over the nominal contact area.

$$R_{co} = \frac{\rho_m}{2\sum_i^n a_i} \tag{2.7}$$

To provide a low and stable contact resistance the electrically-conductive contact area has to be as large as possible. The constriction and hence the contact resistance can be reduced by increasing both: the number of α-spots and their dimensions [21]. As the load bearing area is smaller than the nominal contact area, α-spots must support local pressures that are comparable with the strengths of the materials of the contacting surfaces. If we assume plastic deformation of the contact pairs, the compressive strength σ can be expressed as hardness H of the softer material. Thus, the normal load F_c applied to the electrical interface is given by [20,21]:

$$F_c = A_b H. \tag{2.8}$$

If we assume that the electrical interface does not carry electrically-insulating films and its overall area emerges from a summation of n circular α-spots with radius a_i, distributed within a cluster with radius r_b, the load bearing area can be approximated as [21]:

$$A_b = n a_i = {r_b}^2 \pi. \tag{2.9}$$

With Eq. (2.7), (2.8), and (2.9) the constriction resistance R_{co} becomes:

$$R_{co} = \frac{\rho_m}{2}\sqrt{\frac{\pi H}{F_c}}. \tag{2.10}$$

Inserting Eq. (2.5), (2.8), and (2.10) in Eq. (2.4) the contact resistance R_{ct} can be expressed as:

$$R_{ct} = \frac{\rho_m}{2}\sqrt{\frac{\pi H}{F_c}} + \rho_f d_f \frac{H}{F_c}. \tag{2.11}$$

This equation indicates, that the contact resistance is influenced by the material properties of the contact members and depends on the variable value of the contact force F_c between the two surfaces in contact [1,6,19]. The relationship between the electrical contact resistance and the mechanical contact force is illustrated schematically in Fig. 2.11.

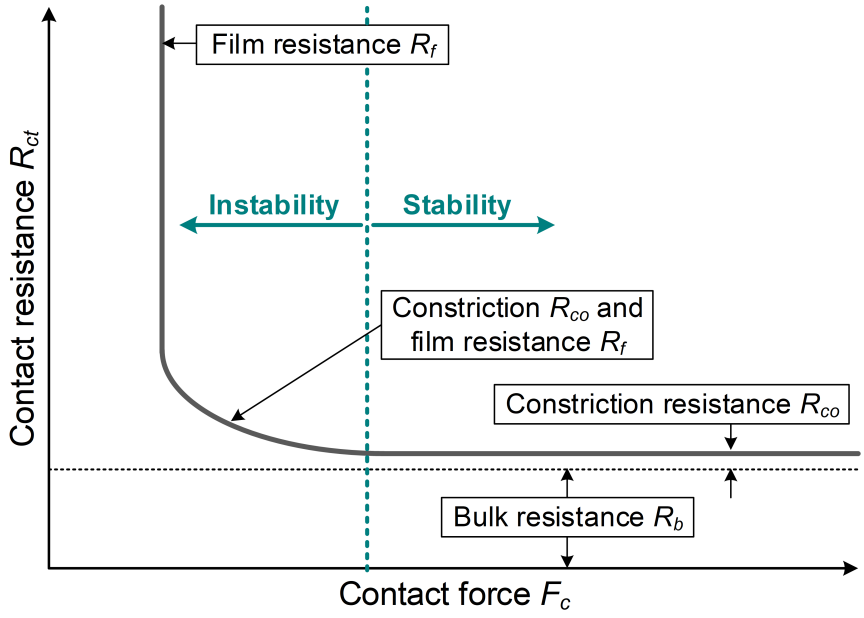

Fig. 2.11. Relationship between contact resistance and mechanical contact load (modified by [18]).

With an increasing number of tested ICs, however, the probes built up more and more adhesive pad or other foreign material at the contact area of the tip. The contamination can cause a not negligible change of the electrical contact resistant. In the worst case the resistance is too high, so that the device does not pass the IC testing resulting in yield loss. To avoid and remove contamination of probe tips, the probe tips are periodically cleaned. The cleaning is usually realized by multiple contacting on special cleaning materials either online, i.e. during wafer test on the prober, or offline, i.e. during probe card maintenance [1,6,22].

2.3 Probing-On-Active-Area

During wafer test every IC must be connected to external devices like a tester or other electronic components. For this purpose, small conductive

connector pins are normally placed on the top side of a die, which are called pads. The pads are not covered by passivation and so capable to be contacted by needles or wires (see Fig. 2.12). The number of pads per die, which are typically made of aluminum (Al), copper (Cu), or Al-Cu metallization, can vary from less than ten up to a few hundred depending on the application and power consumption. Dependent on the FE technology the pad size and thickness can vary, too. The pads have thicknesses between a few hundred nanometers up to several micrometers. The electrical connection to outside devices is realized by test needles (probes) temporarily during wafer test or permanently by bond wires during the assembly process of the chip [1,6].

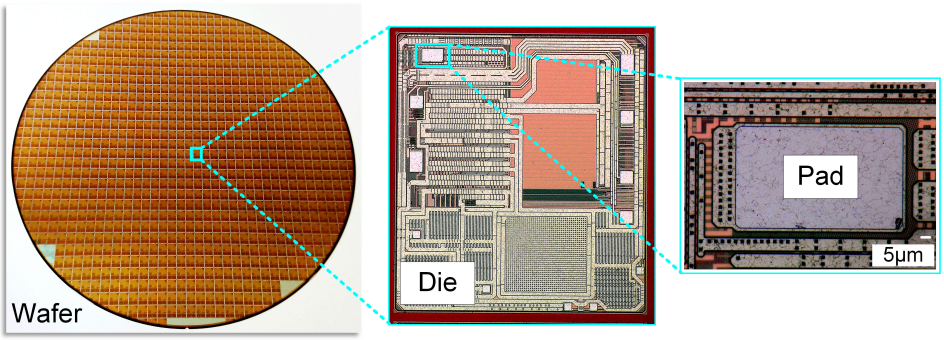

Fig. 2.12. Processed wafer with close-up view to IC die example and contact pad.

2.3.1 Pad Stack of CMOS Technologies

In order to minimize the defect density and power consumption and in parallel to increase the switching speed, the IC area and structural size are continuously shrunk. This fact, together with higher signal integrity, new materials, and design optimizations, brings essential performance benefits and yield improvements. Another effective way to reduce the chip size is to place the contact pads directly above the active structures of the ICs instead of placing them outside the active circuit area on top of pure Si, which was usually done in the past to avoid any damage of the IC. This design concept is called POAA and can reduce the die size up to 20% (see Fig. 2.13). The POAA method, however, creates another challenge for wafer testing. Instead of not having any crack-sensitive layers below the pad with the classical approach, the new POAA approach is facing brittle layer structures underneath, which are mechanically stressed during probing and so causing a reliability risk [16,23].

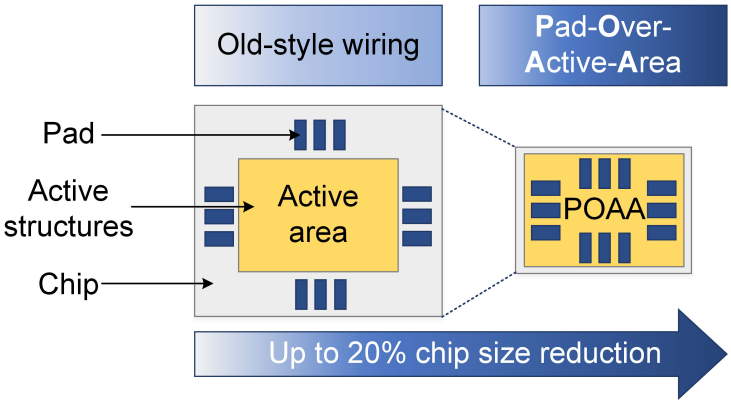

Fig. 2.13. Concept of POAA layout technology for CMOS devices.

In most advanced CMOS technologies the POAA method is implemented into the pad layout. Fig. 2.14 shows a schematic cross-section view of a POAA layer stack, which is typical for a CMOS technology. To interconnect thousands of active components of the IC, a multi-level metal routing technique is needed. Hereto, up to eight metal routing layers are required, which are reinforced and insulated to each other by non-conductive layers (e.g. SiO_x, poly Si, low/high-k materials). The metal layers are routed laterally and connected vertically to each other with small metal fill structures called vias. In the uppermost layer of the metal routing the passivation is removed to provide an external electrical connection to the contact pad [1,16].

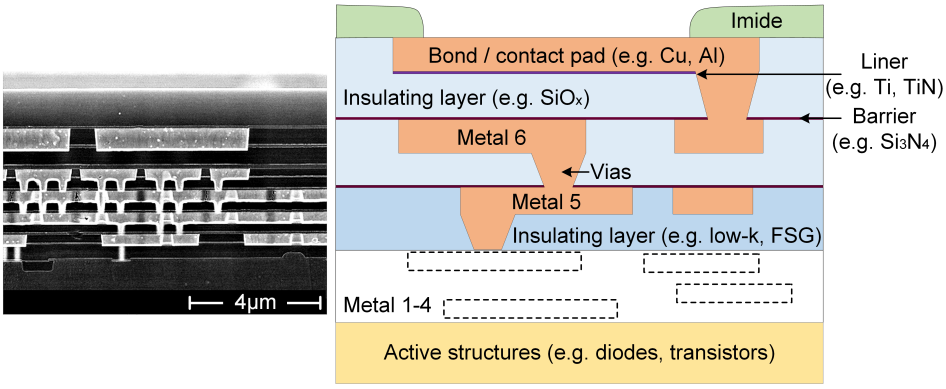

Fig. 2.14. SEM (l.) and schematic (r.) cross-section view of a CMOS BEOL stack.

To achieve a high switching speed with low power losses causing a temperature rise, a metallization with a high electrical conductivity is required enabling a high current density despite minimal dimensions. A low contact resistance through metal lines and transistors is also essential. Al and its alloys like Al-Cu fulfill these requirements. Thus, they have been the choice for routing and pad metallization since many years. The main advantages of Al include its low specific resistance, its excellent adhesion on SiO_x and interlayers like BPSG or PSG ((***B***oro-) ***P***hospho-***S***ilicate ***G***lass), its good intermetallic phase activation with gold (Au) during wire bonding, and its simple structuring in dry etch processes. The disadvantages of Al are that it only meets the requirements in mechanical hardness and resistance against oxidation corrosion. Metals such as silver (Ag) or Au show partly better electrical, chemical, or mechanical properties, but they are more expensive and cannot be etched in dry etching this easily. Instead of pure Al and its alloys, Cu can be used in order to reduce the risk of electromigration [1,24].

For reliable and robust contacts it is important to isolate the Al and Si layers to each other. To this, a diffusion barrier of materials like titanium (Ti), titanium nitride (Ti_3N_4), or W is deposited on top of the SiO_x layer [1,24].

Cu metallization has some significant advantages and thus is a good alternative especially for smaller feature sizes. Cu has a much lower specific resistance (1.7μΩcm) than Al (2.7μΩcm) and is much more efficient in view of power losses. Also the risk of electromigration of Cu is much less compared to Al. Since Al cannot fulfill requirements caused by structure shrinking and performance increase any longer, a metallization conversion to Cu is evident and already implemented for most advanced CMOS technologies [1,23,24].

In addition, for CMOS technologies using SiO_x as an IMD becomes increasingly critical. The ongoing shrinking of the die size causes the conductors for routing moving closer together in vertical and horizontal direction. To keep the value of the parasitic capacity low, which influences the electric properties like the switching speed or the power consumption, dielectrics with a low relative static permittivity ε_r, or simply low-k, are needed. Today low-k materials are often used in multi-level BEOL stacks, as IMD passivation layer as well as for the isolation of trenches. The low-k materials can be divided into the groups: doped oxides, organic materials, ***F***luorinated-***S***ilicate ***G***lass (FSG), porous materials, and combinations of them. The traditional dielectric, SiO_2, has a relative permittivity of 3.9. Low-k materials have lower relative permittivity than SiO_2, down to ca. 2 in case of

porous types [1,24]. Beside of the good electrical properties of low-k materials, the mechanical robustness is getting more fragile. Combined with the POAA approach low-k materials are more critical like SiO_2 layers, and so increasing the risk of mechanical failures during probing.

2.3.2 Pad Stack of Power Semiconductor Technologies

Similar to CMOS technologies, various power semiconductor technology classes are also affected by the POAA challenge in a slightly different way. Here the brittle layers are not evenly stacked alternating with metal routing layers as with CMOS BEOL stacks, but inhomogeneous metal-oxide structures forming the transistor are directly connected with the pad on top of the chip.

A widely used unipolar transistor for low and high power IC applications is the so-called MOSFET (***M***etal-***O***xide-***S***emiconductor ***F***ield-***E***ffect-***T***ransistor). It is applicable due to its low gate drive power, fast switching speed, and a good capability for parallel connectivity. Most power MOSFETs feature a vertical structure with the source and gate electrode on the top and the drain electrode on the bottom side of the die. Fig. 2.15 shows the basic cell structure of two typical power MOSFETs schematically [25–27].

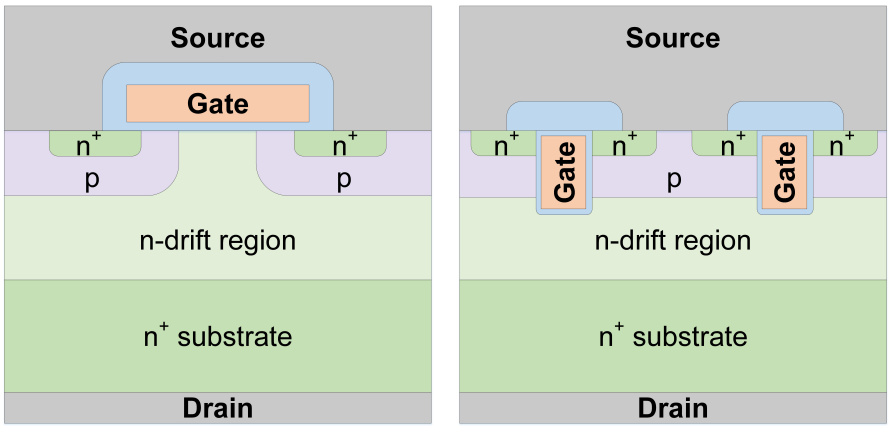

Fig. 2.15. Typical Si power MOSFETs: D-MOSFET with "planar-gate" structure (l.) and U-MOSFET with "trench-gate" structure (r.) (modified by [25]).

As can be seen on the left side, the double-diffused, or D-MOSFET, contains a "planar-gate" structure. The gate electrode (e.g. made of n^+ ploy Si) is located above the body electrode and insulated from all other device regions by a gate dielectric layer (e.g. made of silicon oxide (SiO_x)). Another

typical structure is the Si "trench-gate" power MOSFET, or U-MOSFET, structure that is shown on the right side. Its gate structure is embedded within a trench etched into the Si surface [26,27].

Fig. 2.16 shows a SEM cross-section of multiple trench-MOSFETs after FIB-milling. The power MOSFETs are directly connected to each other by their source metallization, which also serves as the contact pad for probing and wire bonding.

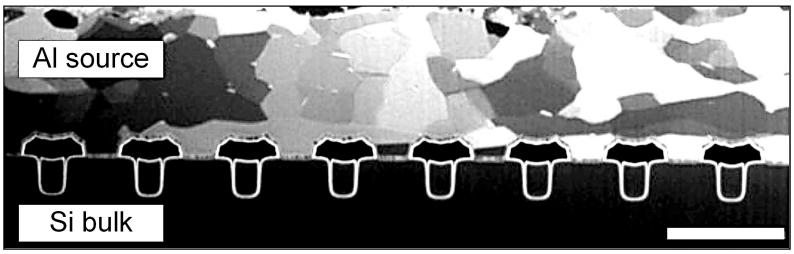

Fig. 2.16. SEM cross-section of multiple trench-MOSFETs after FIB-milling [28].

2.3.3 Crack Generation and Preparation of CMOS Back-End-Of-Line Stacks

Significant mechanical stress to the die and mainly to the I/O pad is applied consecutively during wafer probing, wafer dicing, wire bonding, packaging (molding, trim & form, final test), and finally during handling. In operation, the die can be stressed also thermally due to power losses during on & off state. As a result, any type of (thermo-) mechanical induced crack could propagate by further device processing, handling, and operation, which physically weakens its IC structure.

During wafer probing, the force and the scrubbing motion of a probe tip contacting the pad must be precisely controlled. Probe marks are not allowed to be too large and deep. Furthermore, cracks in brittle isolation layers underneath the probing area increase the risk of immediate or later electrical device failure. In contrast, a sufficient high contact stress is required to ensure stable electrical contacts with low contact resistance [1,29].

Fig. 2.17 highlights the problem schematically for a single *vertical* probe. The needle is contacting the pad, which is placed on top of a BEOL stack based on CMOS technology, inducing a high mechanical stress, which is causing an oxide crack, if the material-dependent fracture stress is

exceeded. Probe-induced stress on top of the stacked layers is mostly compressive within the contact area in case of a pure vertical force vector of the needle. For probes with a lateral scrubbing mechanism (mostly *cantilever* probes), also shear stresses are induced.

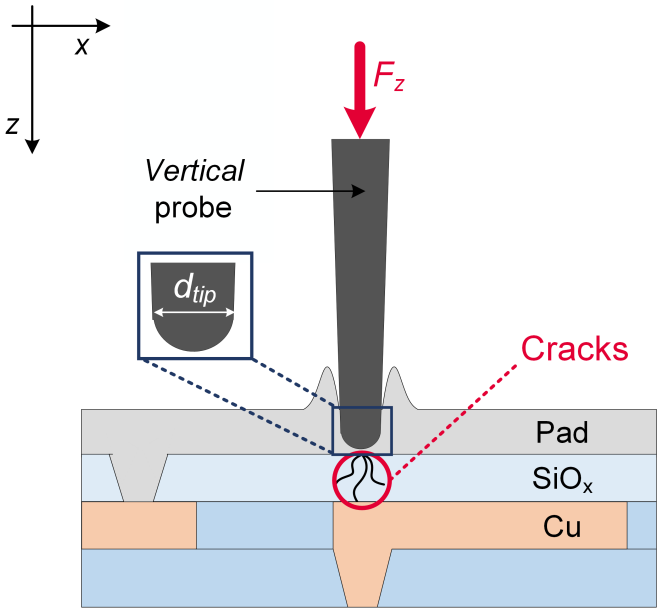

Fig. 2.17. *Vertical* probe contacting a pad over active area and thereby inducing oxide cracks.

Probing induced oxide cracks have typically a very short length (< 100nm) and thin gap size (< 10nm) depending on the brittle layer dimension. Even after the wet-chemical removal of all layers (e.g. pad metal, liner) deposited on top of the oxide, oxide cracks are nearly invisible using a conventional light or confocal microscope (see Chap. 3.1). If an oxide crack cannot be directly seen by a microscope, another method has to be used to indirectly find the crack location by optical microscopy. In this section, a method is described using the advantage of chemical preparation to decorate oxide cracks by improving the contrast of the optical inspection image. The concept of this method is to etch the metal layer below the oxide by an acid that infiltrates through the crack to the metal and so indirectly indicates a crack in the dielectric layer [1].

Fig. 2.18 shows the preparation of oxide cracks schematically for the example of a CMOS based technology with an Al-Cu pad metallization on top insulated from the Cu routing by a SiO_x layer.

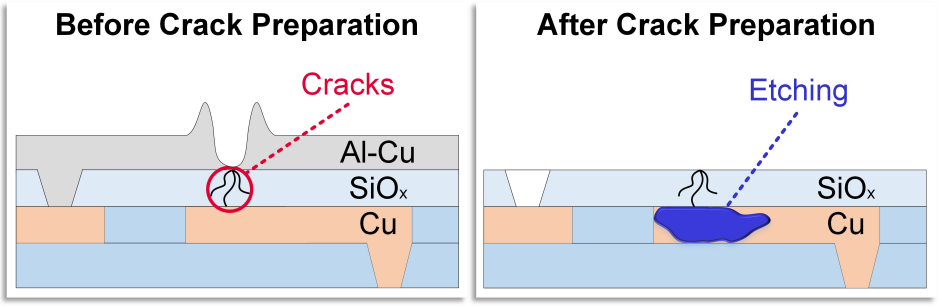

Fig. 2.18. Chemical preparation of oxide cracks.

The Al-Cu pad metallization can be removed by phosphoric acid (H_3PO_4) using a temperature of 70°C. If the subsequent optical inspection shows, that still pad metallization is remaining, this etch step is repeated until the Al-Cu is totally gone. The Al-bottom-liner is again removed wet-chemically. Even this etch step is repeated until the complete liner is removed, i.e. the layer or structures below the exposed SiO_x layer are visible. The etching, or "decoration", of potential cracks next the Cu layer below can be done by nitric acid (HNO_3). After etching, the sample is prepared for the indirect optical crack inspection using a light microscope. Fig. 2.19 shows an example to this.

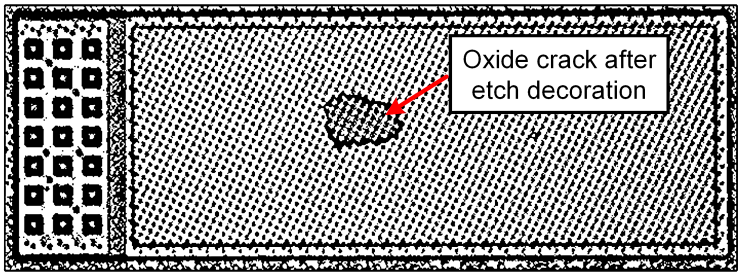

Fig. 2.19. Optical microscope image of an oxide crack after etch decoration.

2.3.4 Crack-relevant Electrical Device Fails

A worst case scenario during IC testing is an oxide crack that is not electrically detected during IC testing, but later on causes an electrical device failure in its working environment.

Relevant for CMOS technologies, the uppermost dielectric oxide layer directly underneath the pad is particularly critical for the IC testing and bonding. As later described in Chap. 7.1, probing induced cracks in brittle insulating layers are most likely related to cracks in diffusion stop layers (e.g. silicon nitride (Si_3N_4)). This layer, which is on top of the Cu metal routing layer, is intended to prevent Cu-diffusion into the isolation layer. Depending on the IC design, the metal routing layer and the pad can have an electric potential difference and so must be isolated to each other. Hence, cracks in diffusion stop and isolation layers can cause electrical leakage or shorts if a conductive path of Cu-metal is formed, driven by electromigration (see Fig. 2.20) [30].

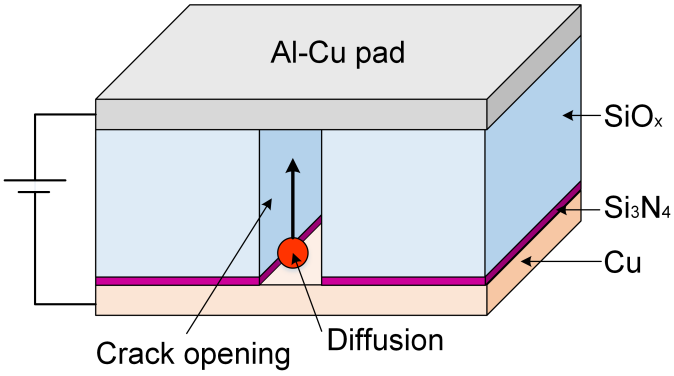

Fig. 2.20. Simplified explanation of Cu-ion electromigration along crack in isolation layer (modified by [1]).

Electromigration is recognized as a potential reliability risk in semiconducting devices. The failure mechanism is caused by mass transport (diffusion) of metal ions along circuit paths, if they are stressed by an electrical field. As shown in Fig. 2.21, the transport of metal ions is driven by two forces. The first one is the direct electrostatic force $\boldsymbol{F_{el}}$, which is caused by the electrical field $\boldsymbol{E_{el}}$ and so has the same direction as the vectors of the electrical field. The second one is the force from the exchange of momentum with other charge carriers $\boldsymbol{F_p}$ acting in opposite direction to the electrical field vectors. In metallic conductors this force is a result of the

so-called “electron wind”. Due to the shielding effect of the electrons, the force $\boldsymbol{F_p}$ is usually the dominant one. In contrast, the force $\boldsymbol{F_{el}}$ is relatively small. Therefore, the metal ions move towards the anode, while the resulting vacancies move in the direction of the cathode [31,32].

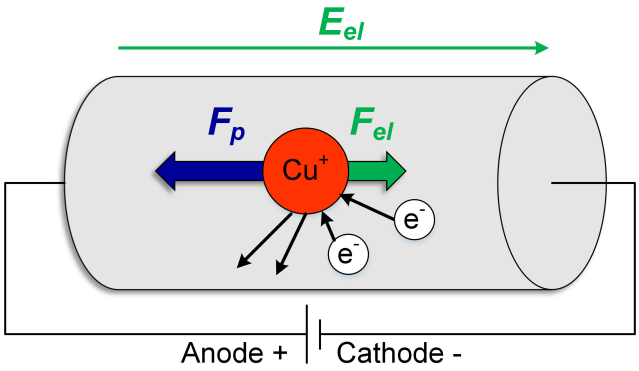

Fig. 2.21. Forces on ions in an electrical field.

According to *J. R. Black* the ***M***edian ***T***ime to ***F***ailure (MTF) is estimated by Eq. (2.12), where K_m is a material constant of the conductor path, J the current density, E_a the activation energy, k_B the *Boltzmann's* constant, and T_K the temperature in the conductor path [32].

$$MTTF = \frac{K_m}{J} \mathrm{e}^{\left(\frac{E_a}{k_B T_K}\right)} \tag{2.12}$$

For diffusion, the energy level of the diffusing ion must be temporarily increased. This energy demand is called activation energy. In general, diffusion processes occur faster at higher temperatures [31,32].

Besides electromigration, the void in the oxide layer can be filled also by Cu-material creeping driven by high mechanical stress. The FIB cross-section image in Fig. 2.22 shows an example to this. Here the Cu has squeezed into the small gap of the oxide crack due to the applied stress and so forming an electrically conductive path.

During wafer probing of MOSFET devices, the gate oxide insulation layer below the metal gate layer is most sensitive to cracks. A crack in the oxide can lead to a short circuit or leakage between the source and gate electrode. Fig. 2.23 shows a practical example to this.

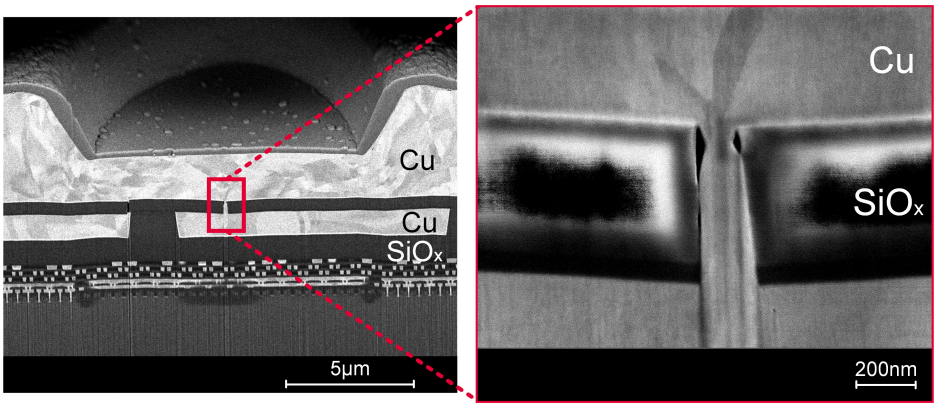

Fig. 2.22. FIB cross-section through the contact area after applying mechanical stress (l.) and close up view (r.).

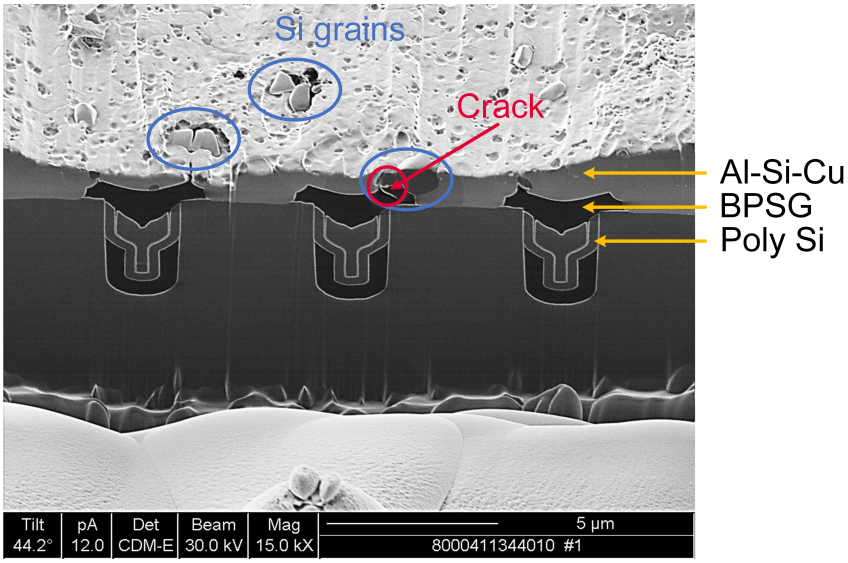

Fig. 2.23. FIB-milled SEM cross-section view of the contact area: Si grains adhere on the BPSG surface and increase its crack risk during contacting.

In the cross section view of a trench MOSFET chip, small Si grains, which are embedded in the Al-Si-Cu gate metal layer, are visible. During probing, the hard Si grains are pressed by the probe tip against the edge of the insulation oxide structure, which causes excessive stress concentrations at the edges of the insulation layer. In this example, the oxide has been cracked particularly at the edges of the trench transistor. The source (e.g. poly-Si)

and gate (e.g. Al-Si-Cu) metallization are shortened and thus can cause an electrical failure of the device.

All above described failure modes are caused by high probing induced stresses on sensitive structures. But there are two limiting factors for an easy detection of mechanical oxide damages. One is the lack of a reliable electrical indicator during wafer or final test, because the device fail must not happen definitely at or immediately after the crack generation. The other difficulty is given by the nano-scale dimensions and locations of cracks below the chip surface in lower brittle layers, which makes them hard and time-consuming to find. This problematic situation has to be solved by providing efficient crack detection methods. In the next chapter conventional inspection methods on pad and oxide damage are described together with technical details of optical and electron microscopes.

3 Conventional Pad and Oxide Damage Analysis

There are several check points during the FE- and BE-manufacturing process starting with a raw Si-wafer and ending with a fully functional, packaged device (see Fig. 3.1). Some quality control steps are done electrically (green arrows), like the ***P***rocess ***C***ontrol ***M***easurement (PCM) or wafer and final test, and some are done optically (purple arrows), as the inspection of the wafer, the wire-bond, the lead frame, or the mold compound. All tests and inspections are required to control, if the previous process was performed according to its specification without harming the wafer or device and if subsequent processes are not affected by any structural failures or damages. In this chapter it is described, which optical inspection methods and microscopes are applicable especially after POAA wafer test and how they are used to detect hidden oxide cracks below the pad metallization.

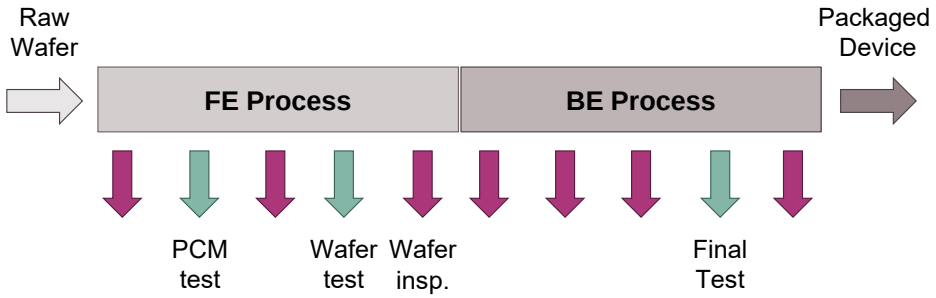

Fig. 3.1. Check points during semiconductor manufacturing process.

After wafer probing, the pads are optically inspected in a non-destructive way to control the allowed scrub or probe mark dimension (size and depth, see Fig. 3.2) and its relative position. Another quality check is to look for any pad metal removal caused by deep probe marks causing exposed oxide. Additionally to that, an optical control of the wafer surface is performed, to examine if there are any passivation imprints or scratches existent. In order to limit the optical inspection time during production, this must be done fast and therefore is only realized by a 2-dimensional image processing instead of doing time-consuming 3D confocal laser inspections.

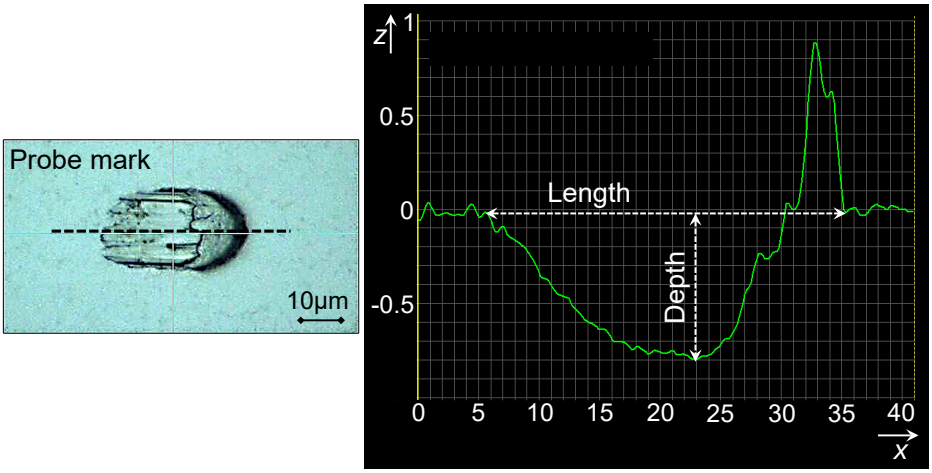

Fig. 3.2. Image of a probe mark (l.) and 2D depth profile (r.).

As described in Chap. 2.3, oxide cracks, which can occur during probing on POAA structures, are normally not visible by standard microscope inspections of the pad surface, so alternative methods must be used. To detect oxide cracks optically in lower layers the pad metal must be removed in advance (see Sect. 2.3.3), which is time-consuming, destructive, and therefore not applicable during wafer manufacturing.

Currently different types of light microscopy are used for pad and oxide damage analysis, like the ***D***ifferential ***I***nterference ***C***ontrast (DIC) or the SEM in combination with a FIB. In this chapter, the principles of the most common microscopy techniques are explained and some examples with typical images of failures are shown.

3.1 Light Microscopy

In the late 19th century the German physicist *Ernst Abbe* (1840 – 1905), who developed and manufactured optical instruments, described the maximal theoretical resolution of a conventional light microscope. Based on his work, the microscopic resolution limit could be considerably improved. Light microscopes have a resolution limit of approx. 0.2µm, which is dependent on the wavelength of the used light source. Such microscopes offer typical magnifications up to 1500 times. Today, modern techniques and processes have been developed and thus the *Abbe* limit has been overcome [33].

3.1.1 Digital Light Microscopy

Digital microscopes are equipped with a digital camera capturing the image of the sample. Hence, the viewing is done by a screen instead of eyepieces. In this work the digital microscope *VHX-6000* of the supplier *Keyence* was used (see Fig. 3.3). Its swing-head zoom lens enables magnifications from 20 up to 2000 times with a measurement resolution between 9.5µm (20 times) and 0.95µm (2000 times) in vertical and lateral direction. The microscope has a motorized stage that can be moved fully automatically with a theoretical resolution of ca. 0.1µm in *z*- and about 1µm in *x*- and *y*-direction. The lighting of the specimens can be done using full or partial coaxial or ring illumination as well as a mixture of them.

Fig. 3.3. Digital microscope *VHX-6000* of the supplier *Keyence*.

The *VHX-6000* is useful to get a quick and reliable 2D measurement of imprints on pad or oxide surface and device structures within a range of less than 1µm up to a few micrometers (see Sect. 3.1.4). Another application for the digital microscope is to measure the dimensions of indenter and probe tips, which will be explained in Chap. 6.1.

3.1.2 Differential Interference Contrast Method

The DIC technique was developed by the Polish physicist *Georges Nomarski* (1919 – 1997) in the 1950s and patented by the French National Center for Scientific Research (CNRS). It is a high-quality contrast method to produce proper images of transparent samples, like silicon dioxide (SiO_2), with high contrast and resolution. Its technique uses gradients in the optical path length and phase shifts to make tiny objects like cracks visible under a light microscope. The gained images are relief-like and seem to have a shadow cast [34].

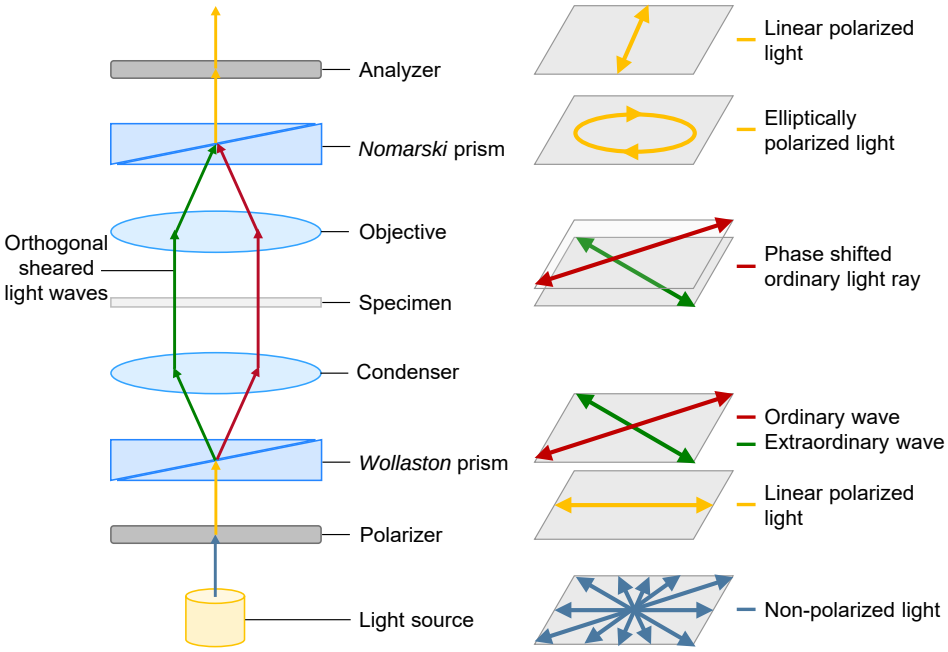

Fig. 3.4. DIC schematic by *Nomarski* (l.) and directions of light wave oscillations, if the ordinary light ray is phase shifted at the specimen plane (r.).

In the DIC method the specimen is illuminated by linear-polarized light, which is produced via a polarizer in front of the condenser (see Fig. 3.4). The *Wollaston* prism, which is placed in the rear focal plane of the condenser, splits the polarized light into two distinct light rays, the ordinary and the extraordinary wave. Both light rays are linear polarized, have orthogonal planes of polarization, and they are extremely close to each other. Due to local differences in the light-scattering and light-refracting properties of

the specimen, the light waves experience different phase shifts. The light waves are brought back together after passing the specimen by another prism, the *Nomarski* prism. Thereby, the light rays interfere with each other. A present phase shift changes the polarization of the light into an elliptical polarization, while linear polarized light that has not experienced any phase shift is now linearly polarized again. The analyzer allows only light out of one polarization plane to pass. Here it is the elliptically polarized light that can partly pass. The analyzer transforms the phase shift into an amplitude shift which leads to different light intensities in the resulting image. Furthermore, the *Nomarski* prism in a DIC capable microscope can be moved in its position in order to give the contrast a preferred direction and to create the impression of a three-dimensional relief-like image [33,34].

In this work, the DIC method was applied using the *Reichert-Jung Polyvar Met* light microscope (see Fig. 3.5).

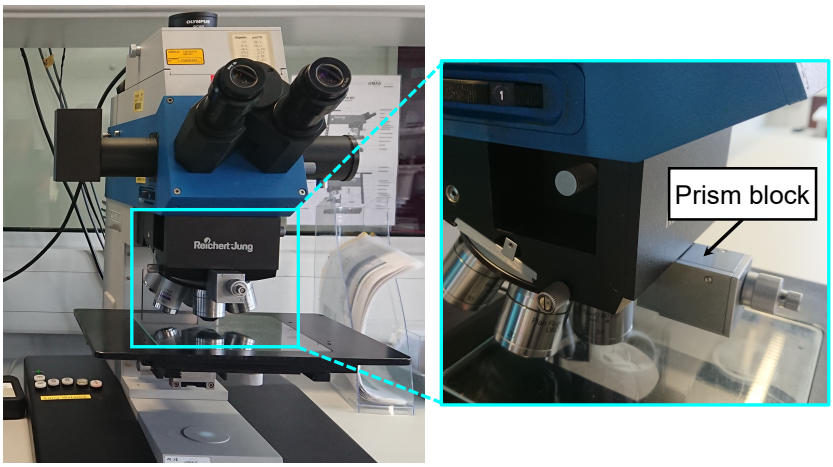

Fig. 3.5. *Reichert-Jung Polyvar Met* light microscope used for DIC method.

The configuration consists of six objective lenses (5x, 10x, 20x, 50x, 100x, and W150x) and two widefield plane compensating eyepieces with 10 times magnification (WPK10x). For the oxide crack inspection the LED light source of the microscope and mostly the 100x objective lens were used. Hereby an optical resolution of 3µm and a 1000x magnification were reached. To perform the DIC method, the prism block of the microscope was pulled in and a polarization filter was installed. To enhance the contrast in transparent samples, like SiO_2, a lambda/4 plate was built-in.

Via the knurled screw of the prism block the staining (any desired color or grey tint) of the object field could be adjusted. The image acquisition and processing was done using the *Olympus SC50* camera and their stream software.

The DIC method was of great interest for this thesis as it enabled a fast and high-accurate optical inspection of various oxide crack types, which were nearly invisible for classical light microscopes, gaining images with high resolution and contrast. Thus, it was the most suitable optical-light method of 2-dimensional inspections for small oxide cracks (see Sect. 3.1.4).

3.1.3 Confocal Microscopy

The confocal microscope principle was patented in 1957 by the US-American scientist *Marvin Minsky* (1927 – 2016). Today, his invention is employed in all modern confocal imaging systems. The main advantage of the confocal microscopy compared to the conventional light microcopy is the ability of the instrument to eliminate "out-of-focus" lens flare. This provides an increase in both lateral and vertical resolution and also the image contrast is improved [33,35].

The main difference between a light and a confocal microscope is the placement of two additional pinholes in the light path (see Fig. 3.6). The first pinhole is placed in front of the light source (e.g. a zirconium arc source or laser) and produces a point source of light. The light rays are deflected by a dichromatic mirror and focused on the surface of the specimen by an objective lens. The reflected light (and emitted fluorescence) from the specimen passes back through the same objective lens and a dichromatic mirror. The second pinhole is placed in front of the detector. Since both pinholes and the focus plane of the specimen are confocal or in focus to each other, only reflected light from the in focal plane passes through the pinhole and strikes the detector (see Fig. 3.6, left). In contrast, the reflected light from out-of-focus planes does not form a spot and thus is mainly blocked by the pinhole (see Fig. 3.6, right) [35].

The detector, which is usually a low noise photomultiplier, produces a signal that is directly proportional to the brightness of the light. In the confocal microscopy precisely focused 3D images are created through thin optical sections. To this, the specimen is scanned sequentially at multiple different focus planes and afterwards the individual images are composed [33,35].

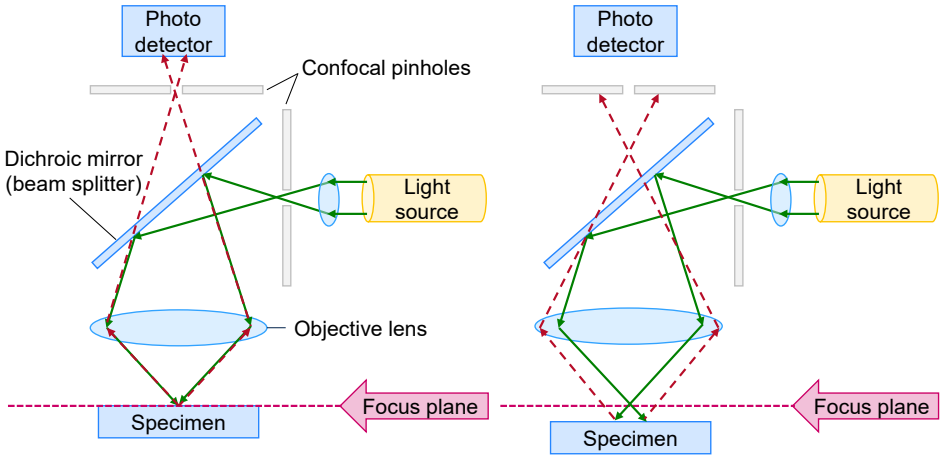

Fig. 3.6. Schematic illustration of the light path in a typical confocal microscope: specimen in focal plane (l.) and specimen not in focal plane (r.).

Fig. 3.7. Confocal laser-scanning microscope *μsurf custom* of the supplier *NanoFocus*.

To take 3-dimensional images of structures and surface topography of samples in nanometer dimensions, the confocal laser-scanning microscope *µsurf custom* of the supplier *NanoFocus* was used within this thesis (see Fig. 3.7). Its sensor technology is based on their patented ***C***onfocal ***M***ulti ***P***inhole (CMP) technology and offers a fast optical 3D surface measurement technique. The available configuration has a LED light source with a wavelength of 505nm. Under use of the lens with highest magnification (100x) and maximal pixel size (2048 x 2048) a theoretical lateral resolution of 0.08µm is achieved. During 3D height measurements the *z*-resolution of the *x*-*y*-*z*- stage is 1nm. For the measurements, the measuring and control software *µsurf metrology* was used. The software *µsurf analysis* enabled the visualization and analyzation of the recorded data.

Because of its high depth of field, the *µsurf custom* has proven to be excellent for measuring the 3D and 2D surface profile of the contacted area and determining the probe mark depth.

3.1.4 Field of Application of Light Microscopy

For 2-dimensional optical probe mark analysis after wafer test, usually the conventional or digital light microscopy is applied to inspect the probe mark position and the probe mark area on the pad (see Fig. 3.8, left).

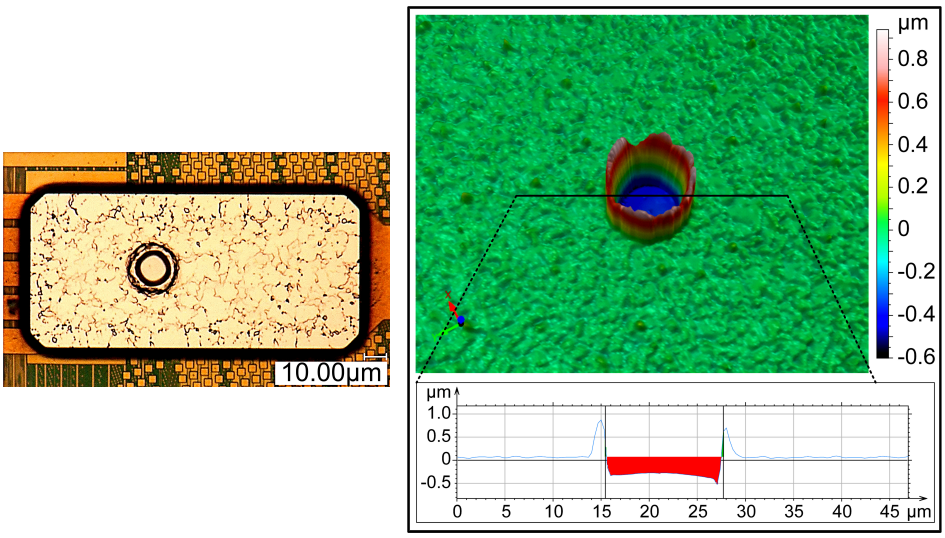

Fig. 3.8. Probe mark inspection (l.) and determination of the surface profile (r.) after indentation with a circular flat-ended 10µm diameter diamond tip.

However, for sub-micrometer 3D probe mark analysis this type of microscopy reaches its limits. The probe marks are usually some ten up to hundred nanometers deep, requiring a vertical measurement resolution in the nanometer scale. In addition, the pad metallization is reflecting and the edge slopes of the imprints are partly very steep. Compared to the *Keyence VHX-6000* the *NanoFocus µsurf custom* confocal laser-scanning microscope is more accurate to measure the 3D profiles. In this work the microscope and its analysis software were mainly used to derive a 2D or 3D profile of the probed surface and to determine the maximal depth of the probe mark (see Fig. 3.8, right). This feature was also applied to evaluate the plastic deformation of the pad metal with a probe mark and hence to assess the stress concentration, which was induced on the layer stack during contacting.

Another feature of optical microscopes is the inspection of oxide cracks below the pad, which are only visible after removal of the non-transparent layers above the cracked oxide. Using a conventional light microscope the detection of "macro-cracks" of micrometer size is relatively simple (see Fig. 3.9, left), while the detection of cracks in the nanometer scale is nearly impossible. To this, the optical microscopy can be extended by two advanced methods to make cracks indirectly visible: the chemical crack preparation (see Sect. 2.3.3) and the DIC method.

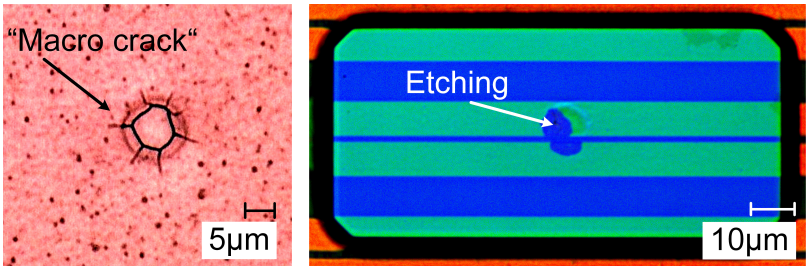

Fig. 3.9. Optical image of a crack with micrometer size (l.) and chemically decorated crack below the pad (r.) generated with a circular flat-ended 10µm diameter diamond tip.

Fig. 3.9, right indicates an oxide crack at the contact area, which was decorated by etching the Cu layer below the transparent oxide layer, in order to gain a higher contrast of the crack location. As the chemical etching method can only be applied if a metal layer is located directly below the crack, it does not work for complex and vertical integrated structures, which are typical for power semiconductor technology chips. Cracks, which have not propagated across the total oxide layer thickness ("semi" cracks)

or having extremely small gap sizes, so that the etchant cannot penetrate them, cannot be decorated by chemical preparation, too [1].

Compared to the normal light microscopy, the DIC method enables an oxide crack inspection to take images with higher contrast and resolution. The method does not require an upstream chemical crack preparation and hence is not limited to cracks with a metal layer underneath. Moreover, using the DIC method the detection of various IMD crack types, like semi and full cracks, is possible. Imprints with light oxide cracks show dark shadow regions around the imprint circumference, if the DIC method is applied. In Fig. 3.10, one can see on the images at the upper and lower left side imprints due to the contacting, but only the lower one shows a dark shadow region on its edge, indicating an oxide crack. The cross-section images on the right side of Fig. 3.10 were taken using the FIB-milled SEM method as a correlation.

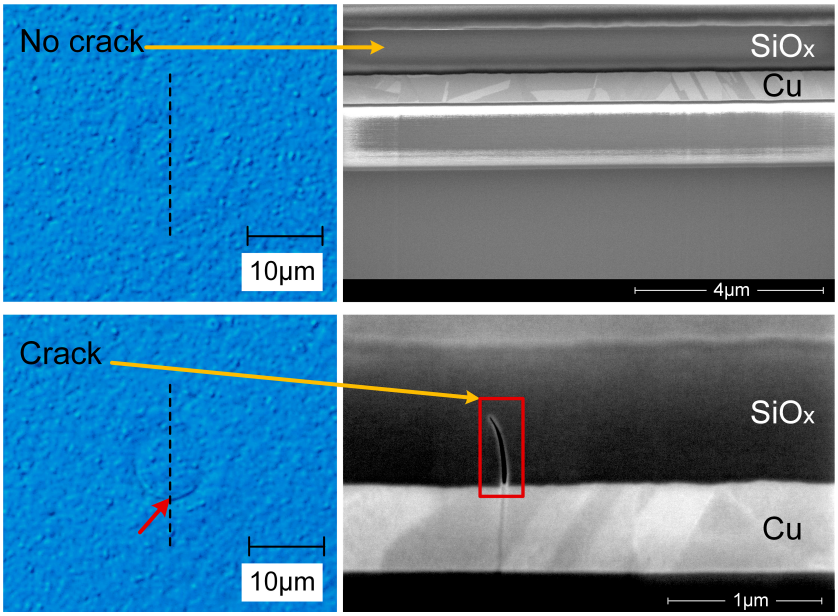

Fig. 3.10. Oxide crack inspection using DIC method (l.) and correlation with FIB-milled SEM images through the imprints (r.) generated with a circular flat-ended 10µm diameter tip.

The DIC method is much faster than the preparation of FIB-milled SEM cross-section images enabling significantly higher statistics. As the DIC method is based on the evaluation of phase shifts (see Sect. 3.1.2), layout-related structures can cause difficulties in interpreting the optical images

(see Chap. 7.3). To this, SEM cross-section images provide results that are more explicit.

3.2 Electron Microscopy

In the previous chapter it was explained, that the optical resolution achieved by DIC method or confocal microscopy is better compared to conventional light microscopes. However, even these kinds of microscopes have limitations in the resolution given by the wavelength of light. So electron microscopy with shorter beam wavelength was also used in this work for crack analysis, in order to get a higher resolution and depth of field.

3.2.1 Scanning Electron Microscopy

The first electron microscope was invented by the German engineer *Ernst Ruska* (1906 - 1988) in the 1930's. In contrast to conventional light microscopes, it uses electrons instead of light beams to create a magnified image. Since electrons have a much shorter wavelength compared to the visible light, electron microscopes achieve much higher resolutions (ca. 1nm) than normal light microscopes (ca. 0.2µm). Furthermore, electron microscopes enable magnifications of more than 100'000 times [33].

As shown in Fig. 3.11, the electrons are generated at the top of the microscope by a metallic filament (e.g. a tungsten hairpin cathode). The emitted electrons are formed into a beam and accelerated down the column toward the specimen. While moving downwards the beam is further thinned (diameter < 5nm possible), focused, and directed onto the specimen by electromagnetic lenses (condenser and objective lenses). Once the electron beam strikes the specimen surface, interactions between the electrons and the specimen surface are released. Thereby, the specimen surface returns electrons (e.g. secondary and backscatter electrons) that can be measured by suitable detectors. After the recorded signal is amplified, it is converted into a greyscale image, where the brightness is equivalent to the measured signal strength. In SEM the electron beam is scanned over the specimen surface by a certain *xy*-raster. The measurement is carried out under high vacuum to avoid any disturbance of the electron beam with air molecules. In case of insulating materials, a thin (ca. 5nm - 10nm), electrically conductive layer, such as Au or carbon (C), is deposited (sputtered) onto the surface of the specimen [33].

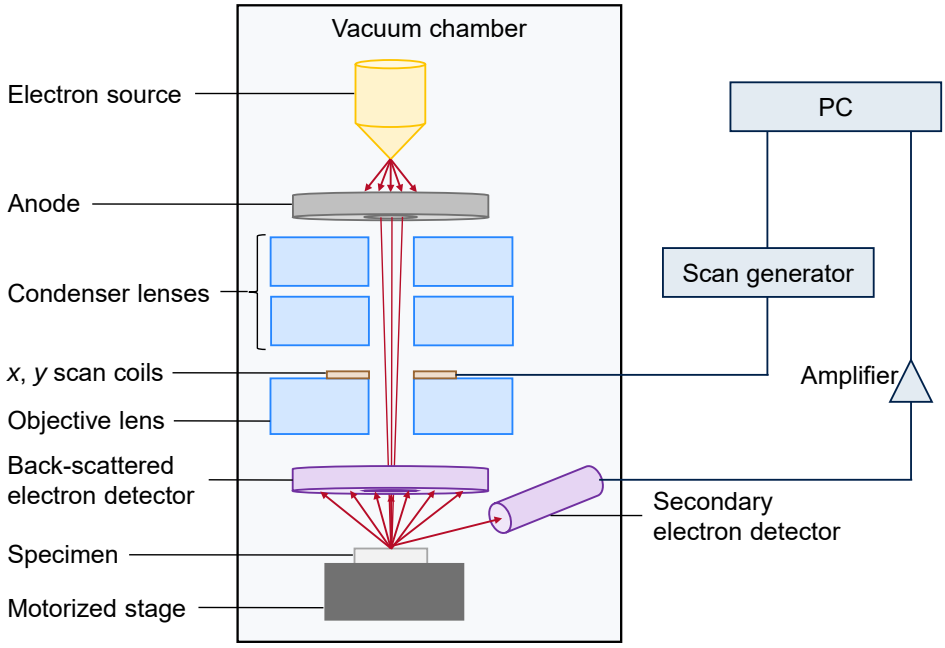

Fig. 3.11. Schematic principle of a SEM.

3.2.2 Focused Ion Beam System

A FIB system is nearly identical to a SEM microscope, but uses a beam of ions (e.g. Ga^+-ions) instead of electrons. Via the sputtering process, the FIB can directly modify or mill the specimen surface with nanometer precision. If the ion beam assisted chemical vapor deposition is used, also material can be deposited with a precision similar to the FIB-milling. Therefore, a small amount of a precursor gas is injected into the vicinity of the beam and then decomposed by the beam. The nonvolatile decomposition products deposit on the specimen surface, while the volatile products are extracted via the vacuum system [36].

3.2.3 Dual Beam Instrument

A FIB combined with a SEM is a more powerful tool as it combines the benefits of both. Using a so-called dual or cross beam instrument, simultaneous observation and nano-machining of materials is possible. This enables immediate, high resolution SEM imaging of the FIB-milled surface [36].

The top-down and FIB-milled cross-section SEM images, which are shown within this thesis, were mainly prepared with the dual beam instruments

Helios NanoLab 660 and *Helios NanoLab 450* of the supplier *FEI Company (*now *Thermo Fisher Scientific Inc.).*

For SEM the sample was glued on top of the sample holder with conductive Ag for grounding and then placed into the sample chamber of the microscope. After the vacuum was drawn up, the sample surface (usually SiO_x) was sputtered with a C layer of 6nm thickness to make it electrically conductive.

For the FIB-milling, a thin protective layer (e.g. 5nm C) was sputtered on the surface of the analysis region at first and then a trench was dug out. To detect even the smallest cracks, the step size of the FIB-milling was partly chosen extremely small, so that up to more than 100 cuttings at different locations per imprint could be made.

In this work, FIB-milled SEM cross-section images through the imprints were prepared to enable a very sensitive inspection of various oxide crack types and their orientation underneath the contact area. This method was also used to inspect the plastic deformation of the pad metallization and top metal layers after contacting.

3.2.4 Field of Application of Electron Microscopy

Compared to the optical methods described in Chap. 3.1, SEM cross-section imaging offers a more accurate crack investigation. The method enables not only the detection of different crack forming, like full and semi cracks, also the exact location and orientation of the crack is visualized in the orthogonal plane of the wafer surface. In the cross-section view in Fig. 3.12 one can see semi-cracks, spreading from the top and bottom side of the uppermost oxide layer.

Analog to conventional light microscopy, also the SEM cross-section imaging is a two dimensional method. To save inspection time it would be advantageous to locate the exact lateral position of the crack within the pad area using faster light microscopy. This, however, is usually not possible and typical oxide cracks propagate only a few hundred nanometers. As a result, the FIB-milling method must be applied in very small layer steps (e.g. > 100 steps per imprint) until the exact crack location is on target. Other disadvantages of SEM microscopy are charging effects by analyzing dielectric layers like SiO_2. Oxide cracks are therefore not easily detectable and there is always the risk that cracks are overlooked. Furthermore, the preparation of FIB-milled SEM cross-section images is very time-consuming (up to 90 minutes per imprint) and thus cost intensive. To reduce the

inspection time, SEM top-down images of the contact area can be made before the FIB-milling. This, however, only works, if the top pad metal layer was removed beforehand and the oxide layer has cracked from the top side.

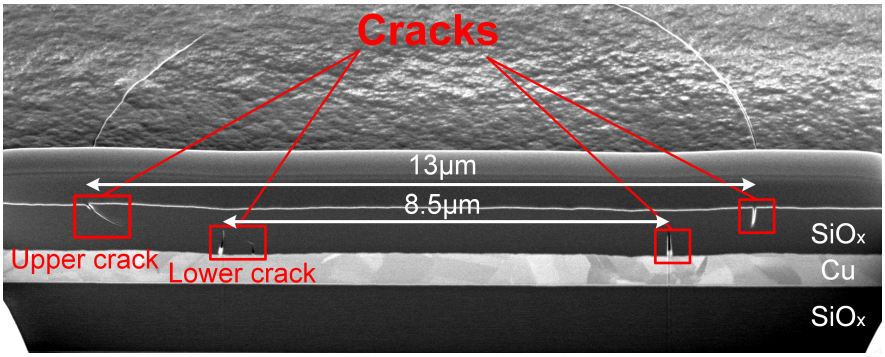

Fig. 3.12. SEM image after FIB-milling through the imprint generated with a circular flat-ended 10µm diameter tip investigating crack types and their location.

As shown in Fig. 3.13, the cross-section images can also be used to investigate plastic deformation of metal layers after contacting. The image on the left side presents an example for the plastic pad deformation, while the one on the right side visualizes the remaining deformation of the top metal layer.

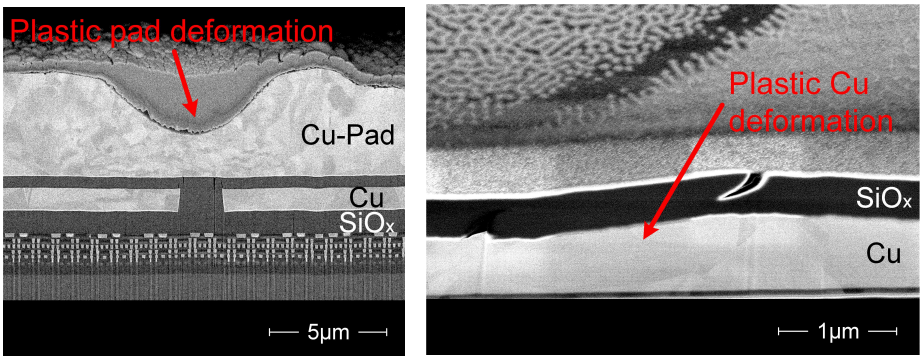

Fig. 3.13. FIB-milling SEM cross-sections through imprints generated with a circular flat-ended 10µm diameter tip revealing plastic deformation of the pad metallization (l.) and the top metal layer (r.).

All previously discussed failure inspection methods based on light and electron microscopy are suitable for an assessment of oxide cracks, which have potentially occurred after POAA probing. However, these methods for

crack detection need a preparation of the sample, which is destructive and time-consuming, and thus cost intensive. Hence, there is a high motivation to find a faster and more accurate method.

To detect cracks, this goal can be achieved by an innovative AE test method. In the following chapters, the concept and development of the novel method is described starting with an analytical and computer-simulation approach of mechanical stress calculations for a simplified contact model and the statistical determination of the crack probability. In the experimental part later in this work, the classical and new crack detection methods are compared and the accuracy is correlated based on the experimental results.

4 Contact and Fracture Mechanics

In this chapter, the theoretical basics of continuum mechanics with a definition of mechanical stress, material properties, and fracture mechanics are explained specifically for the use case of wafer probing on crack-sensitive structures of semiconductors. The theory of failure probability is given according to the *Weibull* model which is adequate to predict cracks on brittle materials. For the special application of probing on thin semiconductor layers, an analytical and computer-aided numerical model of contact mechanics of a flat punch on an elastic half-space solid is described. All this is mandatory for a fundamental understanding of crack occurrence during POAA, which is influenced by material, design, geometry, and mechanical loads of both, the probe tip and crack-sensitive test structures. In the future, the newly developed contact models can be used to predict the crack probability of new wafer technologies with POAA structures in advance by simulations and so to speed-up the expensive qualification effort.

4.1 Continuum Mechanics of Solid Bodies

The theory of continuum mechanics considers volumes of materials showing same physical properties everywhere as a continuum rather than discrete particles on atomic scale. Within this area of mechanics, the reaction of deformable solid bodies on external loads is studied [37,38]. External mechanical forces of a cylindrical solid body (probe), which interfere with the surface of another cubic solid body (sample) of a certain size and mass, are causing a pressure p on the contact area A (see Fig. 4.1). If the body of the sample is not mounted, it is moving from its original position depending on the mass inertia. If the sample is mounted on a fixed base plate as shown here, the reaction force is resulting in elastic or plastic deformations of the two bodies. The reacting contact pressure is a function of the applied force F and the interfering area A of the two bodies.

When a force $\boldsymbol{F}$ is uniformly distributed over a large area A, the traction vector $\boldsymbol{t}$ can be expressed by:

$$\boldsymbol{t} = \frac{\boldsymbol{F}}{A}, \tag{4.1}$$

where $\boldsymbol{t}$ represents the force intensity vector with respect to the surface area on which it is applied. In contrast, if the force varies in direction and

intensity over this area, the traction should be defined at an infinitesimal area which approaches zero (*Cauchy's* principle, Eq. (4.2)) [39].

$$\boldsymbol{t} = \lim_{\Delta A \to 0} \left(\frac{\Delta \boldsymbol{F}}{\Delta A} \right) = \frac{\mathrm{d}\boldsymbol{F}}{\mathrm{d}A} \tag{4.2}$$

The two components of the traction vector $\boldsymbol{t}$ are normal stress σ and shear stress τ, which are normal and parallel to the area's surface (see Fig. 4.1). Using $\boldsymbol{n}$ for the unit normal vector to the surface and $\boldsymbol{s}$ for the unit vector parallel to it, the stresses are:

$$\sigma = \boldsymbol{t} \cdot \boldsymbol{n} \text{ and } \tau = \boldsymbol{t} \cdot \boldsymbol{s}. \tag{4.3}$$

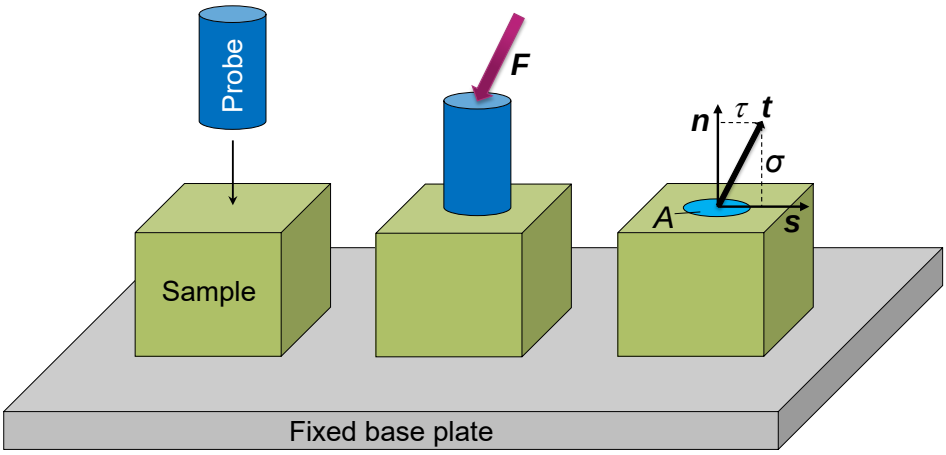

Fig. 4.1. Contact model of two solid bodies.

4.1.1 Mechanical Contact Stress

Per definition, the mechanical contact stress is equal to the normal force F divided by the planar intersection area A of the body under load. Tension and compression are both normal stresses σ, meaning the force vector is rectangular to the intersection area. If the force is applied parallel to the intersection area A, the load is inducing a shear stress τ into the body [37].

Any force, acting on the faces of a volume element, generally produces both normal and shear stresses. Furthermore, the state of stress at a point is three-dimensional. The illustrations of two infinitesimal small bodies in *Cartesian* coordinate systems in Fig. 4.2 depict the idea of stress. The force components $\mathrm{d}F_x$, $\mathrm{d}F_y$, and $\mathrm{d}F_z$ act perpendicular to the plane of the element

in the x, y, and z directions, respectively. When, for example, the force component dF_x acts normal to the plane $dydz$, the stress is a normal stress.

$$\sigma_{xx} = \frac{dF_x}{dydz} \tag{4.4}$$

The different stress components are expressed using two indices. While the first index, i, identifies the plane orientation, the second one, j, defines the direction of the applied force. The symbol σ_{xx} denotes a normal stress, with a plane of consideration and applied force whose normal is in x-direction, respectively. Although the assignment of the sign is purely arbitrary, tensile stresses are typically defined to be positive and compressive stresses negative [37].

The force components also act across other planes. For example, the force component dF_y acts parallel to the $dydz$ plane and so produces a shear stress, which is indicated by τ_{xy}.

$$\tau_{xy} = \frac{dF_y}{dydz} \tag{4.5}$$

Similar to the normal stress the assignment of the sign is purely arbitrary. The shear stress is usually defined to be positive, if the direction of the line of action of the stress inducing forces and the direction of the outward normal to the surface of the volume element are of the same sign.

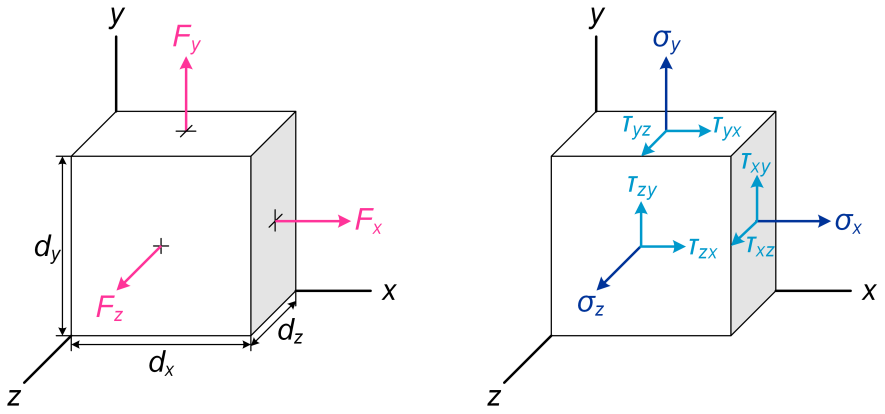

Fig. 4.2. Forces acting on the faces of a volume element and resulting stresses in *Cartesian* coordinates (modified by [37]).

As visualized in Fig. 4.2, each of the three surfaces contains three stress components (e.g. dydz: σ_{xx}, τ_{xy}, τ_{xz}). The stress condition on the volume element d*x*dydz is thus given by a total of nine expressions, which in matrix notation becomes:

$$\begin{bmatrix} \sigma_{xx} & \tau_{xy} & \tau_{xz} \\ \tau_{yx} & \sigma_{yy} & \tau_{yz} \\ \tau_{zx} & \tau_{zy} & \sigma_{zz} \end{bmatrix}. \tag{4.6}$$

This grouping of the nine stress components is the stress tensor $\boldsymbol{\sigma_{ij}}$, which fully describes the state of stress at any point of a body.

$$\boldsymbol{\sigma_{ij}} = \begin{bmatrix} \sigma_{xx} & \tau_{xy} & \tau_{xz} \\ \tau_{yx} & \sigma_{yy} & \tau_{yz} \\ \tau_{zx} & \tau_{zy} & \sigma_{zz} \end{bmatrix} \tag{4.7}$$

The diagonal elements of the square matrix are normal stresses indicated by σ_{ij}, whereby the second index is often omitted, i.e. $\sigma_{xx} = \sigma_x$ and so on. The off-diagonal members are the shear stresses defined by τ_{ij}. In the mechanical equilibrium state of the element area the stress matrix is symmetrical, i.e. $\tau_{xy} = \tau_{yx}$, $\tau_{yz} = \tau_{zy}$, and $\tau_{zx} = \tau_{xz}$. Hence, the nine components of the stress matrix reduce to six independent stress components acting on any infinitesimal volume element of the stressed body [37].

4.1.2 Principle Stresses

In many practical cases, constructional components are externally loaded simultaneously by normal (tensile or compressive) and shear stresses. As in complex structures the maximum normal and shear stresses are often at different positions, it is important to know, at which point of the component the maximum stress is located. In the following text, the concept of principal stress is explained, which is useful to find the location of maximum stress.

In a homogeneous stress field it is possible to find three mutually orthogonal planes which intersect at the point of maximum stress within the solid and are orientated in such a way that the shear stresses get zero. To satisfy the prerequisite of zero shear stress, the orientation of the planes is different at any other point in a solid body. With the only remaining normal components of stress σ_x, σ_y, and σ_z the square matrix of Eq. (4.7) becomes [39]:

$$\boldsymbol{\sigma_{ij}} = \begin{bmatrix} \sigma_x & 0 & 0 \\ 0 & \sigma_y & 0 \\ 0 & 0 & \sigma_z \end{bmatrix}. \tag{4.8}$$

The three planes of zero shear stress are referred to as the "principal planes of stress". The normal stresses, acting on these planes, are termed the "principal stresses". They are extreme values, representing the maximum ($\sigma_x = \sigma_1$), intermediate ($\sigma_y = \sigma_2$), and minimum ($\sigma_z = \sigma_3$) normal stress acting at the considered point within the solid body [37,39].

As the principal stresses give the maximum values of the tensile and compressive stress, they have particular importance in the theory of strength of solid bodies and are valid for brittle materials [37]. According to the ***N***ormal ***S***tress ***H***ypothesis (NSH), the highest amount of normal stress causes material failure and the fracture occurs, if the principle stress exceeds a critical value [1,40].

In a 2D plane stress state the maximal and minimal normal stress values, σ_1 and σ_2, acting at the point of interest (x, y) within the solid body, can be obtained from:

$$\sigma_{1,2} = \frac{\sigma_x + \sigma_y}{2} \pm \sqrt{\left(\frac{\sigma_x - \sigma_y}{2}\right)^2 + \tau_{xy}^2}. \tag{4.9}$$

The principle stresses are labeled so that $\sigma_1 > \sigma_2$. By convention, the tensile stress is defined positive and thus refers to the maximum principal stress σ_1, while the compressive stress with negative sign refers to the minimum principal stress σ_2. The shear stress τ_{xy} acts across a plane, which is orthogonal to the x-axis in the direction of the y-axis and is equal to τ_{yx} (see Sect. 4.1.1) [37].

Later in this thesis it becomes obvious, that the principal stresses are useful to identify the real contact stress distribution within the specimen by FEM-simulations. As the model of the test specimen is 2-dimensional, only the principal stress components σ_1 and σ_2 are used in the following contour plots.

4.2 Material Strength of Solid Bodies

Every solid body of a different material reacts differently to external physical influences like force or temperature. This behavior is described in the material science and independent of the size and geometry of the body. Material properties of solid bodies, such as yield strength, ultimate strength, *Young's* modulus, and *Poisson's* ratio, are part of every material specification and are derived by tensile testing, for instance. The meaning material properties are described in more detail in this chapter.

In tensile test according to DIN EN 10 002, a tensile specimen with circular or rectangular cross-section is stretched at constant velocity in uniaxial direction until it fractures. Thereby, the tensile load F_t is constantly distributed over the cross-section area of the specimen.

During tensile testing (see Fig. 4.3) the tensile force is measured as a function of the specimen extension, $F_t = f(\Delta L)$. If the measured force F_t is referred to the initial cross-section area A_0 and the change in length $\Delta L = L - L_0$ compared to the initial length L_0, one obtains the stress σ (see Eq. (4.10)), which has the dimension force per unit area, and strain ε (see Eq. (4.11)), which is usually given in percentage [19,40].

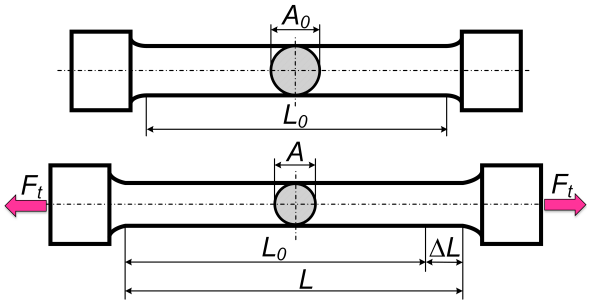

$$\sigma = \frac{F_t}{A_0} \tag{4.10}$$

$$\varepsilon = \frac{L - L_0}{L_0} = \frac{\Delta L}{L_0} \tag{4.11}$$

Fig. 4.3. Deformation of the specimen due to tensile load.

Fig. 4.4 shows a stress-strain curve for a metallic, or ductile, material schematically. In the following, its characteristic points and regions will be explained.

The characteristic region 1 (blue area) is called "*Hooke's* region". It shows a linear relationship between the stress σ and strain ε. Within this region, the material returns to its original dimensions after the load is removed. As there are no permanent deformations, i.e. the atoms return to their original position, this type of deformation is termed reversible, or elastic. The *Young's* or elastic modulus E is the proportionality constant in *Hooke's* law and thus given by:

$$E = \frac{\sigma}{\varepsilon}. \tag{4.12}$$

In general, a high elastic modulus means, that the material has a high resistance to elastic deformability.

The maximum stress reached in the elastic region of the stress-strain curve (blue area) is referred to as upper yield strength σ_{yh}. It is the highest stress

at which a material can be subjected to a uniaxial tensile load without a permanent deformation.

An irreversible deformation is named as plastic, if the atoms are permanently displaced from their positions and so the material cannot fully recover its original dimensions after the load is removed. More precisely, the plastic deformation is based on the movement of one-dimensional errors, the dislocations, on slip planes. As during the movement dislocations are additionally generated and crimp each other, this leads to an increase in strength, the so-called strain hardening. Hence, the plastic deformation becomes more and more difficult with rising load.

Within region 2 (bright green area) the stress-strain curve of materials with pronounced yield strength shows a discontinuity. It starts with the upper yield strength σ_{yh} and ends with a renewed increase in stress. This means the material yields, while the stress immediately decreases at first and then is almost constant. The lower yield strength σ_{yl} is a consequence of the upper yield strength and the smallest stress in the plastic deformation range with increasing specimen extension. The so-called *Lüders* elongation ε_L is defined as the specimen extension at the end of the discontinuity minus the elastic part.

In region 3 of strain hardening (dark green area) and region 4 of necking (pink area) the σ-ε-curve proceeds continuous and arcuate. The peak of the technical stress-strain curve identifies the ultimate tensile strength σ_u of the material. At this stress, the solidification due to microstructural processes and the refortification caused by the reduction in cross-section are in equilibrium. When the tensile specimen is unloaded at the ultimate tensile strength σ_u, its uniform elongation ε_u is given by its total elongation ε_{ut} minus the elastic part. The total elongation ε_{ut} at the ultimate tensile strength indicates that the tensile specimen does not neck up to the ultimate tensile load, but extends uniformly over the entire length of the specimen.

After reaching the maximum, the necking of the specimen starts (pink area). With increasing elongation the cross-section A_o of the tensile specimen decreases until micro-cracks occur, which grow together to form larger cracks and finally it comes to a fracture at the fracture stress σ_f. The ratio of the lateral contraction $\varepsilon_\perp$ to the longitudinal extension ε_{II} of the

specimen is called *Poisson's* ratio ν (see Eq. (4.13)). It is a material constant and thus has to be determined experimentally.

$$\nu = \frac{\varepsilon_{\perp}}{\varepsilon_{II}} \tag{4.13}$$

The elongation at fracture without the elastic part is referred to as fracture elongation ε_f. The total elongation at fracture is given by ε_{ft} [19,40].

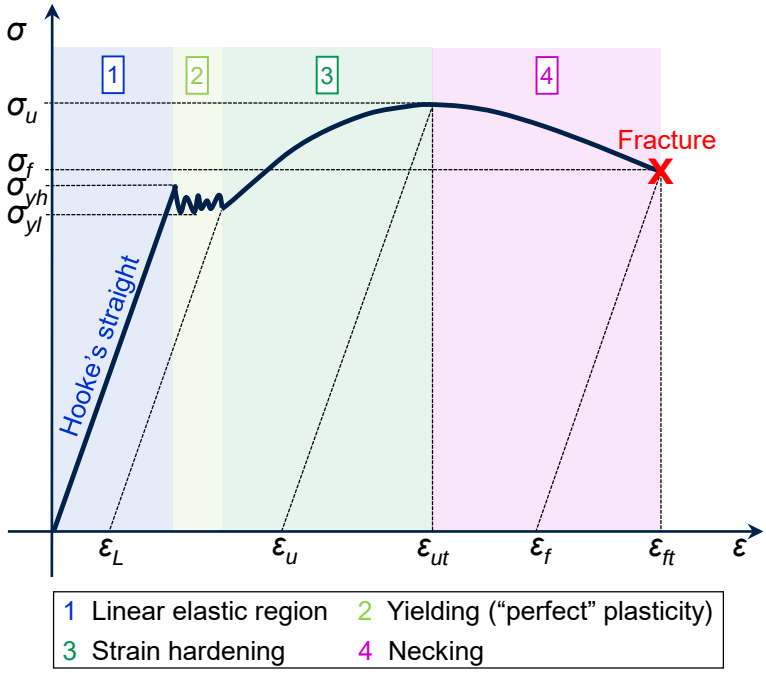

Fig. 4.4. Technical stress-strain curve for ductile materials with pronounced yield strength (e.g. construction steel) naming its characteristic points and regions.

Other than ductile materials described above, brittle materials like ceramics have a smaller fracture elongation and rupture near the elastic limit. The brittle fracture occurs suddenly and the stored deformation energy is released in form of new surfaces, heat, and kinetic energy [1]. Fig. 4.5 exhibits the basic difference in the stress-stain curves for ceramics (a) and metals (b).

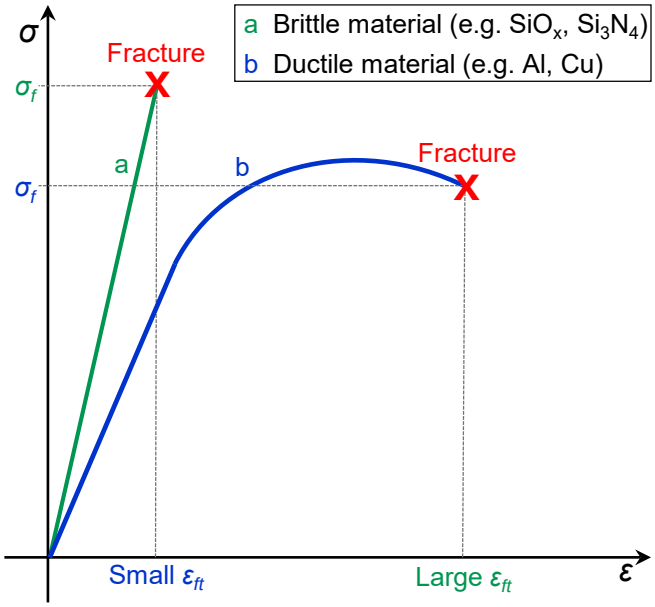

Fig. 4.5. Schematic stress-strain curves for brittle and ductile materials without pronounced yield strength.

Materials like glass or ceramics are brittle at room temperature and become only plastically deformable at high temperatures. The reason for this behavior is due to the differences in the atomic bonding structure of metals and ceramics [1,19]. In general, brittle materials have higher elastic moduli than ductile materials (see Table 7.2 in Chap. 7.1).

The stacks of various FE technologies are usually composed of multiple layers with different material properties and structuring (see Chap. 2.3). Typical materials are metals, like Al or Cu, and ceramics, like SiO_x and Si_3N_4. As each material has different material properties, the stress-strain curves are different as well. If an external force is applied both material types deform according to *Hooke's* law at first. Once the reacting stress exceeds a critical value the fracture characteristic is either brittle (ceramics) or ductile (metals).

4.3 Linear-elastic Fracture Mechanics of Brittle Materials

Within this work, a detailed understanding of ***L***inear-***E***lastic ***F***racture ***M***echanics (LEFM) for brittle materials is of special interest. As shown in Fig. 4.5, ductile (e.g. metals) and brittle (e.g. ceramics and oxides) materials

are fracturing once a certain strain level is reached. It is important to know, that different materials, stress conditions, specimen geometries and sizes, temperatures, and strain rates as well as the presence of micro-cracks in the solid are influencing the generation and propagation of cracks. The theory of LEFM states, that the presence of micro-cracks can modify the local stresses, even if the stress is much less than would normally cause failure in a tensile specimen. When a crack reaches a critical length, it can propagate catastrophically through the structure [38,41]. There are different approaches to calculate the fracture stress σ_f, like the energy-balance approach by the British engineer *Alan A. Griffith* (1893 - 1963) or the stress-intensity approach.

According to *Griffith*, the lines of equal stress in a semi-infinite plate under external tensile stress σ_t with an edge crack of length l_c are concentrated in the region of the crack tip (see Fig. 4.6).

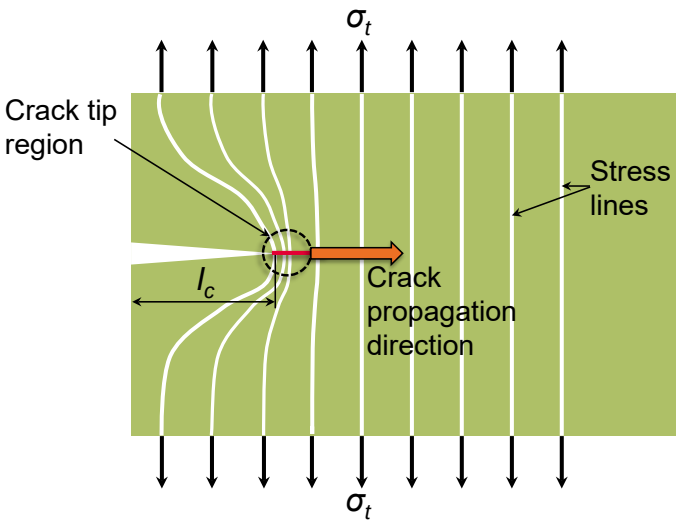

Fig. 4.6. *Griffith* model for edge crack propagation in a semi-infinite plate (modified by [41]).

The crack is growing, if the released elastic strain energy γ_s is at least equal to the energy required to generate a new crack surface. The fracture strength σ_f for a material with an elastic modulus E can be calculated using the *Griffith* equation [41].

$$\sigma_f = \sqrt{\frac{2E\gamma_s}{\pi l_c}} \tag{4.14}$$

With Eq. (4.14) the fracture strength can only be calculated, if one knows the largest existent crack in the specimen. If this is unknown, another way to describe the fracture toughness is needed [41].

In 1958 the American scientist *George R. Irwin* (1907 – 1998) introduced the so-called stress intensity factor K, which depends on the external stress condition, the size of the crack, and the geometry of the specimen. If the mode of the crack propagation is known, this factor can be used to predict the stress state in the tip region of the crack caused by an external load. In Fig. 4.7 one can see, there are three different fracture modes, categorized as Mode I, II, or III [38].

In this work, Mode I is rather relevant for the case of crack propagation in thin brittle layers and thus only considered here. According to theory, a crack always propagates orthogonal to the maximum stress direction, in order to minimize the shear stress [38,42].

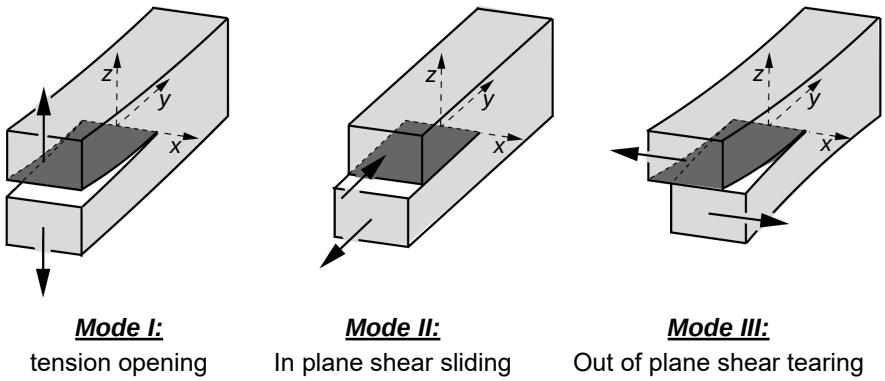

Fig. 4.7. Fracture modes according to *Irwin* (modified by [38]).

If one assumes a specimen with an edge crack of length l_c and an external tensile stress σ_t (see Fig. 4.6) the stress intensity factor K_I is given by:

$$K_I = 1.12\sigma_t\sqrt{\pi l_c}. \tag{4.15}$$

With an increasing external load, the factor K_I is linearly increasing until the maximum strength of the specimen is reached and the crack gets instable. At this point K_I is not further increasing and now called critical stress intensity factor K_{Ic} or fracture toughness. It has the unit $[K_{Ic}]$ = MPa√m and is a material parameter derived from experiments [42]. In Table 4.1 some K_{Ic} values for various ceramics are shown.

Table 4.1. Fracture toughness of brittle materials [42,43].

Ceramics	K_{Ic} **(MPa√m)**
Al_2O_3	3.5 – 5
SiO_2	0.62 – 0.67
Si_3N_4 (sintered)	1.9 – 3.2
SiC[2] (hot pressed)	3.8 – 5

If the fracture toughness K_{IC} of any individual specimen with an edge crack of length l_c is known, the fracture stress σ_f can now be calculated according to [41] by:

$$\sigma_f = \frac{K_{Ic}}{\sqrt{\pi l_c}}. \tag{4.16}$$

4.4 *Weibull* Distribution Function and Crack Probability

Fracture strength measurements of nominally identical ceramic material typically show significant variance in the results. As described in Chap. 4.3, this behavior is due to differences in size, position, and orientation of intrinsic pre-damage causing fracturing of the material [1,43]. Hereby the *Weibull* distribution is of particular interest as it is the method of choice for the statistical data analysis in this thesis.

In material science the *Weibull* distribution, named after the Swedish engineer *W. Weibull* (1887 – 1979), is typically used to describe the crack probability of brittle materials like ceramics or SiO_2. The density function p is derived from the fit curve of the frequency count diagram, which was generated during a crack test on n samples under tensile stress. A schematic example of this is shown in Fig. 4.8.

Analytically, the density function p as a function of the tensile stress σ can be expressed as:

$$p(\sigma) = \frac{m}{\sigma_0}\left(\frac{\sigma}{\sigma_0}\right)^{m-1} \mathrm{e}^{-\left(\frac{\sigma}{\sigma_0}\right)^m}, \tag{4.17}$$

with the parameters m and σ_0. The parameter m is the shape parameter and called *Weibull* modulus m. It is an inverse measure of the distribution width. The scale parameter, or characteristic strength σ_0, is a measure of

[2] SiC: Silicon carbide

centrality at which the percentage probability of failure is 63% [43]. As shown in Fig. 4.8, it is the value at the point of the highest count of cracks of the frequency plot.

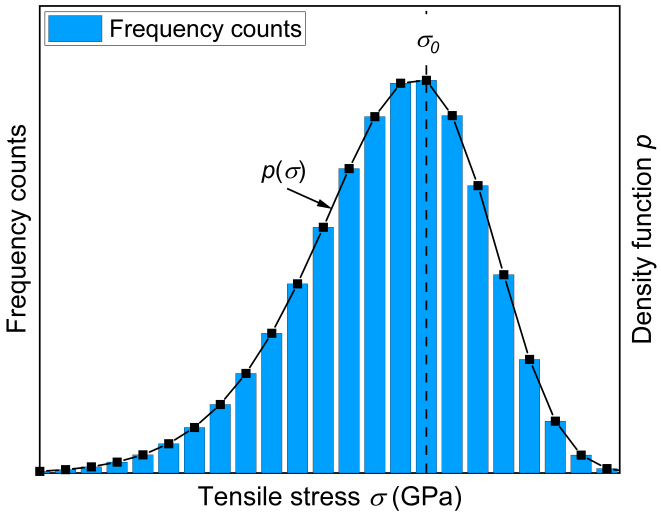

Fig. 4.8. *Weibull* density plot as a function of tensile stress.

Another way to determine the *Weibull* parameters is to calculate the cumulative crack probability P_f, which can be derived from the black fitting curve of the cumulative frequency counts as a function of the tensile stress σ (see Fig. 4.9).

Derived from the 2-parametric *Weibull* density function p (see Eq. (4.17)) the cumulative crack probability P_f as a function of the tensile stress σ is given by:

$$P_f(\sigma) = 1 - \mathrm{e}^{-\left(\frac{\sigma}{\sigma_0}\right)^m}. \tag{4.18}$$

Generally, it is more convenient to use the probability curve for graphical assessments in a linear scale. Therefore, Eq. (4.18) is converted to:

$$\ln\ln\left(\frac{1}{1-P_f}\right) = m\ln(\sigma) - m\ln(\sigma_0). \tag{4.19}$$

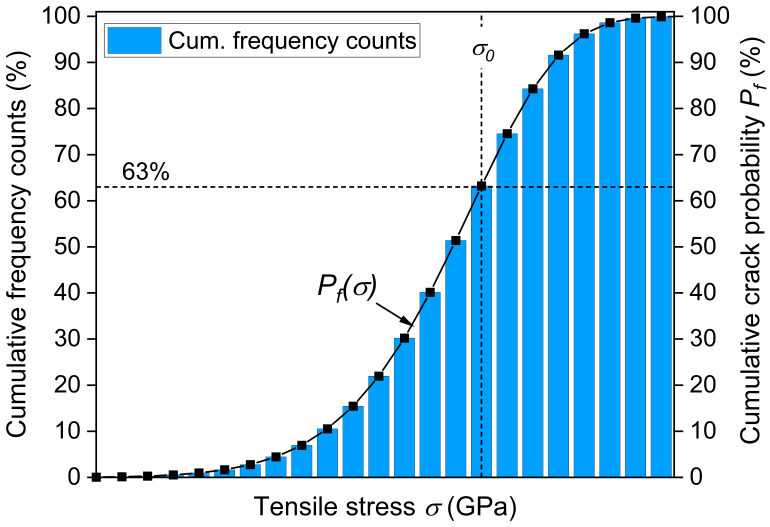

Fig. 4.9. Cumulative crack probability plot in linear scale as function of tensile stress.

The cumulative crack probability P_f can be graphically linearized by scaling the *x*-axis to ln(σ) and the y-axis to ln ln[1/(1-P_f)], in order to fit the *Weibull* parameters *m* and σ_o from a linear regression line through the data points (see Fig. 4.10).

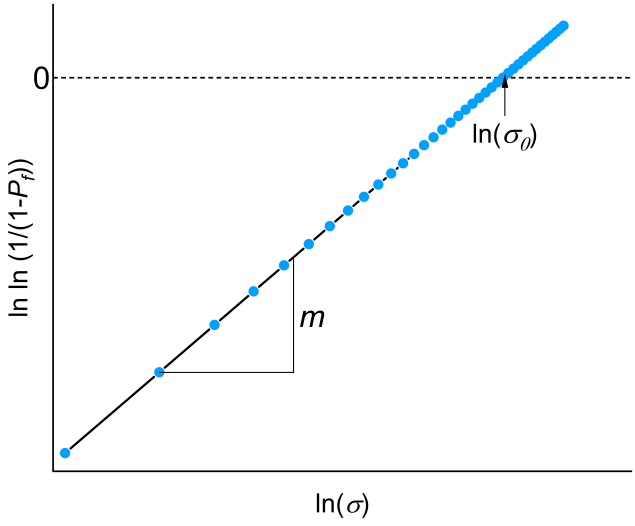

Fig. 4.10. Linearized cumulative crack probability plot with corresponding *Weibull* parameters.

For $\sigma = \sigma_0$ the expression ln ln[1/(1-P_f)] gets to zero. The value for ln(σ_0) can be graphically derived from the intersection of the regression line with the x-axis at y = 0. Subsequently, one gets the characteristic strength σ_0 from Eq.(4.20).

$$\sigma_0 = e^{\ln(\sigma_0)} \tag{4.20}$$

The parameter m is the slope of the linear regression line (see Fig. 4.10) [43]. In Fig. 4.11 it is illustrated in the linear (left) and *Weibull* (right) scale, that with an increasing *Weibull* modulus the slope of the curves is increasing. This means, for a high *Weibull* modulus the variance of the fracture measurement results is low and thus the quality of the material is high. The characteristic strength σ_0 describes the robustness of the material, which is the higher, the higher the value of σ_0 is.

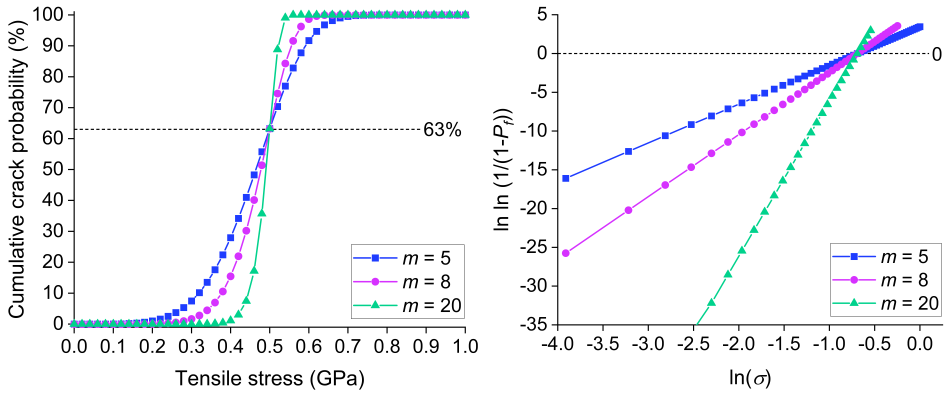

Fig. 4.11. Impact of the *Weibull* modulus m on the curve shapes in linear (l.) and *Weibull* (r.) scale.

4.5 Stress Calculation for Idealized Contact Pair Scenarios

In this thesis the acoustic crack experiments are performed using an indenter with a flat-ended circular diamond tip, which presses vertically on the surface of the structure by simulating the real probing process (see Chap. 5ff.). Therefore, the contact mechanics regarding the indentation of a flat, extensive specimen with a flat-ended cylindrical punch, or indenter, is of particular interest to gain a deeper understanding of the impact of the stresses arising from contacting on the mechanical damage of thin, brittle layers.

Since in the present case only two-dimensional, rotationally symmetrical models are concerned, instead of the *Cartesian* coordinates x, y, and z (see Chap. 4.1), the *Cylinder* coordinates r, φ, and z are used (see Fig. 4.17). For $\varphi = 0$ is:

$$x = r \text{ and } z = z. \tag{4.21}$$

In the further course of this work only tensile and compressive stresses in radial (= σ_r) and vertical (= σ_z) directions are considered, which are dominating for the given load case. Shear stresses τ_{ij} are not taken into account in the analytical and computer-aided calculations.

When two solids are pressed together by a load F_z, a normal stress distribution arises over the contact area, which is referred to as surface pressure (see Fig. 4.1). In the case if one solid of the contact pairs is considered elastic or plastic, the surface pressure is neither isotropic nor constant over the contact surface. Furthermore, the amount of force, the material properties, and the surface contours of the solids are decisive for the resulting stress distribution over the contact area and also its size and shape. To sum it up, the distribution of the reactive stress strongly depends on the assumptions made for the concerned contact scenario [1].

In the following sections, multiple contact scenarios are discussed starting with the ideally, simplified contact scenario of a rigid flat-ended cylindrical punch on a rigid flat specimen without friction (see Fig. 4.12, scenario 1a). Step by step a more realistic scenario is described by including more physical (e.g. elasticity, friction) and geometrical (e.g. tip shape) parameters into the analytical and numerical models. So the realistic behavior of the practical scenario "elastic needle on a BEOL stack" is revealed subsequently.

4.5.1 Analytical Contact Stress Calculation

This section describes two contact scenarios analytically, beginning with the contact between two rigid solids (contact scenario 1a in Fig. 4.12) and continuing with the indentation of a rigid axisymmetric flat punch with sharp edges on an elastic half-space (contact scenario 1b in Fig. 4.12). Both contact scenarios are assumed without friction. The materials are considered homogeneous and isotropic.[3]

[3] This topic is also part of [3].

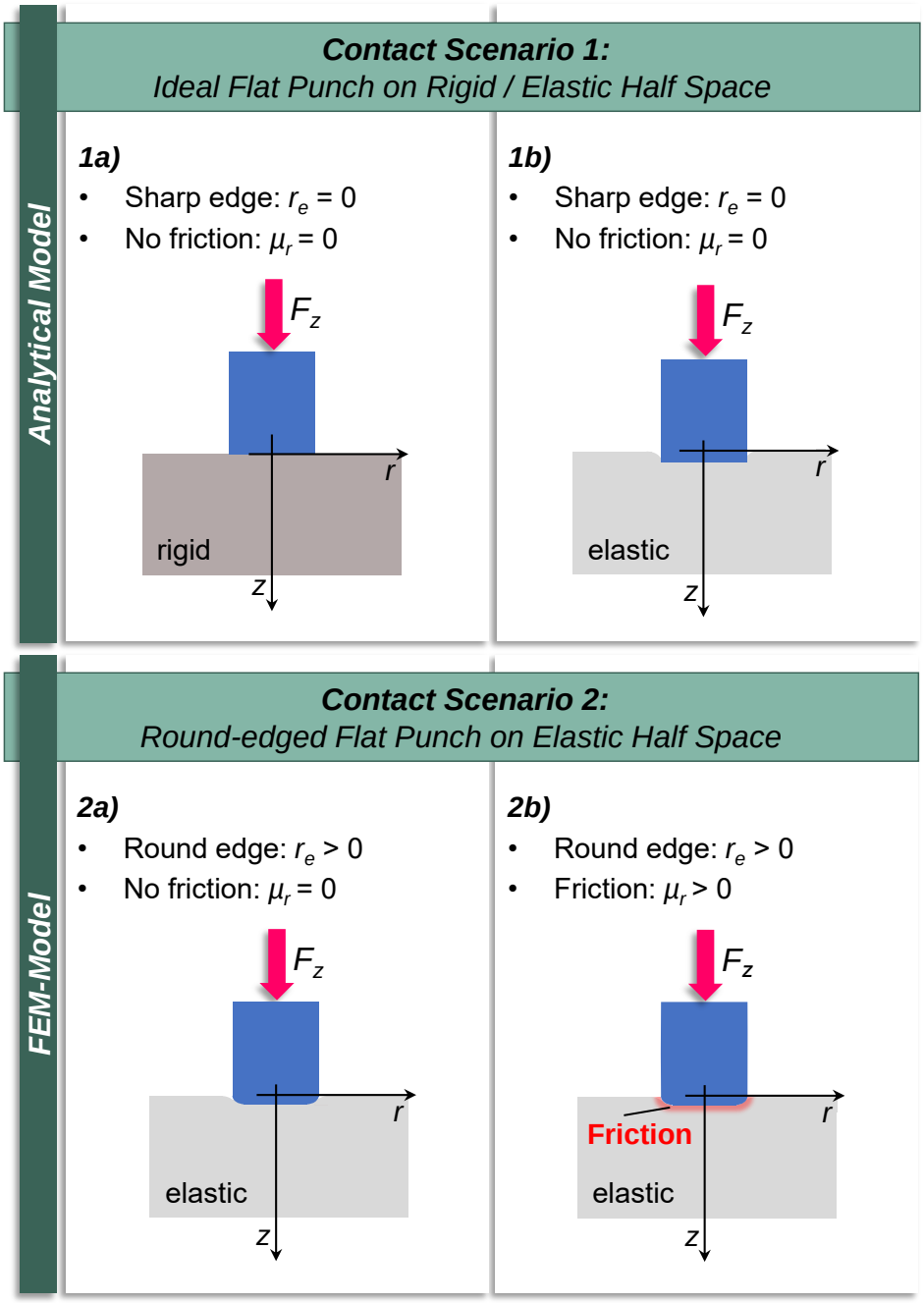

Fig. 4.12. Different contact scenarios of ideal and real contact pairs.

Contact Scenario 1a: Rigid Flat-ended Circular Punch on Homogeneous Rigid Specimen

In the simplest case, the axisymmetric flat-ended punch with sharp edges (r_e = 0) and the half-space are considered rigid and their contact is assumed frictionless.

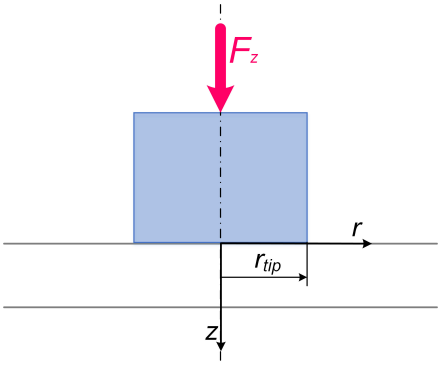

Fig. 4.13. Indentation of a rigid half-space by a rigid flat-ended cylindrical punch.

If the two rigid contact bodies are pressed together with the normal load F_z (see Fig. 4.13), the resulting stress σ_z across the contact surface ($r \le r_{tip}$, z = 0) is constant and given by Eq. (4.22). The contact area A_c has a radius r_{tip}.

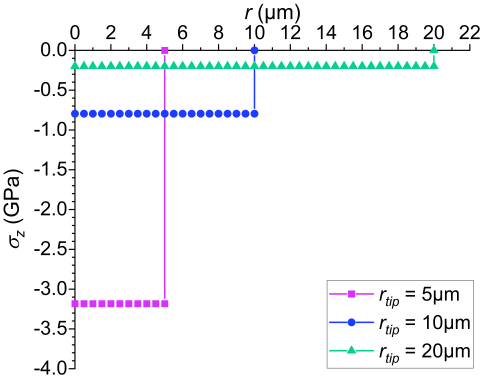

$$\sigma_z(r,0) = -\frac{F_z}{A_c} = -\frac{F_z}{{r_{tip}}^2\pi} \qquad (4.22)$$

Fig. 4.14. Stress distribution σ_z over the contact area ($r \le r_{tip}$, z = 0) for different tip radii r_{tip}.

Fig. 4.14 shows the stress distribution σ_z over the contact surface ($r \leq r_{tip}$, z = 0) for three different tip radii r_{tip} at a normal load F_z of 250mN. It is obvious, that the surface stress, which is a compressive one, increases with a decreasing tip radius r_{tip} of the punch. Moreover, Fig. 4.14 exemplifies the constant pressure distribution across the contact surface ($r \leq r_{tip}$) which drops to zero outside the contact area ($r > r_{tip}$).

Contact Scenario 1b: Rigid Flat-ended Circular Punch on Homogeneous Elastic Half-Space

Following, the flat-ended cylindrical punch with sharp edge (r_e = 0) is considered rigid again, conversely to the half-space, which is now modelled having an elasticity and so considered to be deformable. As shown in Fig. 4.15, the flat punch is pressed vertically on the surface of the elastic half-space with a force F_z.

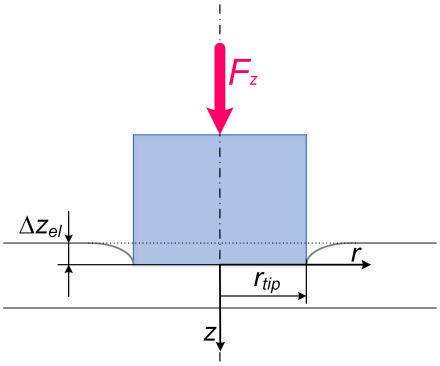

Fig. 4.15. Indentation of an elastic half-space by a rigid flat-ended circular punch.

In order to facilitate the analytical calculations, two further boundary conditions are made [44]:

1. The free surface outside the contact area has no normal stress σ_z acting on it:

$$\sigma_z(r, 0) = 0 \text{ for } r > r_{tip}. \tag{4.23}$$

2. The displacement in z direction u_z is consistent with the flat facet of the rigid punch:

$$u_z(r, 0) = \Delta z_{el} \text{ for } 0 \leq r \leq r_{tip}. \tag{4.24}$$

The penetration of the flat punch Δz_{el} is defined by Eq. (4.25) and depends on the elastic modulus E and *Poisson's* ratio ν of the specimen, the contact load F_z, and the radius r_{tip} of the contact area [45].

$$\Delta z_{el} = \frac{F_z\,(1-\nu^2)}{2Er_{tip}} \tag{4.25}$$

As during indentation with an axisymmetric flat punch the contact area A_c is assumed to remain constant, the mean contact pressure p_m between the flat punch and the specimen is given by [45,46]:

$$p_m = \frac{F_z}{A_c} = \frac{F_z}{{r_{tip}}^2\pi}. \tag{4.26}$$

The normal stress σ_z between the flat punch and elastic half-space ($r \le r_{tip}$, $z = 0$) can be calculated by Eq. (4.27) [44]. According to this equation, at the edge of the flat punch ($r = r_{tip}$) the stresses are theoretically infinite ($\sigma_z \to \infty$), which is in reality prevented by plastic deformation of the contact pairs.

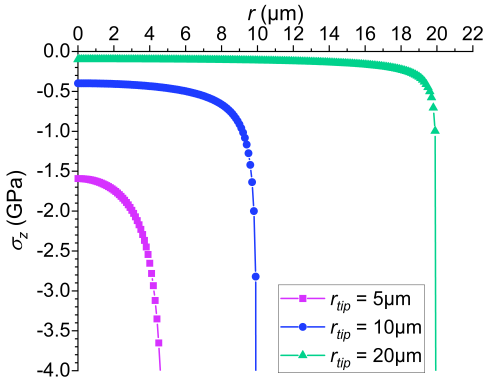

$$\sigma_z(r,0) = -\frac{p_m}{2\sqrt{1-\dfrac{r^2}{{r_{tip}}^2}}} \tag{4.27}$$

Fig. 4.16. Surface pressure σ_z over the contact area ($r \le r_{tip}$, $z = 0$) for different tip radii r_{tip}.

Fig. 4.16 shows the normal stress distribution over the contact surface ($r \le r_{tip}$, $z = 0$) due to indentation of the elastic half-space with flat punches of different tip radii r_{tip} at a contact load of 250mN. Similar to Fig. 4.14, the compressive stress is higher for a smaller radius of the flat punch. Furthermore, in Fig. 4.16 it is visible, that for a flat punch the compressive stress has its minimum at the center point $r = 0$. In contrast, the stress is maximal at the edge of the contact area ($r \to r_{tip}$), where a rigid flat punch provokes

infinite stress above the critical value, which would cause material fracturing in a real application. This demonstrates, that a real brittle material behaves differently during indentation, if elasticity is included and the stress does not saturate at the contact edge, as with the idealized scenario 1a, shown in Fig. 4.14.

The stress distribution for a scenario assuming an indentation of an elastic-plastic material behavior, instead of an elastic one, cannot be solved analytically because of the unknown shape and extension of the plastic field. In addition, the analytical model would be much more complex as the equations are not linear and include some material parameters to describe the plastic behavior [44]. Assuming the punch elastically deformable, instead of rigid, and with an edge radius unequal to zero would cause much more complexity as well. This is true also for a scenario considering the contact with friction. Therefore, it is more efficient to use numerical simulation methods, in order to solve complex contact scenarios closer to reality.

4.5.2 Numerical Contact Stress Calculation using Finite Element Method

In this section, the contact sequence is modelled for different scenarios by the computer-aided numerical analysis using the commercial FEM software *COMSOL Multiphysics version 5.3a*. The presented simulations examine the indentation of a homogeneous elastic half-space with a rigid flat-ended cylindrical punch of different edge radii with and without friction (contact scenario 2a and 2b in Fig. 4.12). To reduce the computing time of the simulations, all presented FEM-models are based on a rotation-symmetrical 2D model.

Contact Model:

As shown in Fig. 4.17, the FEM-model consists of a cylindrical flat-ended punch, which presses vertically onto the surface of the specimen.

The specimen is modelled as 2-dimensional half-space with radius of 300µm and a thickness of 500µm. These geometrical dimensions were chosen to ensure, that the vertical and radial stresses converge to zero outside the contact area. The model of the flat-ended cylindrical punch has a tip radius r_{tip} = 5µm, which is a typical size for probe needles (see Sect. 2.2.2). In order to simulate the influence of the tip edge radius on the vertical and radial stresses realistically, the tip edge radius was varied between 0.01µm, 1µm, 2µm, and 3µm, respectively.

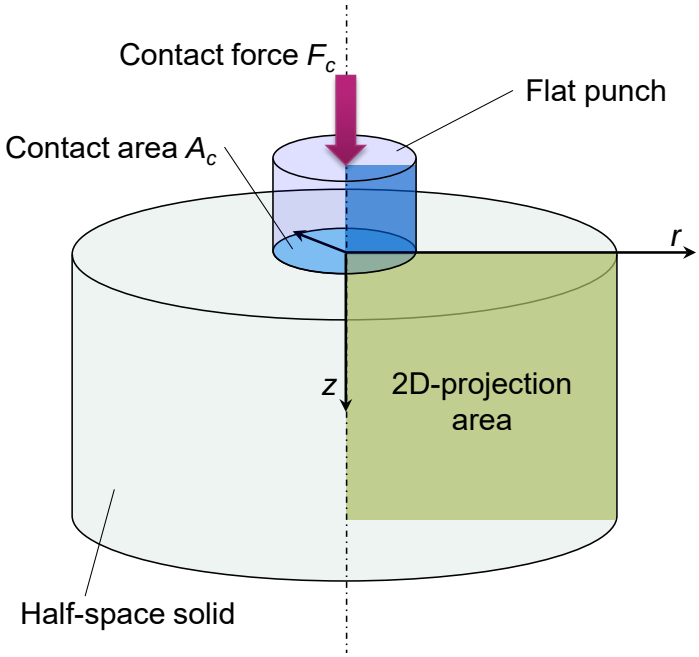

Fig. 4.17. Rotation-symmetric model of flat punch on half space solid.

The material of the solid specimen is considered as homogeneous and isotropic. It is specified by the material parameters of SiO_2 with an elastic modulus E of 70GPa, a density ρ of 2200kg/m³, and a *Poisson* ratio ν of 0.17. For the indentations during the experiments of this thesis (see Chap. 5*ff.*) diamond tips, which have an extremely large elastic modulus, were used. Therefore, the contact area of the flat punch is modelled as "*Rigid Domain*", meaning it is considered as nearly undeformable and thus no stresses and deformations are calculated within the indenter.

As shown in Fig. 4.18, the FEM element mesh of the specimen is divided into multiple areas with different element densities. In the contact zone, with a size of ca. 15µm x 15µm, a structured rectangular mesh ("*Mapped Mesh*") is used. To reach a high resolution of the numerical results, even for sharp indenter edges, the element size is reduced at the contact surface and especially at the edge of the contact area. Within this area a "*Free Quad Node*" is adjacent, followed by two structured rectangular meshes ("*Mapped Mesh*"), whereby the element size is increased with rising distance to the axis of symmetry.

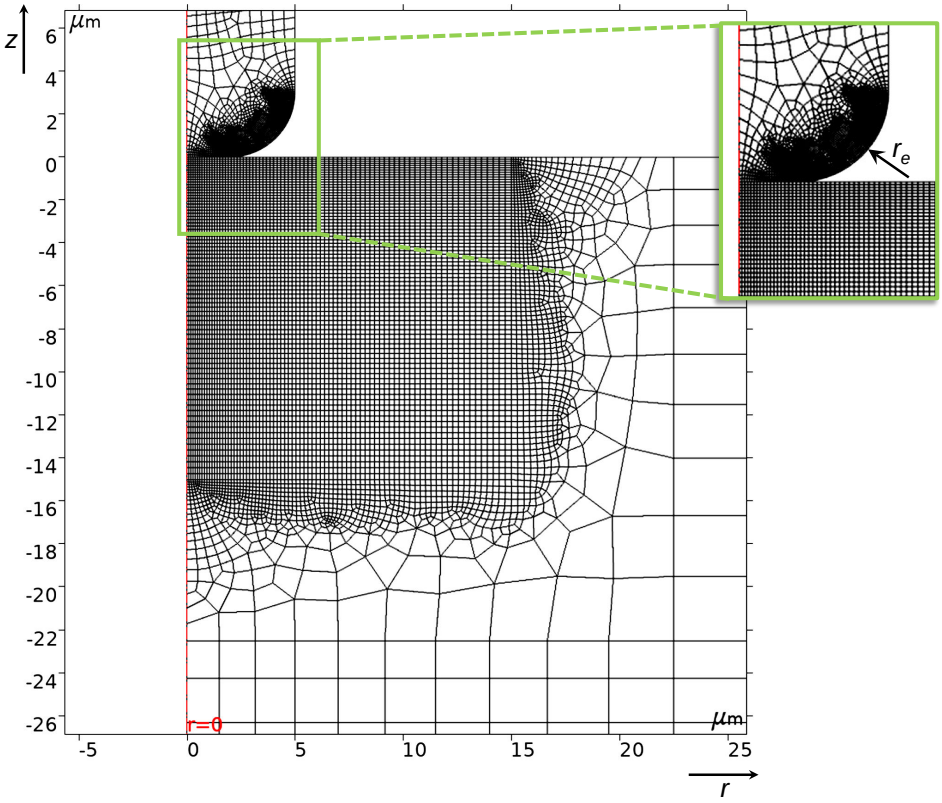

Fig. 4.18. Meshed FEM contact model: punch with rounded edge.

The indenter is meshed by a half-symmetrical "*Free Quad Node*" model having a maximal element size of 0.5µm. The smallest element size, respectively the highest number of elements, is located at the contact area interface and close to the indenter edge, depending on the edge radius r_e of the punch.

The meshed FEM-model is the result of an optimization process to simulate the deformation within the contact zone and close to the punch edge with a good compromise in terms of computation time and accuracy of the results.

The element type of the interface, where the punch and specimen are in contact, is defined as "*Contact Pair*" in order to enable a relative offset and contact force transmission between the solids. During the simulation run of the indentation, the force was usually increased by steps of 4mN until a maximal force of 400mN ("*Auxiliary Sweep*"). In case of no convergence the step size was optimized automatically by the program.

Contact Scenario 2a & 2b: Rigid Flat-ended Circular Punch on Homogeneous Elastic Half-Space

The flat-ended punch with a cylinder radius of 5µm and different edge radii r_e is pressed onto the specimen surface up to a maximal force of 400mN. The surfaces of the solids are assumed frictionless (μ_r = 0) for scenario 2a and including friction using a friction coefficient μ_r of 0.1 (value for "diamond on silicon oxide") [47] for scenario 2b.

Fig. 4.19 shows the colorized contour plot of the first principle stress σ_1 (see Sect. 4.1.2) of the deformed structure after indentation at maximum load with a sharp (left) and round (right) edge radius of the flat punch. Already here one can see, that the maximal stress changes its sign for each load case within the contact area and hence is partly a compressive stress (negative sign) for a sharp edge punch or tensile stress (positive sign) for a round edge punch. Furthermore, the contour plot on the right side indicates, that the stress distribution for larger tip edge radii r_e are non-uniform along and below the contact surface and more difficult to calculate by analytical models.

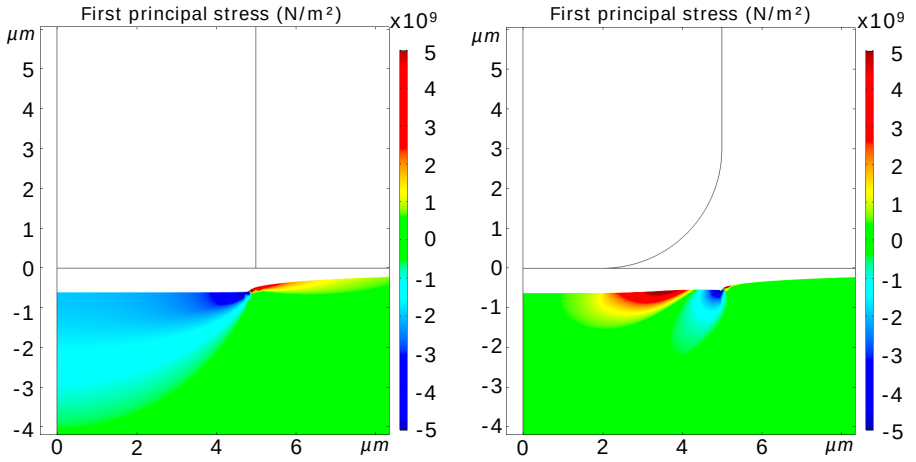

Fig. 4.19. Contour plots of 1st principal stress for contact scenario 2a and 2b: r_e = 0.01µm (l.) and r_e = 3µm (r.).

Next, the stress distribution along the contact surface without friction ($r \geq 0$, $z = 0$, $\mu_r = 0$) for different punch edge radii r_e is discussed. Instead of principal stresses the normal stresses σ_i in vertical and radial direction in

Cylinder coordinates r and z ($\varphi = 0$) are given. Fig. 4.20 shows the simulation results of the vertical stress component $\sigma_z(r)$ and Fig. 4.21 the ones of the radial stress component $\sigma_r(r)$.

Independent of the punch edge radius, both stress components are relatively small within the contact area, as expected according to the analytical model. At the edge of the contact zone (r = 5µm), the stress components reach negative maxima ($\sigma < 0 \rightarrow$ compressive stress). Outside the contact zone, the stress components firstly change their sign ($\sigma > 0 \rightarrow$ tensile stress) and with increasing distance from the edge they converge asymptotically to zero. For an idealized punch with a sharp edge (r_e = 0.01µm) the vertical stress curve (pink line) within the contact area (r < 5.0µm) is similar to the analytical model (see Fig. 4.16). More rounding of the punch edges causes local extrema in the curves of the stress distributions and thus deviations from the ideal curves. The stress of the vertical component is continually compressive within the contact area (r < 5.0µm). In contrast to that, the value of the radial stress component, depending on the punch edge radius, gets positive (tensile stress). As a conclusion one can say, that an increase of the edge radius r_e results in a more uneven distribution for both, vertical and radial stresses, and causes a change of compressive to tensile stresses and vice versa. Later in this work, this effect becomes important when considering the crack probability of inhomogeneous multi-layer stacks.

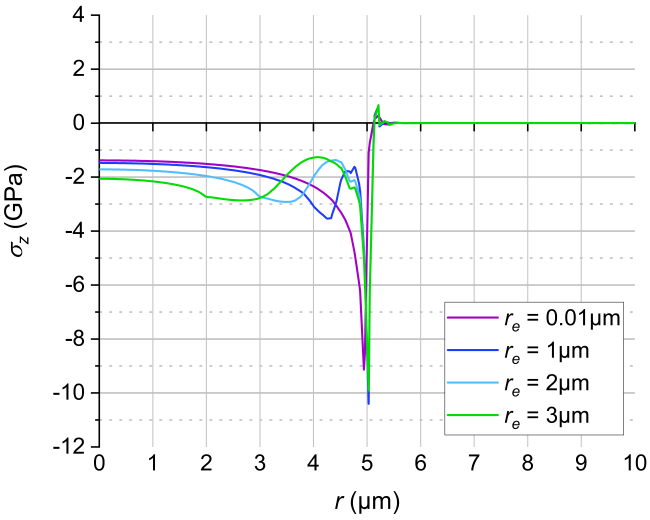

Fig. 4.20. Vertical σ_z stress on top of the contact surface without friction ($r \geq 0$, $z = 0$, $\mu_r = 0$) for different punch edge radii r_e.

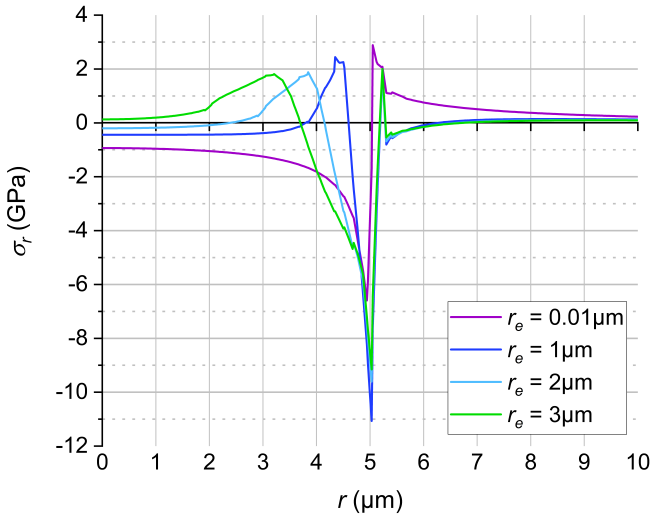

Fig. 4.21. Radial σ_r stress on top of the contact surface without friction ($r \geq 0$, $z = 0$, $\mu_r = 0$) for different punch edge radii r_e.

In an additional simulation run, the influence of friction ($\mu_r > 0$) between the contact surfaces was examined. To this, the following figures show the distributions of the vertical $\sigma_z(r)$ (see Fig. 4.22) and radial $\sigma_r(r)$ (see Fig. 4.23) stress components on top of the contact surface ($r \geq 0$, $z = 0$) with and without friction, each for a punch with sharp ($r_e = 0.01\mu m$) and rounded edges ($r_e = 3\mu m$).

In Fig. 4.22 and Fig. 4.23 the curves for friction coefficient variants are almost identical, showing that friction has no significant influence on the simulated stress distributions for this contact model and so can be neglected.

Already with the presented simulations of an ideal flat punch contacting a homogenous solid body, one can see that the stress distributions and amounts are strongly influenced by both, the elasticity of the half space solid and the punch edge radii. The stress calculations are much more complex than expected from the analytical models. Additional to these models, other research studies were done using advanced computer-aided simulations for this contact problem. For example, *Riccardi et al.* developed FEM-models in terms of indentions on metals by a flat-ended cylindrical punch [44]. The indentation of more complex layer structures with different flat and spherical tip geometries was simulated via FEM-models by *O. Nagler* [1]. However, it should be mentioned, that every simulation is only an approach to reality and hence, it is not yet possible to accurately calculate

the exact amount and location of the contact stress. Furthermore, the models get much more complex, if additional crack initiation and propagation are considered.

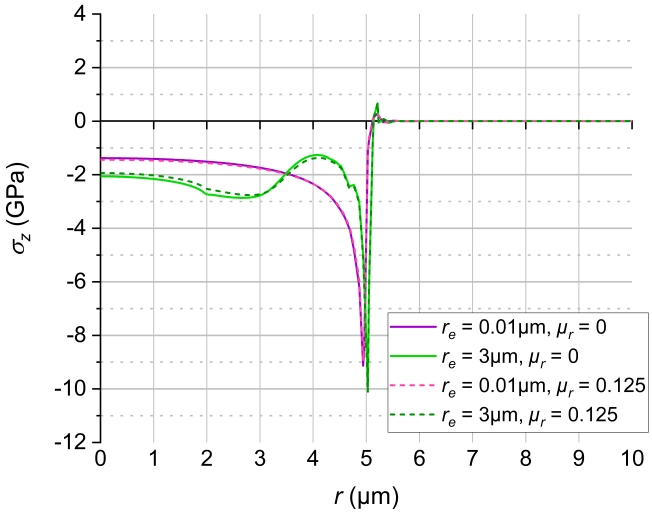

Fig. 4.22. Vertical σ_z stress on top of the contact surface with and without friction ($r \geq 0$, $z = 0$, $\mu_r \geq 0$) for different punch edge radii r_e.

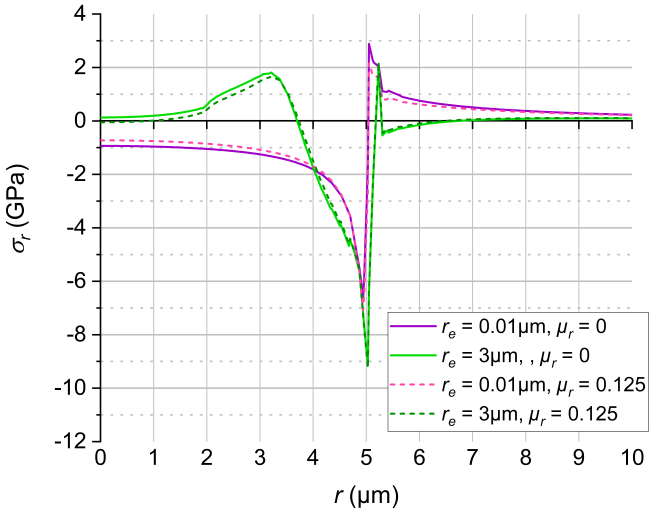

Fig. 4.23. Radial σ_r stress on top of the contact surface with and without friction ($r \geq 0$, $z = 0$, $\mu_r \geq 0$) for different punch edge radii r_e.

4.5.3 Real Pad-Over-Active-Area Contact Pairs

As described in the previous chapter, pressing two solid bodies together always causes an elastic or plastic material deformation of both contact pairs depending on the stress and strain conditions. In the analytical and simulation model, an ideal tip was assumed, but on the microscale, the surfaces of a real contactor are never perfectly smooth and flat. They can be covered by a discrete number of asperities from foreign material built-up, when the contact pairs are brought into contact, or the tip shape is unevenly formed [45].

Real probe tips, which are made of metal or their alloys (see Sect. 2.2.2), are neither perfectly flat nor spherical and often metallic or organic material is collected on top of the tip surface. Hence, they are neither rigid nor as hard as diamond tips and so the probes are elastically or even plastically deformed during contacting. This becomes obvious, if looking at a confocal microscope image showing a 3D surface profile of a probe tip (see Fig. 4.24).

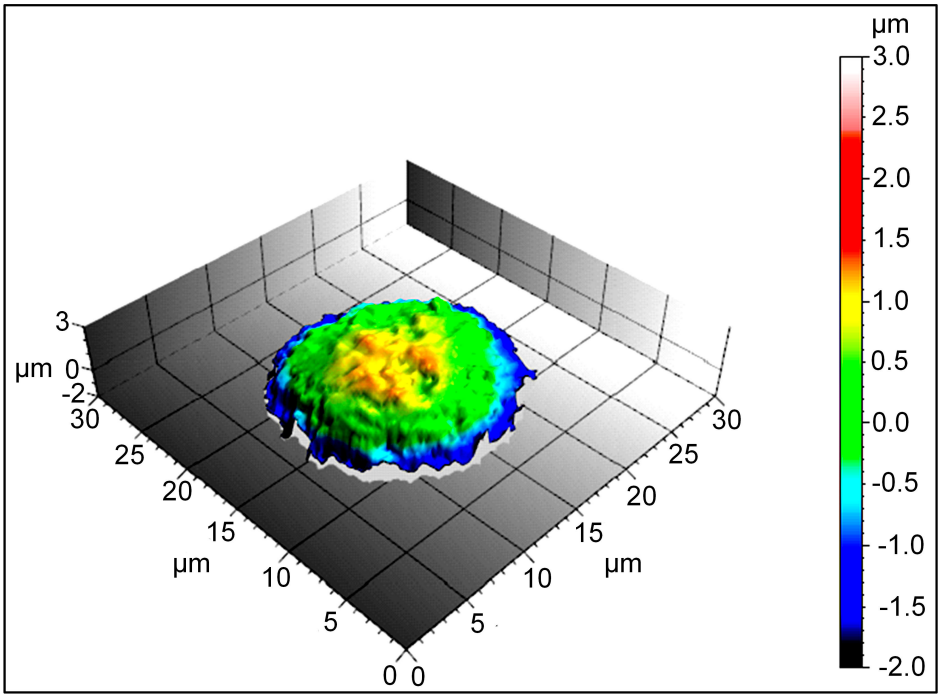

Fig. 4.24. 3D surface profile of a real probe tip.

Moreover, the BEOL stack is not an elastic half-space monolayer with a homogenous and infinite volume. It is composed of multiple layers on top of each other with different material properties (see Chap. 2.3) and different metal routing design.

As explained in Sect. 2.3.4, the probe tip transmits significant mechanical stress mainly to the I/O pad and to the brittle and ductile structures underneath. Fig. 4.25 illustrates the POAA failure mechanism causing stack deformation and oxide cracks during indentation with a flat-ended circular punch exemplary for a CMOS based BEOL stack. The failure mechanism for this effect is extensively discussed in Chap. 7.

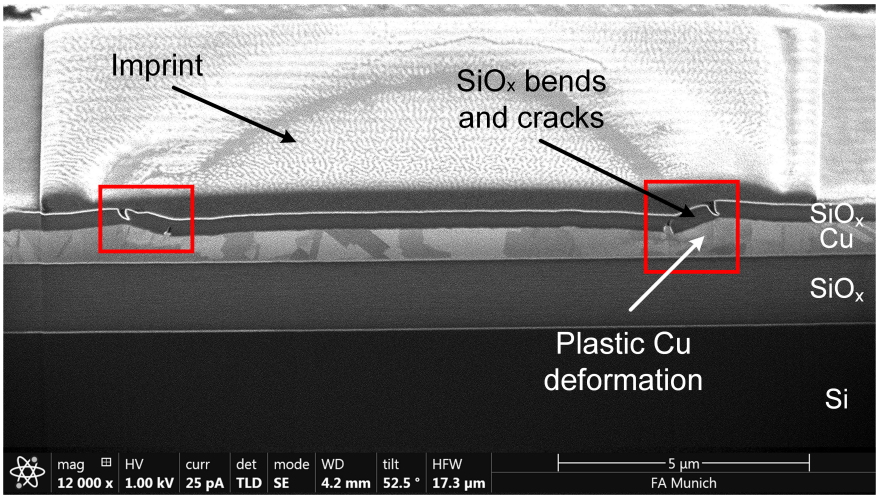

Fig. 4.25. Stack deformation and oxide cracking due to indentation with a flat-ended cylindrical punch.

Because of the mentioned difficulties, the stress distributions, material deformations, and rupture cannot be fully described with existing analytical and computer-aided contact models. In addition, it should be mentioned, that the simplified contact models only give approximations to the reality. As there are certain unknown parameters, it is currently not possible to calculate or simulate precisely the tensile and compressive stress in brittle layers for different combinations of probes and BEOL stacks for various FE technologies. Instead of modelling the contact stress, extensive experiments are needed to evaluate the crack probability in an empirical way. But as mentioned before several times, until today there are only optical inspections applicable to find probing-induced oxide cracks in complex layer structures.

Keeping these facts in mind, for higher crack detection accuracy and shorter inspection time it is crucial to provide a reliable and more efficient quality assurance method for POAA wafer test. Therefore, a novel method is presented in this work to detect cracks in thin brittle layers during contacting in real-time by means of AE testing. In the following chapter, the basics of AE testing are explained and the application of this newly developed method for thin layer characterization is described by theory and FEM-simulations and verified by experimental measurements.

5 Acoustic Emission Testing for Crack Detection

The AE test method is one of the most efficient and versatile techniques used for the ***N***on-***D***estructive ***T***esting (NDT) of materials. It can detect, localize, and monitor material defects during the entire system lifetime, without any destruction of the specimen. For this purpose, AE sensors are physically coupled to the surface of the specimen to detect elastic acoustic waves, which are radiated spherically from the location of a spreading defect [7,48].

The innovative method of acoustic crack detection during probing, which has been developed in this thesis, is based on the already established ***AE T***echnique (AET). The measurement principle has been modified in a way to apply it for the qualification of the wafer probing process, in order to detect low-acoustic signals of IMD cracks in nanometer dimensions (see Chap. 1.1).

This chapter starts with basics of AE testing followed by a description of a modified test setup using the AE test method applied for indentation on thin layers. In order to validate the theoretical background of AE testing, simulations and measurements were done and analyzed, which will be presented here. Once the acoustic crack detection mechanism could be described by a suitable model and was confirmed by experiments, the sensor-indenter system could be modified to improve the sensitivity of the method.

5.1 Basics of Acoustic Emission Technique

Fig. 5.1 gives a schematic view of the AE test method. During solid material fracturing, e.g. due to a mechanical load, the stored elastic energy is released suddenly by producing acoustic shock waves. The volume and surface waves propagate with ultrasonic frequencies (20kHz – 2MHz) at low amplitude and short durations. For this purpose, piezoelectric sensors, which transfer small mechanical deflections into an electrical voltage signal, are coupled on the surface of the solid body for acoustic wave transmission. In addition, low-noise amplifiers and high-resolution A/D converters are required, in order to receive a sufficient high signal gain and quality [3,7].

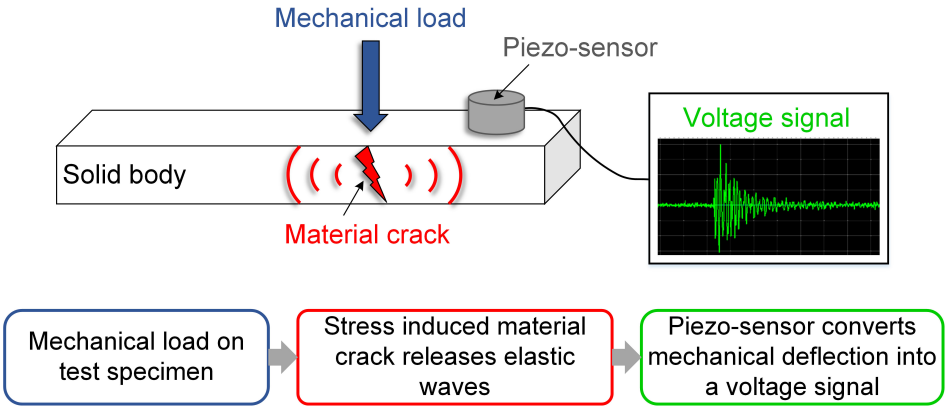

Fig. 5.1. Principle of AE testing: AE formation, propagation, and detection.

5.1.1 Properties of Acoustic Emission Testing

The AE test method is characterized by some of its key properties, which are:

1. *Non-Destructive:*

Even if fracture is necessary for material testing, the AE test method is correctly described as a NDT method. Conversely to other acoustic NDT methods, like ultrasonic testing or ***S***canning ***A***coustic ***M***icroscopy (SAM), which are mostly applied before or after loading a structure for test, AE testing is applied during loading. In addition to other material tests, the AE test method is used for condition monitoring of components under working load (see Sect. 5.1.2). Especially here it becomes clear, that AE testing is a non-destructive method [7,8].

2. *Passive:*

At active NDT a transmitter sends an acoustic wave into the material of a solid body. If the wave is reflected at an *existing* internal crack the receiver measures the reflected signal (see Fig. 5.2, left). In contrast, during passive AE testing the receiver only detects acoustic waves generated by an *emerging* defect within the material (see Fig. 5.2, right). In other words, the AE test method is just "listening" and thus defined as a passive method [7,8,48].

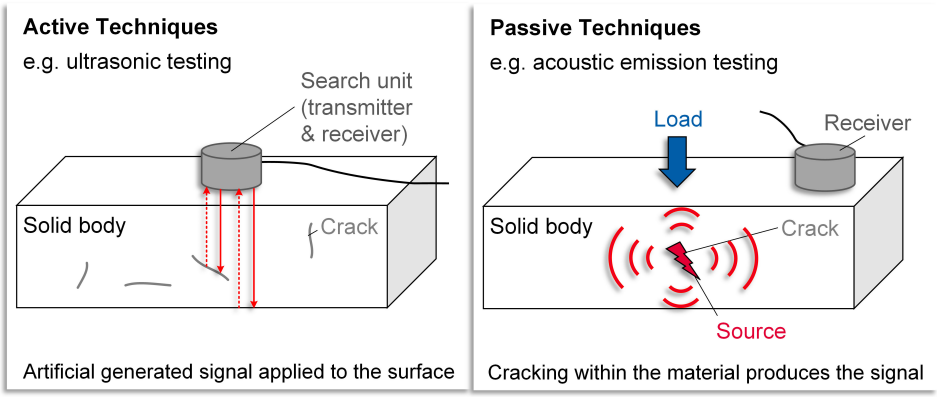

Fig. 5.2. Comparison of "active" (l.) versus "passive" (r.) NDT methods.

3. *Real-time Monitoring:*

The AE test method measures and analyzes acoustic shock waves, which are emitted by a defect within the material, just at the time of occurrence. The reproduction of the AE signal at a later time is not possible. The maximal distance between the AE source and sensor, which is important for the time delay of crack generation and detection, depends on multiple factors like the material properties, the geometric size of the test specimen, as well as working and environmental conditions. In practical applications, the distances reach from millimeters up to more than 100m. This is a special advantage of the AE test method enabling the monitoring of areas which are not accessible for other techniques [7,48].

4. *Dynamic:*

The AE testing only detects active damage processes like the formation of new defects, the propagation of existing defects, and friction. Since pre-existing, stationary damages usually not produce any AE signal they cannot be identified [8,48].

5. *Integral:*

The elastic waves spread spherical from their origin and continue propagating within the material, whereas their attenuation increases. In AE testing usually a small number of AE sensors, which are arranged at fix positions, enables the monitoring of large surfaces. Depending on the location of the AE source the elastic waves arrive at the AE sensors with a time delay. The transit time differences of the detected AE signals indicate the location of the AE source [7,8,48].

5.1.2 Acoustic Emission Sources and Fields of Application

Typical mechanisms of acoustic wave emission (so-called AE sources) are crack generation, crack propagation, friction of crack boundaries, crystal dislocation motion, delamination, material phase transformation, active corrosion, turbulent fluid flow, liquid leakage, and high voltage discharging in large power transformers [8,48].

All materials like metals, ceramics, glass, stones, concrete, brittle polymers, wood, and compound materials, which are generating AE sources having a sufficiently high amplitude are suitable for AE testing [8].

AE sources producing AE waves with a frequency between 20kHz and 2MHz are technically usable. Below this frequency range, the AE signal is superimposed by mechanical disturbances, whereas higher-frequency oscillations show strong signal attenuation [48].

In this work, the mechanisms of brittle crack generation, friction of contact surfaces, and plastic deformation, i.e. dislocation motion, are of particular interest. Crack signals are characterized by AE signals with middle or high amplitude (10µV up to 100mV) and short duration (some 10µs). The relatively high signal strength is due to the sudden release of stored elastic energy at the centers of concentrated stress (see Fig. 4.6), producing elastic shock waves. In contrast, friction and plastic deformation processes normally emit rather continuous AE signals than short ones. While friction emits AE signals of small or middle amplitude, dislocation movements produce only small amplitudes, which can only be sensibly detected in laboratory environment [48,49].

Typical areas of applications of AE testing are material research as well as inspection and control of system engineering in R&D laboratories and various industries [8,48].

Supporting Material Research:

In the field of materials research, the determination of material properties, damage mechanisms and behavior is of particular interest [7,48]. This application area is also applied in this work.

Supporting Material Testing in Production, Maintenance, and Development:

Further on, AE testing is applied at quality inspection of highly loaded components of industry facilities and constructions during stability stress testing.

Examples to this are composite materials of aerospace engineering or industrial metal components. AE testing for the two applications mentioned here are mostly combined with other destructive tests, whereas for the following applications AE testing is commonly used for permanent and non-destructive AE monitoring [48].

Protecting Environment, Structures, and Human Life:

In the field of continuous condition monitoring and material defect localization, AE testing has moved the mainstream as a leading edge technology.

A machine or a construction is applied with a nominal load for a typical operational mode. The target of AE testing is to characterize the manufacturing quality or damage events of components. Moreover, the critical damage conditions before final system failure can be demonstrated and areas of high AE activity and intensity can be localized [7,8].

Here some practical examples are given [48]:

- Monitoring of civil engineering structures like bridges, cranes, etc.
- Testing of vessels containing dangerous products and / or pressure
- Detecting and locating corrosion and fluid leakage (e.g. tank floors)

Finally AE testing is used for heavily thermo-mechanical loaded process monitoring like welding, curing, and sintering [48].

5.1.3 System Components for AE Test Method

Fig. 5.3 shows a schematic view of the AE measurement chain. An AE event releases an elastic wave (green) propagating within the solid body. After the induced AE wave has reached the location of the AE sensor, it penetrates the couplant (green) and then reaches the sensor (yellow). The AE sensor converts the dynamic surface-motion, which is caused by the elastic wave, into an electrical (AC) voltage signal. The AE signal is subsequently amplified and commonly filtered by the preamplifier (yellow) and transmitted to the AE system (yellow) where the signal processing takes place. Finally, the generated data set is transmitted to a computer (blue) where it is stored, evaluated, and displayed [48].

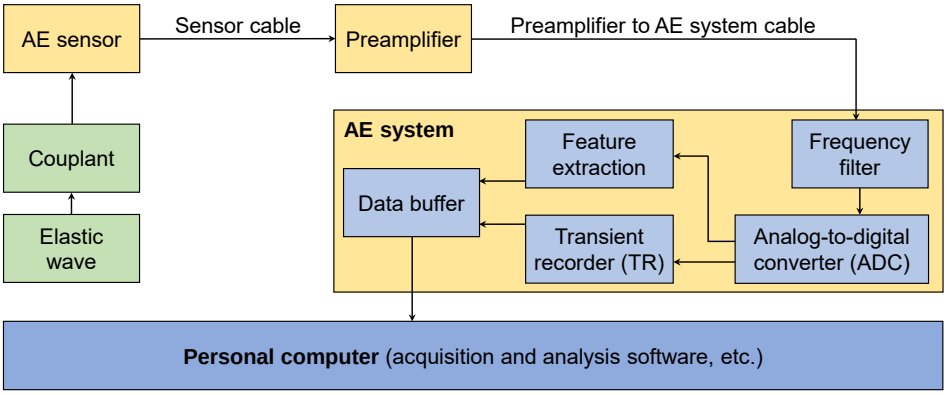

Fig. 5.3. Schematic view of AE measurement chain.

a) Piezoelectric AE Sensors

The AE sensor is the first device in the AE measurement chain. It is of particular importance, as any AE signal the sensor does not detect is lost for further signal proceeding and analysis. So far, piezoelectric AE sensors have proven best for AE testing. They are compact, robust, cost-efficient, and more sensitive than any other sensor techniques, like capacitive, electrodynamic, or laser-optical sensors [7,48].

Piezoelectric sensors enable a very efficient transformation of the elastic wave into an electrical voltage signal. Using this sensor type even wave amplitudes of only 0.01pm are detectable. Due to the special design of the components, the sensor does not saturate even with AE sources of high intensity (e.g. fracture) [48]. Fig. 5.4 illustrates the typical design of a piezoelectric AE sensor schematically.

The piezo-element, e.g. a disk-shaped lead zirconate titanate (PZT) ceramic, is covered by two metallized electrodes and connected to the test specimen, isolated, and protected through a non-conductive ceramic wear plate, e.g. made of aluminum oxide (Al_2O_3). Between the ceramic plate and test specimen usually a couplant is applied to improve the acoustic wave transmission. To protect the sensor element from the environment it is usually covered inside of a metal case, which is filled with a damping material (e.g. epoxy resin).

Once an elastic wave, which was generated within the body of the test specimen, has reached the surface, the piezoelectric element is stimulated by local density fluctuations, which are transported though the coupling

medium and ceramic plate. The acoustic wave induces harmonic elongations and compressions of the sensor element, which results in a potential difference between the two electrodes caused by the piezo-effect. An electrical voltage is measured with a voltmeter, when the instrument is connected with the sensor electrodes by a coaxial cable (e.g. Micro-BNC) [48,50].

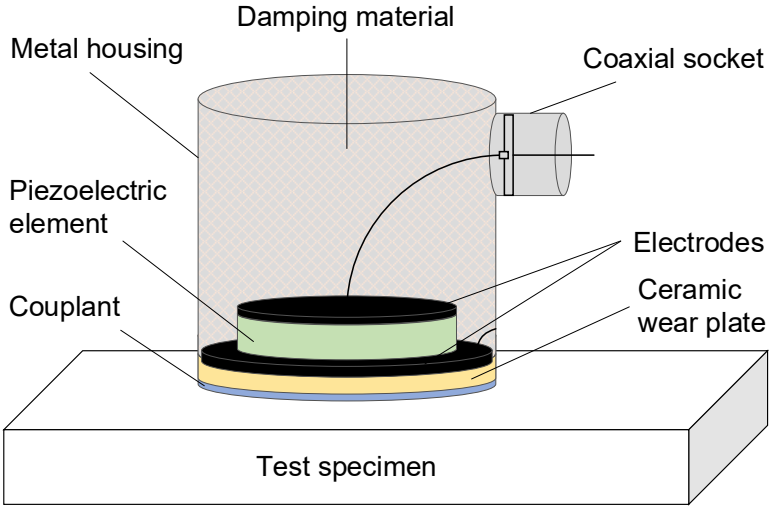

Fig. 5.4. Schematic design of a piezoelectric AE sensor.

Piezoelectric AE sensors can be characterized by their frequency response, which gives their sensitivity as a function of the excitation frequency. The frequency response curve of the sensor shows distinctive regions of highs and lows. The value and the amplitude of the maximum (resonance) and minimum (anti-resonance) frequency depends on the geometry, fixation, and material parameters of the piezo-element as well as the damping material [50].

The sensitivity S of piezoelectric AE sensors is typically in the range of 1mV/µbar in case of a harmonic excitation at its resonance frequency. This means, if the AE sensor is loaded with a pressure of 1µbar, it provides an output voltage of 1mV. Outside the excitation region of the resonance frequency, the sensitivity is orders of magnitude smaller. Hence, it is mostly quoted in dB and refers to a reference value of S_{ref} = 1V/µbar (see Eq. (5.1)).

$$S_{\mathrm{dB}} = 20\ \log\left(\frac{S}{S_{ref}}\right)\ \mathrm{dB\ ref}\frac{\mathrm{V}}{\mu\mathrm{bar}} = 20\ \log\left(\frac{S}{\frac{1\mathrm{V}}{\mu\mathrm{bar}}}\right)\ \mathrm{dB\ ref}\frac{\mathrm{V}}{\mu\mathrm{bar}} \quad (5.1)$$

Commercial AE sensors have a sensitivity of approx. -60 dB ref V/µbar at their resonance frequency and of approx. -100dB ref V/µbar at their anti-resonance frequency [51].

In Fig. 5.5 the frequency response curve of the AE sensor *Vallen VS900-M* [51] is shown within a frequency range between 50kHz and 1MHz. The local peak values are at resonance frequencies of about 160kHz and 340kHz, which are followed by minimum values at anti-resonance frequencies of ca. 180kHz and 380kHz, respectively. Below the excitation frequencies of 100kHz and above 900kHz the sensor sensitivity is strongly decreasing.

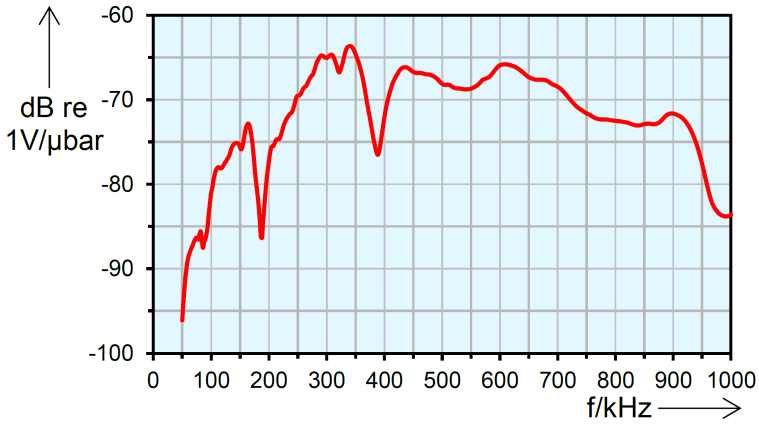

Fig. 5.5. Frequency response curve of the resonant piezoelectric AE sensor *VS900-M* [51].

Depending on the frequency response curve, the AE sensors can be classified into two categories: AE sensors of the resonant type and broadband type. Resonant sensors are characterized by frequency response curves with peaks and lows (see Fig. 5.5). This means, their sensitivity strongly depends on the excitation frequency and is highest at the resonance frequency. The resonant frequency is the key factor for which application the sensor can be used. Resonant sensors, however, are strongly affected by the frequency characteristics of the AE source. Hence, they are particularly suitable for applications in which no spectral analysis of the AE signal is performed and the main focus is applied to the AE feature extraction. It is important to know, that the AE features can only be compared if they are recorded with

the same AE sensor type. In contrast, broadband sensors exhibit a flatter frequency response curve and provide a good sensitivity over a broader, or wider, frequency range. This is often achieved by a sealing compound with highly dampening material properties. However, this is also the reason why the maximal sensitivity of a broadband sensor is usually lower than that of resonance-type sensors. Broadband sensors are mainly applied when the frequency of interest is not known or varies widely and if a spectral analysis of the AE signal should be performed [7].

Both sensor types are commercially available in different frequency ranges between approx. 20kHz and 2MHz. Further commercially available types of AE sensors are, for example, models with integrated preamplifiers or AE sensors with particularly resistant housings for harsh environmental conditions (e.g. high temperature, high pressure, or aggressive media) [51].

The topics of the future are AE sensors with wider and flatter response, higher sensitivity, and standardized calibration standards. Furthermore, currently discussed AE sensor techniques use MEMS, polymer foils with piezoelectric characteristics, and wireless communication [7,8].

b) Sensor Mounting and Coupling

The mounting method has two purposes: the first one is to hold the AE sensor on a fixed position on a test specimen, the second one is to ensure an adequate and constant acoustic coupling. Two common categories of mounting methods are compression mounts and bonding [52].

In compression mountings, the surface of the AE sensor is directly pressed onto the surface of the test specimen using a mechanical load. The fixture can be realized by e.g. springs, magnets, tape, or elastic bands. Nevertheless, the use of an additional couplant is strongly recommended [52].

The bonding method uses a suitable adhesive as couplant to attach the AE sensor directly to the test specimen. In contrast to compression mounts, thus no external force is needed for the fixture [52]. The couplant reduces transmission losses of the AE signal energy between the surface of the AE sensor and test specimen and thus mainly determines the quality of the sensor coupling. For the selection of an appropriate couplant, it is important to consider the boundary conditions, such as temperature, chemical resistance of both surfaces, and removability of the couplant. Moreover, the viscosity, shrinking, and drying time of the couplant has to fit the work operation. To optimize the coupling, the coupling surfaces need to be flat, clean (no dust, no dirt, etc.), and smooth (roughness < 50µm). In addition,

the couplant should be used sparingly and thinly pressed, in order to keep the wave attenuation low. Typically used couplants are, for instance, Si grease, oil, and adhesive [52,53].

To avoid disturbances, the AE sensor should be mounted to the test specimen without sliding or vibrations and without any cable bending and movement. Furthermore, the quality of the sensor coupling should be controlled after the sensor mounting and periodically, in order to check the sensor response signal, e.g. by a pencil lead breakage or an automatic coupling test [52,53].

c) Cable Connections

To minimize transmission losses of the sensor signal, a shielded cable, which connects the AE sensor with an external preamplifier, has to be as thin and short (≤ 1.2m) as possible. This coaxial cable protects the signal against EM radiation, but can possibly transmit mechanical vibrations into the piezoelectric element. Hence, a tensile load has to be avoided and the cable must not be sharply bent or stretched particularly at the connectors. Another coaxial cable, which could have a length of up to several meters, connects the preamplifier and the AE system. This cable is not sensitive to mechanical loads [48,51].

d) Preamplifier with Frequency Filter

The preamplifier is either separated or integrated into the AE sensor. It amplifies the signal voltage with a gain of up to 1000 and transmits the signal into the AE system. A low input noise is one of its key factors, so that even the smallest sensor signals can be separated from electrical noise. To process large amplitudes without overdrive, a high dynamic range is also indispensable. Moreover, different preamplifier designs include built-in or replaceable frequency filters, in order to attenuate unwanted frequencies and so optimize the ***S***ignal-to-***N***oise ***R***atio (SNR) [48].

e) AE System

The ***A***nalog-to-***D***igital ***C***onverter (ADC) of the AE system converts the analogue AE signal after pre-amplification and filtering into a digital signal. The requirement to the signal processor card regarding measurement dynamics and sampling rate are also very high. The AE signals typically have frequencies between 20kHz and 2MHz. Therefore, commercially available AE systems support sample frequencies of up to some 10MHz, in order to enable a high reproducibility of the output signal. The AE system records

the digital AE data either continuously or threshold-based (see Sect. 5.1.4). It buffers the AE data, extracts the AE features out of the received wave packets into AE feature data sets, and transfers the buffered data to the PC, where the data can further be processed and analyzed. Additional to one or more AE channels, some AE systems contain parametric channels, in order to measure the AE signals time-synchronized with external parameters, such as load (e.g. force, pressure) and ambient conditions (e.g. temperature, humidity) [48].

5.1.4 Data Recording and Processing

The waveforms arise by connecting many individual data points, which are obtained from many individual samples in a constant time period. For that, digital AE systems provide sampling frequencies f_s of a few tens of megahertz. This requires enormous memory for data storage of each and every data set. For example, at a sampling frequency f_s of 10MHz the digital AE system samples the AE signal every 100ns ($T_s = 1/f_s$), i.e. 10 million times per second. Thus, already a waveform over a duration of 100µs is created out of 1000 samples [48].

An important task of the AE system is to record only the AE signals and convert them into compact data sets and to ignore the relatively continuous background noise. For this, the system uses an AE detection threshold voltage U_{th}, which has to be set by the user to a reasonable value (see Fig. 5.6). If the AE signal exceeds the absolute value of the detection threshold in positive or negative direction, the recording time of a burst signal (= "AE hit") starts [48,54].

The term "AE hit" refers to a single burst signal, which is caused by an AE event (e.g. a crack) and measured by an AE sensor. It starts with the first threshold crossing and ends when the input voltage does not cross the detection threshold for a specified period of time, the so-called ***D***uration ***D***iscrimination ***T***ime (DDT). The number of hits per time interval is a measure for the AE activity [48].

a) AE Feature Extraction

At AE testing, however, one usually has to deal with hundreds or thousands of burst signals that can only be evaluated statistically in practice. The statistical evaluation of waveforms requires meaningful features. Features are meaningful, if their statistical distribution differs between a "good" and "bad" test specimen. The AE system extracts the AE features out of the

recorded burst signals and generates one data set per burst, containing all important AE features [48].

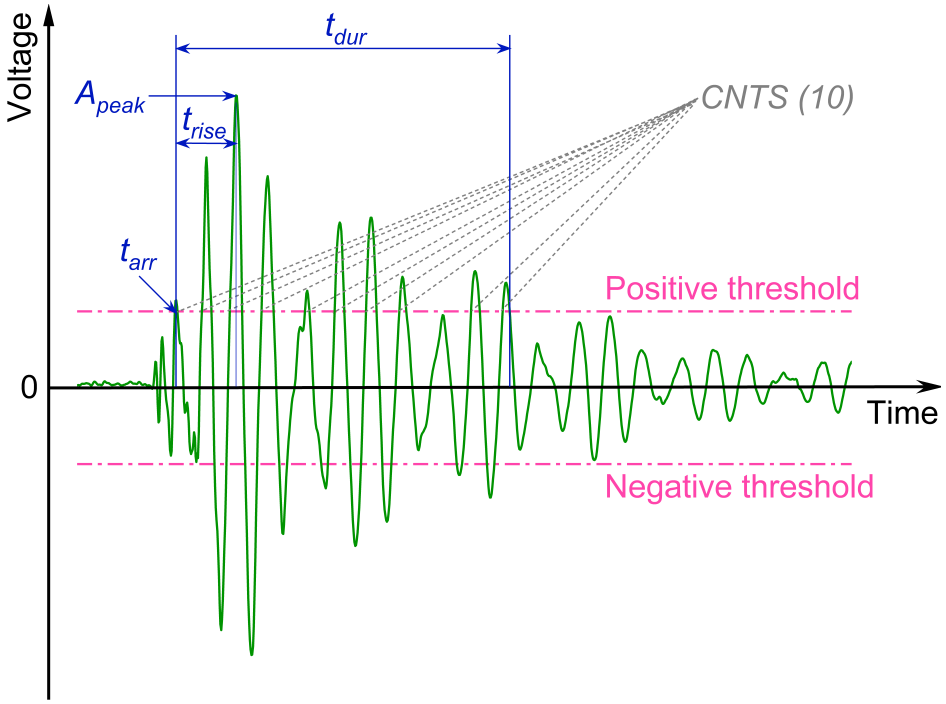

Fig. 5.6. AE features describing a burst signal in time domain.

Fig. 5.6 shows a typical AE signal in the time domain with a definition of most common AE features [54]:

1. *Arrival Time t_{arr}:* The arrival time is the absolute time when the burst signal crosses the detection threshold voltage for the first time.
2. *Burst Signal Peak Amplitude A_{peak}:* The peak amplitude indicates the maximal voltage excursion within a hit.
3. *Burst Signal Rise Time t_{rise}:* The time difference between the first threshold crossing and the peak amplitude of the hit is termed signal rise time.
4. *Burst Signal Duration t_{dur}:* The signal duration refers to the time difference between the first and last threshold crossing of a burst signal.

5. *Ring Down Counts CNTS:* *CNTS* are the number of threshold crossings of the hit in one polarity. The example signal, shown in Fig. 5.6, has 10 *CNTS*.

In AE testing the characteristic voltages, e.g. the peak amplitude A_{peak} or detection threshold voltage U_{th}, are typically given in dB_{AE}. This unit refers to a reference value U_0 of 1µV (see Eq. (5.2)) [54,55]. Table 5.1 shows some examples of the dB_{AE}- to µV-scale conversion.

$$U_{dB_{AE}} = 20\ \log\left(\frac{U}{U_0}\right) dB_{AE} = 20\ \log\left(\frac{U}{1\mu V}\right) dB_{AE} \tag{5.2}$$

Table 5.1. dB_{AE} to µV conversion.[4]

dB_{AE}	-20	0	20	34 (= 40 – 6)	40	46 (= 40 + 6)	60	80	100
µV	0.1	1	10	50 (= 100 / 2)	100	200 (= 100 • 2)	10^3	10^4	10^5

The burst signal energy E_{burst} is another important feature of a hit. It is defined as the released elastic wave energy by an AE event and used as a filter criterion for the AE data within this work. According to EN 1330-9 [54] the burst signal energy E_{burst} is the integral of the squared AE signal voltage U over time t in units of V^2s.

$$E_{burst} = \int_0^t U^2(t)\mathrm{d}t \tag{5.3}$$

The signal processor card *ASIP-2/A*, which is used in this work, calculates the burst signal energy from voltage samples, i.e. it is the sum of all squared voltage samples U_i of a hit (i = 1, 2 … n) multiplied by the sampling time interval T_s and has the unit eu (1eu = $10^{-14}V^2s$).

$$E_{burst} = \sum_1^{i=n} {U_i}^2\, T_s \tag{5.4}$$

By definition, the reference resistance is 10kΩ, which is used to scale the units V^2s to Joule. Using this resistance, 1eu corresponds to 10^{-18}J [55].

Burst signals can be generated by both defects and disturbances. Therefore, it is important to identify AE features to distinguish between relevant and disturbing signals. According to many AE testing applications, the peak amplitude A_{peak} and the burst signal energy E_{burst} are the most relevant AE

[4] The values are rounded for demonstration, i.e. $6dB_{AE}$ gives a factor of 1.99526 instead of 2.

features of a burst signal, as they describe best the intensity and type of an AE event [48].

b) Methods of AE Signal Analysis

Currently the interpretation of the results from AE testing is mainly based on the analysis of extracted AE features in the time domain. Thereto differential or cumulative distributions of the AE features as a function of the time or external parameters (e.g. force, pressure, etc.) can be created. Correlation plots of the AE features and multi-dimensional parameter classifications are also used to interpret the AE signals. To improve the data analysis, today's technology enables a flexible logical filtering of the AE features. It should be noted, that filtering always captures the risk of overlooking or misinterpreting burst signals. In addition, regarding the data interpretation one should take into account losses due to the wave propagation in the material, the frequency-dependent sensitivity of the AE sensor, and the gain of the preamplifier [8,48].

5.2 Modified Acoustic Emission Test Concept for Thin Layer Crack Detection

The innovative approach of the modified concept is based on the already established AE test method, which was described in Chap. 5.1. During wafer probing, elastic contact probes mechanically stress the crack sensitive layer structures below the pad. Under certain stress conditions cracks in brittle layers can be generated, which release acoustic shock waves moving further into the body and onto the surface of the wafer. The acoustic waves are transmitted into an AE sensor, which is placed either on the surface of the chip or connected with the contact probe [56]. This progressive method enables both crack generation and detection simultaneously (see Fig. 5.7).

Probing induced IMD cracks have sizes down to nanometer dimensions (see Sect. 2.3.3) with very small released crack energy. This requires very high sensitivity and resolution of the AE sensor system and elimination of disturbances. In order to use the modified AE test method for the wafer probing process qualification, the measurement concept was adapted to reach these goals.

In a first step, the influencing factors and disturbances of the new measurement setup and process, that are present in the AE crack detection, are detailed described. In a second step, the test bench called ***PROFIT*** (***Pro***be ***F***orce ***I***nvestigation ***T***ool) used for single probe experiments, which was already available at the company-owned lab, was extended by a commercial

AE control system of the supplier *Vallen Systeme GmbH*. Based on this configuration, the components of the test bench could be defined, modified, and optimized accordingly.

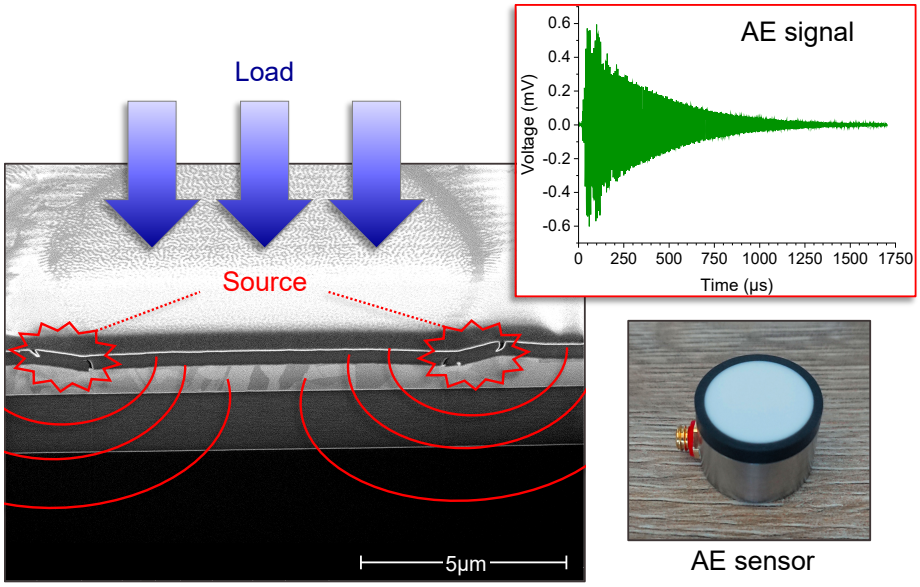

Fig. 5.7. Concept for simultaneous crack generation and detection.

5.2.1 Root Cause-Effect Analysis

For a systematic investigation of the oxide crack probability, a root cause effect diagram (i.e. *Ishikawa* diagram) was first compiled, in order to identify all influencing factors. The theoretical basic concept of the AET (see Chap. 5.1) and the first experimental findings with the existing test bench *PROFIT* proved to be helpful. For the definition of the following experiments, it was first of all important to evaluate the process parameters, disturbances, and influencing variables of the individual components. All factors were assigned to the five main categories "man, machine, method, material, and measurement". The *Ishikawa* diagram according to the 5M-method is shown in Fig. 5.8.

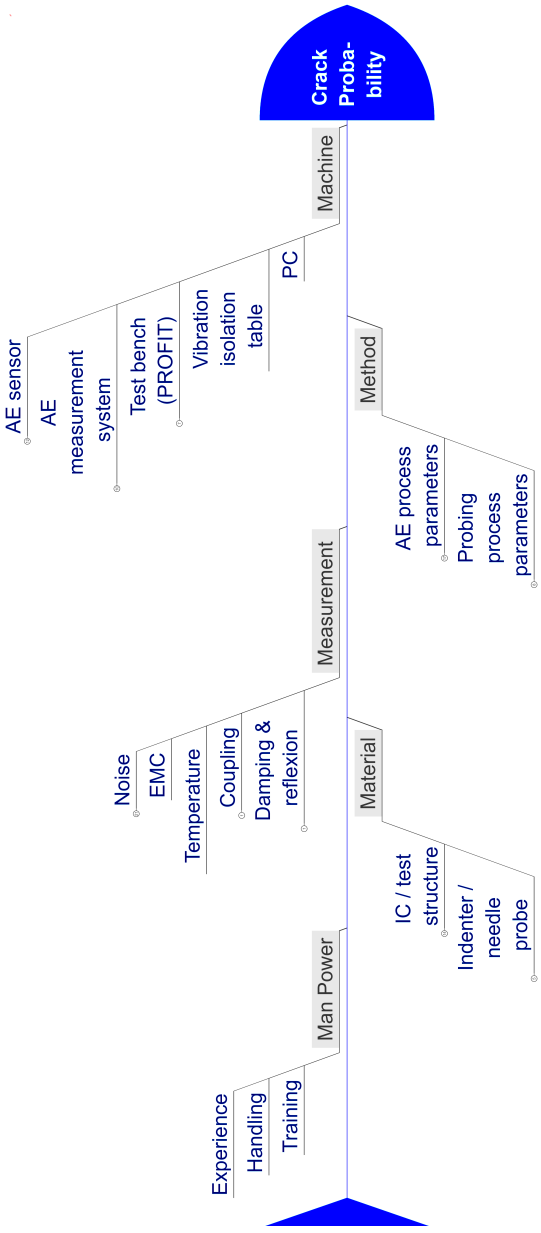

Fig. 5.8. *Ishikawa* diagram: Influencing factors affecting crack probability.

After collecting the influencing factors and their effects on the crack probability, it was possible to create an experimental plan for the existing test bench, in order to optimize the AE test method. The electrical and mechanical parameters of the various components were first evaluated.

Subsequently, the possible disturbance variables were identified in various test series. The measuring range, the sensitivity, and the specification of the individual system components could be extracted from the data sheets of the manufacturers. Because of the multitude of variables, it was important to identify those factors that have the most significant effect on the signal quality of the AE measurement.

The following influencing factors were selected from the *Ishikawa* diagram in Fig. 5.8 and implemented into the new test concept:

I. Sensor holder coplanarity und force calibration procedure
II. Electromagnetic and mechanical disturbances
III. Gain of AE measurement signal
IV. Stiffness of the contact needle
V. Indenter-sensor coupling
VI. Test chip design and manufacturing process

The optimized test bench concept is covered in items I – III (see Sect. 5.2.2). The items IV and V will be discussed in detail in Sect. 5.2.3 and the item VI in Chap. 6.1.

5.2.2 Optimized Test Bench Configuration

The test bench *PROFIT* was developed by *O. Nagler* during his PhD work at the *Infineon Technologies AG* in Munich in cooperation with the *Universität der Bundeswehr München*. In its original configuration the *PROFIT* was used for probing process characterizations. At this, different designs and concepts of single needles were evaluated regarding their mechanical and electrical performance on various contact materials. Thereto, the *PROFIT* was developed to set the overdrive and to measure the probe's normal and lateral force and the electrical contact resistance during contacting. Using this tool all probing-relevant physical parameters could be simultaneously controlled and measured in real-time under realistic conditions [16].

Fig. 5.9 shows the schematic of the *PROFIT* in its original configuration. The test structure is fixed on its backside to the surface of a sample holder, called chuck, by a vacuum system. The chuck is mounted on a 3-axis linear positioning stage from the supplier *PI*. Within a maximum vertical travel range of 12.5mm, the model *M501* reaches a vertical travel resolution of 25nm. The tool uses two single low force sensors for measuring the vertical

(*z*) and lateral (*x*) probe force. Both force sensors are load cells of the supplier *HBM* and based on strain gauges enabling measurements with a resolution of less than 0.5mN. The electrical contact resistance between the probe tip and the test structure is measured using a 4-pole measurement concept. The single needle is mounted on a PCB, which is flipped over and fixed to a metal frame. During contacting, the chuck with the test structure on top moves towards the fixed probe. The microscope and CCD camera allow an optical control of the probing process in real-time [1,16].

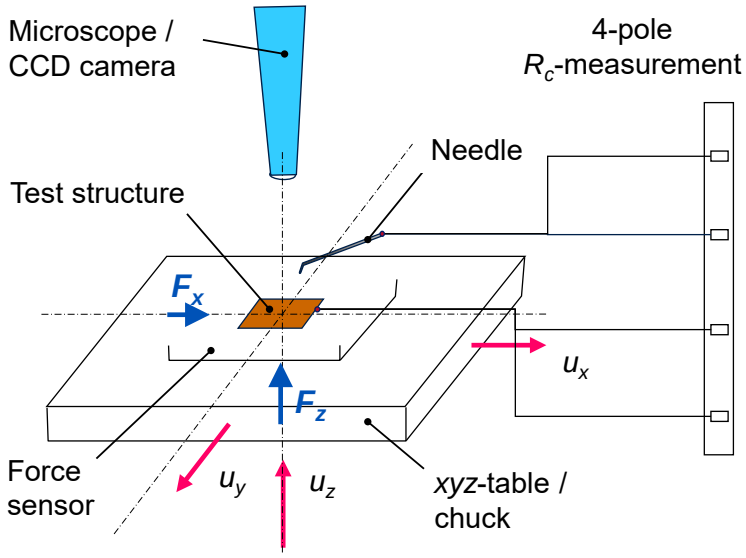

Fig. 5.9. Schematic of the *PROFIT* in its original configuration (modified by [16]).

A single-channel measuring amplifier of the supplier *HBM*, model *ML35B*, is used for electronic data acquisition and recording. The position control of the chuck as well as the data acquisition of the force sensors are done on the computer using a *NI Labview* program. In order to minimize external disturbances due to vibrations, human interactions, etc., the test bench is placed on a vibration damping table [1].

In this work the *PROFIT* tool was modified and extended and later on used for the acoustic crack experiments. The modifications and extensions where carried out in cooperation with *Infineon Technologies AG* in Regensburg, department *Automation and Equipment Technology*.

a) Sensor Holder

In order to place and fix the acoustic sensor below the sample, a new sensor holder replaced the previous design. The high-precision force sensor requires a bracket with high strength and rigidity. However, the sensor holder must have a low weight, to avoid overloading on the vertical positioning stage. The new bracket was hence manufactured from a lightweight material that still has enough strength and stability. Due to the sensitive AE measurement, further on an electrically insulating material was chosen.

b) Sample Holder Plate

To reach higher sensitivity, the contact probe (indenter) was placed on the surface of the AE sensor instead of test structure (see Sect. 5.2.3). Therefore, the design of the PROFIT (see Fig. 5.9) was modified with a new sample holder plate (see Fig. 5.11, top right). As the plate highly affects the frame rigidity of the overall system, the new component was accordingly designed and made of steel to achieve a high strength and rigidity.

c) Optical Alignment System

Another extension of the existing test bench was the installation of an alignment camera unit to ensure an accurate placement of the indenter tip on the test structure, which made it possible to use structured test chips, too. In Fig. 5.10 the mounted optical system (lens with camera, deflection mirror, and sensor holder) can be seen.

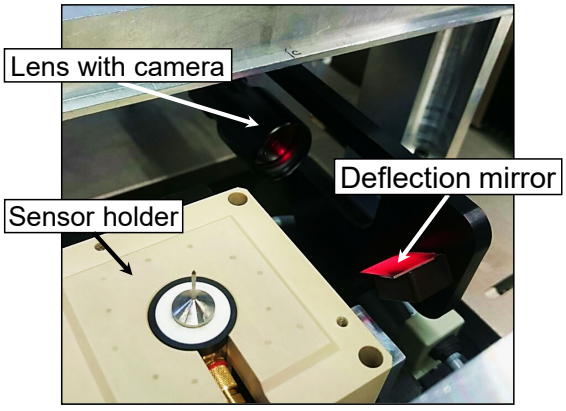

Fig. 5.10. Installed alignment camera unit on existing test bench.

d) AE Measurement Components

Furthermore, the *PROFIT* tool was equipped with a commercial AE control unit made from the supplier *Vallen Systeme GmbH*. The hardware consists of a piezoelectric sensor (model *VS900-M*), a preamplifier (model *AEP3N*), and the Vallen *AMSY-6* AE system with an integrated AE signal processor card (model *ASIP-2/A*). The data acquisition and analysis is done by the *Vallen AE-suite* software tools *Vallen Acquisition* and *VisualAE*. The acquisition software configures and controls the hardware and collects data for further processing via the computer. The analysis software is used for the online and offline data acquisition and processing. The extended test bench including the *Vallen* AE components is shown in Fig. 5.11.

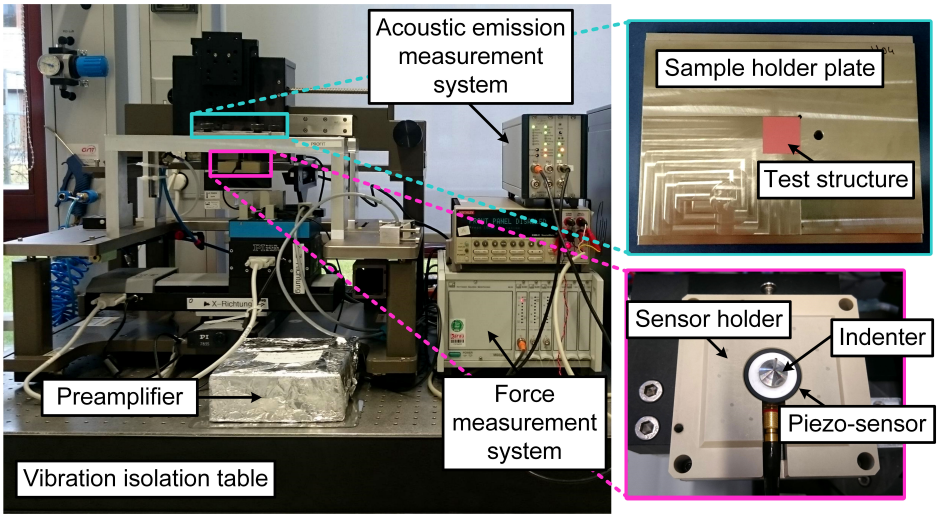

Fig. 5.11. Extended test bench *PROFIT* for acoustic crack experiments.

The indenter is glued on top of the piezoelectric sensor and mounted in upright position on the 3-axis linear precision stage. The test structure is glued (e.g. with nail polish) on its backside to the sample holder plate, which is fixed flipped over on a metal frame. During contacting the indenter tip presses vertically to the surface of the test structure (see Fig. 5.12) and transmits the acoustic wave from the indenter into the piezo-sensor. The electrical AE signal is sent into the preamplifier and filtered (bandpass 95kHz – 1MHz). For data acquisition, recording, and further processing, the AE signal is fed into the signal processor card *ASIP-2/A*, which is connected to a PC for graphical output and post-processing. The force sensor signal is

transmitted into the parametric channel of the AE system and synchronized with the AE signal.

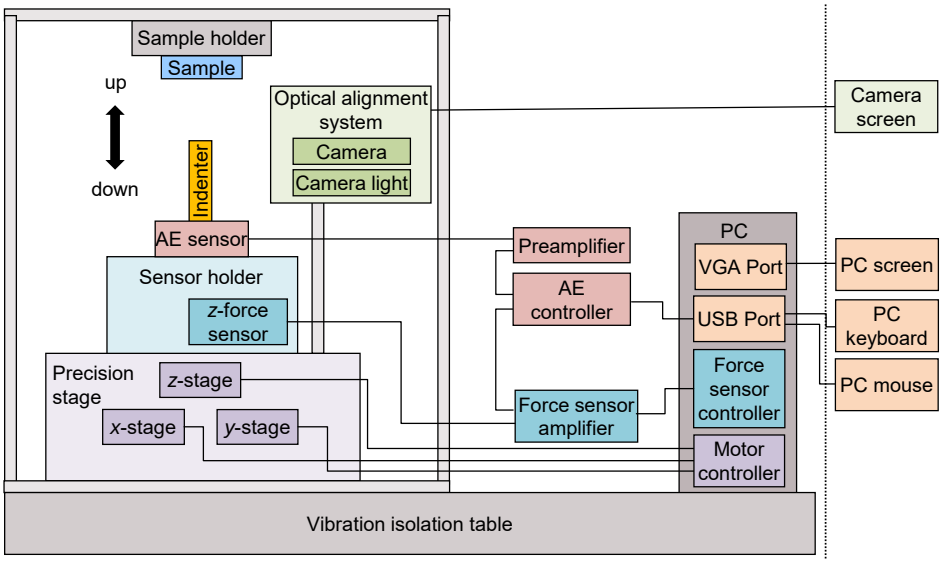

Fig. 5.12. Test bench schematic for acoustic crack detection.

e) Sensor Holder Coplanarity and Force Calibration Procedure

The coplanarity, stiffness, and elasticity of the sensor holder may potentially influence the force linearity in lateral and vertical directions. Hence, at first the coplanarity error of the sensor holder surface was measured using a micrometer gauge and levelled. The coplanarity error (vertical deviation from the initial *z*-position) after levelling reached maximal ±5µm across the surface (edge length approx. 10mm).

Following, the linearity of the vertical force was checked (see Fig. 5.13) by gradually increasing and measuring the load with calibrated weights (2-cent Euro coins). From this, the linearity error of the vertical force F_z could be determined. In the specific case, the linearity error was about 2% of nominal load, which is acceptable for the required measurement accuracy.

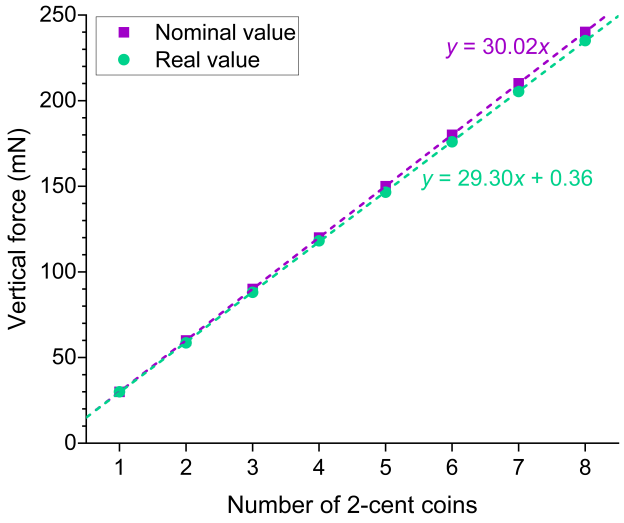

Fig. 5.13. Linearity of vertical force.

f) Electromagnetic and Mechanical Disturbances

Electromagnetic fields can lead to interference and falsification of the measurement of sensitive electronic devices with low currents or voltages without shielding. Therefore, it had to be ensured that all cables and devices are ***E***lectro***m***agnetic ***C***ompatibility (EMC)-proof. Although the components of the AE system were already adequately shielded by the manufacturer, it was found during the tests on the test bench, that the AE measurement is very sensitive to EM-radiation at high gain (61dB). To improve the sensitivity, the preamplifier was hence wrapped with Al foil. The mechanical interference effects, which were transferred from external vibrations and sensor cables into the force sensor, could be reduced by attaching cable clamps and by removing the lateral force sensor, which was part of the original test bench configuration, but not required anymore.

g) Gain of AE Measurement Signals

The *Vallen AEP3N* preamplifier and the *ASIP-2/A* signal processor card offer the possibility to choose different levels of amplification for the AE signal. Combining both devices, a gain between 34dB up to 61dB can be selected in steps of 3dB. As has been shown in measurements with different signal amplification, a maximum gain of 61dB for the detection of oxide cracks with the AE test method was best and thus chosen as standard in the further experiments.

5.2.3 Modification of Sensor-Indenter Concept

Many different types of probes for wafer test generate a lateral force in addition to a vertical force to reduce the contact resistance through lateral scrubbing motion (see Sect. 2.2.2). However, this scrubbing motion also causes an acoustic noise which overlays with a possible oxide crack. This fact led to a new approach to the preliminary experiments. Instead of a conventional, spring-like *cantilever* needle, a rigid, vertically arranged needle (= indenter) is used, which acts exclusively perpendicular to the sample during the contact, without causing a lateral scrub.

In Fig. 5.14 two measuring arrangements for the acoustic crack detection are shown schematically. In each case a contact probe is shown, which presses with a mechanical force vertically on the contact pad of the chip to close an electrical contact.

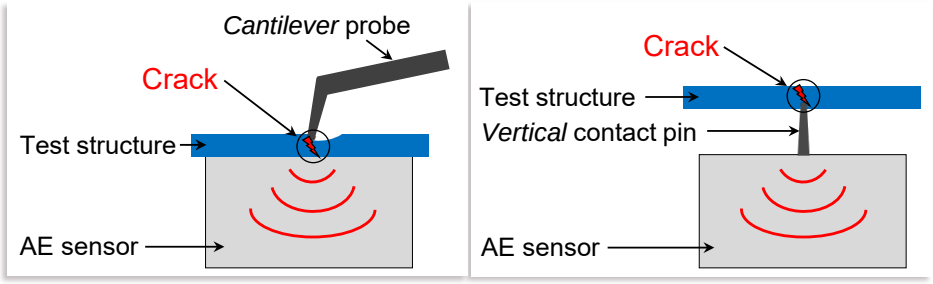

Fig. 5.14. Modification of the contact needle and sensor coupling concept.

As can be seen, in addition to the type of contact probe also the sensor coupling has been changed. Instead of placing and gluing the sample (test chip) on the AE sensor, the probe is arranged vertically and directly coupled to the AE sensor. This has the advantage, that the acoustic wave is coupled at the location of the maximum sensor sensitivity, which is in the center of the cylinder surface. Moreover, the newly developed coupling concept eliminates the time-consuming and complicated gluing as well as removing of the chip from the sensor, which can cause a destruction of sensitive structures.

For the AE experiments, mostly a rigid indenter with a conical flat diamond tip of 10µm diameter was used. This new concept better meets the requirements of the AE measurement in terms of stability, strength, and accuracy.

The indenter had to be permanently connected to the sensor surface and secured against tilting. For this purpose, various brackets were specially manufactured by the in-house workshop. In Fig. 5.15, left one can see a sketch of the first structure and right the realized solution with the AE sensor in the holder.

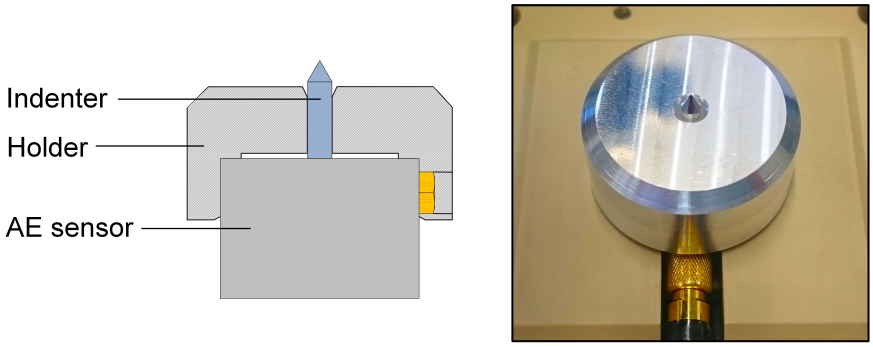

Fig. 5.15. Indenter fixture on top of AE sensor.

It can be seen, that the indenter is perpendicular placed on top of the AE sensor and glued to it with a cyanoacrylate adhesive. In order to prevent sliding or tilting of the indenter under load, it is also secured by a holder specially designed for this solution, which is inserted over the sensor housing. The assembled sensor-indenter construction was then connected to the BNC cable, placed to the sensor holder (see Fig. 5.15, right), and tightened. As previously mentioned this arrangement prevents lateral movement of the tip and ideally applies only a vertical force to the test structure.

Using this concept, acoustic crack measurements were carried out on the modified *PROFIT* test bench on unstructured test chips. However, the results of the acoustic and optical crack checks were inconsistent. Therefore, it was assumed that many AE signals were generated due to disturbances such as friction, particles, or air compression between the indenter shaft and its holder. Because of the rigid holder, the indenter was inhibited in its free oscillation. In addition, it was assumed that the free oscillation of the indenter was increasingly blocked by the holder during the course of the experiments, which led to a reduced measuring sensitivity for the acoustic crack detection. Hence, it was concluded, that this solution was unsuitable for the further AE measurements and that an improved construction was required.

The aim of the new holder concept was to reduce the mentioned disturbances as much as possible. Moreover, during the design of the new fixture, attention was paid to developing a concept with a lower mechanical rigidity, in order to allow a free oscillation of the indenter and hence achieve a higher sensitivity for the acoustic crack detection. At the same time, the new holder should support the indenter to a sufficient extent to avoid a moving or tilting of the indenter from its vertical position.

The new mounting concept was the so-called 2-component solution. Here the indenter was inserted into a centric fitting hole of a conical fixing ring (see Fig. 5.16). Both components were then glued on the top side with the sensor surface using a cyanoacrylate adhesive. Although the measuring sensitivity could be significantly increased with the new 2-component concept, this fixation variant also produced disruptive effects, albeit to a lesser extent than before.

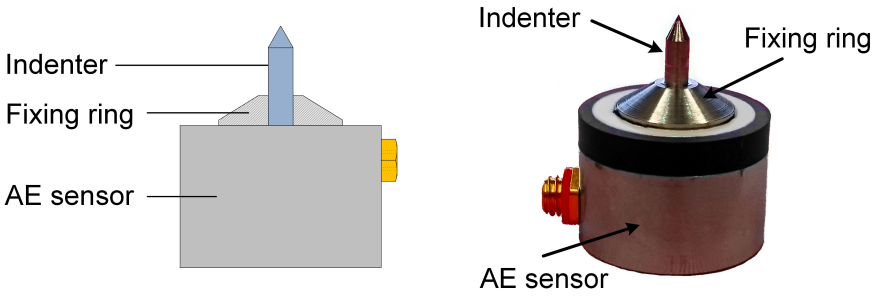

Fig. 5.16. 2-component sensor-indenter system.

In order to further eliminate the effects of interference by friction, to increase the measuring sensitivity even further, and to facilitate the process of gluing, the indenter and fixing ring were subsequently made in one piece, the so-called 1-component or *monolithic* solution. The advantages of the final solution over the previous solutions are discussed in detail in the next chapter and Sect. 6.2.3.

5.3 Sensor-Indenter System Optimization

The frequency of an acoustic wave based on previous FEM-simulations, resulting from the cracking of a thin layer, is several hundred MHz or even above one GHz. AE signal measurements, that are presented and described in detail in Chap. 6 and 7, however, have frequencies in the range of 100kHz to 1MHz, which is in contradiction to the classical AE theory. Therefore, in

this chapter a newly developed model about the generation of crack-induced acoustic signals on thin layers is presented and verified by simulations and measurements. This model is mandatory to develop and manufacture a novel sensor-indenter system with higher sensitivity as before, which was then successfully applied for further AE crack measurements on test structures consisting of thin layer stacks.[5]

5.3.1 Crack Pulse Excitation of an Oscillating Indenter Rod

As described in Chap. 5.2, instead of the direct coupling of the test specimen with the surface of an AE sensor, the indenter with its one end was first positioned vertically on the sensor. Fig. 5.17 shows the principle schematically.

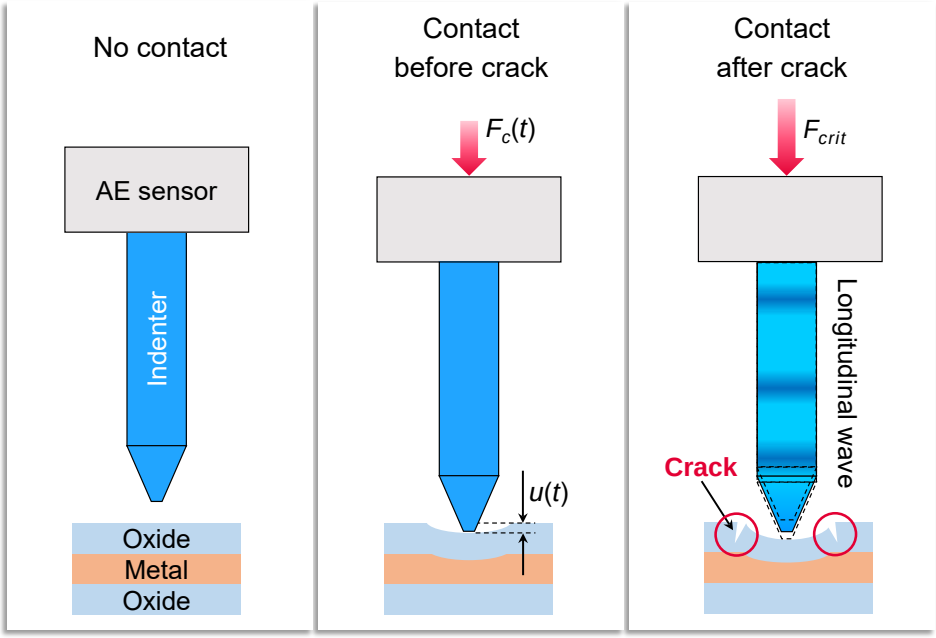

Fig. 5.17. Vertical indenter pressing on thin layer stack.

In this case, the test specimen consists of a layer composite of oxide - metal - oxide corresponding to a typical material combination of CMOS semiconductor structures (see Sect. 2.3.1). The pointed end of the indenter is then pressed with an increasing force F_c over the time t perpendicular to the

[5] This topic is also part of [3].

specimen (see Fig. 5.17, center). The surface load causes a vertical deflection $u(t)$ of the brittle material, which is linear within the elastic strain region (see Fig. 4.5).

In Fig. 5.17 on the right, the contact force F_{crit} has reached the critical level, where the brittle material breaks and thus the displacement u is abruptly increased by the amount Δu. This leads to a pulse-like excitation of the indenter, which is thereby set in harmonic oscillation at its damped natural frequency. In the graphs of Fig. 5.18, the contact force F_c as a function of the displacement u (left) and the displacement u as a function of the indentation time t (right) for the cases before, during, and after the crack event are shown separately.

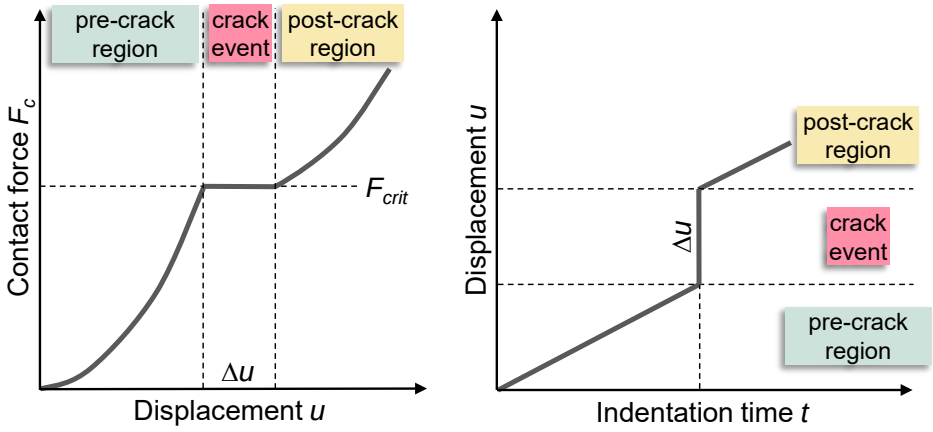

Fig. 5.18. Force and displacement plots during indentation on a thin layer stack.

After theoretically describing the cracking mechanism of an indenter, which is stimulated impulsively into oscillation, one can model the system as a spring-mass oscillator and describe it analytically.

As shown in Fig. 5.19, the indenter can be considered as linearly damped oscillator with a single mass m_{os}, the constant spring rate k_{os}, and the degree of damping d_{os}.

The solution of the equation of motion describes mathematically a harmonic oscillation, which is derived from the equilibrium of forces of a damped spring-mass system. Oscillating systems, which usually change its position periodically with the time t, can be described by suitable state variables. The value $x(t)$ is the displacement of the mass from its rest position

($x = 0$) [57,58]. In the following, the equation $x(t)$ for describing the impulse response of the oscillator will be derived.

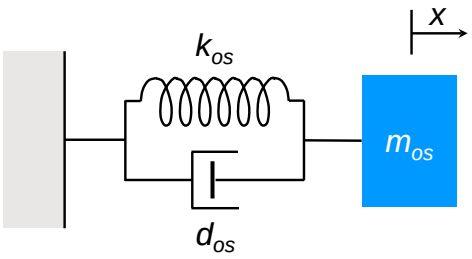

Fig. 5.19. Damped spring-mass oscillator.

If one observes a single point on the oscillating mass m_{os}, it moves in positive and negative x-direction at a constant circular velocity ω on a circle of radius A. The displacement $x(t) = A\sin(\omega t)$ can be plotted over ωt (see Fig. 5.20) [59].

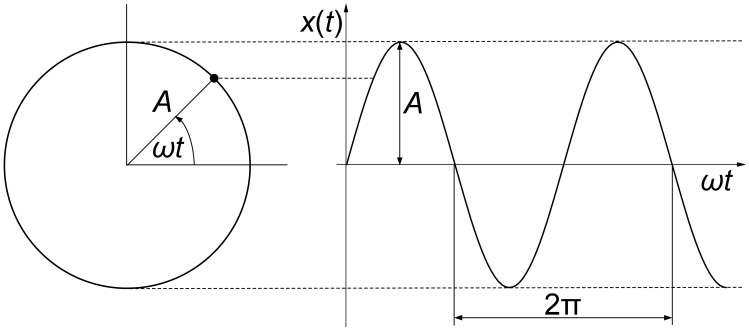

Fig. 5.20. Sinusoidal oscillation.

The mass deflection $x(t)$ over time of the harmonic oscillation is given in Eq. (5.5):

$$x(t) = A \sin \omega t, \tag{5.5}$$

where A is the amplitude and ω the angular frequency, measured in rad/s.

The relationship between the angular frequency ω, the frequency f, and the oscillation time or period T is:

$$\omega = 2\pi f = \frac{2\pi}{T}. \tag{5.6}$$

The frequency is defined as $f = 1/T$ and has the unit $[f] = 1\text{Hz} = 1/\text{s}$ [59].

By establishing the equilibrium of forces of the damped spring-mass oscillator from the drawing in Fig. 5.19, where F_i is the inertia force, F_d the damping force, and F_k the spring force,

$$F_i + F_d + F_k = 0 \tag{5.7}$$

the equation of motion, which can be written as linear differential equation of the second degree with constant coefficients is obtained according to [57,58]:

$$m_{os}\ddot{x} + d_{os}\dot{x} + k_{os}x = 0. \tag{5.8}$$

With definition of the natural angular frequency of the undamped oscillator

$$\omega_0 = \sqrt{\frac{k_{os}}{m_{os}}} \tag{5.9}$$

and the so-called dimensionless *Lehr attenuation*

$$D = \frac{d_{os}}{2m_{os}\omega_0} \tag{5.10}$$

the differential equation in Eq. (5.8) becomes:

$$\ddot{x} + 2D\omega_0\dot{x} + \omega_0^2 x = 0. \tag{5.11}$$

Eq. (5.11) can be solved by using the substitution approach for the term $x(t)$ and its first and second derivations[6]:

$$x(t) = \underline{A}e^{\lambda t} \tag{5.12}$$

$$\dot{x}(t) = \lambda\underline{A}e^{\lambda t} \tag{5.13}$$

[6] The underscore indicates a complex number.

$$\ddot{x}(t) = \lambda^2 \underline{A} e^{\lambda t}. \tag{5.14}$$

By inserting Eq. (5.12) until (5.14) in Eq. (5.11), the differential equation can be written as:

$$(\lambda^2 + 2D\omega_0\lambda + \omega_0^2)\underline{A} e^{\lambda t} = 0. \tag{5.15}$$

In addition to the trivial solution for $\underline{A}$ = 0, one can find two non-trivial solutions via the quadratic equation in λ:

$$\lambda^2 + 2D\omega_0\lambda + \omega_0^2 = 0. \tag{5.16}$$

The solutions of Eq. (5.16), the so-called eigenvalues of the differential equation, are:

$$\lambda_{1,2} = -D\omega_0 \pm \omega_0\sqrt{D^2 - 1}. \tag{5.17}$$

There are several solutions for Eq. (5.17) possible, but here we only focus on rule case $D < 1$. By further introducing of the decay factor

$$\delta = D\omega_0 \tag{5.18}$$

and the natural angular frequency of the damped oscillator

$$\omega_d = \omega_0\sqrt{1 - D^2} \tag{5.19}$$

Eq. (5.17) becomes:

$$\lambda_{1,2} = -\delta \pm j\omega_d, \tag{5.20}$$

with the complex eigenvalues λ_i and the imaginary unit j^2 = -1.

Inserting Eq. (5.20) into Eq. (5.12) one gets two linearly independent solution equations:

$$\underline{x_1} = \underline{A_1} e^{\lambda_1 t} = \underline{A_1} e^{(-\delta + j\omega_d)t} = \underline{A_1} e^{-\delta t} e^{j\omega_d t} \tag{5.21}$$

$$\underline{x_2} = \underline{A_2} e^{\lambda_2 t} = \underline{A_2} e^{(-\delta - j\omega_d)t} = \underline{A_2} e^{-\delta t} e^{-j\omega_d t} \tag{5.22}$$

with $A_{1,2} \in \mathbb{Q}$.

The general solution of the differential equation in Eq. (5.11) can thus be written as linear combination of the two solutions in Eq. (5.21) and (5.22):

$$x(t) = \underline{A_1} e^{\lambda_1 t} + \underline{A_2} e^{\lambda_2 t} = e^{-\delta t}\left(\underline{A_1} e^{j\omega_d t} + \underline{A_2} e^{-j\omega_d t}\right). \tag{5.23}$$

For dividing the solution into the real and imaginary part, it is useful to transform the complex coefficients $\underline{A_1}$ and $\underline{A_2}$ in the exponential form:

$$\underline{A_1} = r_1 e^{j\varphi_1} \text{ and } \underline{A_2} = r_2 e^{j\varphi_2}. \tag{5.24}$$

Then Eq. (5.23) becomes:

$$x(t) = e^{-\delta t}\left(r_1 e^{j\varphi_1} e^{j\omega_d t} + r_2 e^{j\varphi_2} e^{-j\omega_d t}\right) \tag{5.25}$$

$$x(t) = e^{-\delta t}\left(r_1 e^{j(\varphi_1 + \omega_d t)} + r_2 e^{j(\varphi_2 - \omega_d t)}\right). \tag{5.26}$$

The fact that this motion is an oscillation becomes clearer, if one uses the *Euler* formula

$$e^{\pm j\alpha} = \cos\alpha \pm j \sin\alpha \tag{5.27}$$

to transform the exponential functions with imaginary arguments into sine and cosine functions. This applies:

$$\begin{aligned} x(t) = e^{-\delta t}\{&r_1[\cos(\omega_d t + \varphi_1) + j\sin(\omega_d t + \varphi_1)] \\ &+ r_2[\cos(-\omega_d t + \varphi_2) + j\sin(-\omega_d t + \varphi_2)]\} \end{aligned} \tag{5.28}$$

$$\begin{aligned} x(t) = e^{-\delta t}\{&r_1\cos(\omega_d t + \varphi_1) \\ &+ r_2\cos(-\omega_d t + \varphi_2) + j[r_1\sin(\omega_d t + \varphi_1) \\ &+ r_2\sin(-\omega_d t + \varphi_2)]\}. \end{aligned} \tag{5.29}$$

To obtain a physically meaningful solution, the imaginary part Im(x) must disappear:

$$Im(x) = r_1\sin(\omega_d t + \varphi_1) + r_2\sin(-\omega_d t + \varphi_2) = 0 \tag{5.30}$$

$$\Leftrightarrow\ r_1\sin(\omega_d t + \varphi_1) = r_2\sin(\omega_d t - \varphi_2) \tag{5.31}$$

$$\Rightarrow r_1 = r_2 \text{ and } \varphi_1 = -\varphi_2. \tag{5.32}$$

By inserting Eq. (5.32) into Eq. (5.29), the real part is given by:

$$Re(x) = r_1 \cos(\omega_d t + \varphi_1) + r_2 \cos(-\omega_d t + \varphi_2) \tag{5.33}$$

$$= r_1 \cos(\omega_d t + \varphi_1) + r_1 \cos(-\omega_d t - \varphi_1) \tag{5.34}$$

$$= r_1 \cos(\omega_d t + \varphi_1) + r_1 \cos(\omega_d t + \varphi_1) \tag{5.35}$$

$$= 2r_1 \cos(\omega_d t + \varphi_1)\,. \tag{5.36}$$

If one defines the constant

$$B = 2r_1 \tag{5.37}$$

and the phase shift

$$\varphi_1 = -\varphi_0, \tag{5.38}$$

the general solution of the differential equation of the damped single-mass oscillator (see Eq. (5.11)) is obtained by:

$$x(t) = \; e^{-\delta t} B \cos(\omega_d t - \; \varphi_0) \;\text{ with } B, \varphi_0 \in \; \mathbb{R}. \tag{5.39}$$

The freely selectable constant B, which here is the amplitude at t = 0, and phase angle φ_0 are determined by the physical initial conditions of the oscillator at t = 0. Depending on the choice of the initial conditions, this results in a clear solution of the general solution of the differential equation [57,58,60].

If the damped oscillator is excited by a single rectangular pulse $f(t)$ of a duration of $\Delta\varepsilon$ (so-called *Dirac* pulse, see Fig. 5.21) this shock results in a change of the velocity state of the oscillator. The normalized unit pulse ΔI is calculated by the integral in Eq. (5.40) [57,60].

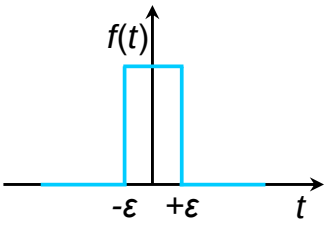

$$\Delta I = \int_{-\varepsilon}^{+\varepsilon} f(t)\mathrm{d}t = 1. \tag{5.40}$$

Fig. 5.21. *Dirac* pulse.

The oscillator with a mass m_{os} experiences a velocity change v_o from v = 0 to the value

$$v_0 = \frac{\Delta I}{m_{os}}. \tag{5.41}$$

In the case of a *Dirac* pulse at time t = 0 on the resting oscillator, the initial conditions are:

$$x(0) = 0 \tag{5.42}$$

$$\dot{x}(0) = v_0. \tag{5.43}$$

Inserting these initial conditions, the constants B and φ_o can be determined from Eq. (5.11) and thus giving the impulse response of the oscillator [58]:

$$x(t) = \frac{v_0}{\omega_d} e^{-\delta t} \sin \omega_d t. \tag{5.44}$$

The amplitude of the free oscillation of the damped spring-mass oscillator following a unit pulse is attenuated more or less fast, depending on the amount of damping. If plotting the deflection x over time t of Eq. (5.44), one gets a typical damped oscillation graph (see Fig. 5.22). In this example the amount of the natural frequency f_o is assumed as 100kHz with different attenuation factors D and an initial velocity v_o of 1.0m/s.

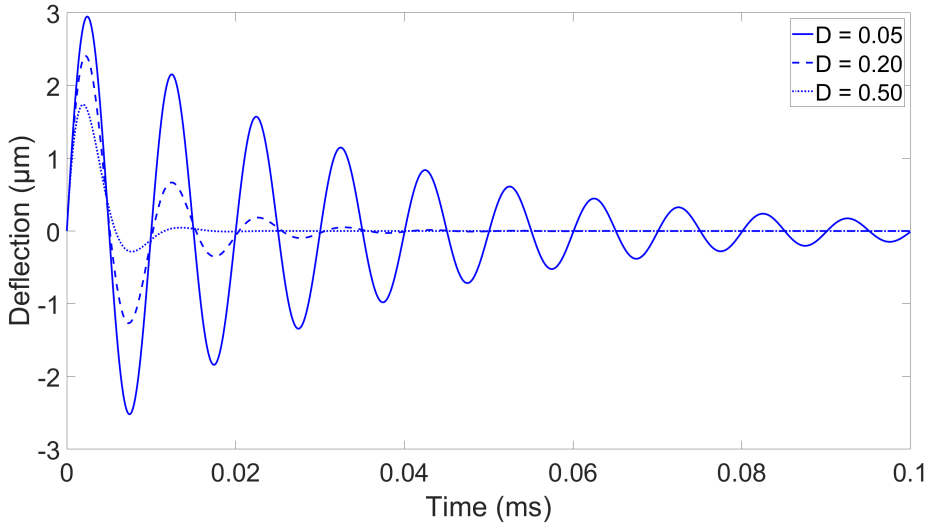

Fig. 5.22. Unit pulse response of a damped oscillator.

According to Eq. (5.44), the value of v_0 has no influence on the characteristics of the response but only on the amplitude. *Dirac* pulses are capable of exciting systems broadband, that is largely independent of the location of the Eigen frequencies of the system [60]. Thus, it is now possible to determine the pulse response (i.e. AE signal) of the oscillating indenter experimentally and by means of FEM-simulation, which will be described later in this section.

5.3.2 Characterization of a Resonating Sensor-Indenter System

Numerous experiments have shown that the sensor-indenter system gets into resonance at its natural frequencies if excited by external loads. By matching the natural frequencies of the sensor and indenter, the sensitivity of the method can be significantly improved again. For this purpose, the model of the indenter as a spring-mass oscillator was first described analytically and the resonance frequencies of the real system were determined by means of mechanical and laser *Doppler* vibrometer measurements. Afterwards, the sensor-indenter system was modeled by FEM-simulation and thus the natural frequencies of the AE sensor and indenter were tuned through design optimization of the indenter in a parametric study until the optimum was determined.

a) Natural Frequency of the Indenter

The analytical model of the indenter is similar to a rod of a length l with a constant diameter (no transversal contraction), which is fixed on a rigid plate on one end and free on the other end (see Fig. 5.23). Caused by an external harmonic stimulation on the free side, the rod gets into a longitudinal oscillation. The undamped resonance frequencies f_k of the indenter can be calculated by Eq. (5.45) [61].

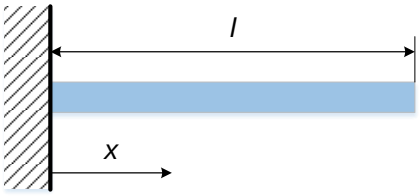

$$f_k = \frac{(2k-1)c_l}{4l} \tag{5.45}$$

Fig. 5.23. Schematic of one-sided fixed rod.

Here c_l is the longitudinal sound velocity of the material and l its free length. The parameter k (k = 1, 2 ... n) defines the order of the natural frequencies. The natural frequencies for k = 1, 2 ... 5 are calculated in Table 5.2 for a one-sided fixed steel rod (c_l = 5100m/s) with 10mm and 15mm length, respectively. Furthermore, it should be noted that Eq. (5.45) is independent of the diameter of the rod.

Table 5.2. Analytical natural frequencies f_k of a one-sided fixed steel rod (c_l = 5100m/s).

	k	1	2	3	4	5
l = 10mm	f_k (kHz)	128	382	637	893	1148
l = 15mm	f_k (kHz)	85	255	425	595	765

If a pulse excites the rod at its free end in the x-direction, it comes into a longitudinal oscillation, which gets smaller by time depending on the degree of damping (see Fig. 5.22).

In the case of a harmonic excitation of the spring with an angular frequency ω according to Eq. (5.46)

$$x_e(t) = x_0 \cos \omega t, \tag{5.46}$$

with a constant excitation amplitude x_o at the free end of the rod, the equation of motion can be written as:

$$\ddot{x} + 2D\omega_0\dot{x} + \omega_0^2 x = x_0 \cos \omega t. \tag{5.47}$$

According to [57], the solution for the spring deflection $x(t)$ is obtained from this differential equation and applies:

$$x(t) = x_0 V \cos \frac{\omega}{\omega_0} t. \tag{5.48}$$

Here ω_o is the natural angular frequency of the undamped rod and V is the so-called magnification function, which indicates the relationship between the excitation and oscillation amplitude in dependence of the excitation frequency ω. For V applies in this case [57,59]:

$$V = \frac{1}{\sqrt{\left(1 - \left(\frac{\omega}{\omega_0}\right)^2\right)^2 + \left(2D\frac{\omega}{\omega_0}\right)^2}}. \tag{5.49}$$

Damping is assumed to increase for higher frequencies due to friction effects, for instance. Substituting in Eq. (5.49) the calculated natural frequencies of a length l = 10mm from Table 5.2 and the estimated damping factors D_1 until D_4, V can be calculated. Subsequently, the magnification function can be graphically shown as a function of the excitation frequency f for longitudinal rod oscillation orders 1 - 4 in linear (see Fig. 5.24) and logarithmic scale (see Fig. 5.25).

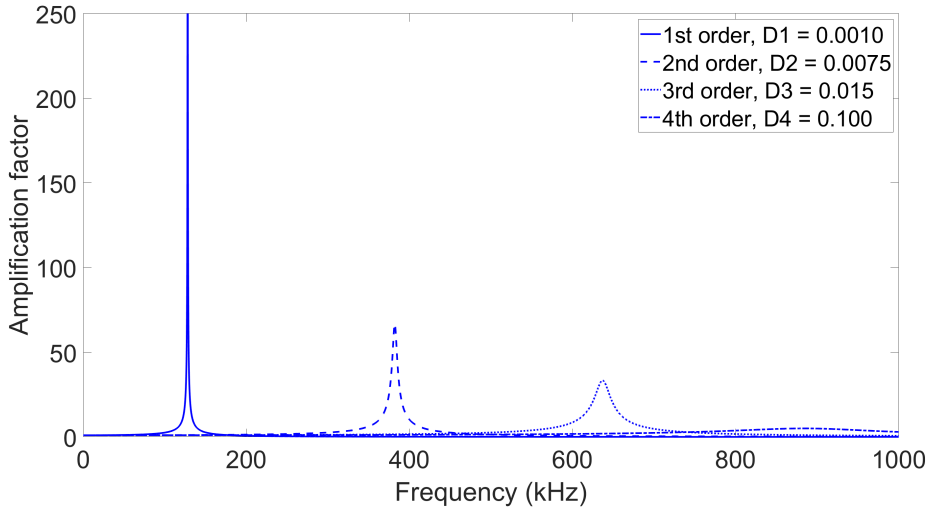

Fig. 5.24. Frequency response curves in linear scale for orders 1 - 4 with different damping coefficients.

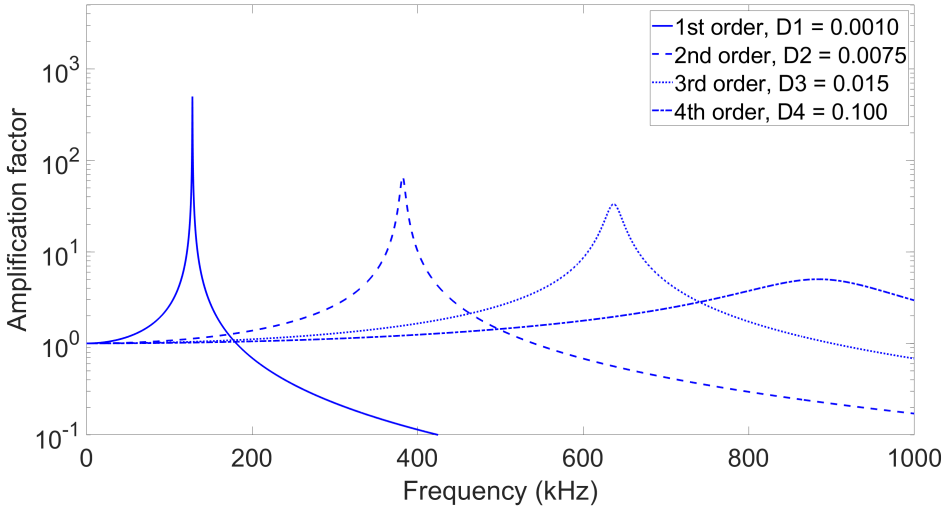

Fig. 5.25. Frequency response curves in logarithmic scale for orders 1 - 4 with different damping coefficients.

As can be seen from the shape of the curves the amplification factor drops at higher frequencies with increased attenuation, thereby widening the bandwidth of the frequency response. This behavior was also observed in the measurements, as shown in the following sections.

b) Measurements

To determine the natural frequencies of the sensor and indenter experimentally, acoustic measurements were carried out and validated with optical (laser *Doppler* vibrometer) measurements. Here, the AE sensor *Vallen VS900-M* with a relatively flat frequency response was used within a bandwidth of approx. 100kHz to 900kHz (see Fig. 5.5). Important criteria in the selection of the AE sensor in addition to a high sensitivity over a wide frequency band were a low noise limit, a short response time, the robustness, and not least the price of the sensor. The indenter consists of a steel pin with a 60° cone at the free end. It has a flat diamond tip of 10µm in diameter on top. Regarding the geometry of the steel indenter three variants were considered, which differ either in their rod length l_{rod} of 10mm and 15mm with a rod diameter d_{rod} of 2.5mm or 1mm (see Table 5.3).

Table 5.3. Indenter geometries.

Indenter ID	**Rod length (mm)**	**Rod diameter (mm)**
Indenter 1	10	2.5
Indenter 2	15	2.5
Indenter 3	10	1.0

The aim of the measurements was to determine the frequency response for harmonic excitation of the sensor-indenter systems at a specially designed measuring station (see Fig. 5.26 and Fig. 5.27). For the experiments, the 2-component indenter type was used (see Fig. 5.16). An *Olympus V103* ultrasonic emitter, driven by voltage waveforms from the *Keysight 33509B* waveform generator, generates harmonic distortion signals. The ultrasound emitter is pressed onto the center of the sensor surface with a contact load of approx. 500mN using a specially designed manual positioning stage. The harmonic excitation generated by the emitter is transmitted to the sensor-indenter system and further to the preamplifier *Vallen AEP3N*. To power up the preamplifier, it is connected to a *Toellner 8732* power supply with a 28V DC supply voltage, which is decoupled by a decoupling box *Vallen DCPL2*. The analog sensor signal, which is amplified by a gain of 49dB and filtered to frequencies below 2MHz in the preamplifier, is fed into an *Agilent Infiniium 54825A* digital oscilloscope. The digital signal is fed into a PC for post-processing.

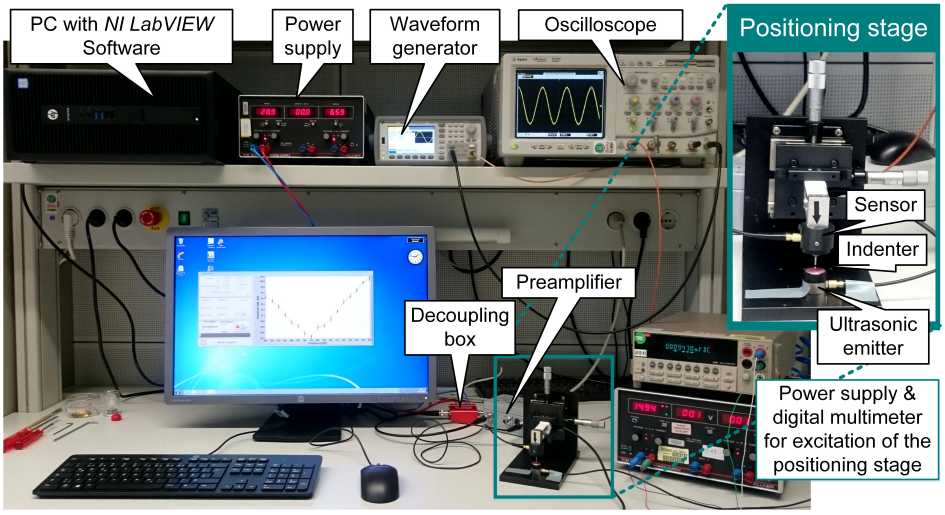

Fig. 5.26. Test bench for characterization of various sensor-indenter systems.

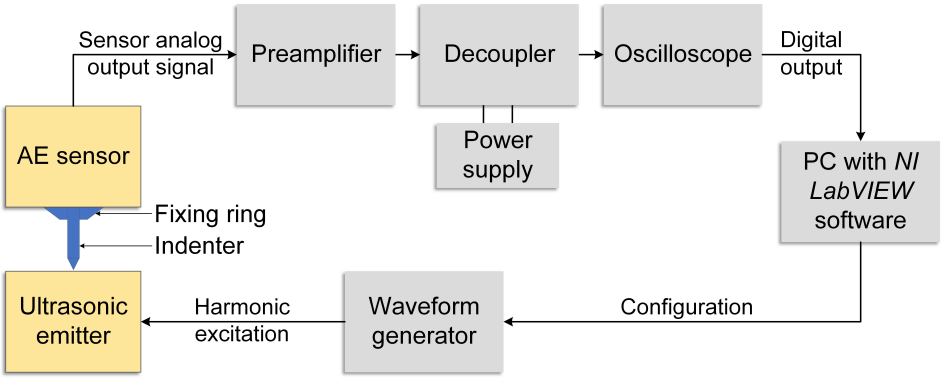

Fig. 5.27. Measurement principle for characterization of various sensor-indenter systems.

The measurements were controlled by the PC using *NI LabVIEW* software, which also configures the waveform generator to generate 1V amplitude harmonic signals over the 50kHz to 1MHz frequency range with 1kHz measurements. The amplified and filtered sensor output signal is further transmitted from the oscilloscope to the computer, where it is recorded and analyzed. At each frequency step of 1kHz the amplitude was measured 10 times and from these values the mean and the standard deviation were calculated. The determined standard deviations are of the order of a few 0.01dB and hence the scattering is negligible. The electrical voltage signals are displayed in dB_{AE}. The amplification factor of 49dB was subtracted from

all measured values and thus only the unamplified output voltage from the sensor was considered. Also the frequency response curve of the ultrasonic emitter was subtracted from the measured signals.

In a first step, the frequency response curve of the single AE sensor without indenter was evaluated. Therefore, the AE sensor under test was coupled face-to-face with the ultrasonic emitter using a vertical contact load of 10N. Machine oil was used to improve the coupling. The measured sensor signals were high enough, so that no pre-amplification of the signal was necessary.

In a next step, the indenter and fixing ring were glued on top of the surface of the AE sensor. The sensor-indenter system was stimulated with a harmonic oscillation of the emitter, which was now loaded by a vertical contact force of approx. 500mN on the indenter tip, with the same frequency range as described before.

Fig. 5.28 shows the measured frequency response curves of the maximum amplitude in units of dB_{AE} of the sensor without indenter (green dashed line) and the sensor-indenter system with Indenter 3 (blue solid line) as a function of the excitation frequency.

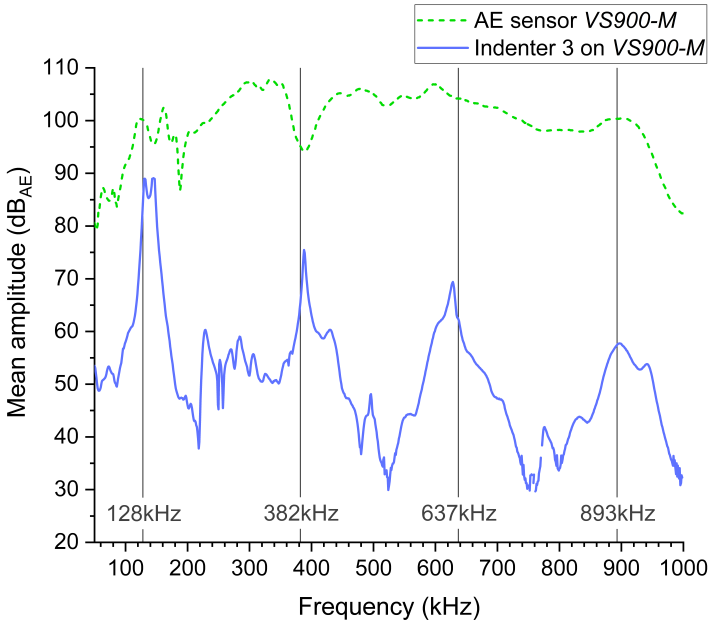

Fig. 5.28. Measured frequency response curves and analytical natural frequencies (vertical lines).

The excitation signal of the complete sensor-indenter system is lower than the output signals of the *VS900-M* with direct coupling of the sensor and the ultrasonic emitter over the full frequency range. This is primarily due to the different contact load of 10N compared to 500mN as well as the smaller contact area of the small diameter of the indenter tip (10µm) compared to the sensor surface of about 20mm diameter. Moreover, compared to the frequency response of the sensor without indenter, which has a relatively flat frequency response curve, the sensor-indenter system shows several peaks close to the analytically calculated natural frequencies of the rod (see Table 5.2). This proofs that the sensor-indenter system oscillates at its resonance frequencies in longitudinal mode caused by a harmonic excitation. In addition, the sensor-indenter system reaches maximum excitation amplitudes at the coupled resonance frequencies.

Fig. 5.29 exhibits the measurement of the frequency-dependent sensitivity for three variants of the sensor-indenter system (see Table 5.3) if using the *VS900-M* sensor.

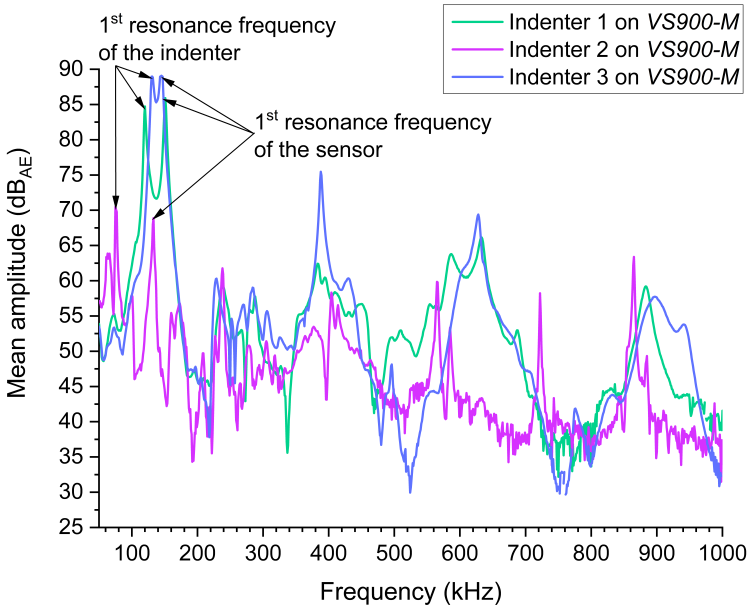

Fig. 5.29. Frequency dependent sensitivity for various sensor-indenter systems.

Here, too, the frequency-dependent sensitivity with pronounced frequency peaks of the sensor-indenter systems becomes clear. The peaks at 120kHz of 85dB$_{AE}$ for variant 1, at 76kHz of 71dB$_{AE}$ for variant 2, and at 131kHz of

89dB$_{AE}$ for variant 3 are in good agreement with the first order resonance frequency of the associated indenter. In addition, further maxima arise at the resonant frequencies of the sensor (see marking in Fig. 5.29 and Table 5.4).

Table 5.4. Acoustically determined natural frequencies and amplitudes for indenter and sensor.

Indenter ID	**Indenter resonance**		**Sensor resonance**	
	Frequency (kHz)	Amplitude (dB$_{AE}$)	Frequency (kHz)	Amplitude (dB$_{AE}$)
Indenter 1	120	85	150	86
Indenter 2	76	71	133	63
Indenter 3	131	89	145	89

However, the sensor resonance is presumably altered by the additional mass and rigidity of the fixing ring and indenter on the ceramic surface of the sensor. The resonance peaks with lower amplitude at higher excitation frequencies can be well assigned to the natural frequencies of higher orders of the indenter (see also Fig. 5.25).

Clearly pronounced amplitude maxima in the resonance values were also observed during contactless measurements with a laser *Doppler* vibrometer *Polytec MSA-500*. The *VS900-M* sensor, which can also act as an actuator, was stimulated by the waveform generator with a harmonic voltage signal over a frequency range of 50kHz to 500kHz. By means of the *Doppler* shift of a laser beam, which was first focused on the fixing ring and then on the indenter tip, the frequency-dependent oscillation amplitude of the surface deflection was measured. The optical measuring principle made it possible to observe the oscillating sensor-indenter system isolated from the influence of the ultrasonic emitter and the mechanical coupling to the indenter. *Polytec's* software was used to configure the waveform generator and to analyze the data. The schematic measurement setup is illustrated in Fig. 5.30.

In a first step, the mechanical vibration spectrum, which is shown in Fig. 5.31 for the *VS900-M* sensor coupled with Indenter 2 (see Table 5.3), was measured with the laser as described above.

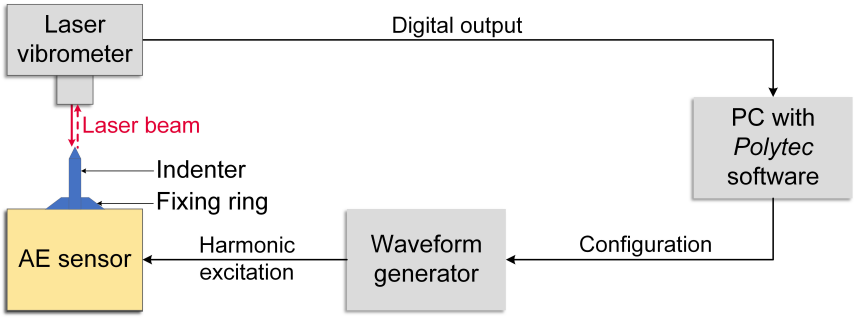

Fig. 5.30. Schematic structure of the laser *Doppler* vibrometer measurement.

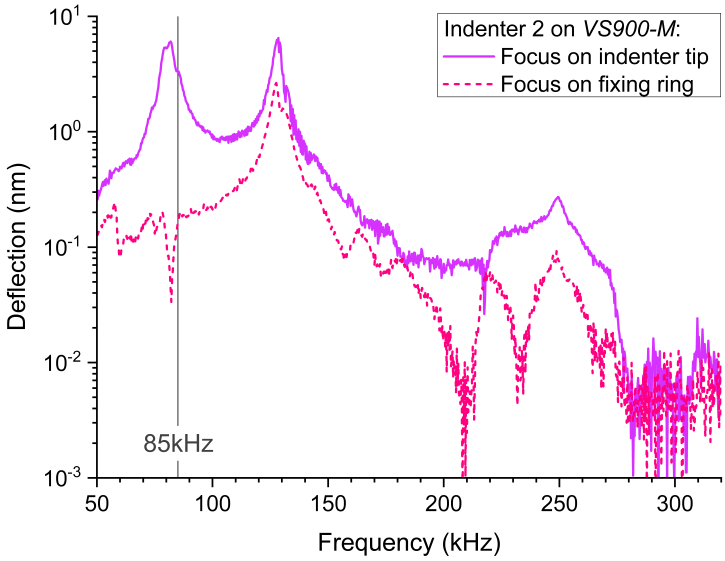

Fig. 5.31. Frequency response curve measured with laser *Doppler* vibrometer for variant 2.

The vertical deflection of the tip and the fixing ring in nanometers is plotted in logarithmic scale against the frequency in kilohertz. The measured deflection of the fixing ring shows a resonance at about 128kHz with a maximum amplitude of about 2.7nm, which is related to the sensor resonance. The deflection measured at the indenter tip also shows a maximum at this frequency, whereby the value here is about 6.7nm. In addition, the measured spectrum has a further maximum at a frequency of about 82kHz with a displacement of about 6.2nm. This value is in good agreement with the analytically determined first-order resonant frequency of the indenter of 85kHz (see Table 5.2). For excitation frequencies above approx. 250kHz,

the measurement on the laser *Doppler* vibrometer only yields statistical noise, since the deflections are below the frequency-dependent resolution of the instrument of about 0.1pm/√Hz.

In the next step, the frequency spectra for the three variants of sensor-indenter systems (see Table 5.3) were determined using the same measuring principle. Fig. 5.32 illustrates the measured frequency responses with the laser each focused on the indenter tip.

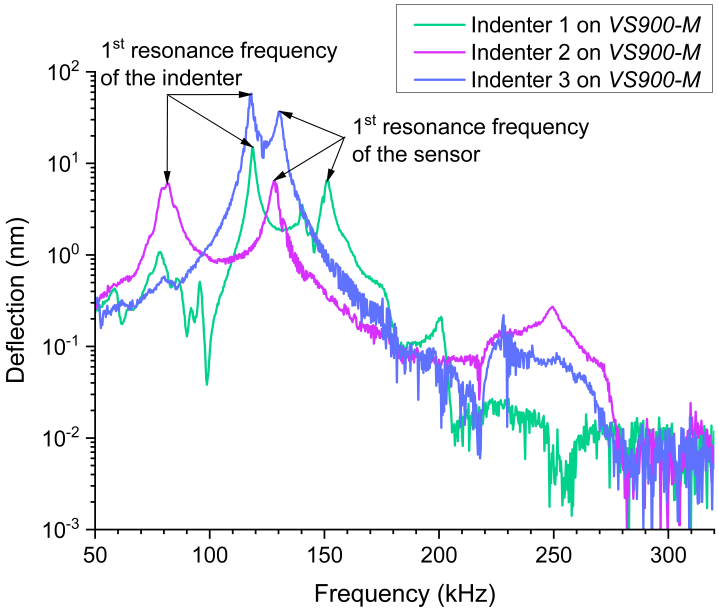

Fig. 5.32. Frequency response curve measured with laser *Doppler* vibrometer for variants 1 - 3.

The measured curves have two maxima for each sensor-indenter system, which correspond well to the natural frequencies of the indenter and sensor. In the measurements shown, the resonant frequencies of the sensor vary between 128kHz and 151kHz with maximum deflections between 6.3nm and 37nm (see also Table 5.5). The change in the sensor resonance can be explained, as already mentioned, by the additional mass on the ceramic of the sensor as well as by gluing the indenter and fixing ring. For measurement with variant 1, the resonance frequency of the indenter is at 119kHz (amplitude: approx. 15nm), for measurement with variant 2 at 82kHz (amplitude: approx. 6.3nm), and for measurements with variant 3 at 118kHz (amplitude: about 60nm). Table 5.5 summarizes the optically measured values of the *VS900-M* sensor for the three indenter variants.

Table 5.5. Optically determined natural frequencies and amplitudes for indenter and sensor.

Indenter ID	Indenter resonance		Sensor resonance	
	Frequency (kHz)	Deflection (nm)	Frequency (kHz)	Deflection (nm)
Indenter 1	119	15	151	6.9
Indenter 2	82	6.3	128	6.3
Indenter 3	118	60	130	37

As a conclusion, the values of the first resonance frequencies and corresponding amplitudes for the acoustic and optical measurements agree well despite different excitation and vibration conditions (see Table 5.6). In comparison of the evaluated sensor-indenter system variants, the excitation of variant 3 achieves the highest amplitudes with the smallest difference between the sensor and indenter resonance frequencies.

Table 5.6. Comparison of analytical, acoustic, and optical frequency analysis of various sensor-indenter systems.

1st resonance frequency (kHz)	Sensor with Indenter 1		Sensor with Indenter 2		Sensor with Indenter 3	
	Sensor	Indenter 1	Sensor	Indenter 2	Sensor	Indenter 3
Analytical	---	128	---	85	---	128
Acoustic	151	120	133	76	144	131
Optical	151	119	128	82	130	118

5.3.3 Indenter Optimization by Finite Element Simulations

Based on the analytical model of the resonating indenter and the frequency response measurements of the sensor-indenter system, the dimensions of the indenter design could be further optimized by FEM-simulations (see [62])[7]. The target of the simulations was to precisely match the 1st order resonant frequency of the indenter with the frequency of the first amplitude peak of the sensor. This method is called frequency tuning. By doing so, the maximum amplitude of the output signal could be significantly increased during a pulsed excitation of the sensor-indenter system. In the following, the result of the FEM design study of the indenter is described.

[7] The master thesis in [62] was conducted and supervised within the scope of this doctoral thesis.

Starting from the design of Fig. 5.16, a 2D rotational model of the 2-component indenter with the FEM program *COMSOL Multiphysics version 5.3a* was defined. The model consists of a metallic cylinder with a conical tip (= indenter), which is plugged vertically into a metallic fixing ring and mounted on the surface of the AE sensor (see Fig. 5.33). The sensor *VS900-M* is modeled as a round ceramic plate, which is clamped on the circumference, and a piezo ring mounted underneath. The material parameters, e.g. the modulus of elasticity and density of the various components, were assigned to the model (see [62]). Afterwards, a modal analysis of the FEM-model of the 2-component sensor-indenter system was carried out to determine the Eigen modes and resonance frequencies with a harmonic excitation. In the contour plot in Fig. 5.33, at an excitation frequency of 120kHz, one can see the 1st order resonance of the indenter with an oscillation in lateral direction. The sensor and fixing ring, however, are not in resonance at this frequency.

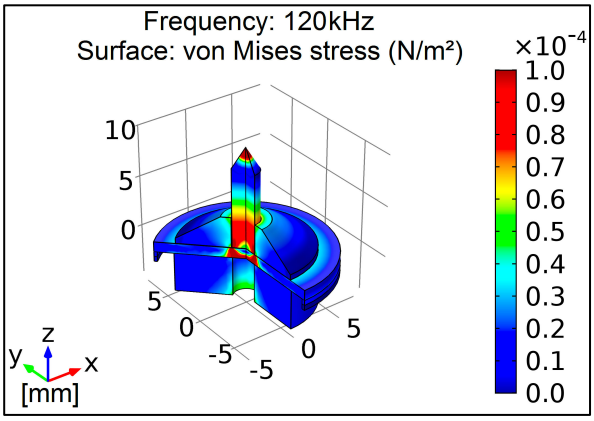

Fig. 5.33. Contour plot of resonating 2-component sensor-indenter system.

The corresponding frequency response curve for an indenter of 10mm length and 2.5mm diameter (Indenter 1), that is fixed on the *VS900-M* sensor, is shown in Fig. 5.34. Also in this graph the amplitude peak of the resonating indenter at a frequency of approx. 120kHz is visible, but the amplitude peak of the resonant sensor is slightly higher at approx. 160kHz.

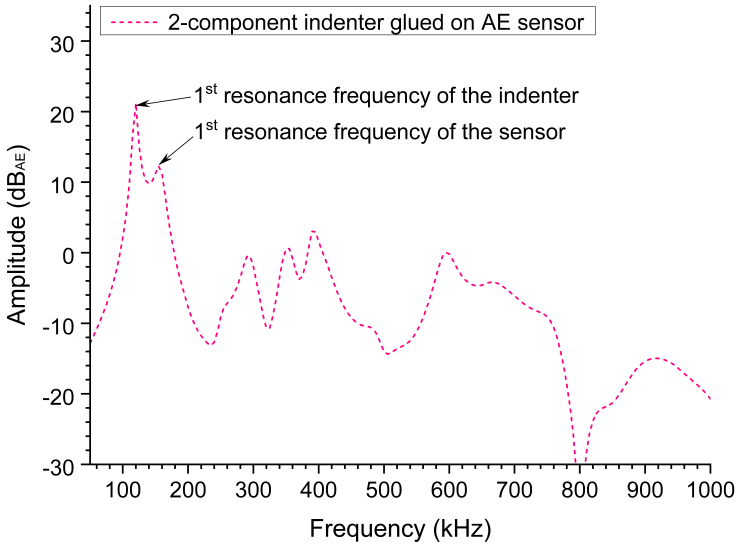

Fig. 5.34. Simulated frequency response curve of 2-component sensor-indenter system.

Using the parametrized FEM-model of the sensor-indenter system, it was possible within the simulations to tune the natural frequency of the indenter with the one of the AE sensor. By appropriate size and design changes of the indenter, the resonance frequency changes accordingly. As described in Sect. 5.2.3, the 2-component indenter has some disadvantages, like friction between the indenter rod and fixing ring or the small contact area at the base of the rod. To overcome these problems, a new indenter design was developed, the so-called monolithic indenter solution. The monolithic indenter design eliminates friction and enlarges the contact area between the indenter base and the sensor surface. Due to these design changes, disturbances are minimized and a better coupling increases the system sensitivity. Therefore, only the monolithic indenter is considered for the further FEM-simulations.

Fig. 5.35 shows a 2D drawing of the monolithic indenter made of steel, which has a cylindrical base with a diameter d_{base} and a height h_{base}. The base of the indenter reduces conically over the length h_{cone} along the indenter rod of the length l_{rod} to the diameter d_{rod}. At the free end of the indenter, the rod tapers over a 60° cone to a tip diameter of 10µm. The optimal dimensions of l_{rod}, d_{rod}, d_{base}, h_{base}, and h_{cone} were determined in a FEM parameter study aiming to get maximum amplitude at the first resonance frequency of the indenter and sensor. The initial values of the

dimensions are listed in Table 5.7 and were based on the previous 2-component system for indenter variant 1 (see Table 5.3).

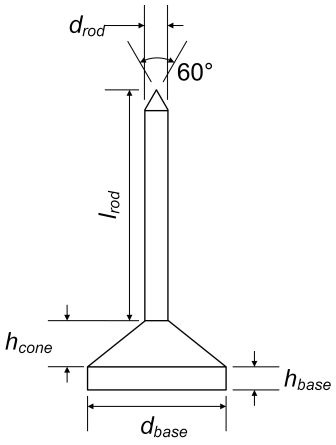

Fig. 5.35. Drawing of monolithic indenter.

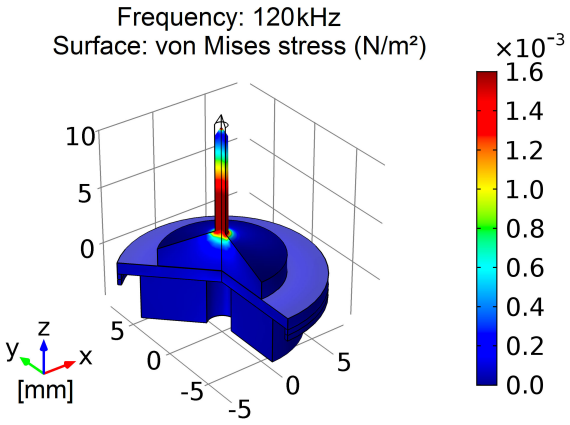

Fig. 5.36. Stress contour plot of monolithic indenter on AE sensor.

In the first step, the optimum length l_{rod} and diameter d_{rod} of the indenter rod were defined by simulation, which have the highest influence on the natural frequency of the indenter and thus decisively determine the measuring sensitivity.

The dimensions of the possible lengths of the indenter rod are between a production-related minimum length of 4mm and a maximum length of 14mm due to the maximum possible height of the sensor-indenter system in the experimental setup. For this purpose, the frequency-dependent output signal was modeled and simulated together with the *VS900-M* sensor for the indenter rod lengths 4mm, 6mm, 8mm, 10mm, 12mm, and 14mm. In Fig. 5.36 one can see a stress contour plot for one variant performed in a modal analysis. Here, the longitudinal oscillation of the rod is clearly visible.

Subsequently, the maximum amplitude of each simulated variant was evaluated and plotted as a function of the indenter rod length. As can be seen in Fig. 5.37, the maximum amplitude increases with the indenter rod length to saturation. When using the *VS900-M* sensor and an indenter rod diameter of 2.5mm, the optimum length of the indenter rod is approx. 14mm (see Fig. 5.37). The simulated output here is 66.2dB$_{AE}$ and hence 6.0dB$_{AE}$ higher than the simulated output of the 4mm system (60.2dB$_{AE}$).

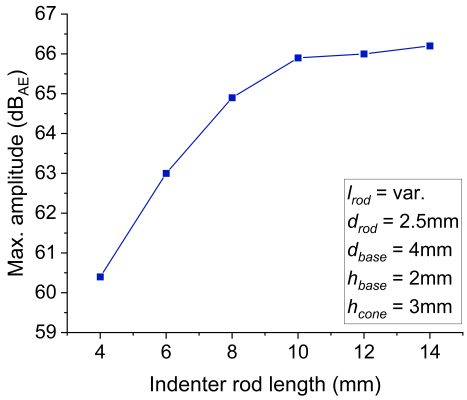

Fig. 5.37. Simulated maximum amplitude with variation of the indenter rod length.

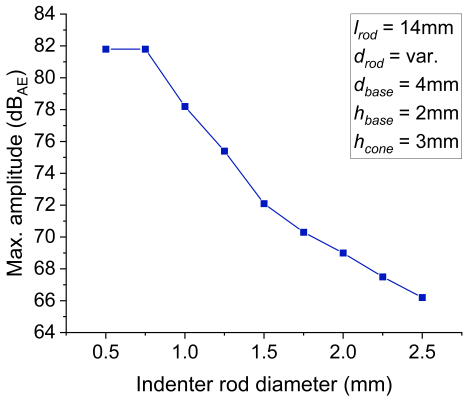

Fig. 5.38. Simulated maximum amplitude with variation of the indenter rod diameter.

For a length of the indenter rod of 14mm and an initial value of the base diameter of 4mm, a parameter study for the rod diameter of the indenter was then carried out. A lower limit based on manufacturing is at 0.5mm and an upper limit of 2.5mm was used in steps of 0.25mm. As before, the maximum amplitude of each simulated variant was evaluated and here plotted as a function of the indenter rod diameter. Fig. 5.38 shows, that the maximum amplitude decreases with the indenter rod diameter and becomes a maximum for diameters of 0.5mm and 0.75mm. For both values, the maximum amplitude is 81.8dB$_{AE}$, which is 15.6dB$_{AE}$ higher than when using the initial value of 2.5mm.

Based on the simulation results, the sensor-indenter system achieves the maximum excitation amplitude with an indenter rod length of 14mm and a rod diameter of approx. 0.50mm - 0.75mm. For an easier manufacturing process and safer handling during the crack experiments, a slightly shorter rod length and larger rod diameter of the indenter are an advantage due to the higher mechanical stability. Therefore, a compromise has been made between the simulated optima and the mechanical stability requirements of the system. The final design is an indenter with a rod length of 10mm and a rod diameter of 1mm. The 3.8dB$_{AE}$ reduction in amplitude over the optimal geometry (rod length 10mm instead of 14mm and rod diameter 1.0mm instead of 0.75mm) is negligible and hence acceptable for the target design of the indenter.

In the next step, FEM parameter studies were performed with a variation of the base diameter, base height, and cone height using the above mentioned indenter geometry values. The influence on the amplitude is

not significant and sometimes even contra dictionary. Hence, a detailed description is omitted in this work. Table 5.7 summarizes the initial and final dimensions of the monolithic indenter design.

Table 5.7. Initial and final dimensions of the monolithic indenter design.

	l_{rod} (mm)	d_{rod} (mm)	d_{base} (mm)	h_{base} (mm)	h_{cone} (mm)
Initial	10	2.5	4.0	2.0	3.0
Final	10	1.0	10.0	1.5	3.0

The final prototype of the monolithic indenter, which was manufactured by the Swiss supplier *Synton MDP*, is outlined in Fig. 5.39. This indenter design was used successfully in the AE crack experiments of this thesis, which are described in Chap. 6 and 7. Fig. 5.40 shows an image of the realized monolithic indenter glued on the AE sensor.

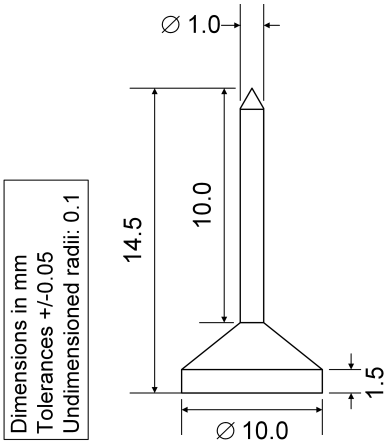

Fig. 5.39. Detailed drawing of the optimized monolithic indenter.

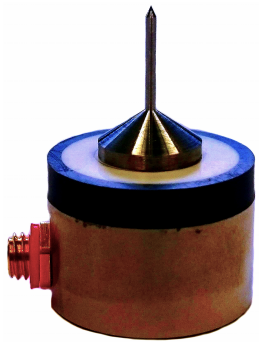

Fig. 5.40. Manufactured monolithic indenter on sensor *VS900-M*.

To highlight the advantage of the monolithic indenter compared to the previous 2-component system, a FEM modal analysis of the optimized sensor-indenter system was performed. Fig. 5.41 shows the simulated frequency response curves in dB_{AE} over the excitation frequency. Within a frequency range of 100kHz - 500kHz the amplitude is mostly approx. 10dB_{AE} higher when using the monolithic indenter. The peaks of the first resonance frequencies of the sensor and the monolithic indenter fit very well.

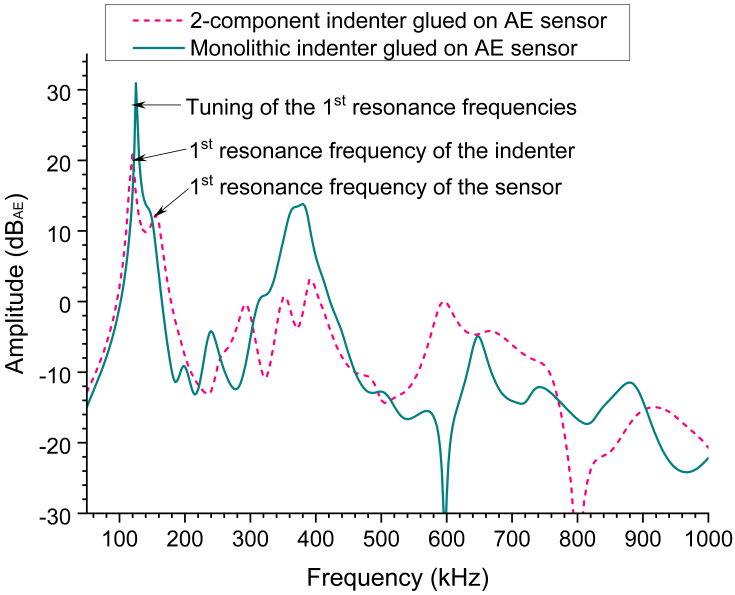

Fig. 5.41. Simulated frequency response curves for 2-component and monolithic indenter.

At the end of this section, the frequency response curves of the modelled and measured system are compared based on the target design of the monolithic indenter. The graphs for the analytically calculated (blue), FEM-simulated (green), and experimentally measured (pink) results are shown in Fig. 5.42. As one can clearly see, the peaks of the resonant frequencies for the first and higher orders are in good conformity for all three curves.

The frequency response curve obtained by computer simulation was taken from Fig. 5.41. The acoustic measurement from the harmonic emitter excitation was determined with the aid of the available test bench (see Fig. 5.26) over a frequency range of 50kHz - 1000kHz for the target design of the indenter and the sensor *VS900-M*. In the analytical calculation of the magnification function V of the longitudinally oscillating rod (see Eq. (5.49)) an increasing damping factor D was assumed at the Eigen modes of the k-th order (k = 1, 2, 3, 4). The value increases from D_1 = 0.0010 for the 1st order vibration mode to D_4 = 0.10 for the 4th order. If assuming an increasing attenuation for higher order modes of the oscillating indenter, the amplitudes and resonance peaks also correlate well.

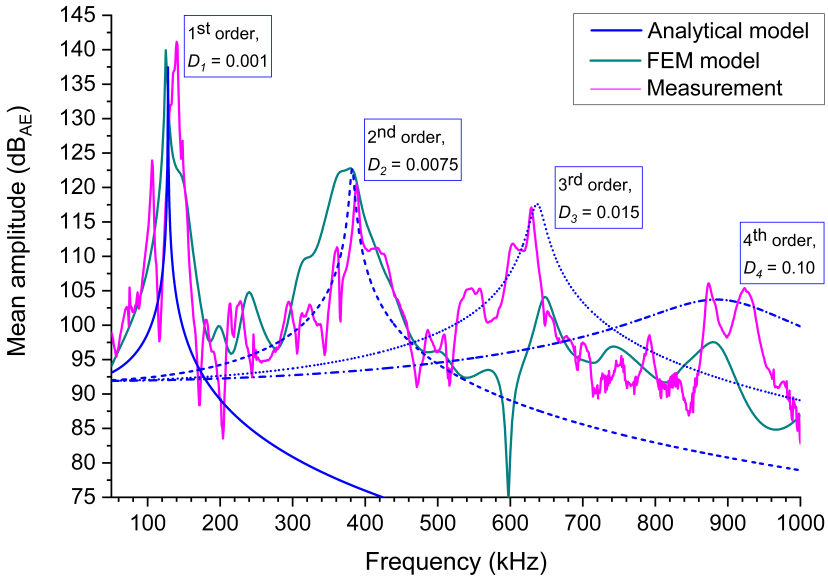

Fig. 5.42. Calculated and measured frequency response curves of the indenter target design.

The good correlation of the calculated, simulated, and measured frequency response curves proof the capability of the concept and mechanism of AE testing on thin layers with a resonating sensor-indenter system. In the next chapter, the AE test method is applied using the target design of the indenter on various test specimens and the accuracy of the test setup is analyzed experimentally.

6 Experimental Proof of Concept on Thin Layer Test Structures

After modifying the measurement principle and eliminating the disturbances, experiments were carried out on suitable test structures to evaluate the suitability, repeatability, and accuracy of the AE test method for the detection of oxide cracks on semiconductor structures using the modified test bench *PROFIT* as described in Chap. 5. Once the test samples were defined and processed and the equipment was available and set up, the structures were stressed up to the maximum permissible contact force until crack generation, acoustic signals were acquired, and the data were recorded. After setting a suitable threshold to filter the hits for the respective "first acoustic crack" event per contact cycle, the measuring capability of the AE test method for crack detection was examined in repeat and reproducibility tests. In addition, the higher sensitivity of the monolithic compared to the 2-component indenter was confirmed in successive contact cycles. Subsequently, the crack probability of the oxide layer for a selected test structure, which was contacted by the indenter directly on the SiO_x layer, was determined experimentally and tested on the predicted *Weibull* distribution that, according to the theory, is characteristic for the fracture behavior of brittle layers (see Chap. 4.4). Finally, the suitability of the AE test method was confirmed also for contacting on a ductile pad metallization, instead on a brittle SiO_x layer, analogue to the practical case at operational wafer test. By following optical crack inspections of various test samples, the results of acoustic measurements, which were performed at room temperature, could be verified.

6.1 Measurement Setup

In this chapter first an overview of the design of processed test samples, which were used in the experiments, is given. Further, the geometry of the indenter tip as well as the settings of the AE measuring system are described. The combination of both the layer stack and tip together with the contact and measurement parameters are relevant for the observed crack probability.

6.1.1 Test Samples

For the crack detection in brittle semiconductor layers by means of the AE test method, it was first necessary to provide crack-sensitive test structures.

Those design and materials should be comparable to typical layer stacks of CMOS processed semiconductor chips (see Sect. 2.3.1). A metal pad (e.g. Al, Cu, Au, etc.) is processed as the top layer, where the needle probe is contacting with a certain contact force during the wafer test. Below the pad layer, various deposition and diffusion layers made out of Ti or tantalum (Ta) alloys are deposited. The next underlying layer is made of SiO_x, which is isolating the conductive metal layers in different levels of the stack. The oxide is most relevant for cracks during the AE measurement. Below that there is a thin diffusion barrier made of Si_3N_4 followed by a Cu metal layer underneath. Cu layers serve as routing connections in the circuitry of CMOS chips and can be plastically deformed under a high mechanical load. Further oxide or Si-layers in deeper levels are not crack-sensitive and therefore not considered at the AE measurement in this work. Fig. 6.1 shows the schematic layer structure of the test samples and the respective dimensions of the layer thicknesses in Table 6.1[8]. The name of the test samples is defined by the abbreviation W (***W***afer) and a sequential number.

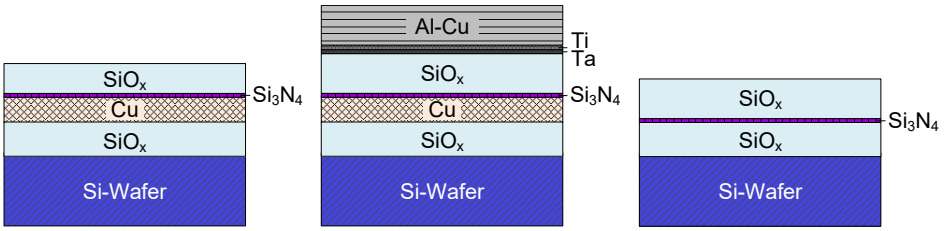

Fig. 6.1. Schematic layer stack of test samples: W01 - W04 (l.), W05 (center), and W06 (r.).

In this work, the influence of the thickness of the SiO_x and underlying Cu layer on the formation of oxide cracks was investigated. Therefore, the layer thicknesses of the test structures W01 - W04 are different in the upper SiO_x (380nm or 1000nm) and Cu layer (700nm or 400nm) (see Table 6.1). Moreover, all variants except W05 were processed up to the second SiO_x layer only (see Fig. 6.1). In order to proof the AE test method with regard to crack detection while contacting the pad metallization, test structure W05 with an Al-Cu layer on top and a Ti/Ta layer beneath was additionally processed (see Fig. 6.1, center). The thickness of the SiO_x and Al-Cu layer was defined to be relatively high (3000nm), in order to achieve a better separation of the AE signals for oxide cracks and pad deformation. Test structure W06 (see Fig. 6.1, right), without a Cu layer between the upper and lower SiO_x layer, was used as reference to the test structures W01 - W04. By comparing

[8] The split plan of the test samples is attached in the Appendix.

the test structures with and without a Cu layer, it can be proven, that the plastic deformation of the Cu layer under the oxide layer is acoustically detectable, too.

Table 6.1. Layer stack and thicknesses of unstructured test samples.

Test structure	**W01**	**W02**	**W03**	**W04**	**W05**	**W06**
	Layer thickness (nm)					
Al-Cu	-	-	-	-	3000	-
Ti	-	-	-	-	40	-
Ta	-	-	-	-	50	-
SiO_x	380	1000	380	1000	3000	3000
Si_3N_4	50	50	50	50	50	50
Cu	700	700	400	400	700	-
SiO_x	ca. 1900					
Si-Wafer	ca. $500 \cdot 10^3$					

To reduce the complexity of the test structures during the experiments, only wafers without structured Cu-routing were used. The samples were processed on 200mm wafers using standard FE-processes by the *Infineon Technologies AG* in Dresden. To simplify the test sample gluing process, the wafers were diced into separate chips of 20mm x 20mm in size.

6.1.2 Indenter Geometry and Assembly

Various indenters with cylindrical flat-ended 10µm diameter diamond tips (see Fig. 6.2), which is a typical size for wafer test on CMOS chips (see Sect. 2.2.2), were applied for the experiments. Except during correlation experiments of 2-component and monolithic indenter designs, which are described in Sect. 6.2.3, always the monolithic indenter design was used. The name of the indenters is defined by the abbreviations FP (***F***lat ***P***unch), C for a 2-***C***omponent or M for a ***M***onolithic indenter, and the value of the tip diameter in microns. During this work one 2-component (FP10-C-1) and three identical monolithic (FP10-M-1 ... 3) indenters were used.

Initially, the contact area of each indenter tip was measured using the *Keyence VHX-6000* microscope. Fig. 6.3 shows the tip area measurement procedure and Table 6.2 summarizes the values of the measured tip area A_{tip} for all indenters. This microscope was frequently utilized to check the indenter tip for damage and contamination, too.

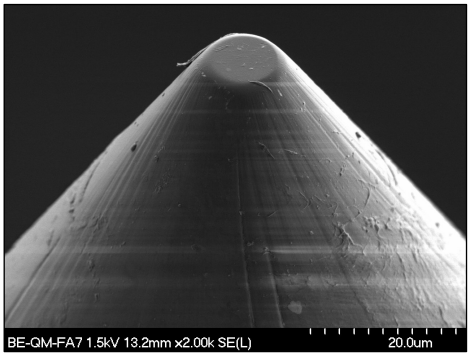

Fig. 6.2. SEM image of a cylindrical flat-ended 10µm diameter diamond tip (FP10-C-1).

Table 6.2. Indenter tip area measured via *Keyence VHX-6000* microscope.

Indenter ID	Tip area (µm²)
FP10-C-1	81.78
FP10-M-1	82.12
FP10-M-2	95.21
FP10-M-3	90.48
FP20-M-1[9]	361.92

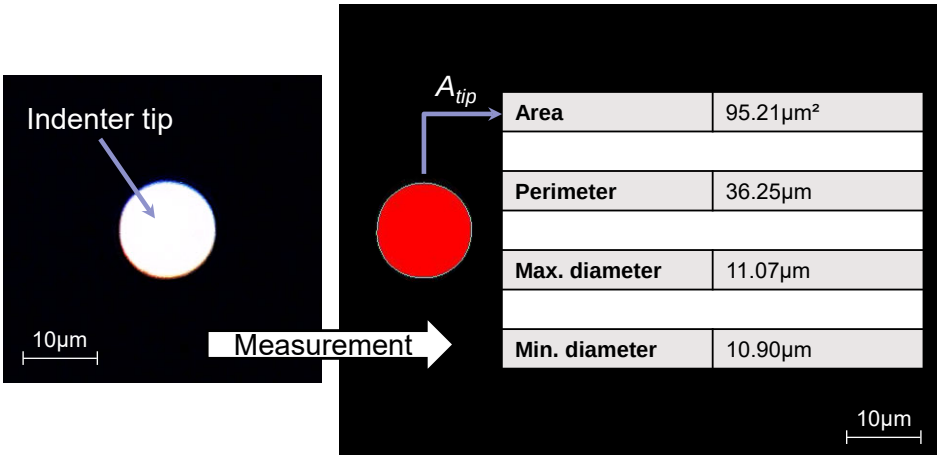

Fig. 6.3. Measuring the tip area of indenter FP10-M-2 using the *Keyence VHX-6000* digital microscope.

Each indenter was fixed with its base on the top side of a *Vallen VS900-M* AE sensor according to the process described in Sect. 5.2.3. According to the "Guide on Acoustic Emission Sensors Couplants" [53], on a flat, smooth surface an adhesive such as cyanoacrylate provides the best transmission of both longitudinal and shear displacement. The WEICON *VA 1401* contact cyanoacrylate adhesive also meets the requirements for the force measurement (i.e. high elastic modulus and low brittleness) and thus was chosen

[9] In Sect. 7.2.1 another monolithic indenter with a tip diameter of 20µm (FP20-M-1) was used for the experiments, which is listed in the table for the sake of completeness.

as couplant. This product is an adhesive with a medium viscosity (100-150mPa·s), which can be applied evenly with very thin layer thickness (< 0.15µm) with a short curing process time.

Before the indenter was glued onto the AE sensor both surfaces were cleaned using acetone, in order to remove all particles from the surfaces and so to establish optimal coupling conditions. As mentioned in Sect. 5.2.3, the sensitivity of the *Vallen VS900-M* AE sensor is highest in its center. Therefore, the widened end of the indenter was aligned centered on the sensitive surface of the AE sensor and the correct position was marked using a fine-liner pen. Afterwards, a very small amount of adhesive was evenly applied on the indenter base. Right away after, the indenter was carefully pressed onto the marked position on the surface of the AE sensor, so that the adhesive could spread evenly below the components to achieve a thin, planar filling without air bubbles.

After min. 8h of exposure time in acetone as solvent, the indenter can be removed from the AE sensor by carefully applying a small shear force. However, to avoid any accidental damage of the sensor or the indenter, the coupled components should only be separated if necessary.

6.1.3 Instrument Settings

a) Positioning Stage Settings

The vertical contact force is measured by a strain gauge force sensor, which is a component of the test bench *PROFIT* (see Sect. 5.2.2). As the *PROFIT* tool is controlled by a *LabVIEW* program, the force measurement series are executed automatically using self-written control macros (see example in Appendix). The graphical output of the force data is displayed in real time and stored for further processing on a PC.

Due to the modified arrangement of the rigid indenter on the AE sensor below the flipped metal plate with the test chip (see Sect. 5.2.2), the stiffness of the measuring setup is very high in contrast to conventional *cantilever* probe cards (see Sect. 2.2.2). This configuration is causing a strong increase of the contact force, depending on the vertical travel distance (= "overdrive") of the positioning table, of about 100mN per 1µm. Hence, the contact force was no longer controlled by the "overdrive", which is typical for wafer probing, but directly by a feedback loop in the program. For each indentation only one contact cycle, i.e. one ***T***ouch***d***own TD, per pad position was performed.

Fig. 6.4 shows an example of a typical contact cycle with a vertical contact force over time. Here test structure W01, which has an oxide layer thickness of 380nm (see Table 6.1), was contacted with a monolithic indenter. The force is increased linear up to a maximum amount of 200mN and subsequently, after a short waiting time, linearly relieved down to 0mN.

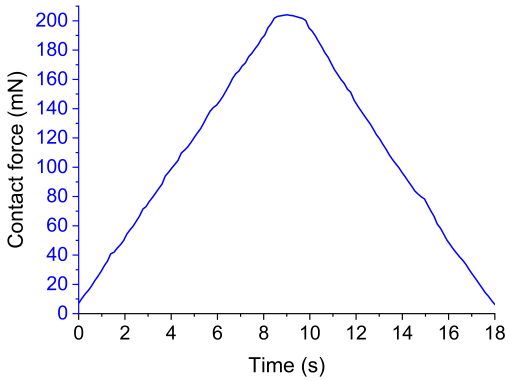

Fig. 6.4. Online monitoring of the vertical force as function of time using the *LabVIEW* software.

Table 6.3. *PROFIT*: Process parameters.

Process parameter	**Value**
z-velocity (µm/s)	1
z-step width (nm)	25
Max. z-force (mN)	var.
Number of TDs	1

To perform one contact cycle, the z-stage (chuck) of the *PROFIT* with the inserted sensor-indenter system is moved up towards the sample surface. After reaching a force threshold of 5mN, which is the "find contact" limit of the indenter tip, the measurement starts and the chuck is moved up until the force has reached the previously defined maximum value. After a short waiting time (e.g. 2s) at maximum force, the indenter tip is relieved by moving the chuck downwards. A flow chart diagram of one typical contact cycle is attached in the Appendix.

The vertical resolution of the z-stage of the *PROFIT* has a minimum step size of 25nm at a chuck speed of 1µm/s (see Table 6.3). These minimal values were chosen to ensure force measurement with an optimal accuracy and resolution. One contact cycle lasts typically up to 60s, depending on the maximum load, which is quasi-static and much longer compared to a high-dynamic contact insertion at operational wafer test (< 1s). However, a low chuck speed was better for the AE signal separation and classification.

b) AE System Settings

All acoustic crack experiments used *VS900-M* AE sensors with high sensitivity over a frequency range from 100kHz to 900kHz (see Fig. 5.5). The

preamplifier *AEP3N* for the AE signal amplification has a maximal gain of 49dB. A band pass filter from 95kHz up to 1MHz is set in the preamplifier, in order to synchronize the working frequency ranges of the preamplifier and AE sensor and to neglect disturbing signals and noise with lower and higher frequencies. The signal processor card *ASIP-2/A* amplifies the sensor output signal with another gain of 12dB and does again a filtering using a digital band pass filter from 100kHz to 1MHz. The *ASIP-2/A* enables the recording of AE signals in continuous and threshold-based mode, performs an AE feature extraction, and buffers the "AE data". The wave form data are recorded via an additional ***T***ransient ***R***ecorder (TR) module and thus termed "TR data". For the crack experiments during this work, the AE feature data ("AE data") are of particular interest. They were recorded using a sampling frequency of 10MHz, which is the minimal selectable value by the AE system. The waveform data ("TR data") were first sampled at 10MHz and later at 2MHz. As the resonant frequency of the optimized sensor-indenter system is around 130kHz (see Sect. 5.3.3), a sampling frequency of 2MHz is sufficient for a high reproducibility of the signal.

The voltage signal of the force sensor, which is converted into a calibrated contact force, is measured parallel to the AE signals in time-synchronization. Therefore, the analog sensor signal is fed into the parametric channel of the *Vallen AMSY-6* AE system, where the synchronization takes place automatically.

c) Data Processing

The *Vallen Acquisition* software manages and stores the measured data records in *SQLite3* ***D***ata***b***ases (DBs), whereby two DBs are stored per measurement. The DB file with the file extension *.pridb contains the feature-extracted AE data as well as the force measurement data in mV and the file with the extension *.tradb contains the data of the waveform in time domain. The data are subsequently imported into the *MATLAB* program for further analysis, converted into the appropriate units, and suitable *.txt files were created, which is needed for post-processing using the software *ORIGIN*.

The signal processor card *ASIP-2/A* considers the preamplifier gain for the data processing. Thus, the electrical voltage signals, which are shown in the following graphs, always refer to the raw sensor output signals [55].

6.1.4 Noise Level and Threshold Voltage

a) Continuous Measurement: Determination of the Noise Level

Before performing the AE crack experiments the noise level had to be determined. To this, three different case studies (C1 – C3, see Table 6.4) were performed. During the first test (C1) the noise level of the AE measurement equipment was examined without any other powered-up components of the *PROFIT* tool. The next noise level test (C2) was executed to investigate the impact of the powered-up measurement equipment of the *PROFIT*. For a simulation of a crack experiment, the chuck of the *PROFIT* was moved up and down. Hence, during the last test (C3) the chuck was moved 5µm up and down in vertical direction. For each case (C1, C2, and C3) the AE signal was recorded in continuous mode for ca. 60s and two test series (A and B) were performed, respectively. The acoustic measurement parameters, like the signal gain, filter settings, and the sample frequency, were chosen similar to the crack experiments in order to simulate realistic conditions. The acoustic data were stored in so-called data sets, each containing the data for a time period of 512µs.

The box plots in Fig. 6.5 show the noise level variance of the measured peak amplitudes, accumulated from all data sets, in units of dB_{AE} for all test series.

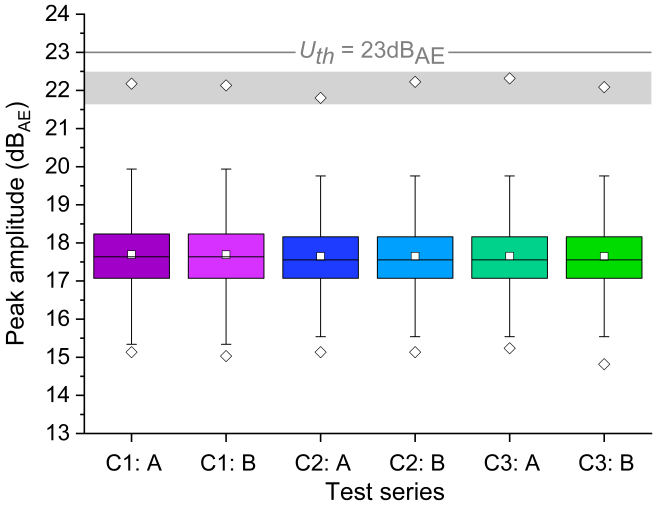

Fig. 6.5. Investigation of the noise level and definition of the detection threshold.

The mean values differ by less than 0.05dB$_{AE}$ (seeTable 6.4) and the tolerance between the maximal and minimal measured values (see diamond symbols) is about 7dB for all tests. This confirms a high repeatability and reproducibility of the noise level. The maximal values of the data sets are in between 22.32dB$_{AE}$ (C3: A) and 21.80dB$_{AE}$ (C2: A). All these results indicate, that the noise was mainly caused by the electrical noise of the AE measurement devices and is not negatively affected by other electronic or mechanical components of the *PROFIT*. Hence, the setting of a detection threshold voltage above the noise level during AE data recording was possible, which highly reduces the data amount. For the following acoustic crack experiments a threshold voltage U_{th} of 23dB$_{AE}$ (ca. 3.2µV) was set.

Table 6.4. Noise level: Mean and max. value.

Test series	**Mean (dB$_{AE}$)**	**Max. value (dB$_{AE}$)**
C1: A	17.69	22.18
C1: B	17.69	22.13
C2: A	17.65	21.80
C2: B	17.65	22.23
C3: A	17.65	22.32
C3: B	17.65	22.09

b) Threshold-based Measurement: Acoustic Crack Detection

As mentioned before, the AE measurement is force-triggered, i.e. the "AE data" recording does not start until the force F_z reached a threshold of 7mN and ends at the same force-relieving value. The reason for this was to ensure that only AE signals above a certain force level are recorded during contacting. In contrast to the acoustic data, the force data are permanently recorded over the entire contact cycle.

The AE and force signals are fed into the channels of the *ASIP-2/A* and checked for exceeding both threshold values for F_z > 7mN and U_{th} > 23dB$_{AE}$. Only if these thresholds are passed over, the acoustic data are permanently stored for a defined period of time. The "AE data" must be buffered and rejected, as long as no recording takes place. The period of permanent data storage is extended in time, meaning when a threshold value is exceeded, a minimum time period is always recorded before (e.g. 20µs) and afterwards (e.g. 200µs). The recording time is extended until the threshold value has fallen and remains permanently below the threshold value for a configurable post-triggering time, the so-called DDT. The unit of time is given in

microseconds. The AE signal duration of one crack event does typically not exceed two milliseconds. Table 6.5 summarizes the settings for the AE measurement.

Table 6.5. AE measurement parameters.

Process parameter	**Value**
Gain (dB)	61
Bandpass (kHz)	100 - 1000
Threshold force (mN)	7
Detection threshold (dB_{AE})	23
Sampling rate for "AE data" (MHz)	10
Sampling rate for "TR data" (MHz)	2
Duration discrimination time (µs)	200

Fig. 6.6, which is an extension of Fig. 6.4, has a second *y*-axis for the peak amplitude on the right side in addition to the time-dependent contact force on the left *y*-axis.

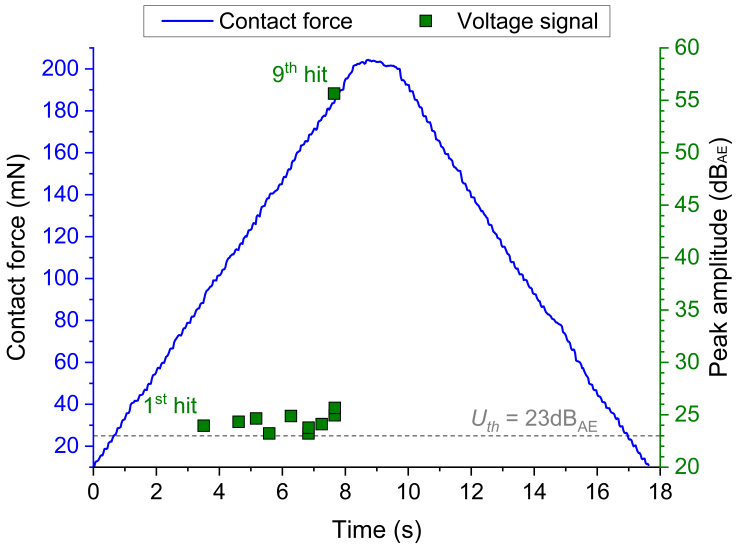

Fig. 6.6. Contact cycle with time-synchronous force and acoustic measurement.

The graph shows the associated acoustic-induced voltage signals as green dots, the AE hits. The peak amplitude of each acoustic event is plotted in dB_{AE} (reference value 1µV). In the shown example, 11 hits were measured,

which are above the threshold voltage U_{th} of 23dB$_{AE}$. The harmonic wave signal of each AE hit can be plotted with a higher resolution over the whole burst signal duration time. An example for a typical waveform signal in the time-domain is given in Fig. 6.7.

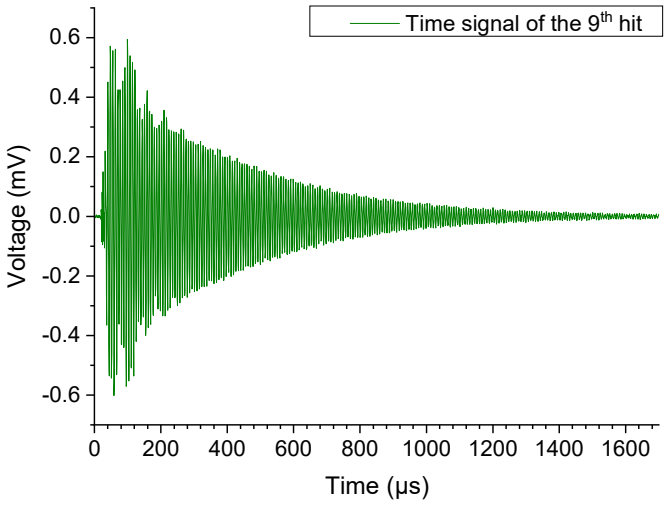

Fig. 6.7. Acoustic-induced voltage signals of the 9th hit.

6.2 Measurement System Analysis

During the ***M***easurement ***S***ystem ***A***nalysis (MSA) for the AE test method described in this chapter, the ability of the test equipment on reliable crack detection was assessed for the used test structures. The measurement results are rated in terms of accuracy, reproducibility, repeatability, and traceability. In a first step, the burst signal energy of the measured acoustic hits was determined as a function of the applied contact force. These data were filtered above a certain energy level to cluster the hits regarding "first oxide crack" events. From this, the cumulative crack probability was derived. Furthermore, in a variance analysis the required number of repeated contacts was evaluated to get statistical proven results, while in an additional step the reproducibility of the sensor-indenter system was examined. In the last step, a comparison of the previous 2-component indenter with the novel monolithic indenter was performed to demonstrate the higher sensitivity of the AE test method.

6.2.1 Determination of Burst Signal Energy and Crack Probability

During the qualification of the probing process (see Sect. 2.3.4) the determination of the fracture stress of the oxide layer as an indicator for the stack robustness is particularly important. However, the location and the amount of mechanical stress that results in an oxide crack when contacting by a thin needle is dependent on the shape and surface condition of the tip.

As described in Chap. 4.5, the stress curve during indentation on the surface and below is not constant, but has areas of maxima and minima with tensile and compressive stress especially in the edge region of the tip. Since in the practical case it is not possible to determine the maximum fracture stress leading to an acoustic event (= crack) exactly, the crack probability as a function of the contact force instead of the stress will be evaluated experimentally for a particular indenter type (flat with variable diameter). A detailed investigation to this is given in Chap. 7.

According to literature [48], an increasing intensity of AE burst signal parameters, such as the peak amplitude and energy (see Sect. 5.1.4), indicate a crack event. In this work, the burst signal energy is used to filter the measured AE signals, since the crack signals are clearly distinguishable from the other signals, like plastic deformation, in terms of higher amplitudes and signal lengths (see Sect. 6.2.3). The signal separation is well possible by means of correlation plots in the form of "log (energy) as a function of force" and thus used for the following series of experiments. Later in this chapter, in Chap. 6.3 the burst signal energy as an indicator of oxide cracks is verified based on the AE test results.

To define the filter criterion for the "first crack" event, 1000 contact cycles were performed sequentially on test structure W03 (see Table 6.1). The test structure was stressed up to a maximal contact force of 250mN to achieve nearly 100% crack probability while using the sensor-indenter system with the monolithic indenter (FP10-M-2).

Fig. 6.8 shows the burst signal energy in logarithmic scale as a function of contact force for all hits derived during 1000 contact cycles. Here one can see, that the burst signal energies are low until a critical contact force of ca. 160mN, meaning no acoustic crack event was observed. For a contact force higher than 160mN, the burst signal energy of the acoustic hits is increasing. Those hits with a high burst energy correlate well the with optical inspection data and hence can be used for further analysis (see Chap. 6.3). In case of a crack event, the burst signal energy E_{burst} is assumed to be higher

than 10eu. A lower filter limit of E_{burst} = 10eu is used for data analysis of the following experiments. For the determination of the fracture stress of the oxide layer, the mechanical contact force at which the "first oxide" crack appears is most relevant. Therefore, only acoustic hits with energy higher than 10eu of each contact cycle, occurring at a certain mechanical load, will be considered and utilized for further data evaluation.

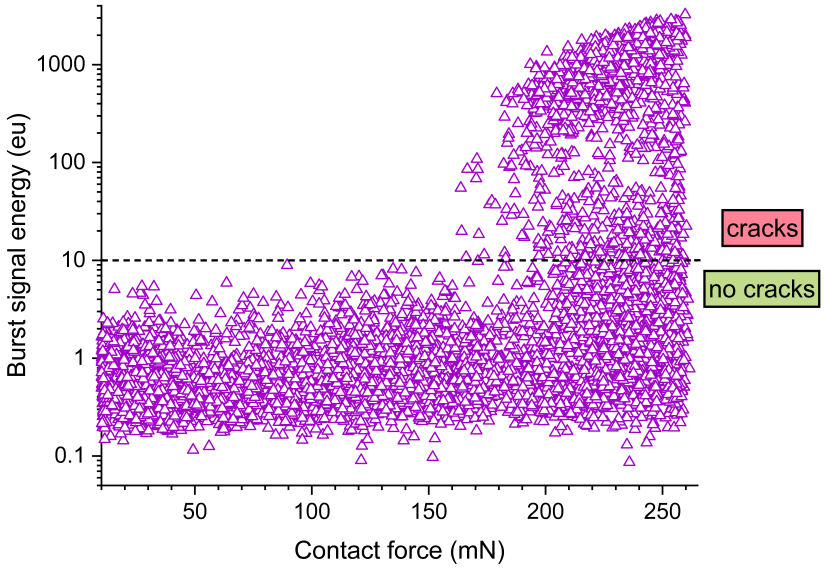

Fig. 6.8. Burst signal energy of all hits recorded for 1000 contact cycles on test structure W03 as function of contact force.

By filtering the data from Fig. 6.8 above a burst signal energy of 10eu and selecting only those hits that have occurred for the first time per indent ("first oxide crack"), the critical contact forces can be statistically evaluated from the remaining data points. Fig. 6.9 shows the result for all 1000 indents as a histogram plot (left) and cumulative frequency plot of the crack probability (right) over the contact force. Both graphs show a blue fitting curve that has been adapted to the data points.

The force dependent data points in the right-hand graph follow a *Weibull* distribution function P_f of the form:

$$P_f(F) = 1 - \mathrm{e}^{-\left(\frac{F}{F_0}\right)^m}, \tag{6.1}$$

with the *Weibull* modulus m and the characteristic contact force F_0.

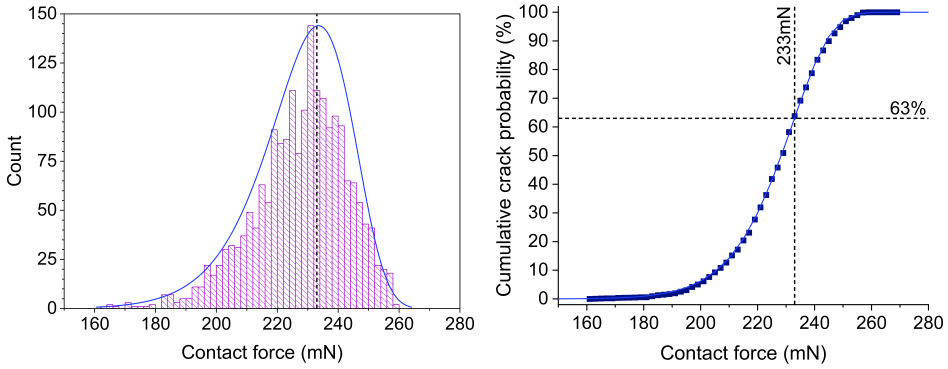

Fig. 6.9. Histogram (l.) and cumulative probability (r.) of 1st crack events for 1000 contact cycles on test structure W03 as function of contact force; bin size 2mN.

It can be seen from the enveloping curve in the left illustration that the maximum frequency of cracks occurs at a force of 233mN. By definition, this corresponds to the characteristic contact force F_o with 63% crack probability and confirms the theory from Chap. 4.4, that the crack forces of brittle materials follow a *Weibull* distribution. Substituting a *Weibull* modulus m = 18 and the value F_o = 233mN in Eq. (6.1) yields the blue curve in the right graph, which perfectly follows the data points from the AE measurement.

6.2.2 Variance Analysis

In order to analyze the variance of the characteristic contact force for several test runs with 25, 100, 400, and 1600 indents, test structure W01 was contacted to derive the necessary sample size of contacts for reproducible measurement series. A crack probability of nearly 100% was expected at a maximum force of 250mN, when using the monolithic indenter FP10-M-3. After the test run, the respective "first acoustic crack" event out of all contact cycles was filtered and plotted graphically in box plots (see Fig. 6.10).

The mean values (white rectangle symbol) of the characteristic contact force are at ca. 180mN for the runs of 25 and 400 indents and at ca. 181mN for those with 100 and 400 indents, respectively. According to statistical calculations, neither the mean nor the median (line symbol) values are significantly different for a significance level of 0.05. The interquartile range Q3-Q1 (box height) is between 19mN for 100 indents and 22mN for 1600 indents and thus almost identical for the different number of indents. However, the scatter of the measured data and the number of outliers (diamond symbol) increase with the number of contacts per test run.

Possible reasons for the scattering of the results are tolerances of the layer thickness caused by the deposition processes, the impact of the underneath Cu layer, the surface roughness, residual strain pattern resulting from the manufacturing process, and micro-segregation of chemical elements. Based on the statistical data evaluation a sample size of 100 contacts per measurement series is recommended to get accurate results.

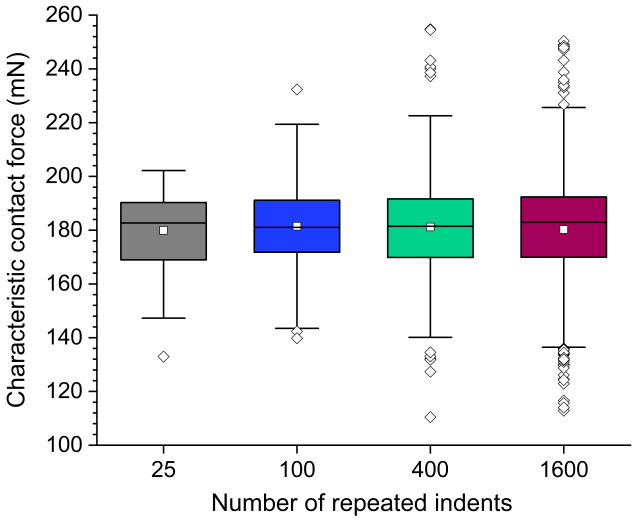

Fig. 6.10. Variance analysis of characteristic contact force of sample W01 for different sample sizes.

To validate the repeatability and reproducibility (Gage R&R) of the AE test method a variance analysis using two different sensor-indenter systems S1 (FP10-M-2 on VS900-M-2) and S2 (FP10-M-3 on VS900-M-3) was done. To prove the repeatability for variant S1, two test runs (A and B) each with 100 contact cycles were performed on test sample W02 (see Table 6.1). The sample was stressed up to a maximal force of 400mN to achieve approx. 100% crack probability. The reproducibility check (S1: A versus S2: A) was done in an additional test run using the second sensor-indenter system S2 with same test conditions as described before. The box plots in Fig. 6.11 show the variance analysis of the characteristic contact force for all test runs.

In Fig. 6.12, left the mean values for test run S1: A with 316mN and a standard deviation of ±27mN (vertical line) and for test run S1: B with 312mN and a standard deviation of ±26mN are shown. For a significance level of 0.05 the results of the repeatability test show that the mean values of the characteristic contact force are not significantly different.

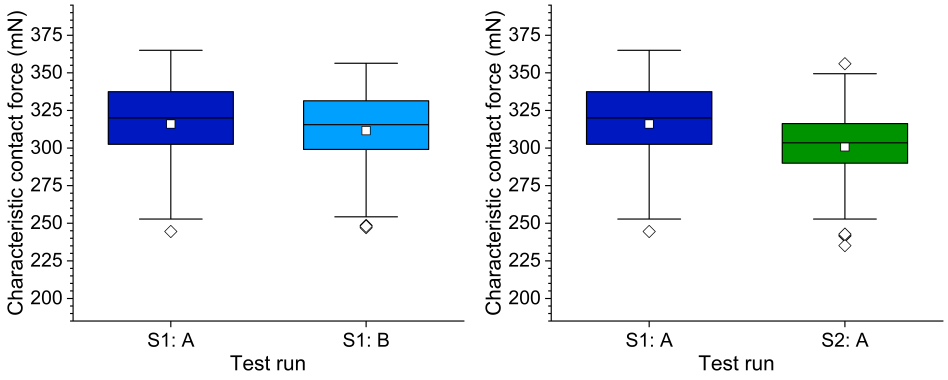

Fig. 6.11. Box plots of repeatability (l.) and reproducibility (r.) check for test structure W02.

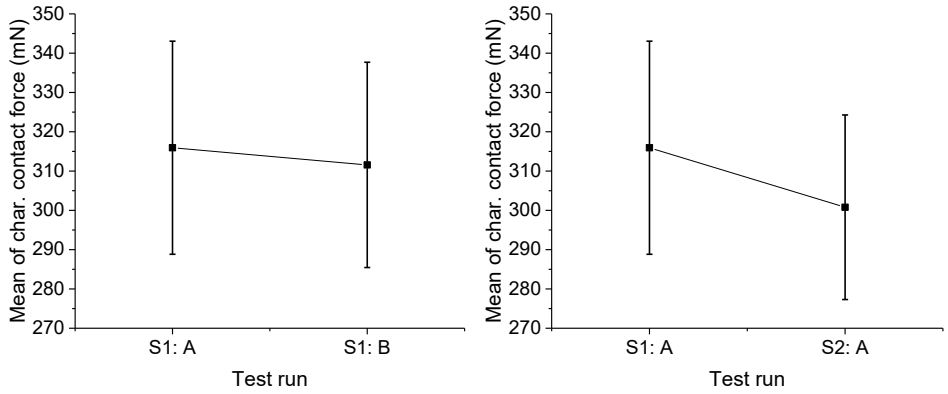

Fig. 6.12. Mean value plots of repeatability (l.) and reproducibility (r.) check for test structure W02.

The right graph of Fig. 6.12 shows the reproducibility test results for the mean values of the characteristic contact force again for S1: A (values see above) and S2: A with a mean value of 301mN and a standard deviation of ±24mN. By comparing the mean values of the characteristic contact force in this case for a significance level of 0.05 one gets a significant difference. This fact can be explained by the slightly different contact area (see Table 6.2) of the indenters FP10-M-2 and FP10-M-3 caused by manufacturing tolerances. The tip contact area of different indenters is never identical to each other and so it is important to measure the tip surface very accurately before the experiments and not exchange the indenter during a measurement series.

6.2.3 2-Component Indenter vs. Monolithic Indenter

Acoustic crack tests were also carried out using the monolithic indenter (FP10-M-1) in comparison with the 2-component indenter (FP10-C-1) on test structure W01 (see Table 6.1), in order to demonstrate the higher accuracy of the optimized sensor-indenter system after modification.[10]

Fig. 6.13 shows a time-dependent force graph (left *y*-axis) of a single contact cycle with the corresponding AE hits (right *y*-axis). The test structure W01 was stressed by both indenter types with a linearly increasing force up to a maximum value of 200mN and subsequently released to 0mN.

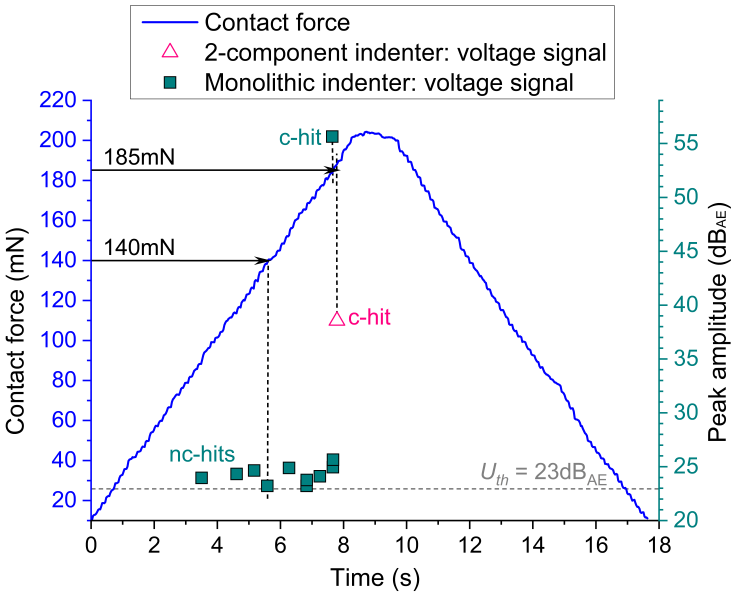

Fig. 6.13. Contact cycle of both sensor-indenter systems.

When using the 2-component indenter, only one acoustic hit (triangle symbol in Fig. 6.13) occurred above the threshold voltage with peak amplitude of 38.5dB$_{AE}$ at a corresponding vertical contact force of 187mN. If using the monolithic indenter, more hits (rectangle symbols in Fig. 6.13) occurred, but only one AE event, named here as "c-hit", is interpreted as an oxide crack. The crack event happened at a contact force of 184mN with a peak amplitude of 55.6dB$_{AE}$. Compared to the 2-component indenter, at nearly the same contact force here the peak amplitude of the crack signal is about

[10] This topic is also part of [3].

17.1dB$_{AE}$ higher. Acoustic hits with peak amplitudes lower than 26dB$_{AE}$, labeled here as "nc-hits", are most likely caused by atomic dislocation motions in the crystal plane of the metal (plastic Cu-deformation) and friction between the indenter tip and the surface of the test structure (see Chap. 6.3). This observation emphasizes again the higher sensitivity of the system with the monolithic indenter instead of the previously used 2-component indenter.

The associated waveforms and frequency spectra of the respective "c-hit" and first "nc-hit", measured with the monolithic indenter, are shown in the graphs in Fig. 6.14 in time-domain and in Fig. 6.15 in frequency-domain.

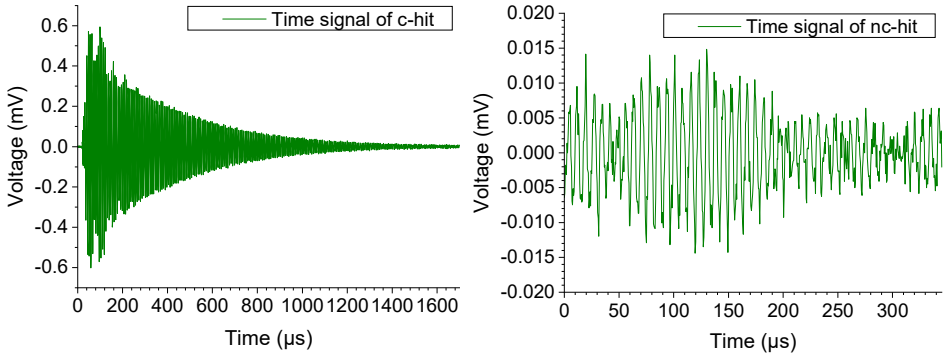

Fig. 6.14. Single AE hit in time-domain: the c-hit refers to an oxide crack (l.) while the nc-hit (r.) is mainly due to plastic deformation of the Cu-layer.

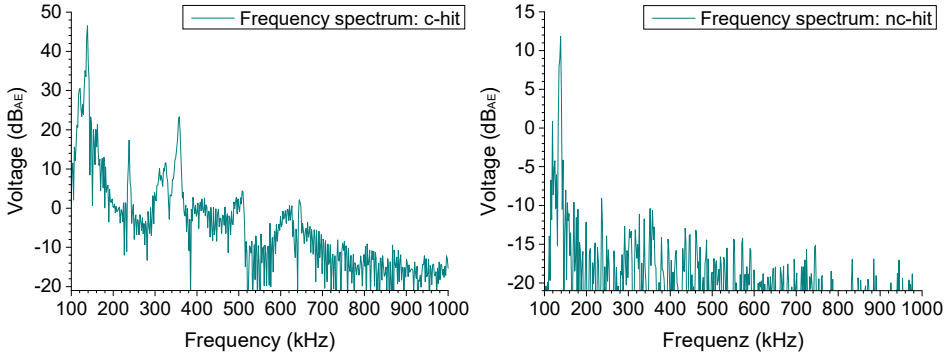

Fig. 6.15. Single AE hit in frequency-domain: the c-hit refers to an oxide crack (l.) while the nc-hit (r.) is mainly due to plastic deformation of the Cu-layer.

The AE signal indicating a crack (see Fig. 6.14, left "c-hit") has a higher peak amplitude of about 0.6mV and a length of up to 2ms. The AE signals, which are "no-crack" events, typically have a much lower amplitude (< 20µV) and a shorter duration (< 500µs) (see Fig. 6.14, right "nc-hit"). Due to the stronger excitation of the sensor-indenter system caused by a crack, the resonance peaks in the associated frequency domain (see Fig. 6.15, left) are much more pronounced compared to the frequency spectra of the "nc-hits" (see Fig. 6.15, right). In the context of this thesis, the topic of "signal analysis in frequency domain" will not be discussed further.

6.3 Validation of Crack Probability on Different Layer Stacks

After the test bench setup and measurement settings were optimized and the measuring system analysis was done for the sensor-indenter system on different test structures, experiments were carried out to determine the crack probability on brittle and ductile top layers. In parallel, the suitability of the AE test method was verified by proven crack inspection methods (see Chap. 3), which were applied after indentation at different stress levels.[11]

6.3.1 Crack Probability on Brittle Top Layer

To exclude interferences due to plastic deformation of the overlying pad metallization, damping effects, and reflection as far as possible, the acoustic measurements on test chip with indenter were initially made directly on the SiO_x surface. This section presents the exemplary results for test structure W03 (see Table 6.1), which was stressed by using the monolithic flat punch FP10-M-2 up to a maximal force of 250mN to achieve nearly 100% crack probability.

All AE hits out of 1000 indents, which were filtered on "first cracks", are graphically shown as a cumulative probability plot in linear and *Weibull* scale as a function of the contact force (see Fig. 6.16).

The *Weibull* modulus m is graphically derived from the linear regression line with a value of 18.9 and the characteristic contact force F_o is 233mN. In addition, Fig. 6.16, right shows that all data points are nearly within the 95% confidence band. This result denotes the high accuracy of the novel AE test method almost without disturbances, enabling a highly sensitive determination of the crack probability risk.

[11] The experimental results in Sect. 6.3.1 and 6.3.2 are also part of [3].

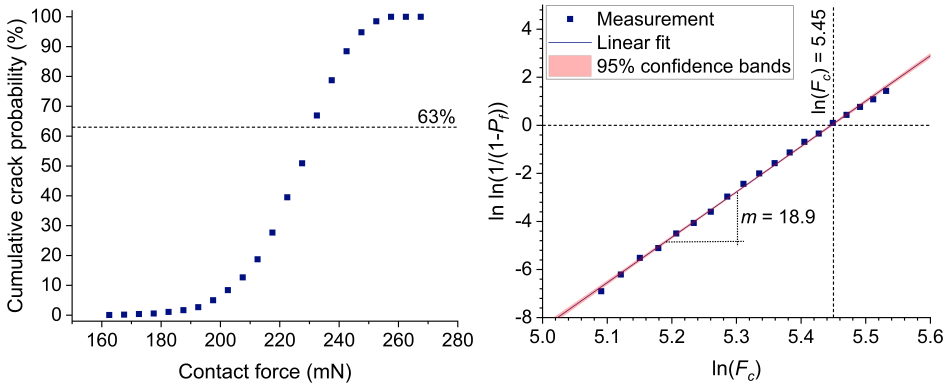

Fig. 6.16. Cumulative probability of 1st crack events for 1000 contact cycles on sample W03 in linear (l.) and *Weibull* (r.) scale as function of contact force; bin size: 5mN.

6.3.2 Crack Correlation after Indentation on Oxide Top Layer

The SEM images in Fig. 6.17 show two examples of test structure W01 after indentation using the monolithic indenter FP10-M-1. After contacting by a maximal force of 140mN plastic deformation of the contact area is visible (see Fig. 6.17, top left). During this test no acoustic crack signal was detected and the associated cross-section image shows no oxide layer crack (see Fig. 6.17, top right). If the maximal force was increased to 185mN, a crack event was observed during the acoustic measurement (see Fig. 6.13), which is well proofed by SEM inspections of the surface imprint (see Fig. 6.17, bottom left) and the correlating cross section image (see Fig. 6.17, bottom right).

The correlation of AE crack tests and subsequent optical crack inspections was continued for a higher amount of contact cycles. The test structures W01, W02, W03, and W04 (see Table 6.1) were contacted up to appropriate stress levels to achieve a crack probability of at least 50% up to 70%. 30 contact cycles were performed on each test structure using the monolithic flat punch (FP10-M-1).

Table 6.6 summarizes the experimental results. For test structure W02, W03, and W04 all generated cracks, which were measured by the AE test method were also observed after optical inspection. For test structure W01 there was only a discrepancy for one data point. In total, the experiments proved a very good correlation of the AE test method with the optical inspection.

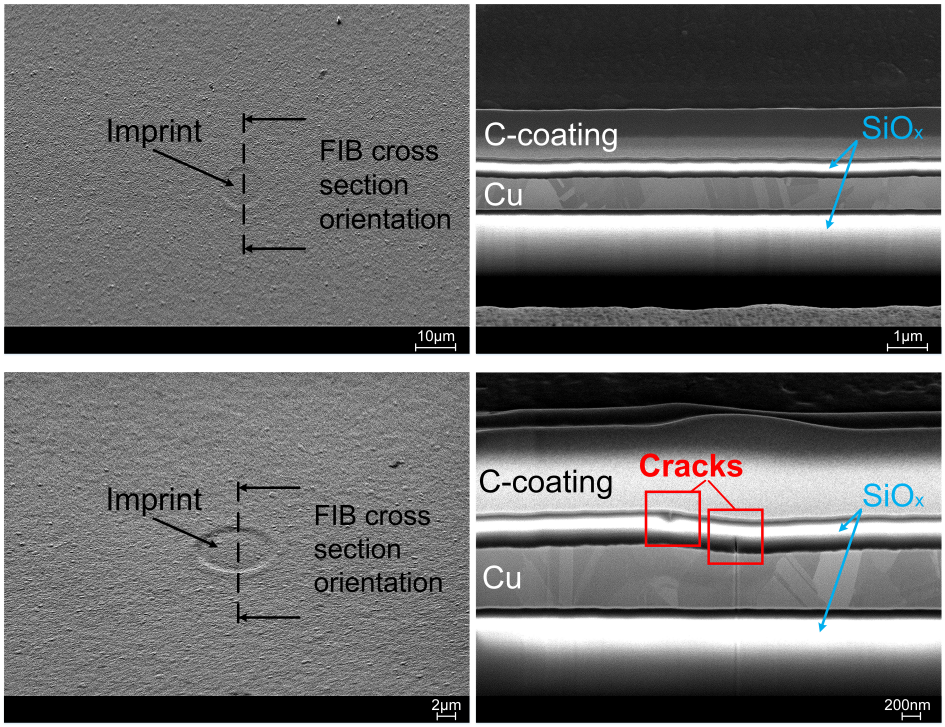

Fig. 6.17. SEM images of FIB-milled cross-sections at a maximal force of 140mN (top) and 185mN (bottom) on test structure W01.

Table 6.6. AE test method vs. optical inspection.

No. of detected cracks	**W01**		**W02**		**W03**		**W04**	
	crack	no crack	crack	no crack	crack	no crack	crack	no crack
AE test method	13	17	13	17	24	6	20	10
Optical method	14	16	13	17	24	6	20	10
Delta Δ of detected cracks	1		0		0		0	

Acoustic hits with small amplitudes (≤ 26dB$_{AE}$, see Sect. 6.2.3) can be observed even at contact forces below the fracture stress of the oxide, when using the monolithic indenter. This effect is probably caused by plastic deformation of the Cu layer underneath the upper SiO_x layer (see Fig. 6.1, left). To proof this hypothesis, AE tests were carried out on test structure W06,

which has no Cu layer (see Table 6.1) below the top oxide. The target of this experiment was to produce solely AE hits caused by oxide cracks, when stressing the structure up to a maximum load of 1000mN. Fig. 6.18 shows one contact cycle exemplarily out of a total of 20 contacts.

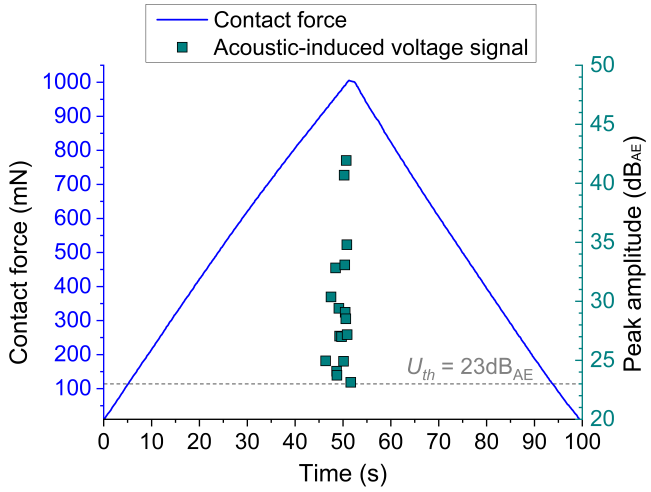

Fig. 6.18. Contact cycle on test structure W06.

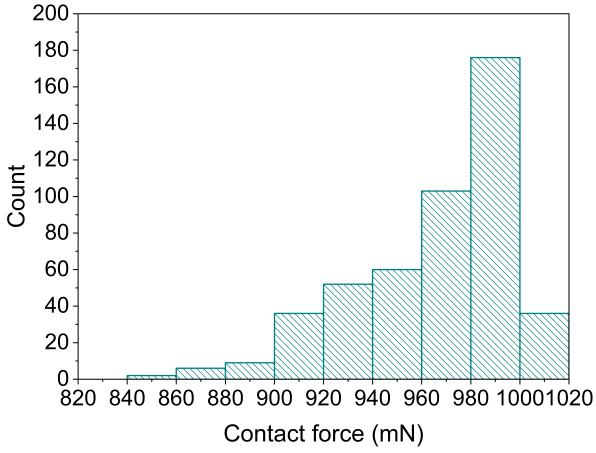

Fig. 6.19. Frequency count plot of hit associated contact force; bin size: 20mN.

Compared to the contact cycle in Fig. 6.13 in Sect. 6.2.3, no hits of low amplitude at smaller forces were detected. For all 20 contact cycles, hits only occurred when the contact force exceeded the critical force level for oxide

crack generation. The frequency count plot of the hit associated contact force is displayed in Fig. 6.19. These observations prove that hits with small amplitudes at contact forces below the oxide crack level are exclusively caused by plastic Cu-deformation. In this experiment, the maximum contact force was relatively high and so a large number of crack-related AE hits was measured and the appearance of oxide cracks looked different (see Fig. 6.20). Another reason for that is the missing Cu layer below the oxide, which results in an altered stress distribution.

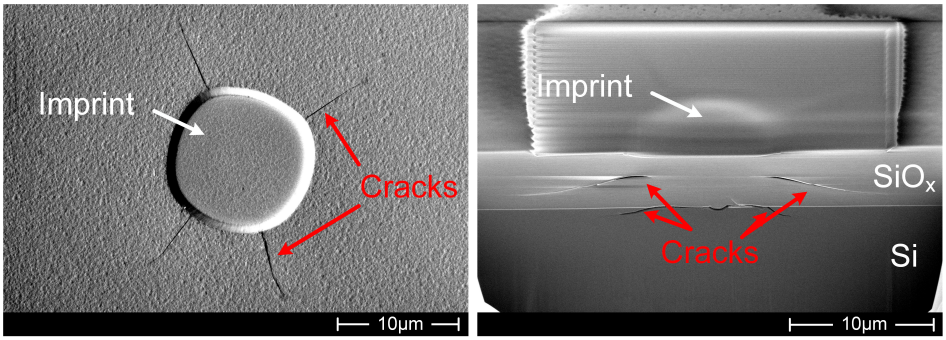

Fig. 6.20. Top down SEM image (l.) and FIB-milled SEM cross-section image (r.) showing the imprint and extensive cracks after indenting on test sample W06.

6.3.3 Crack Correlation after Indentation on Ductile Top Layer

Processed chips have metallized pads usually made of Al, Cu, or Au, which are contacted during operational wafer test. Such metal layers on top of the oxide layer have a ductile material behavior (see Chap. 4.2) and are deformed elastic-plastic during indentation in contrast to the brittle behavior as described in Sect. 6.3.1. Therefore, it was essential to examine the suitability of the novel AE test method for crack detection not only on top of oxide, but also on metallized layers.

The following experiments were performed with test samples having an Al-Cu layer on top of the SiO_x layer. To simplify the separation of AE signals caused by plastic deformation from oxide crack signals, the indentations were executed on test structure W05 (see Table 6.1) having a SiO_x layer thickness of 3000nm. Because of the thicker oxide layer compared to the test samples W01 - W04, the characteristic contact force causing oxide cracks was assumed higher for W05. This means, at relatively low contact forces only AE hits from plastic pad deformation are generated and at

significantly higher contact forces oxide crack signals should occur. All contact cycles were done using the monolithic indenter FP10-M-3.

In a first step, the crack probability was determined for test sample W05 on top of the SiO_x layer, wherefore the Al-Cu metallization and the liner were previously removed by wet-chemical etching (see Sect. 2.3.3). In the next steps, the indents were made initially on SiO_x, then on Ti, and finally on the Al-Cu layer at different maximum contact forces. By this approach it was possible to compare AE test characteristics on various layers regarding their peak amplitude, burst signal energy, and corresponding characteristic contact force. Additionally, multiple optical inspections using the chemical crack preparation and DIC method for crack inspection and the confocal microscopy for measuring the imprint depth on the Al-Cu layer were executed and correlated with the AE signals.

Step 1: Crack Probability on Brittle Top Layer

To identify the *Weibull* module *m* and the characteristic contact force F_0, test structure W05 without the Al-Cu layer on top was stressed in 100 contact cycles up to a maximal contact force of 650mN directly on the SiO_x layer. The cumulative crack probability of "first crack" events as a function of the contact force was calculated and the curves were plotted in linear (see Fig. 6.21, left) and *Weibull* scale (see Fig. 6.21, right).

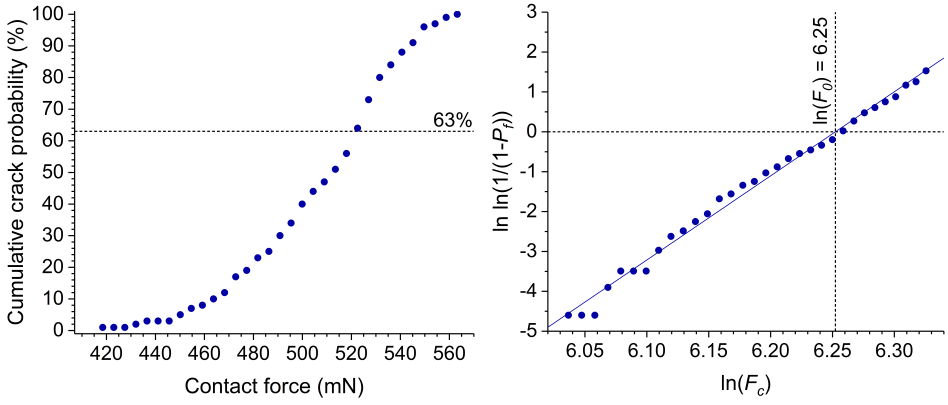

Fig. 6.21. Cumulative probability of 1st crack events for 100 contact cycles on sample W05, when directly contacting the SiO_x layer, in linear (l.) and *Weibull* (r.) scale as function of contact force; bin size: 5mN.

Derived from the data points in Fig. 6.21, left initial oxide cracks were observed at a contact force of approx. 415mN. The characteristic contact force F_o and the *Weibull* modulus *m* were determined graphically using the *Weibull* plot (see Fig. 6.21, right). The value for F_o is 519mN and the value for *m* is 21.1. Compared to test structure W03, for instance, which has a characteristic contact force of 233mN (see Fig. 6.16), the robustness of W05 with a thicker oxide layer is much higher.

Step 2: Crack Correlation after Indentation on Ductile Top Layer

Next, the applicability of the AE test method for test structures with a top metal layer was evaluated. Therefore, consecutively the SiO_x layer, the Ti layer, and the Al-Cu layer were contacted. Taking the result of the previous experiment into account, the maximum forces per contact cycle were increased from 50mN up to 650mN in steps of 50mN, in order to get AE measurements with and without generating oxide cracks. Using the monolithic indenter the samples were contacted 20 times for each set of force, respectively. To categorize the type of AE signals with regard to intensity and burst signal energy, optical inspections were subsequently performed to evaluate the appearance and propagation of cracks.

The following graphs show a contact cycle with AE tests on SiO_x (see Fig. 6.22) and Ti (see Fig. 6.23) layer for a maximum force of 650mN.

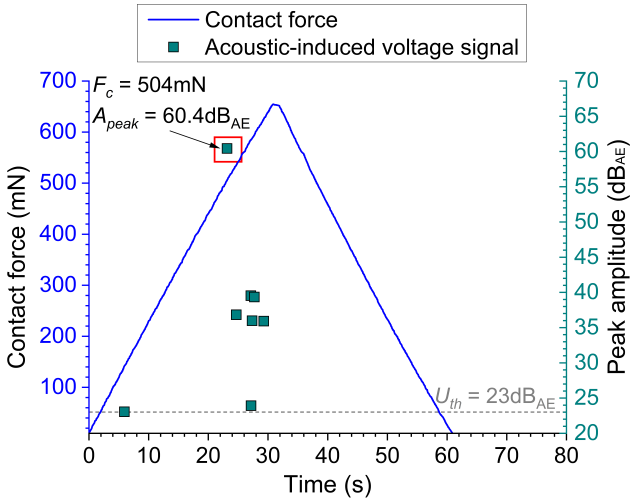

Fig. 6.22. Contact cycle: SiO_x indentation.

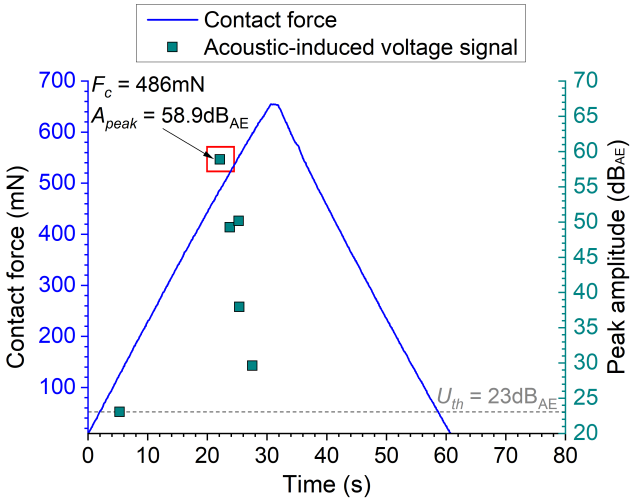

Fig. 6.23. Contact cycle: Ti indentation.

During contacting of the SiO_x layer a total of 8 hits was detected, while upon contacting of the Ti layer a total of 6 hits was detected above the threshold voltage of 23dB$_{AE}$. The "first acoustic crack" event occurred on SiO_x indentation at a contact force of 504mN with peak amplitude of 60.4dB$_{AE}$. When contacting the Ti layer, the "first acoustic crack" event was already detected at a contact force of 486mN, which is approx. 18mN lower. The maximum peak amplitudes of the signals are almost the same.

Fig. 6.24 shows a comparison of the measurement results cumulated for all 20 contacts on both SiO_x and Ti layer at a maximum contact force of 650mN. Here, the burst signal energy of the hits is plotted on the logarithmic scale over the contact force. Both in contacting on the SiO_x and Ti layer, acoustic crack events were measured above a contact force of about 450mN, which match very well with the optical crack inspection results (see Fig. 6.29, row 1 and 2).

In Fig. 6.29 a collection of microscope images is shown after contacting different top layer materials at various maximum loads. While no visible oxide crack appears during contacting the SiO_x layer up to a maximum load of 450mN (see Fig. 6.29, row 1), the oxide crack probability increases above this force.

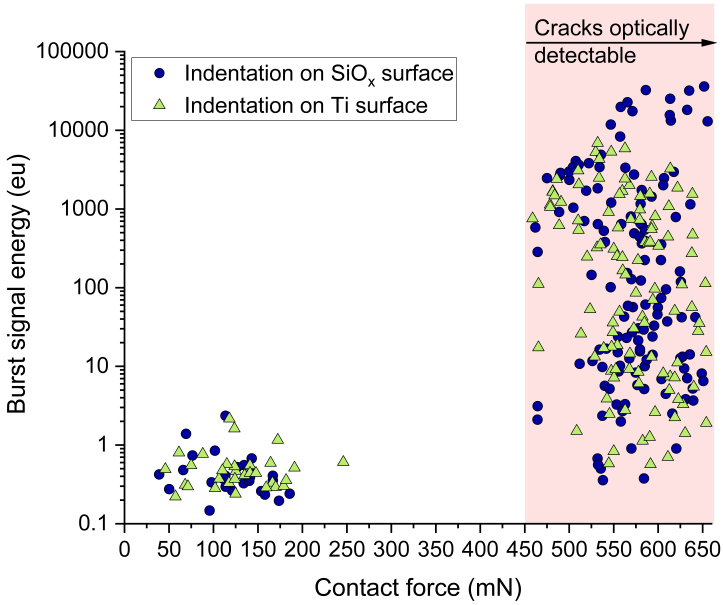

Fig. 6.24. Burst signal energy derived from the hits of each 20 contactings on SiO_x and Ti surface as function of the contact force.

Fig. 6.25, left shows an imprint made after indenting on the Ti layer with a maximum contact force of 600mN. After contacting, the Ti and Ta layers on top of the oxide were removed wet-chemically (see Fig. 6.25, right), in order to inspect the relating oxide cracks.

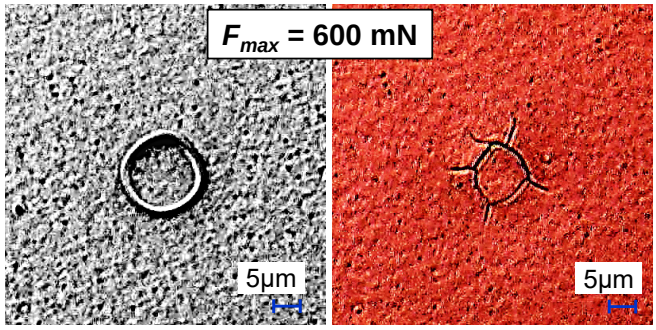

Fig. 6.25. Imprint on Ti layer before (l.) and after (r.) removal of the Ti and Ta layer revealing oxide cracks.

Comparing the images of the first row (contacting on SiO_x layer) and the images in the second row (contacting on Ti layer), no significant differences in the appearance of oxide cracks are obvious. The crack results from the

optical inspection fit well to the AE test results above a contact force of about 450mN, as shown in Fig. 6.24. Differences only arise above a contact force of about 550mN. Compared to the AE test characteristics on the SiO_x layer the intensity of the acoustic crack signals when contacting the Ti layer is slightly lower, which may be explained by a higher signal attenuation caused by the Ti layer.

Fig. 6.26 shows a contact cycle for contacting the Al-Cu layer with a maximum contact force of 650mN. Compared to the contact cycles for the SiO_x and Ti layers (see Fig. 6.22 and Fig. 6.23), there are clear differences in the force curve as well as in the number and intensity of the acoustic hits. Up to a contact force of approx. 230mN, the time-dependent force curve increases non-linearly, while at the same time many acoustic hits occur. Both are related to the fact that the indenter penetrates in the Al-Cu layer with increasing load, which is plastically deformed with increasing indentation depth (see Fig. 6.27). The number of hits and their amplitude level decreases accordingly with increasing penetration depth. After saturation of the indentation depth, the force curve is linear and only isolated hits of low amplitude occur. The "first acoustic crack" event in the oxide layer during contacting on Al-Cu is already measured at a contact force of 367mN with peak amplitude of 55.9dB$_{AE}$ compared to contacting on SiO_x with 504mN and a peak amplitude of 60.4dB$_{AE}$.

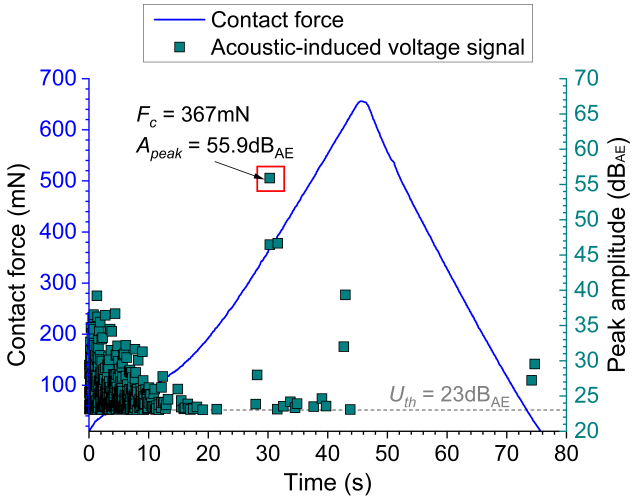

Fig. 6.26. Contact cycle: Al-Cu indentation.

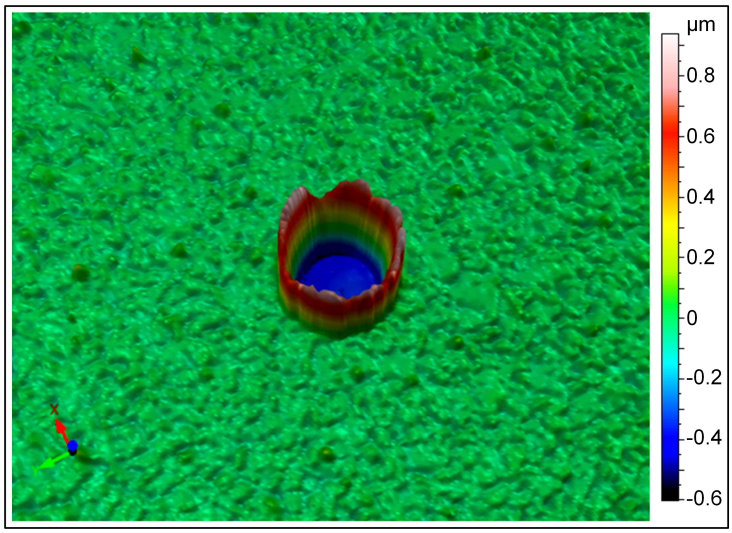

Fig. 6.27. Measuring the imprint depth after Al-Cu indentation using a confocal microscope.

Fig. 6.28 shows the accumulated AE hits when contacting the Al-Cu layer with a maximum contact force of 650mN for a total of 20 contact cycles. On the left *y*-axis, the burst signal energy of each hit is plotted on the logarithmic scale over the contact force. The right *y*-axis relates to the remaining imprint depth of the indenter tip into the Al-Cu layer in linear scale. At each force level (50mN - 650mN in steps of 50mN) the imprint depth of a total of 10 contact cycles was measured with a confocal microscope (see example in Fig. 6.27) and the mean value was calculated.

As one can see, the burst signal energy level is decreasing with increasing imprint depth, which can be explained by weakening of the plastic deformation of the top metal layer at higher load. After saturation of the imprint depth at approx. 2.5µm, the burst signal energy of the AE hits is rising again with continuously increasing load higher than 300mN. Considering an Al-Cu layer thickness of 3.0µm of test structure W05, the results of the AE crack test and imprint depth measurements are proving, that oxide cracks only start once the plastic deformation of the pad has saturated.

The oxide crack generation starts at a contact force of approx. 300mN for contacting on the Al-Cu layer, which is about 150mN lower compared to contacting on the SiO_x layer (see Fig. 6.24 and Fig. 6.28). The lower level of the critical contact force is also confirmed by the optical crack inspection. At the image at the left in the bottom row of Fig. 6.29 an oxide crack is visible already at a contact force of 350mN.

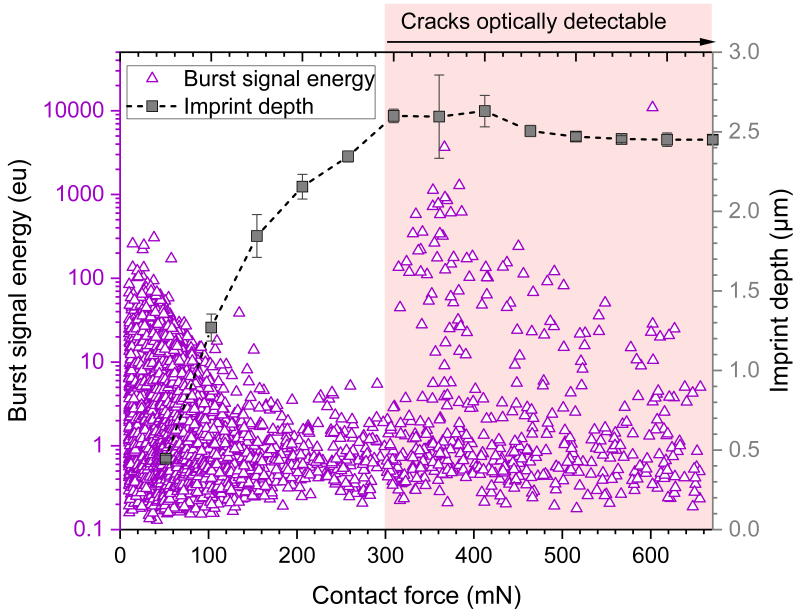

Fig. 6.28. Burst signal energy and imprint depth over contact force during Al-Cu indentation.

The optical images in the last row of Fig. 6.29 also show clear differences in the crack patterns. For indentation on the Al-Cu layer, the oxide layer shows a star-like crack shape starting from the center of the contact area. Different crack patterns are caused by differences in the stress distribution when contacting on Al-Cu in comparison with SiO_x or Ti layers. The burst signal energy of the "first crack" signals is almost an order of magnitude lower for the Al-Cu contacting compared to the SiO_x contacting (see Fig. 6.24 and Fig. 6.28). This may be due to the remaining Al-Cu layer thickness of about 500nm after saturation of the imprint depth and thus possibly causing a higher signal attenuation.

The filtering and classification of AE crack signals during contacting directly on a metal layer is more complex than for SiO_x contacting. As graphically shown in Fig. 6.30, for filtering of the "first crack" events here an energy limit of $E_{burst} > 7$eu and a force limit of $F_c > 300$mN were chosen.

Out of the filtered AE signals from Fig. 6.30, the cumulative crack probability was plotted as a function of the contact force and the *Weibull* parameters were derived. Fig. 6.31 shows a comparison of the characteristic contact forces F_o and *Weibull* moduli m when contacting on the Al-Cu (20 indents) and SiO_x layer (100 indents, see Fig. 6.21).

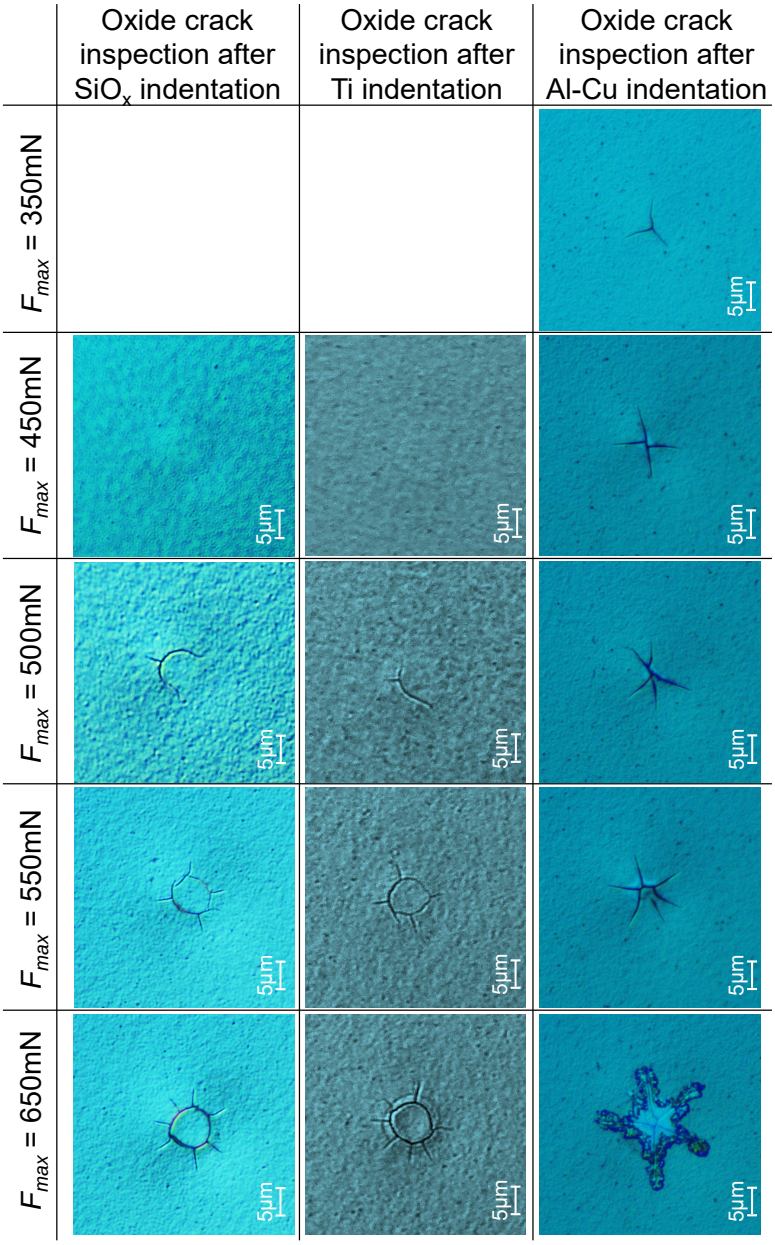

Fig. 6.29. Microscopy images of oxide cracks after indentation on SiO_x (row 1), Ti (row 2), and Al-Cu (row 3) layer at different maximal contact forces.

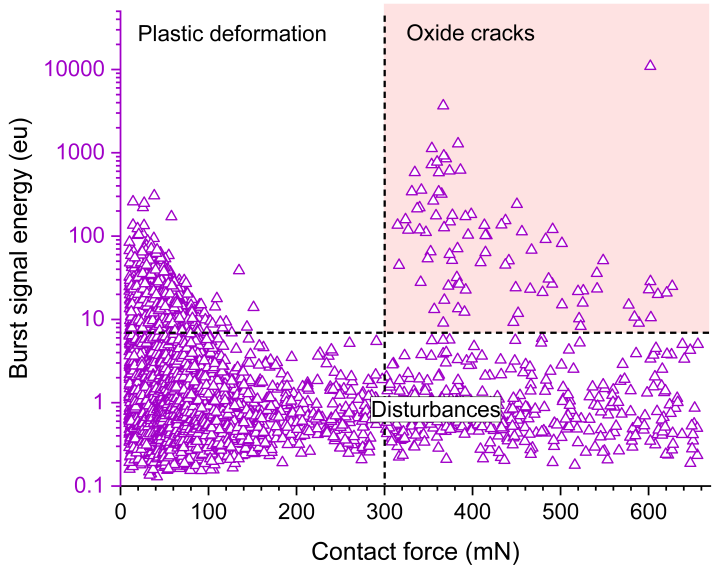

Fig. 6.30. Clustering of AE signals during Al-Cu indentation.

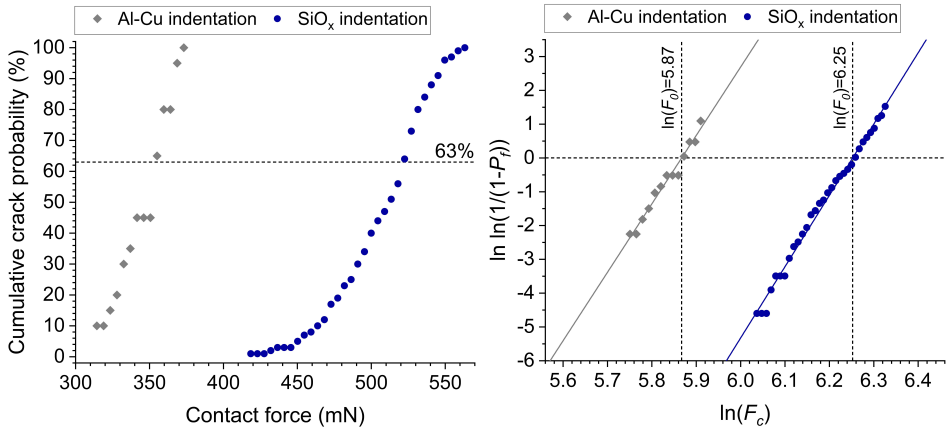

Fig. 6.31. Cumulative probability of 1st crack events as function of contact force in linear (l.) and *Weibull* scale (r.): Al-Cu vs. SiO_x indentation; bin size: 5mN.

For the contacting on Al-Cu, the value for F_o is about 166mN lower than for SiO_x (353mN compared to 519mN). The values for the *Weibull* modulus m are almost identical with 20.2 for Al-Cu and 21.1 for SiO_x indentation.

As a conclusion of this section, the results prove a good correlation of the acoustic crack detection and optical inspection. Hence, the acoustic crack detection method also works accurately for the Al-Cu layer indentation. It

was observed, that the top layer material is strongly influencing the robustness of the oxide layer on crack probability, but also the crack pattern and propagation is different. Compared to SiO_x contacting, the characteristic contact force is lower for the Al-Cu indentation and the stress distribution is different from the SiO_x indents. The filtering and clustering of the AE crack signals, however, out of the total number of hits is more difficult. With the newly developed AE test method it is now much more efficient and accurate to determine the oxide crack probability of various multi-layer stacks of different brittle and ductile material properties.

7 Acoustic Emission Test Method for Multi-Layer Crack Characterization

Chap. 7 is structured in three sections, starting with contact FEM-simulations on a representative multi-layer test sample. From this, the mechanical stresses and deformations in the layer stack during contacting with a flat rigid tip are derived and correlated with AE crack detection experiments and optical inspections to identify the location and propagation of oxide cracks. In the second part, AE crack tests on several unstructured multi-layer samples were performed with a variation of tip diameter and layer thickness to evaluate the influence of the different design parameters on the crack probability. The experiments were again correlated with simulations and optical inspections to confirm the results. In the last section of this chapter, the crack probability of a processed CMOS chip with POAA structures was determined to proof the efficiency of the AE test method. From the results of the simulation and crack experiments, important POAA rules for the design and material selection of semiconductor structures can be gained in the future.

7.1 Stress Concentration and Crack Formation in Layer-to-Layer Interphase

This section explains, how mechanical stress during indentation on complex layer structures, which are typical for CMOS semiconductors, initially causes cracks in the nanometer range in thin oxide. The cracks propagate further within the brittle layer along the region of highest stress concentration. For this purpose, FEM contact simulations in form of a project study (see [63]) were conducted and supervised within the scope of this doctoral thesis.

At the beginning, a parametrized FEM-model was designed to simulate regions of stress concentration when contacting a multi-layer structure with a flat-ended diamond tip with rounded edges. The experimental results of the AE test method were finally correlated with optical analyzes for the plausibility check of the simulation. Table 7.1 lists the different ***L**oad **C**ases* (LC01 - 09) with the respective test structure (see Sect. 6.1.1, Table 6.1) and indenter variants (see Sect. 6.1.2, Table 6.2), which were simulated and experimentally performed.

Table 7.1. Load case parameters for FEM-simulation and experimental studies.

Load case	Test structure	Indenter type	Tip diameter (µm)	Max. contact force (mN)	No. of indents
LC01	W01	FP10-M-2	10	184	30
LC02	W01	FP10-M-3	10	320	100
LC03	W01	FP10-M-3	10	260	400
LC04	W01	FP10-M-2	10	185	100
LC05	W01	FP10-M-3	10	350	100
LC06	W01	FP10-M-3	10	300	100
LC07	W04	FP10-M-3	10	500	100
LC08	W01	FP20-M-1	20	1000	100
LC09	W04	FP20-M-1	20	1500	100

7.1.1 Finite Element Simulation of Contact and Inter-Layer Stress

Initially, a 2-dimensional, rotationally symmetric half-model of the test structure W01 (see Sect. 6.1.1, Table 6.1) was designed for the FEM-simulations, which again was done by the program *COMSOL Multiphysics version 5.3a*. The rotational half-model of the diamond tip, according to the dimensions of the physical indenters, has a variable tip diameter d_{tip} of 10µm and 20µm and a tip edge radius of 1µm. During the contact simulation, the tip presses with increasing load on the SiO_x surface (see Sect. 4.5.2). Fig. 7.1, left shows a section of the parameterized FEM-model with the components indenter and multi-layer test structure. On the right side, the multi-layer structure with details of the materials is shown schematically. The uppermost layer is modeled as an elastic SiO_x layer overlying a thin Si_3N_4 layer. Immediately below is a Cu layer, which is plastically deformable. The Si substrate in the lower layer has a total thickness of 500µm and a width of 300µm. For the subsequent evaluation of the stresses in the upper oxide layer the reference levels SiO_x top and SiO_x bottom are marked in Fig. 7.1.

In the next step, the FEM-model was meshed (see Fig. 7.2) and the material parameters were assigned to the various components (see Table 7.2). When defining the element size and density of the FEM-mesh, care was taken to ensure that the finest possible and optimized mesh was available, particularly in the area of the contact surface between the indenter tip and the

oxide surface as well as near the edge radius and within the thin intermediate layers. This is important for better iteration convergence, shorter computation times, and correct calculation of stresses and deformations.

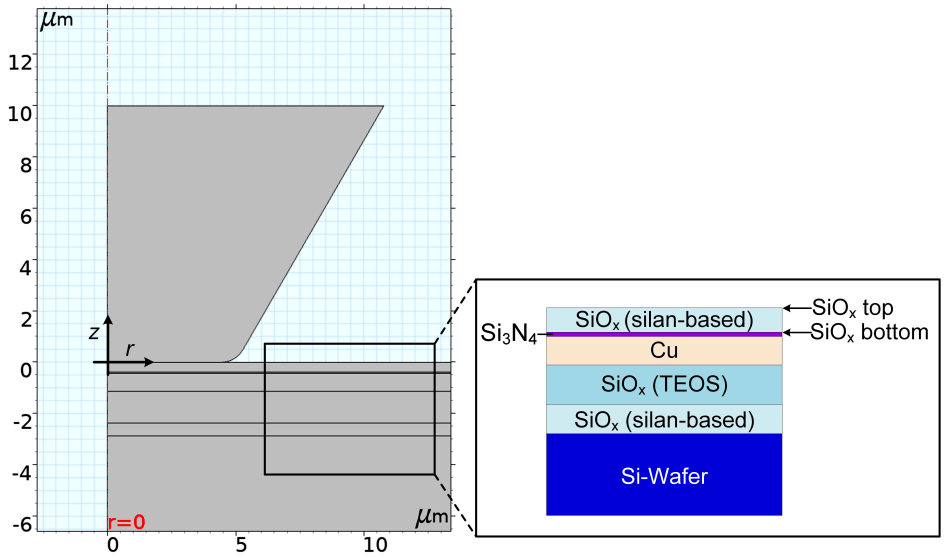

Fig. 7.1. Unmeshed FEM 2D half-model of the indenter (l.) and multi-layer stack with material naming (r.).

Table 7.2. Material parameters of system components in FEM-simulation by [63].

Material	**Diamond (100)**	**Si (111)**	**SiO_x (TEOS)**[12]	**Si_3N_4**	**Cu**	**SiO_x (silan-based)**
Density (kg/m³)	3515	2329	2200	3100	8960	2200
E-module (GPa)	1050	168.9	72	160	110	67
Poisson's ratio	0.1	0.262	0.17	0.24	0.34	0.17
Von Mises yield stress (GPa)					0.2	
Isotropic hardening (GPa)					0.395	
Fracture energy (J²/m)				20		

[12] TEOS: ***T***etra***e***thyl ***O***rtho***s***ilicate

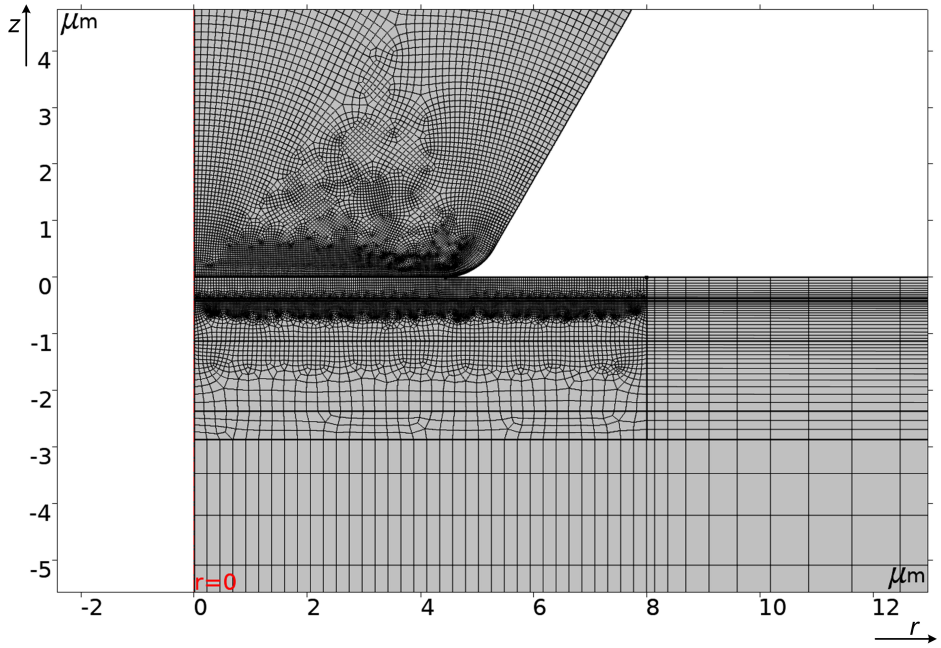

Fig. 7.2. Meshed FEM 2D half-model of the indenter and test structure.

Subsequently, various mechanical simulation runs with stepwise increasing contact force were carried out to determine the maximum deformations and stresses using the optimized solver settings of the program. For a more detailed description of the program settings on the solver refer to [63]. Here, the friction coefficient μ_r between the diamond tip and the oxide surface was assumed to be zero in the model.

Fig. 7.3 shows a contour plot of the first principle stress σ_1 (see Sect. 4.1.2) for load case LC01. For a flat tip of 10µm diameter and at a contact force of 184mN, the highest stress values are approx. $\pm 8 \cdot 10^9 N/m^2$ (= 8GPa) and are located near the edge of the indenter tip as well as in the region of the Si_3N_4 layer below the upper oxide layer.

With increasing contact force, the oxide layer is elastically deflected downwards, since at the same time the Cu layer is plastically deformed under vertical load. This creates an S-shaped deformation of the uppermost layers in the region of the tip edge. The upper oxide layer and the nitride layer of the structure are subjected to alternating tension and compression during the indentation essentially in the radial direction. The Cu layer and the area below the indenter are predominantly under compressive stress in vertical direction. Immediately beneath the right edge of the tip is a region of high

stress concentration, which is expected for the case of "flat-ended circular punch on flat surface", as detailed elaborated in Chap. 4.5.

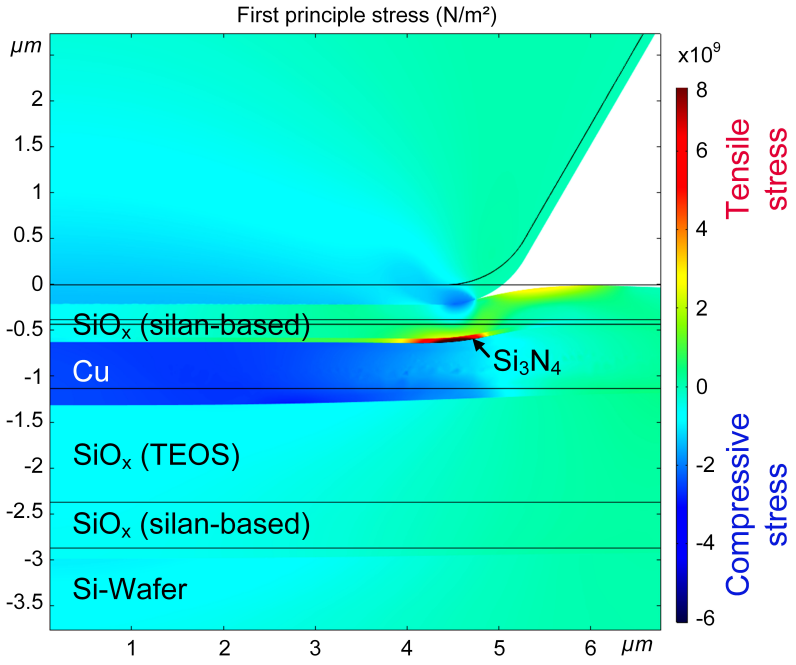

Fig. 7.3. First principal stress contour plot of test structure W01 with indenter of 10µm tip diameter for contact force F_c = 184mN (load case LC01).

Fig. 7.4 exhibits a DIC microscopy image of a permanent imprint on test structure W01, which was made with the indenter FP10-M-2 at a maximum contact force of 184mN (LC01).

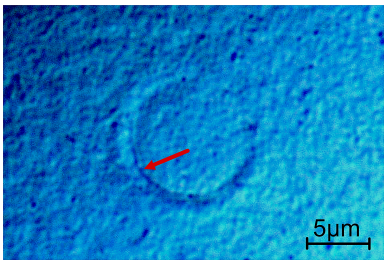

Fig. 7.4. DIC microscopy image of indenter imprint on SiO_x surface of sample W01 after contact load F_c = 184mN (load case LC01).

One can see a height profile, which indicates a permanent plastic deformation of the Cu layer and agrees well with the simulation results. A closer look also reveals a darker line (see red arrow) around the perimeter of the imprint. As will be seen later in the FIB cross-sections (see Sect. 7.1.2), this line indicates a crack on the oxide bottom side. Obviously, cracks first appear on the bottom side of the oxide and then spread out into higher levels.

The graphical illustrations as colored contour plots of mechanical stresses, separated in the radial $\sigma_r(r)$ and vertical $\sigma_z(r)$ direction (see Fig. 7.5), are well suited to locate the region of maximum stress, in order to understand and interpret the crack initiation and propagation.

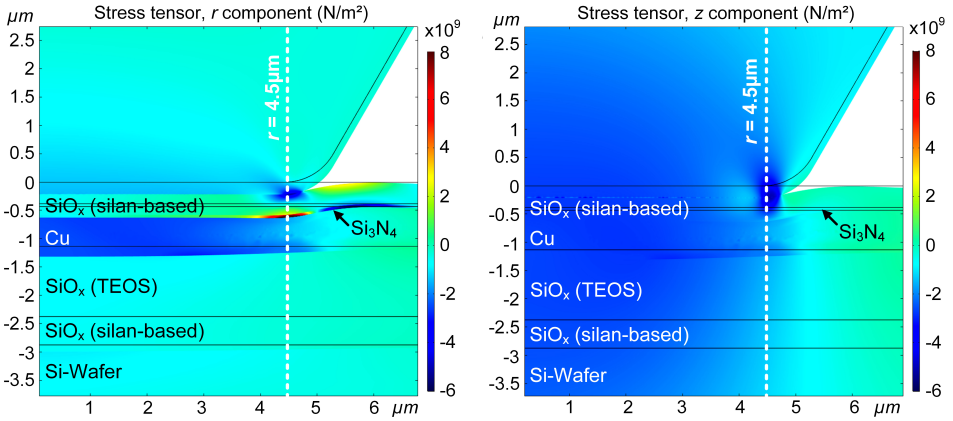

Fig. 7.5. Radial (l.) and vertical (r.) stress contour plots of test structure W01 with indenter of 10μm tip diameter for contact load F_c = 184mN (load case LC01).

As shown in Fig. 7.5, left, the largest absolute values of the radial stress $\sigma_r(r)$ for load case LC01 are approx. 8GPa and are located at a radial distance of r = 4.5μm (see dashed white line) from the symmetry axis below the edge of the indenter within the Si_3N_4 layer. At the top of the oxide layer outside the contact area and at the bottom of the oxide layer below the edge of the indenter, the radial stresses are maximal (positive = tensile stress) within the oxide layer. At the tip edge within the contact area, the oxide layer is subjected to pressure load (negative = compressive stress).

The absolute value of the vertical stress $\sigma_z(r)$ (see Fig. 7.5, right) is lower in comparison with the radial stress $\sigma_r(r)$ and acts predominantly as compressive stress (blue = negative). As already explained in Fig. 7.3, a stress maximum is visible directly below the tip edge, which corresponds to the analytical model of a "flat-punch on half-space" (see Sect. 4.5.1).

In the following, the stresses are shown as *xy* plots along the interface of the different layer planes (see Fig. 7.1). The *x*-axis corresponds to the radial distance *r* from the axis of symmetry and the *y*-axis to the radial or vertical stress. First, the stresses along the free surface of the oxide layer are considered in Fig. 7.6.

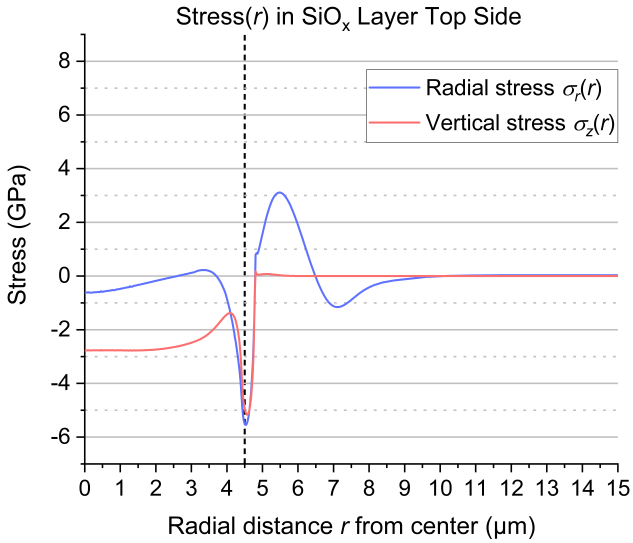

Fig. 7.6. Radial (blue) and vertical (red) stress as function of radial distance from center on SiO_x layer top side at contact force F_c = 184mN (load case LC01).

The blue curve shows the radial stress $\sigma_r(r)$. When approaching the tip edge within the contact area at a distance of r = 4.5µm (dashed black line), the stress first drops from zero to a minimum of about -5.5GPa (= compressive stress). Subsequently, the radial stress rises to a maximum (= tensile stress) and then falls back to zero after a brief change of sign (tension → compression). The red curve shows the vertical stress $\sigma_z(r)$. The stress also drops to a minimum (compressive stress) up to the *x*-position of r = 4.5µm from an already negative value and then rapidly increases to zero outside the contact region. The minima of the two stress curves are approximately equal in magnitude.

In Fig. 7.7 the stresses along the bottom side of the oxide layer are shown. The radial stress $\sigma_r(r)$ (blue curve) initially increases continuously up to a maximum of approx. 6.5GPa at r = 4.5µm and then drops to a minimum of approx. -4.5GPa. With increasing distance of r from the symmetry axis, the stress-value approaches zero again. The vertical stress $\sigma_z(r)$ (red curve) initially remains largely constant within the contact region at a negative value of approx. -3.0GPa (= compressive stress) and then rises back to zero. It should be noted, that the amount of maximum tensile stress for the radial component at the bottom side of the oxide layer (ca. 6.5GPa, see Fig. 7.7) is more than doubled compared to the radial stress at the top side (ca. 3.0GPa, see Fig. 7.6).

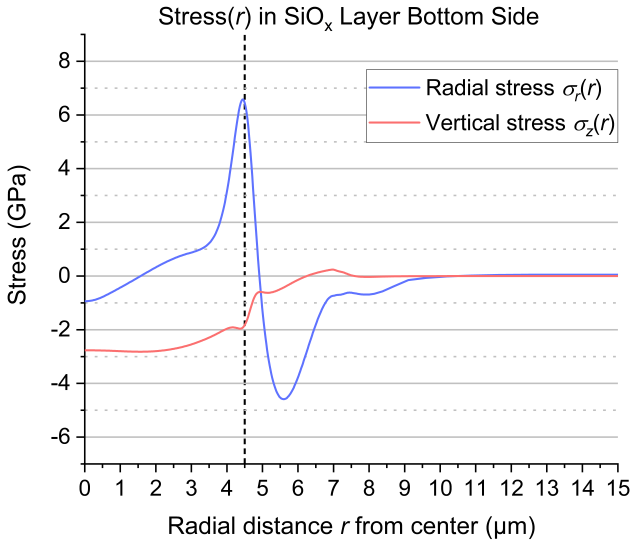

Fig. 7.7. Radial (blue) and vertical (red) stress as function of radial distance from center on SiO_x layer bottom side at contact force F_c = 184mN (load case LC01).

Finally, if one considers the stress distributions along the Si_3N_4 layer (see Fig. 7.8), one can see a largely identical profile as at the bottom of the SiO_x layer (see Fig. 7.7). However, the values of the maximum tensile radial stress (blue curve) of approx. 8.0GPa and the minimum compressive stress of approx. -5.5GPa are higher. From this it can be concluded, that the tensile stress in the Si_3N_4 layer and along the bottom of the oxide layer is maximal at a radial distance of r = 4.5µm close to the circumference of the indenter and thus the risk of cracks is highest there. Cracks most probably start at this location first and then spread further, which agrees well with the experimental results (see Fig. 7.4).

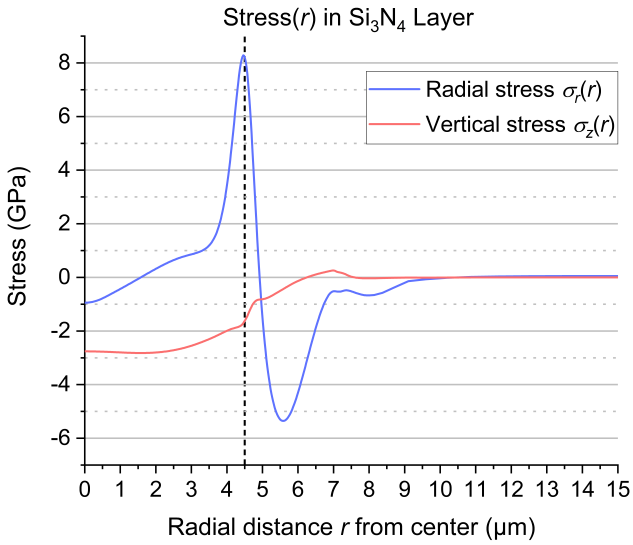

Fig. 7.8. Radial (blue) and vertical (red) stress as function of radial distance from center on Si_3N_4 layer at contact force F_c = 184mN (load case LC01).

If the contact force during contacting with a flat tip with a diameter of 10µm is further increased up to a value of F_c = 320mN (load case LC02, see Table 7.1), the tensile and compressive stress in the layers continues to rise as can be seen in the radial stress contour plots in Fig. 7.9 for LC01 (left) and LC02 (right).

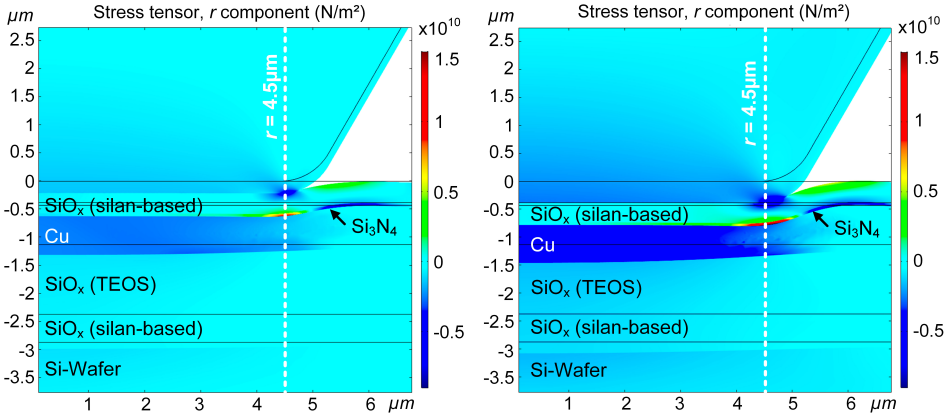

Fig. 7.9. Radial stress contour plots of test structure W01 with indenter of 10µm tip diameter for contact force F_c = 184mN (l.) and F_c = 320mN (r.).

It is to be expected, that the brittle layer on the upper side of the top oxide layer will rupture completely once the fracture stress of the material is exceeded.

In Fig. 7.10 the radial stresses along the top and bottom oxide layer planes for load case LC01 (purple curves) and LC02 (blue curves) are again plotted as a function of the radial distance r from the symmetry axis at r = 0. Since, as previously shown, vertical stresses are significantly smaller compared to radial stresses and only act as compressive stress, a further examination of the vertical stress is omitted here. The curve characteristics are largely identical for low and high contact loads, but the amounts of the maximum and minimum stresses differ significantly. The radial distance of the maximum and minimum stress outside the contact area (r > 4.5µm) moves slightly to the right in positive x-direction as the load increases, whereas the location remains constant close to the edge radius.

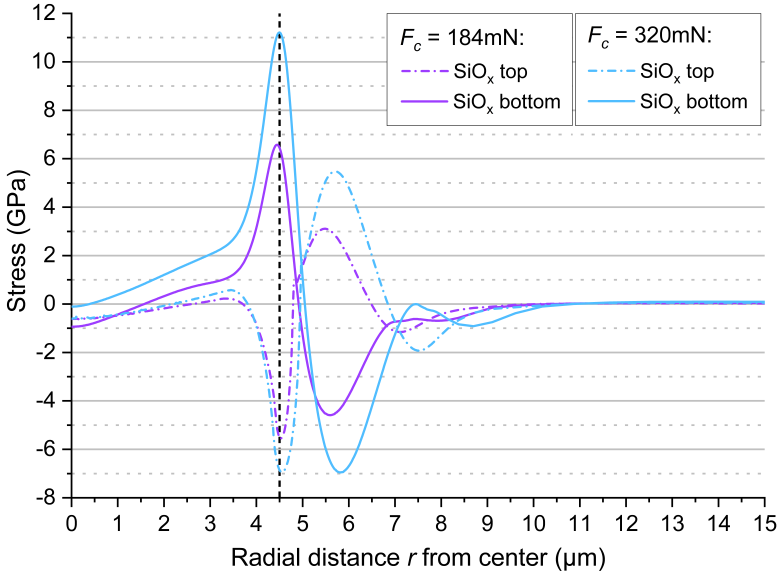

Fig. 7.10. Radial stress in top and bottom side of SiO_x layer at contact force F_c = 184mN (purple) and F_c = 320mN (blue).

Thus, the structure always cracks initially near the indenter tip edge (here: r = 4.5µm) at the oxide bottom side and propagate further into the material regardless of the tip diameter and layer thickness. Once the tension stress on the top side has reached the critical fracture value, the oxide layer also cracks at the point of maximum stress. The amount of stress based on the

FEM-simulations for SiO_x here is about 5-6GPa, which is a significantly higher value than specified in the literature of a value below 1GPa [64].

To confirm the simulation results, in Fig. 7.11 a DIC microscopy image of an imprint on the oxide surface of sample W01 after a load of 320mN can be seen (load case LC02). One can clearly see there the crack course as a dark circular line, which runs exactly along the circumference of the indenter.

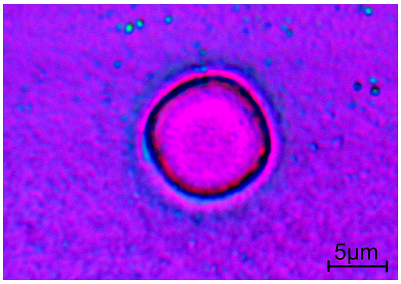

Fig. 7.11. DIC microscopy image of indenter imprint on SiO_x surface of sample W01 after contact load F_c = 320mN (load case LC02).

7.1.2 Correlation of Crack Locations for Simulation and Measurement

Now the results of the simulation shall be compared with the experimentally determined values of the AE measurement and microscope inspections. For this, test structure W01 was first loaded with the indenter FP10-M-3 up to a contact force of 260mN (see Table 7.1, load case LC03), in order to measure the occurring AE hits from oxide cracks and plastic deformations with the AE test method. A total of 400 successive contact cycles was carried out. Fig. 7.12, left shows the burst signal energy E_{burst} of all accumulated hits on a logarithmic scale as a function of the contact force F_c.

Above a contact force of approx. 120mN and a burst signal energy threshold of 10eu, a certain number of acoustic events (hits) occur, while below the threshold many hits with low energy occur over the entire force range. As described in Chap. 6.2, those hits having a high burst energy can be assigned to oxide cracks (see red area) and those hits having a burst energy lower than 10eu are caused by plastic deformation of the Cu layer and other disturbances. By filtering hits with values E_{burst} > 10eu and selecting only the first hit out of each contact cycle, one obtains the force-dependent cumulative crack probability in percentual units, which is shown in Fig. 7.12,

right in linear scale. As can be seen from the shape of the blue fitting curve, a characteristic contact force of approx. 185mN is expected to cause a 63% crack probability for LC03.

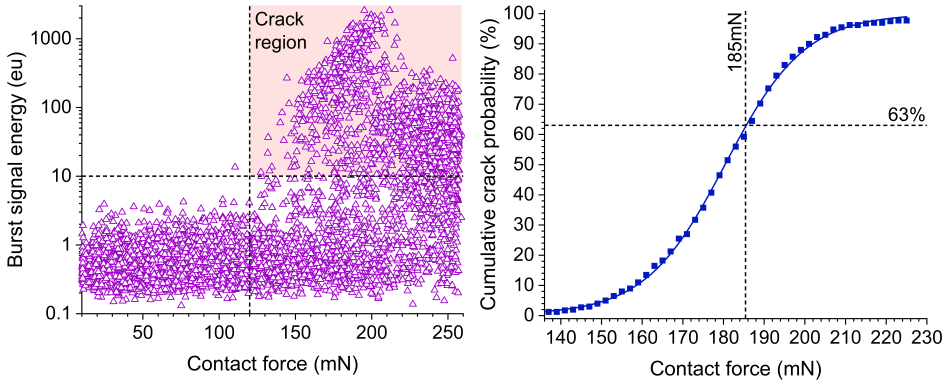

Fig. 7.12. Summarized burst signal energy of all hits (l.) and cumulative crack probability (r.) as function of contact force for load case LC03; bin size: 2mN.

a) Crack Generation at Maximum Contact Force of 185mN

In order to confirm the previously determined crack probability of 63%, test structure W01 was stressed in a further experiment up to a characteristic contact load of F_c = 185mN to measure cracks with the AE test method (load case: LC04). In this experiment, 100 contact cycles were performed repeatedly. The result of the statistical evaluation can be seen in Fig. 7.13.

The lower graph shows the frequency count of the AE hits over the contact force within the range from 140mN to 185mN with a bin size of 5mN. One observes a continuous increase in the number of cracks with increasing contact force. Plotting the cumulative frequency of cracks in a linear scale, one gets a 63% crack probability for a contact force of 183mN at the intersection point of the horizontal and vertical dashed lines (see Fig. 7.13, above).

Based on the FEM-simulations it can be assumed, that for a contact load of 185mN cracks occur only at the bottom side of the oxide layer, because the induced tensile stress has just reached the fracture level there (see Sect. 7.1.1).

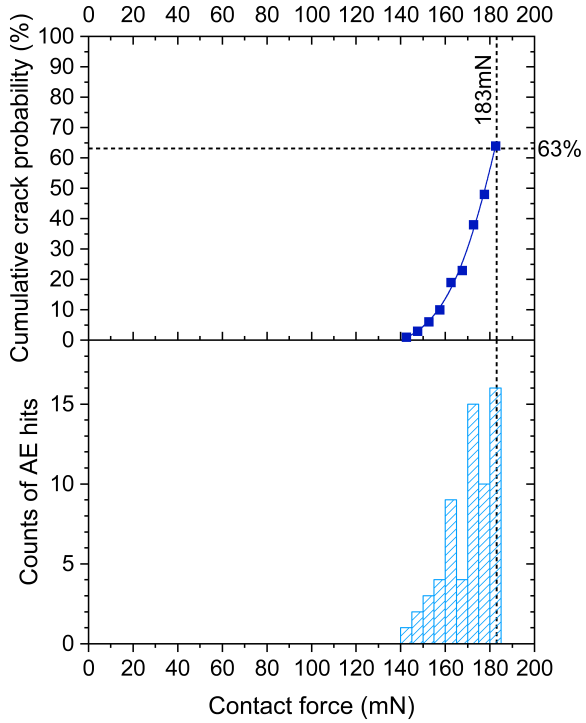

Fig. 7.13. 63% crack probability of test structure W01 for LC04; bin size: 5mN.

Subsequently to the experiments, crack inspections were performed using the SEM microscope and FIB-milling through the vertical cross-section of the imprints to correlate the results of FEM-simulation and AE measurements. Fig. 7.14 shows the SEM image in top-down view for an indent of load case LC04. Clearly visible is a circular dark imprint on the surface without any obvious crack in the layer. In order to find potential cracks below the surface, FIB cuts were made afterwards within the imprint area along the dashed line A - A.

In Fig. 7.15, the vertical cross-section view can be seen of the layer stack along A - A of Fig. 7.14. Exactly at the edge of the imprint small gaps (see red arrows) can be seen on both sides, from where cracks propagate from the bottom side further up into the oxide layer.

If the crack area is further enlarged, one can see in Fig. 7.16 that the crack starts exactly at the edge of the indenter imprint. The Si_3N_4 layer cannot be distinguished from the oxide layer in the SEM image because of the too low contrast. Nevertheless, it can be assumed that the crack starts from there, because the tension stress σ_r there is also at its maximum (see Fig. 7.8).

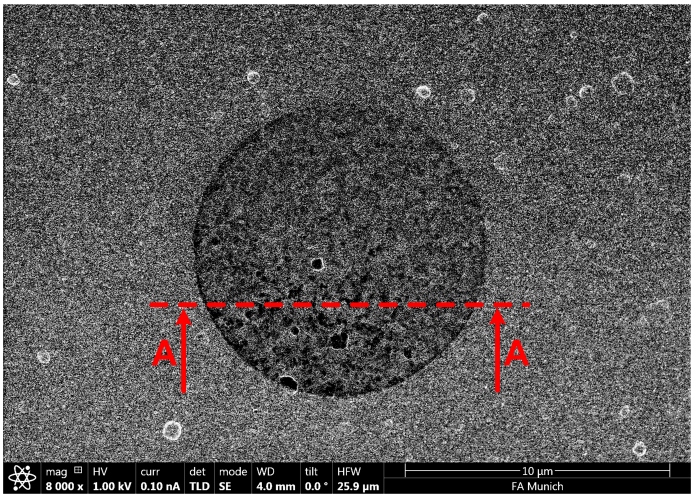

Fig. 7.14. Indenter imprint on sample W01 after contact force F_c = 185mN (load case LC04) in SEM top-down view.

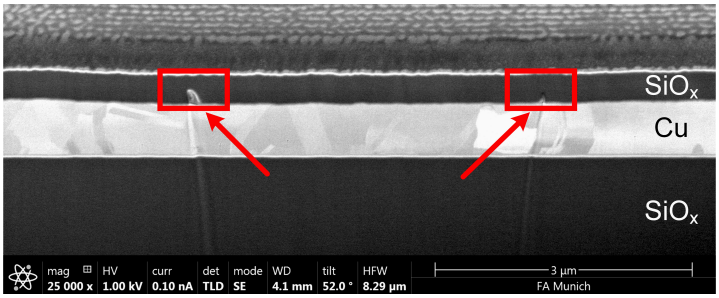

Fig. 7.15. Oxide cracks in test structure W01 for load case LC04 in cross-section view.

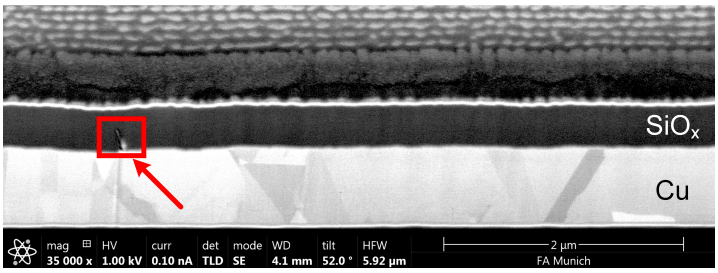

Fig. 7.16. Oxide crack in W01 for LC04 in detailed cross-section view.

b) Crack Generation at Maximum Contact Force of 350mN

In another experiment, test structure W01 was loaded 100 times using indenter FP10-M-3 at different points up to a contact force of 350mN (see Table 7.1, load case LC05). According to the results of the FEM-simulations a 100% crack probability with complete crack propagation from oxide layer bottom to top side is expected. In Fig. 7.17, left, the burst signal energy in logarithmic scale of all accumulated AE hits versus the contact force is shown.

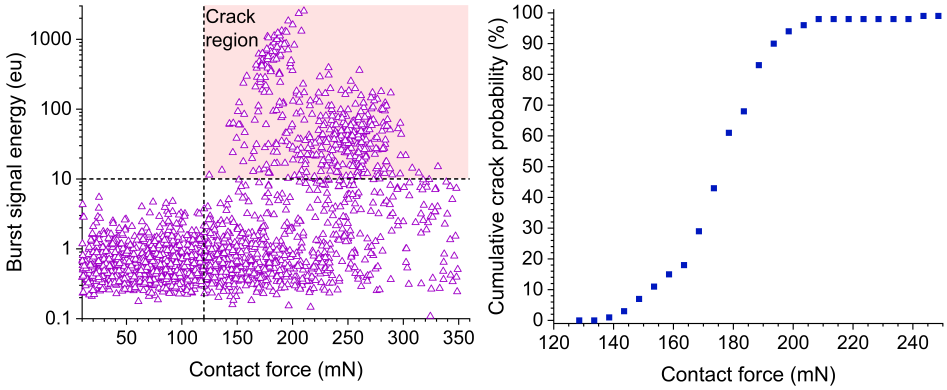

Fig. 7.17. Summarized burst signal energy of all hits (l.) and cumulative probability of 1st crack events (r.) as function of contact force for load case LC05; bin size: 5mN.

By filtering the hits with E_{burst} > 10eu and selecting only "first crack" events, one can again determine the cumulative crack probability over the contact force (Fig. 7.17, right). As expected, the crack probability increases steadily with increasing contact force reaching almost 100% at F_c = 240mN. The test structure was then again optically inspected for occurrence of cracks. Fig. 7.18 shows a SEM image in top-down view for load case LC05.

On the surface one can clearly see a circumferential open crack (blue dashed circle). The imprint area of the indenter tip has a slight smaller diameter (green dashed circle). The radius of the area with a circumferential crack is about 1µm higher than the radius of the inner imprint area. If one compares the difference Δr for both experiment and FEM-simulation (see point of maximum radial stress of blue curves in Fig. 7.10), the delta is 1.0µm - 1.5µm for both cases.

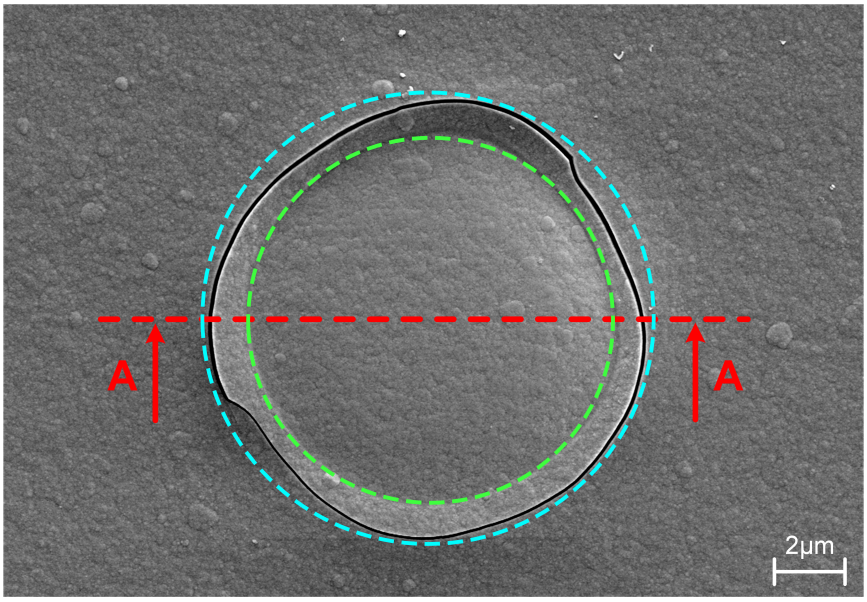

Fig. 7.18. Circular surface crack on test structure W01 after contact force F_c = 350mN (load case LC05) in SEM top-down view.

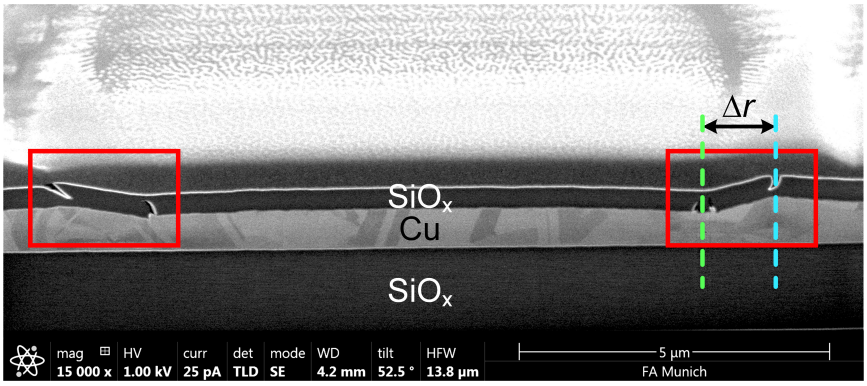

Fig. 7.19. Oxide cracks in sample W01 for load case LC05 in cross-section view.

After performing a FIB cut along line A - A (see Fig. 7.18), one can see in the cross-section view in Fig. 7.19 the two sided cracks (red circles) located on the lower and upper side of the oxide layer. The locations fit again very well with the stress plots from the simulation. In Fig. 7.20 the cracks are again shown on an enlarged scale. The distance Δr between the upper and lower cracks is again about 1.0µm.

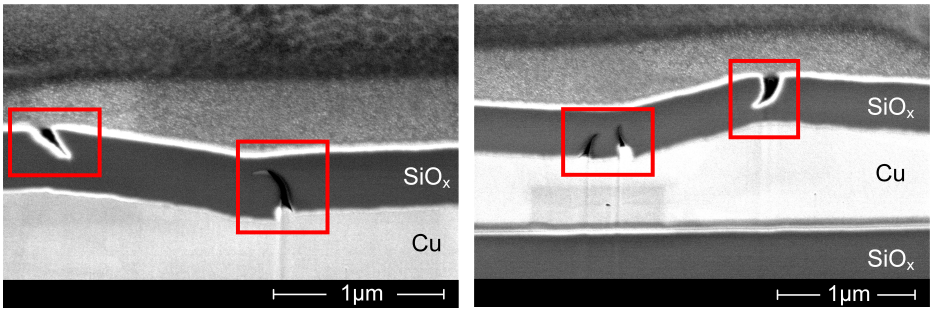

Fig. 7.20. Oxide cracks in sample W01 for load case LC05 in detailed cross-section view.

In summary, it is confirmed by AE test experiments and optical inspections, that the crack characteristics regarding formation and location correspond very well with the stress calculations from the FEM-simulation. Thus, cracks always start from the bottom side of a brittle oxide layer on top of a plastic deformable metal layer when loaded by a circular, flat-ended tip and only then emerge at the upper side of the oxide layer at higher loads. The lateral distance between the upper and lower cracks depends on the edge radius and the thickness of the layer. The AE test method has made a decisive contribution to the targeted generation and detection of cracks in multi-layer structures.

7.2 Crack Characterization on Unstructured Multi-Layer Devices

Having an understanding of the stress-induced generation and location of oxide cracks when loaded with a circular, flat-ended indenter tip, as described in Chap. 7.1, the influence of different test variables can be determined by means of the AE test method in various parameter studies. Again the experimental results were compared with the computer-simulated stress calculations. First, the influence of the tip diameter on the crack probability for two different test structures has been investigated and is presented here. Second, the impact of the thickness of the upper SiO_x and the Cu layer of the test structures W01 - W04 (see Table 6.1) on the crack probability has been revealed and is also presented in this chapter.

7.2.1 Variation of Indenter Tip Diameter

The aim of this evaluation was to acoustically determine the difference of the 63% crack probability and hence the increase of the characteristic contact force if doubling the tip diameter and to compare it with the simulation

results at an identical load. Irrespective of the tip diameter and the geometry of the test structure, an approximately equal maximum stress in the oxide layers should occur at a corresponding characteristic contact force. Two different test structures were used for the experiment.

Initially, AE measurements were performed for four different load cases (see Table 7.1, LC06 - LC09) each with 100 successive contact cycles. For test structures W01 and W04 (see Table 6.1), two flat tip indenters each with a diameter of 10µm (FP10-M-3) and 20µm (FP20-M-1) were used. Following the experiments, a statistical data analysis was carried out. The result of the cumulative crack probability as a function of the contact force is shown graphically in Fig. 7.21.

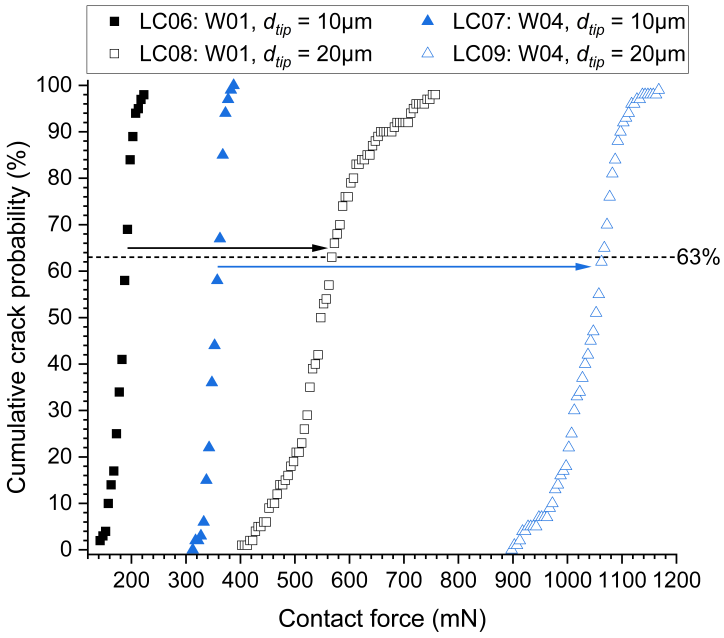

Fig. 7.21. Cumulative probability of 1st crack events for load cases LC06 - LC09 in linear scale as function of contact force; bin size: 5mN.

First, the result for test structure W01 (black rectangles in Fig. 7.21) are discussed. The crack probability for LC06 (d_{tip} = 10µm) within a range of the contact force of 140mN - 225mN increases from nearly 0% to almost 100%. Here, the value of the characteristic contact force at a 63% crack probability (see dashed horizontal line) is around 192mN. When doubling the diameter for load case LC08 (d_{tip} = 20µm), the position of the curve shifts to the right, whereby the characteristic contact force at a 63% crack probability rises

approximately by a factor of 3 to about 571mN. However, the variance of the contact force affecting the crack probability for load case LC08 is slightly larger than for LC06.

When considering the test structure W04 (blue triangles in Fig. 7.21), similar crack characteristics for respectively higher characteristic contact forces can be seen. For load case LC07 (d_{tip} = 10µm) the characteristic contact force is approx. 361mN. The variance of the critical force between 0% and 100% crack probability is here again relatively small. When using the indenter with a tip diameter of d_{tip} = 20µm (LC09), the characteristic contact force again triples up to about 1069mN compared to load case LC07.

Fig. 7.22 shows the results of the four measurements LC06 - LC09 in the *Weibull* scale. The fitted *Weibull* regression lines have a largely identical *Weibull* module *m* if indenting the same test structures with indenters of different tip diameters. Each regression line for the same test structure is offset in parallel by the value $\ln(\Delta F_o)$ = 1.1. If one calculates from these results the increase factor $f_{\Delta Fo}$ of the characteristic contact force F_o when doubling the diameter, again a factor of $f_{\Delta Fo} = e(\ln(\Delta F_o))$ = 3.0 is obtained.

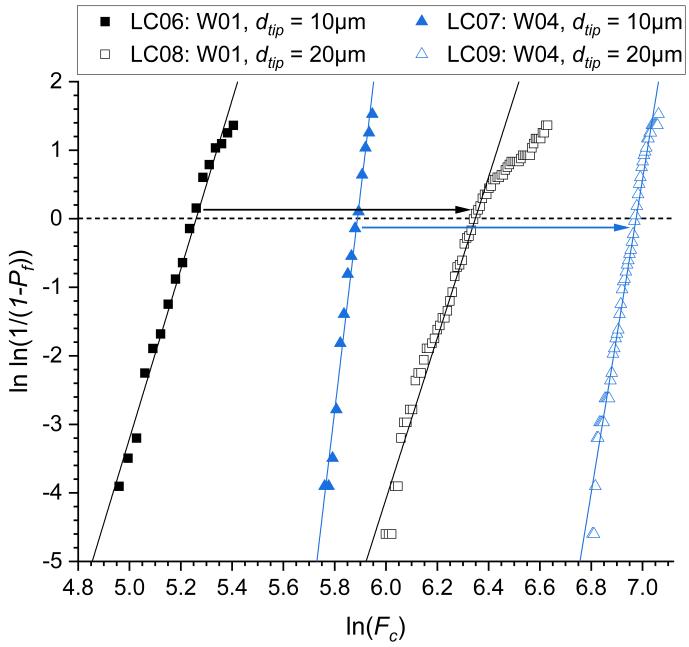

Fig. 7.22. Crack probability of 1st crack events for load cases LC06 - LC09 in *Weibull* scale as function of contact force; bin size: 5mN (regression line for LC08 fitted for $\ln(F_c) < 6.43$).

The experimental results are now compared with the FEM-simulations. The radial stresses $\sigma_r(r)$ were calculated using the approximated values of the characteristic contact forces at 63% crack probability from the previous experiments. In the following graphs the results are plotted as a function of the radial distance r from the rotation axis at r = 0 along the interface of the SiO_x top and bottom side and the Si_3N_4 layer for the test structures W01 and W04.

The radial stress curves along the top side of the SiO_x layer for load cases LC06 and LC07 for the tip diameter d_{tip} = 10µm and for LC08 and LC09 for d_{tip} = 20µm are shown graphically in Fig. 7.23.

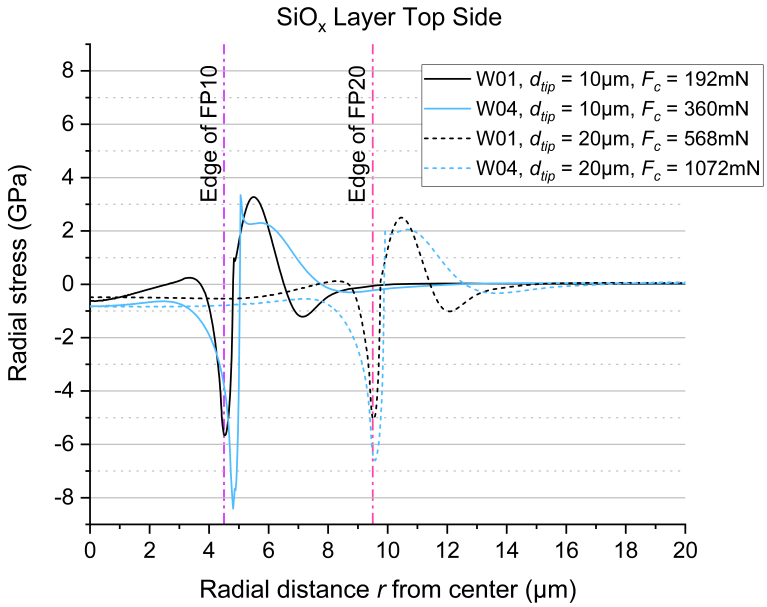

Fig. 7.23. Simulated radial stress in SiO_x layer top side for 63% crack probability for load cases LC06 - LC09.

The characteristic of the curves for all four load cases corresponds here again to the curve in Fig. 7.6. As expected, the radial stresses for both diameters at the edge of the indenter are respectively minimal (compressive stress) and outside the contact region reach a maximum (tensile stress) with largely the same absolutes values for all given characteristic forces.

A similar graph can be seen in Fig. 7.24 plotting the radial stresses of the four load cases at bottom side of the SiO_x layer.

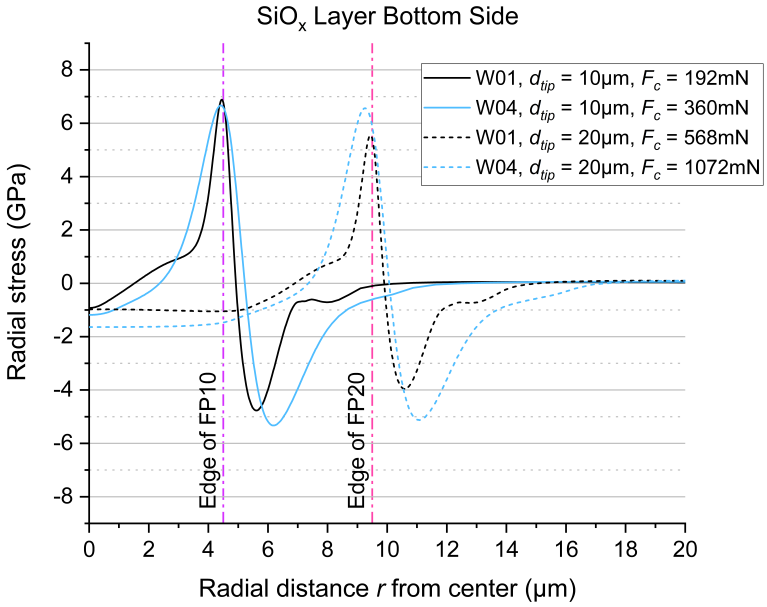

Fig. 7.24. Simulated radial stress in SiO_x layer bottom side for 63% crack probability for load cases LC06 - LC09.

The characteristics of the radial stress curves are similar here again compared to Fig. 7.7. Regardless of the tip diameter and the chosen structure, the maxima and minima of the stresses for the different forces in relative position to the indenter edge and magnitude are almost the same. The maximum tensile stress at the bottom side of the oxide layer for all shown load cases is about 6GPa ± 0.5GPa, if the layer stack is loaded with the corresponding characteristic contact force. Confirmed by the experiments, this value is obviously the critical fracture stress causing cracks in brittle oxide layers.

Finally, the same conclusion applies to the stresses in the Si_3N_4 layer, which are shown in Fig. 7.25. Also in this layer the extreme stress values and corresponding radial distances to the symmetry axis are almost identical.

In summary, based on the stress calculations from the FEM-simulation it can be confirmed that the experimental results of varying the diameter for a circular, flat-ended tip are correct. The statement "doubling the tip diameter from 10µm to 20µm reduces the characteristic contact force by a factor of 3" is valid for the shown load cases.

For all presented load cases, the maximum tensile stress on the bottom side of the oxide layer and within the Si_3N_4 layer is located at the same radial

distance r from the symmetry axis close to the indenter edge. The radial tensile stress reaches its maximum for a radial distance r from the rotational axis at a value of $0.5d_{tip}$ - 0.5µm. This is valid and independent of the tip diameter causing a radial stress value of 6GPa ± 0.5GPa. Based on these results, an indenter with a diameter d_{tip} = 10µm can be used as a standard to determine the characteristic contact force F_o and the *Weibull* modulus m, in order to specify the robustness with a 63% crack probability when indenting multi-layer structures with a circular, flat tip.

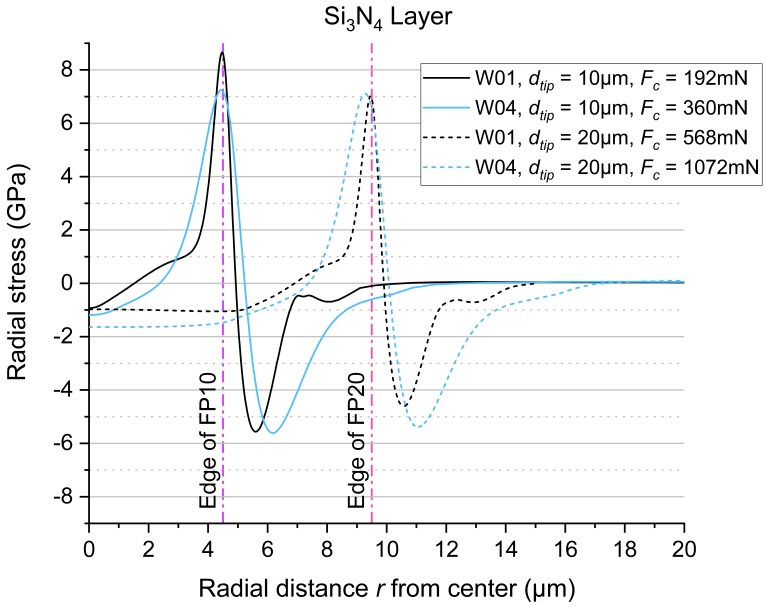

Fig. 7.25. Simulated radial stress in Si_3N_4 layer for 63% crack probability for load cases LC06 - LC09.

7.2.2 Variation of Layer Thickness

In this section, the layer thickness influence of various unstructured multi-layer structures was examined on the crack probability with the aid of the AE test method. To this, the robustness parameters F_o and m for the flat punch of 10µm diameter were determined. In the experimental parameter study, 100 subsequent contact cycles were done on each test structure W01 - W04 (see Sect. 6.1.1, Table 6.1), which differ in the thickness of the upper SiO_x layer of 380nm and 1000nm in combination with the thickness of the Cu layer of 400nm and 700nm.

To achieve approx. 100% crack probability, the test structures with an oxide layer thickness of 380nm (W01 and W03) were stressed using the indenter FP10-M-3 up to a maximal contact force of 260mN. The ones with an oxide layer thickness of 1000nm (W02 and W04) are expected to have a higher robustness and thus were stressed up to a maximal contact force of 410mN. In Fig. 7.26 the data of the cumulative crack probability for all four variants are shown in linear scale as a function of the contact force.

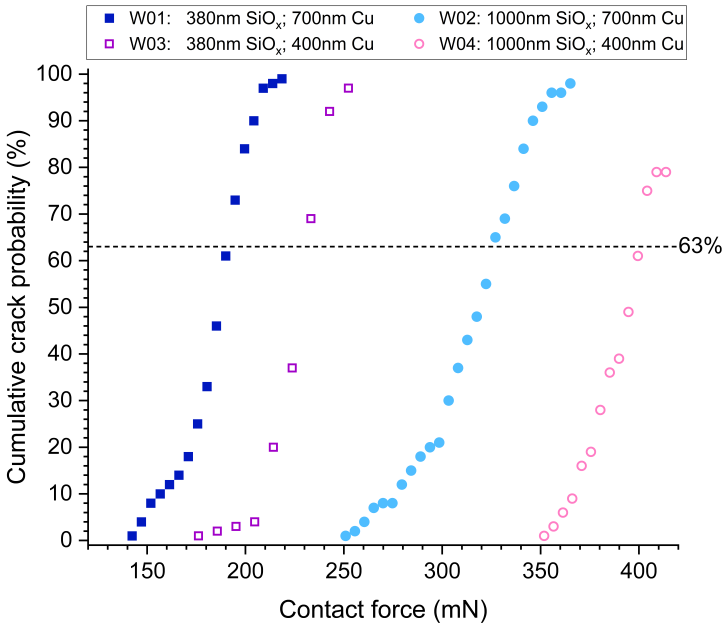

Fig. 7.26. Cumulative probability of 1st crack events of 100 indents on test samples W01 - W04 in linear scale as function of contact force; bin size: 5mN.

In order to derive the robustness parameters graphically, the data are plotted in *Weibull* scale with linear fitting curves, shown in Fig. 7.27. By graphical determination of the intersection point with the *y*-axis and the slope of the regression lines, the robustness parameters can be derived for each test structure. For an indenter of 10µm diameter, the characteristic contact force $F_{0,FP10}$ at a 63% crack probability and the corresponding *Weibull* modulus *m* are given in Table 7.3 including the standard error.

It can be seen from the results, that an increase in the oxide thickness significantly increases the resistance to cracks in the oxide and hence reduces the crack probability. At the same time, the robustness increases with the reduction of the Cu layer thickness underneath the uppermost oxide layer.

While the positive influence on robustness of the oxide thickness can be explained by a larger stiffness of the layer, the decrease in robustness in the case of a thicker Cu layer is not directly obvious. A possible explanation for this is the larger plastic deformation of a thicker Cu layer during contacting, which in turn increases the vertical deflection and so the mechanical bending stress of the overlying oxide layer at the same load.

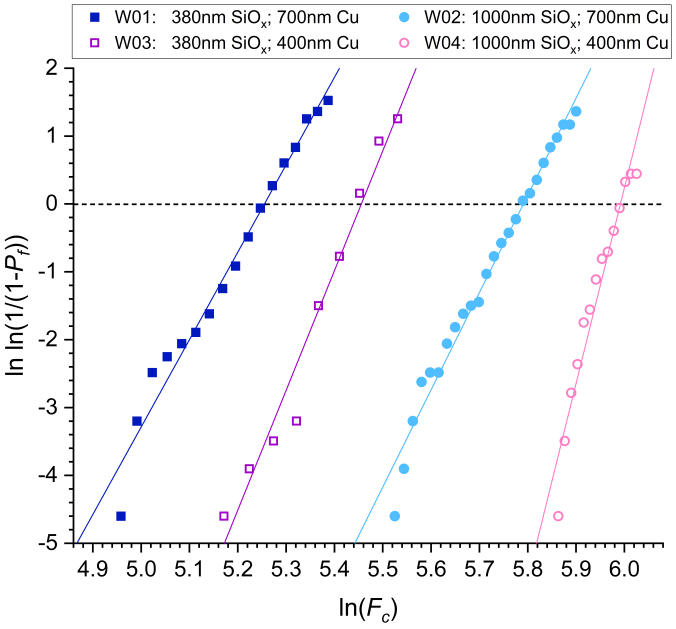

Fig. 7.27. Cumulative probability of 1st crack events of 100 indents on test samples W01 - W04 in *Weibull* scale as function of contact force; bin size: 5mN.

Table 7.3. *Weibull* modulus *m* and characteristic contact force $F_{o,FP10}$ for structures W01 - W04.

Test structure	**W01**	**W02**	**W03**	**W04**
m	12.88 ± 0.52	14.33 ± 0.41	17.64 ± 1.15	28.82 ± 1.98
$F_{o,FP10}$ (mN)	191.5 ± 1.0	327.4 ± 1.0	234.1 ± 1.0	400.1 ± 1.0

The slope of the regression lines (i.e. *Weibull* module *m*) is highest for test structure W04, followed by test structure W03 (see Table 7.3). In general, a higher *m* is better regarding accuracy and risk of crack generation during contacting of brittle layer stacks. Here, the variance of the observed "first crack" events as a function of contact force is lower for a layer stack with a

thinner Cu layer. The variance is also positively influenced by a larger thickness of the SiO_x layer in comparison of test structure W01 with W02 and W03 with W04, respectively.

The results presented in Sect. 7.2.2 are relevant to the robustness when probing semiconductor layers on wafer level and will be applied in the future to optimize the design of BEOL stacks of structured chips against cracks. In the next chapter, investigations on processed chips will be presented using AE tests to demonstrate the application of the method.

7.3 Crack Risk Assessment on 40nm CMOS Chip

The efficiency of the AE test method was verified on a 40nm CMOS technology chip with Cu metallization and oxide crack-sensitive layer structures. The target of the investigation was to determine the crack probability of the oxide layer during indentation on three different BEOL stack layouts and thereby revealing the influence of the layer structuring of the metal routing below the pad.

Similar to Sect. 6.3.3, also here the indenting was first performed directly on top of the upper oxide layer and afterwards on top of the Cu-pads. For both cases the crack probability was determined and additionally verified with optical failure analysis methods. In the last section of this chapter a comparison of the crack probability when contacting the Cu-pad or the SiO_x surface is given.

For the following indenter experiments the monolithic indenter FP10-M-3 with a tip diameter of 10µm was used. The sample size of the measurements was kept relatively small, due to the sometimes inaccurate positioning of the *xy*-stage of the *PROFIT* test bench, causing time-consuming experiments.

7.3.1 Back-End-Of-Line Stack Layout and Metal Routing below Pads

Fig. 7.28 shows a schematic view of the investigated BEOL stack of the upper conductive and isolating layers based on 40nm CMOS Cu-technology. The contact pads are placed on top of the active circuitry area and hence the chip design is a POAA configuration. The top Cu-layer dimension has a thickness of 3300nm ± 360nm with a thin (<100nm) adhesive layer ("liner") underneath. The next underlying insulating layer is the oxide TEOS with a thickness of 580nm, which is most sensitive to cracks during probing. Below this layer follows a diffusion barrier with a thickness of

100nm processed in silicon carbon nitride (SiCN). In total, there are seven Cu metal layers in the BEOL stack. The IMD between metal layer M7 and M5 is made of FTEOS (***F***luorinated ***T***etra***e***thyl ***O***rtho***s***ilicate) and the other ones between M5 and M1 are processed in a low-k material. The design of the metal routing below the pad is different for various pad locations. In total, the chip has 478 pads and a chip size of ca. 8mm x 8mm. The chips were processed on 300mm wafers. Before the experiments, the wafer was diced into grouped samples of 3 x 3 dies each, i.e. 24mm x 24mm in size.

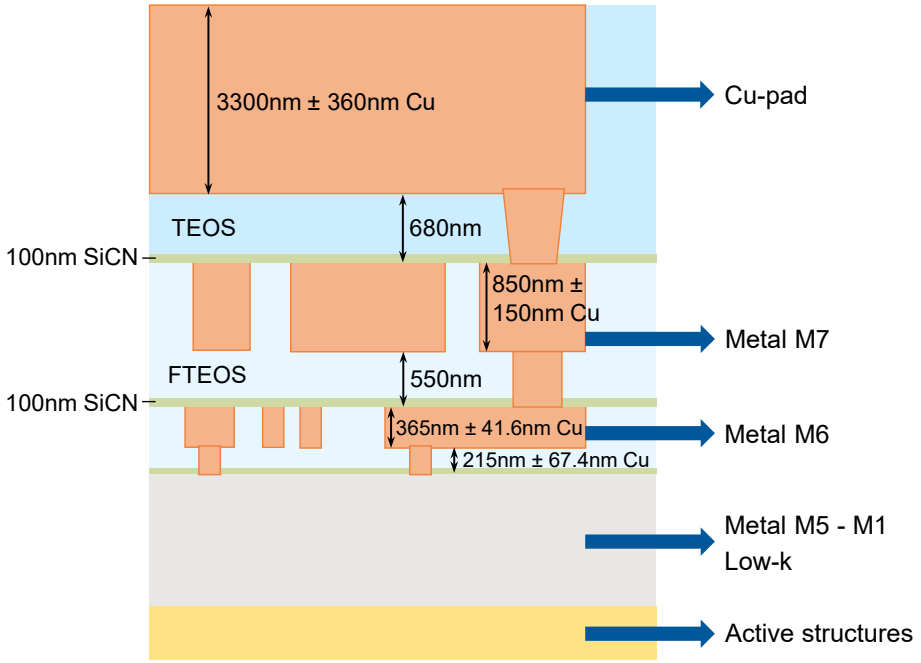

Fig. 7.28. Schematic layer stack of POAA Cu based 40nm CMOS technology.

For the AE crack tests, one pad at the east side (Pad 127) and two pads at the west side (Pad 383 and Pad 453) of the chip were selected. The location of the pads can be obtained from the chip layout attached in the Appendix. All three pad types have a passivation opening of 60µm x 75µm. For the crack experiments, only the layers below the Cu-pad until metal layer M6 (see Fig. 7.28) are considered, as the IMD crack generation during probing is mostly relevant within these layers, in contrast to deeper layers from M1 until M5. The thicknesses of the metal layers are indicated in Fig. 7.28 with values of 850nm ± 150nm for M7 and 365nm ± 41.6nm for M6.

The top view of the pad layout in Fig. 7.29 shows the routing of the metal layers M7 and M6 of the selected pad variants. The Cu structures are colored in green for M7 and in blue for M6. For both layers, the red color refers to the fill structures made of Cu. The black color represents the oxide (TEOS).

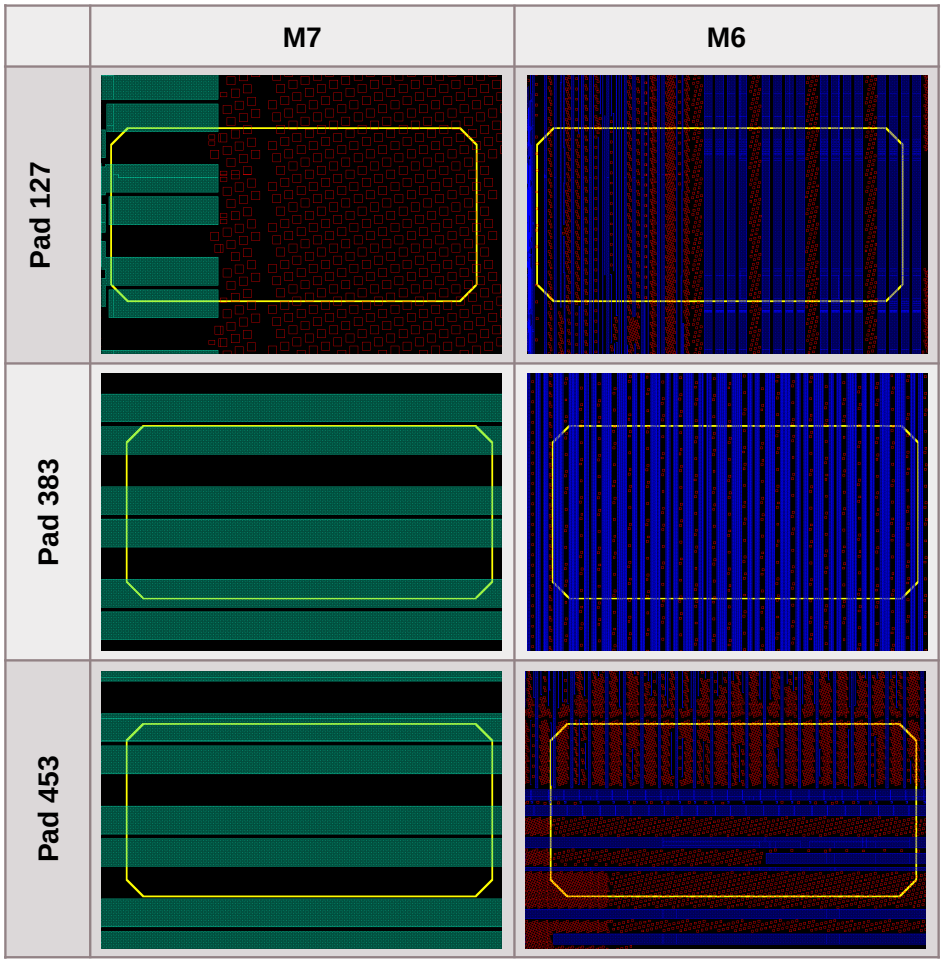

Fig. 7.29. Layer structure of M7 and M6 of selected pads (oxide structures: black, Cu fill structures: red, further Cu structures: green for M7 and blue for M6).

The metal layer M7 of Pad 127 (see Fig. 7.29, top row) is composed of longitudinal Cu stripes (green) on its left side and Cu fill structures (red) in the remaining area. Vertical Cu stripes (blue), which are separated by fill structures (red), show routing of metal layer M6.

In contrast to Pad 127, the structure of M7 for Pad 383 and Pad 453 (see Fig. 7.29, center and bottom row) is nearly the same with both having longitudinal Cu stripes (green) from left to right side. The routing of the two pads is significantly different in metal layer M6. While Pad 383 includes only vertical Cu stripes (blue), Pad 453 has some in vertical and also longitudinal direction. Furthermore, Pad 453 contains a higher amount of Cu fill structures (red) than Pad 383.

7.3.2 Crack Assessment for Indentation on Oxide Surface

In the first experiment, the pads were directly contacted on the SiO_x surface after removal of the Cu metallization including the liner by a wet-chemical etching process.

a) Determination of Crack Probability by AE Test Method

Using the indenter FP10-M-3 a total of 73 pads of different metal routing designs was stressed up to a maximal contact force of 400mN to reach approx. 100% crack probability. Three pad variants have been contacted, 27 pads of variant 127, 25 pads of variant 383, and 21 pads of variant 453.

In Fig. 7.30, the burst signal energy of all measured acoustic hits in logarithmic scale as a function of the contact force is shown separately for each pad layout variant.

For pads of variant 127 (see Fig. 7.30, top) using the filter criterion $E_{burst} > 10$eu is suitable to identify those hits of "first crack" events. For pads of variant 383 and 453 (see Fig. 7.30, centre and bottom) multiple hits with burst signal energies up to approx. 40eu occurred at contact forces below 100mN. This is probably caused by the larger Cu-metal routing area in M7 compared to the pad layout of variant 127 (see Fig. 7.29). To identify the "first crack" events in case of pads of variant 383 and 453, filter criteria for burst signal energy $E_{burst} > 10$eu and an additional for contact force $F_c > 100$mN were applied.

By filtering the hits on "first crack" events, one can again determine the cumulative crack probability as a function of the contact force, which is shown in Fig. 7.31 in linear (top) and *Weibull* (bottom) scale. As expected, the crack probability increases steadily with increasing contact force for all pad variants.

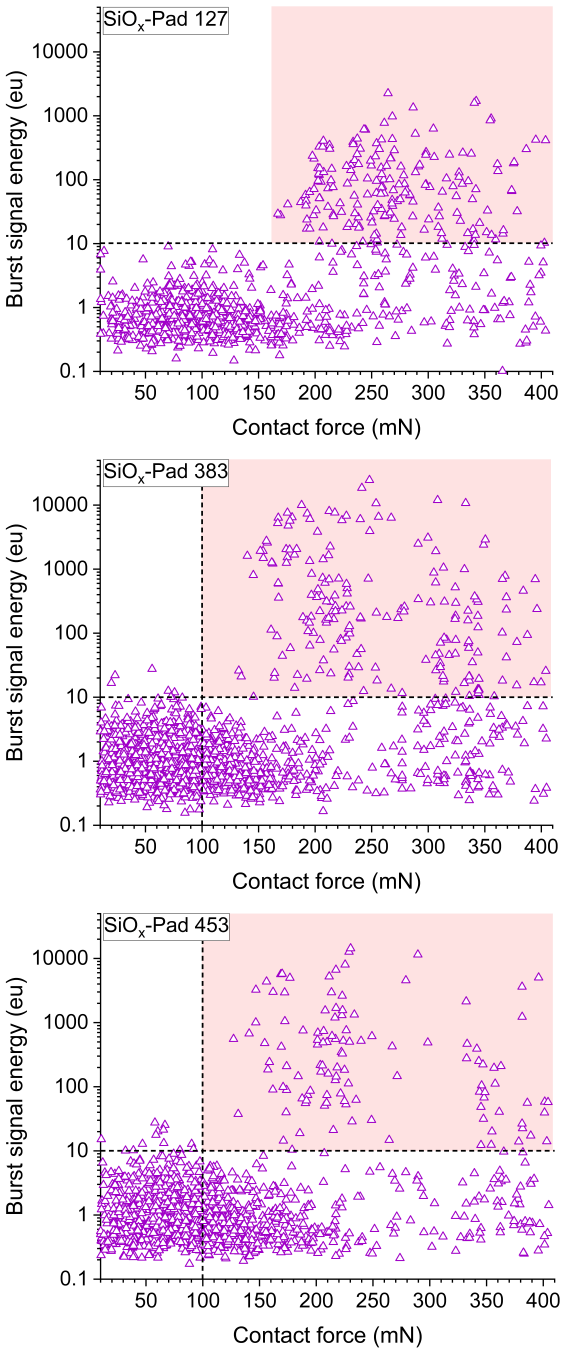

Fig. 7.30. Determination of filter criteria for 1st crack events for pad variants 127 (top), 383 (center), and 453 (bottom) when indenting on the SiO_x surface.

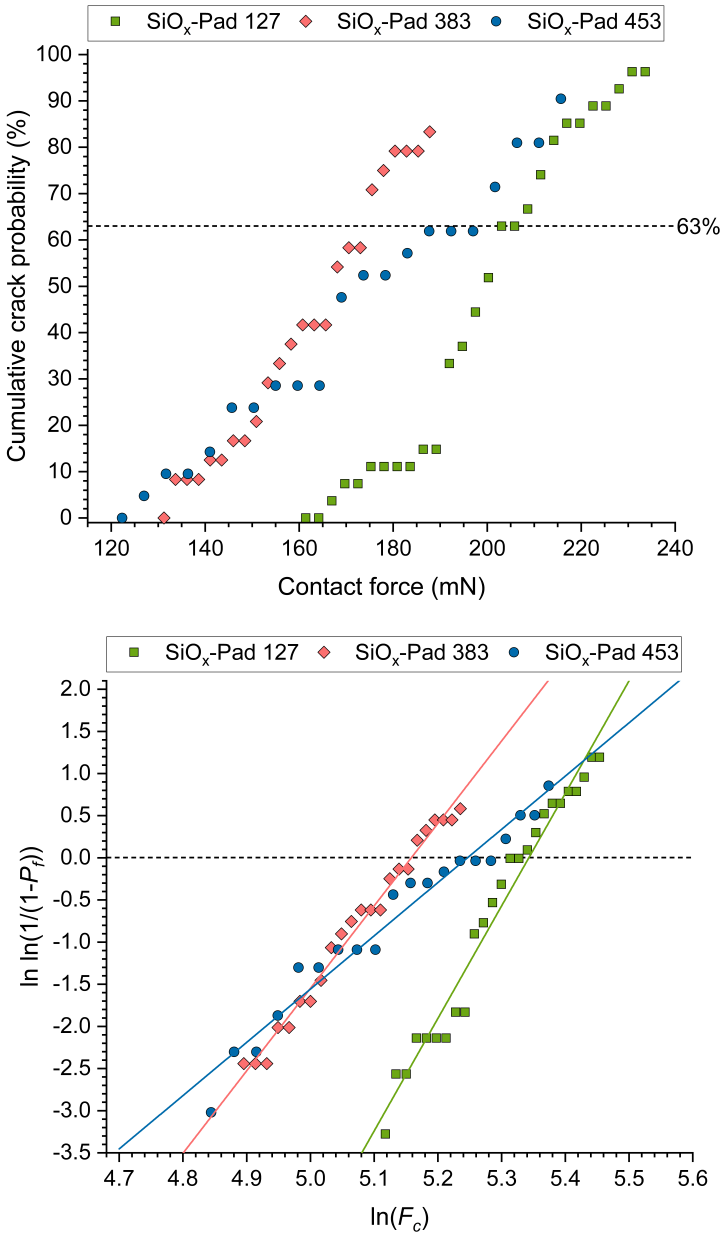

Fig. 7.31. Comparison of crack probability in linear (top) and *Weibull* scale (bottom) for contacting the SiO_x surface of pad variants 127 (27 indents), 383 (25 indents), and 453 (21 indents); bin size = no. of indents per pad variant.

Derived from the *Weibull* plot, the characteristic contact force $F_{o,FP10}$ at a crack probability of 63% is 173.9mN for pad variant 383, 189.9mN for pad

variant 453, and 209.1mN for pad variant 127. All values are listed in Table 7.4, including the statistical error relative to the linear equation of the regression line. The pad variant 383 shows the highest crack risk (lowest characteristic contact force), while the lowest risk (highest characteristic contact force) is given for variant 127. When comparing the metal routing in M7 of the pad variants 127 and 383 (see Fig. 7.29), one can see that variant 127 uses Cu fill structures instead of Cu stripes. Furthermore, clear differences are visible in the routing design of M6. Comparing the regression lines of pad variants 383 and 453 in Fig. 7.31 indicates that the Cu-routing in M6 also has a significant impact on the mechanical robustness of the stack. As mentioned above, the routing of M6 of pad variant 453 uses a higher amount of Cu fill structures instead of evenly arranged Cu stripes.

The *Weibull* moduli *m* listed in Table 7.4 were also derived from the *Weibull* plot in Fig. 7.31. It is highest for pad variant 127 with a value of 13.35 and lowest for pad variant 453 with a value of 5.246, which is small compared to the previous experiments presented in Chap. 6.3 and 7.2.2. This is most likely caused by the uneven metal routing below the pads (see Fig. 7.29), causing a larger scattering for a small sample size, which was used here.

Table 7.4. Indents on SiO_x surface: *Weibull* modulus *m* and characteristic contact force $F_{0,FP10}$.

Pad ID	**SiO_x-Pad 127**	**SiO_x-Pad 383**	**SiO_x-Pad 453**
m	13.35 ± 0.49	9.78 ± 0.26	5.246 ± 0.01
$F_{0,FP10}$ (mN)	209.1 ± 1.0	173.9 ± 1.0	189.9 ± 1.0

As a conclusion one can say, that the crack probability increases if using Cu stripes compared to Cu fill structures for metal routing. Furthermore, one can state a generic design rule to keep the routing area density of the metal layer below the top oxide layer as small as possible, in order to minimize the crack probability.

b) Crack Correlation for AE Test Method and Optical Inspection

In order to validate the accuracy of the AE test method applied on structured test samples, indentations were performed to reach a controlled crack probability of approx. 50% up to 70%. During this experiment 17 pads of variant 127 were stressed up to a maximal contact force of 195mN and 18 pads of variant 383 up to a force of 165mN using the indenter FP10-M-3. After indentation, the samples were inspected for oxide cracks using the

DIC method. Ideally, the number of cracks determined by the AE test method should be exactly the same as the number of cracks detected by optical inspection for a given sample size.

In Fig. 7.32 one contact cycle without (top) and one with (bottom) an oxide crack, exemplary for pad variant 383, is shown. The graph on the left shows no acoustic hit of an oxide crack, but in the right graph one can see an acoustic crack event with peak amplitude of 61.5dB$_{AE}$, which was detected during contacting at a contact force of approx. 147mN. The associated optical images of the indents are depicted in Fig. 7.33. Here, too, the results of the optical crack inspection correlate well with the acoustic ones.

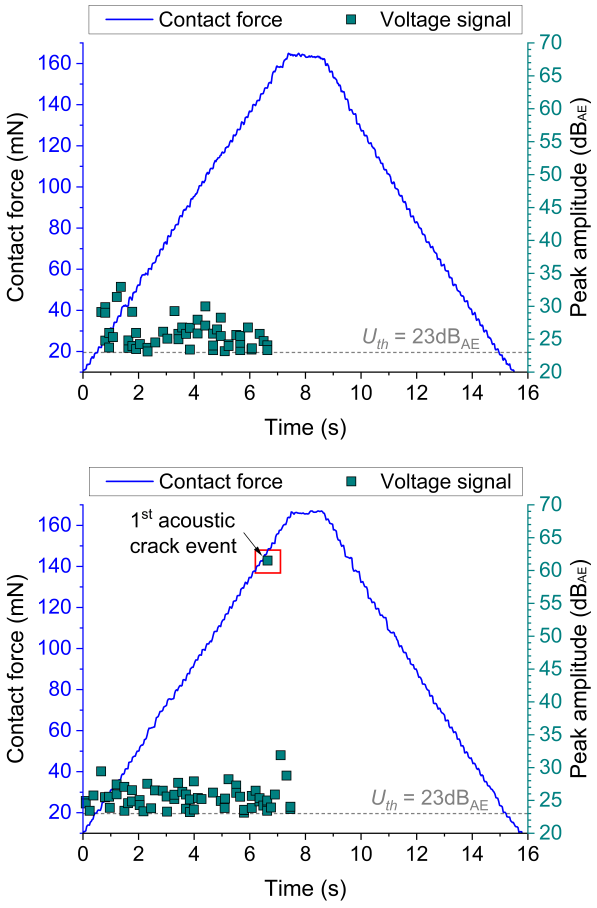

Fig. 7.32. Contact cycle on the SiO_x surface of pads of variant 383 without (top) and with (bottom) an acoustic crack event.

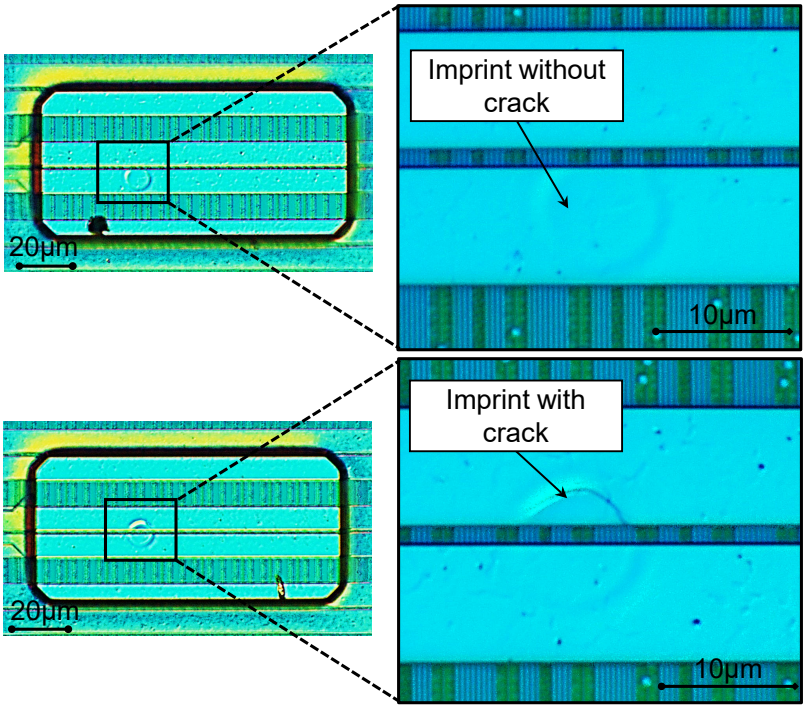

Fig. 7.33. Imprints on pads of variant 383 after contacting the SiO_x surface without (top) and with (bottom) oxide crack.

In Table 7.5 the correlation results of the acoustic and optical crack inspection are summarized for all indented pads.

Table 7.5. Indents on SiO_x surface: AE test method vs. optical inspection.

No. of detected cracks	**Pad 127**		**Pad 383**	
	crack	no crack	crack	no crack
AE test method	12	5	16	2
Optical method	10	7	16	2
Delta Δ of detected cracks	2		0	

On all inspected pads of variant 127 with optically detected cracks also acoustic crack events were measured during contacting, but two additional acoustic crack events were measured without finding any optical crack (12 AE crack events compared to 10 optical cracks). This is probably caused by the inaccuracy of the optical crack inspection method for pad layouts

with metal fill structures, which are present here in the routing design in layer M7 (see Fig. 7.29).

For all 18 pads of variant 383 a 100% correlation between the acoustic and optical oxide crack detection method was reached, proving a good correlation of the AE test method with the optical crack inspection.

7.3.3 Crack Assessment for Indentation on Cu-Pad

In the following experiments, the AE crack test was performed on top of the Cu-pads, which would be the standard contact method during operational wafer test in case of Cu-metallization. Here, too, the pad variants with highest (Pad 383) and lowest (Pad 127) SiO_x crack probability were analyzed.

a) Determination of Crack Probability by AE Test Method

During this crack experiment, 38 pads each for variant 127 and 383 were contacted. First, six pads of variant 127 were contacted up to a maximal contact force of 250mN. While here no acoustic crack events could be detected, the maximal force was increased up to 300mN for additional 17 pads and finally up to 350mN for the remaining 15 pads until a crack probability of at least 50% was reached. For pads of variant 383 a maximal contact force of 250mN was selected, which proved to be sufficient to achieve a crack probability higher than 50%.

To derive the filter criteria for the "first acoustic crack" events, the burst signal energy of all measured acoustic hits was again plotted in logarithmic scale over the contact force. On top of Fig. 7.34 the accumulated AE hits for 15 contact cycles on pad variant 127, which were stressed by a maximal contact force of 350mN, are shown. All AE hits from 38 contact cycles on pad variant 383 are shown on bottom of Fig. 7.34. For both pad variants the filter criteria for $E_{burst} > 10$eu and $F_c > 150$mN were appropriate to select only the hits of "first crack" events. In Fig. 7.34, the high amount of occurred hits at forces below 150mN is mainly caused by the plastic deformation of the Cu-pad and further underlying Cu layers in M7 and M6.

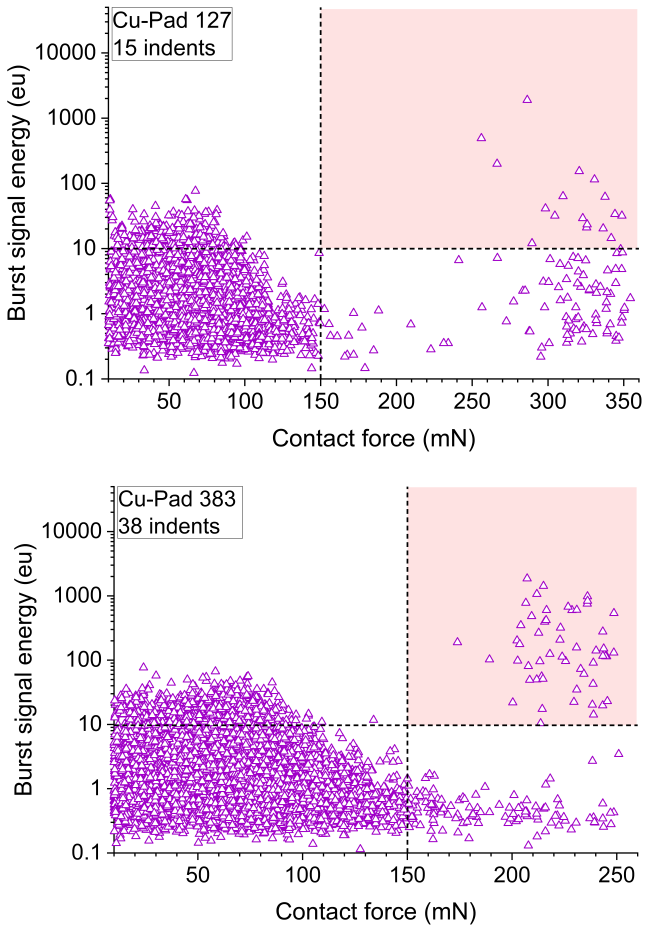

Fig. 7.34. Determination of filter criteria for 1st crack events for pad variants 127 (top) and 383 (bottom) when indenting on the Cu-pad.

Subsequently, the cumulative crack probability as a function of the contact force was determined. On the left side of Fig. 7.35 the graphs are shown in linear scale and on its right side in *Weibull* scale.

Like the results when indenting on the SiO_x surface, also during contacting the Cu-pad of variant 383, the results show a higher crack probability, i.e. a lower mechanical robustness, compared to pads of variant 127. The characteristic contact force $F_{o,FP10}$ at a crack probability of 63% is 228.3mN for pads of variant 383 and 346.9mN for pads of variant 127. Furthermore, the *Weibull* moduli *m* were derived by the *Weibull* plot in Fig. 7.35 with values of 17.43 for pads of variant 127 and 14.11 for pads of variant 383. In Table 7.6 all robustness parameters inclusive the statistical error are summarized.

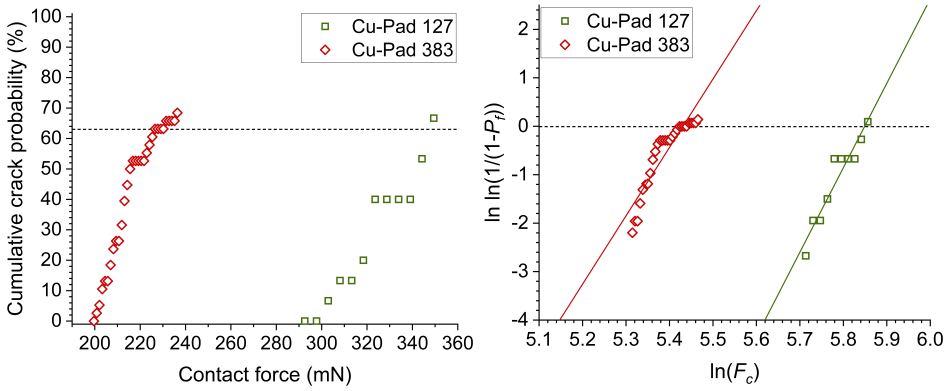

Fig. 7.35. Comparison of crack probability in linear (l.) and *Weibull* scale (r.) for contacting the Cu-pad of variants 127 (15 indents) and 453 (38 indents); bin size = no. of indents per pad variant.

Table 7.6. Indents on Cu-pad: *Weibull* modulus *m* and characteristic contact force $F_{o,FP10}$.

Pad ID	**Cu-Pad 127**	**Cu-Pad 383**
m	17.43 ± 1.90	14.11 ± 1.19
$F_{o,FP10}$ (mN)	346.9 ± 1.0	228.3 ± 1.0

The characteristic contact forces at 63% crack probability and also the *Weibull* moduli are higher when contacting the Cu-pad instead of the SiO_x surface (see Table 7.4), which is discussed in more detail in Sect. 7.3.4.

b) Crack Correlation for AE Test Method and Optical Inspection

After AE testing, the test samples were treated by Cu-pad delayering and inspected for IMD cracks using conventional and DIC microscopy again to evaluate the accuracy of the AE test method. Partly also cross-sectioning failure analysis techniques (FIB) were applied.

At first, the time-dependent contact force graphs and AE test results are presented. In Fig. 7.36 graphical results of two single contact cycles are shown, which were made during the previous described experiment on pad variant 383. In contrast to the contact cycle on top with no acoustic crack event, some crack events were detected during the contact cycle shown on the bottom. Moreover, similar to the indentation on the unstructured Al-Cu layer, which was detailed described in Sect. 6.3.3, one can see that

the contact force has a nonlinear gradient during the loading phase up to a value of approx. 200mN.

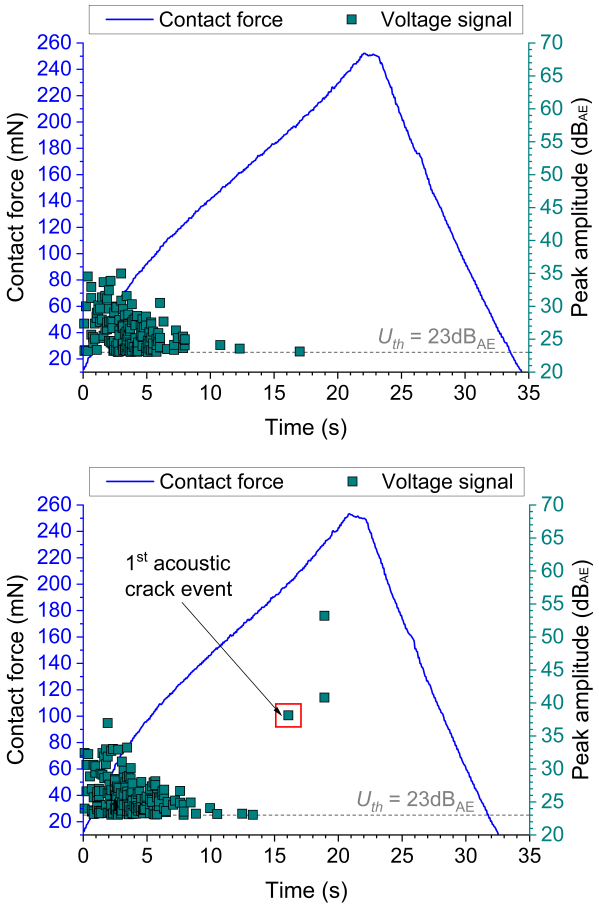

Fig. 7.36. Contact cycle on top of Cu-pads of type 383 without (top) and with (bottom) acoustic crack events.

Within a force range up to 150mN a certain amount of AE hits with decreasing amplitude can be observed. As already mentioned, these hits are mainly caused by the plastic deformation of the Cu-pad and are decreasing in number with increasing contact force due to the saturation of the penetration depth into the Cu-pad.

After contacting the pads, optical microscope images were taken in order to check the correct position of the imprint (Fig. 7.37, left top and bottom). Afterwards the Cu-pad and liner were wet-chemically removed and

thereby, if possible, the cracks were chemically decorated as well. If no crack was inspected using conventional optical microscopy, additionally the DIC method was applied. The optical analysis results of the imprints of Fig. 7.37 prove a good correlation between the acoustic and optical crack inspection.

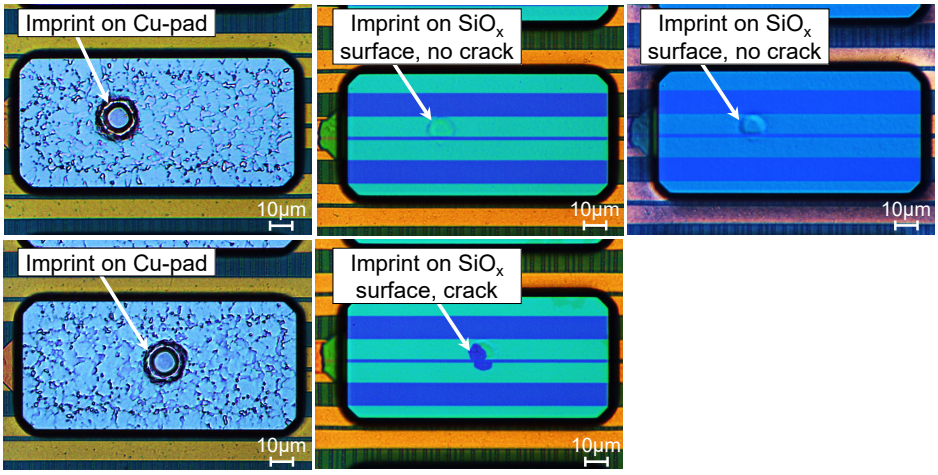

Fig. 7.37. Optical imprint and crack inspection after contacting Cu-pads of variant 383 without (top) and with (bottom) oxide cracks.

It was demonstrated, that cracks in the upper SiO_x layer are occurring before the indenter tip has fully penetrated the Cu-pad metallization during contacting. In this experiment, the Cu-pad metal has a remaining thickness of approx. 1µm. The FIB-milled cross-section image in Fig. 7.38 shows an example to this for an imprint on pad variant 383.

The correlation results of the acoustic and optical crack assessment are summarized for all 38 stressed pads of variant 127 and 383 in Table 7.7. As mentioned in Sect. 7.3.2, for pads of variant 127 it was more difficult to find the oxide imprints by optical inspection compared to cracks below pads of variant 383. This could be the reason for the higher amount of cracks detected by AE test method (18 indents with cracks) compared to the number of detected cracks by DIC method (15 indents with cracks). In contrast, for pads of variant 383 all detected cracks, which were measured by the AE test method, were also seen after optical inspection.

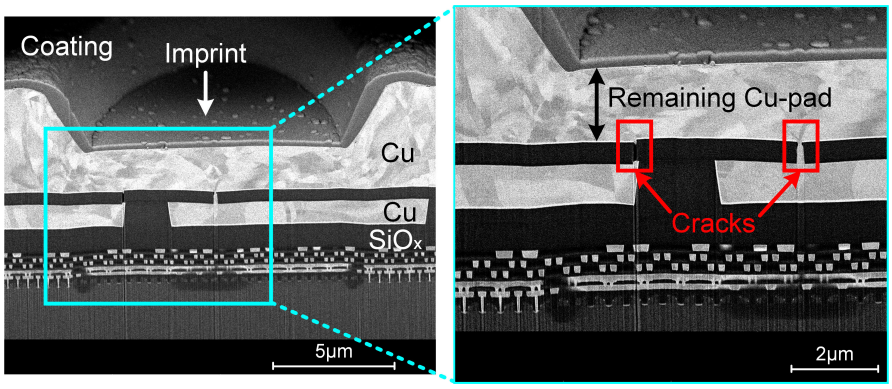

Fig. 7.38. FIB-milled SEM cross-section image after indentation on Cu-pad variant 383 revealing oxide cracks despite a remaining Cu-pad thickness of about 1µm.

Table 7.7. Indents on Cu-pad: AE test method vs. optical inspection.

No. of detected cracks	**Pad 127**		**Pad 383**	
	crack	no crack	crack	no crack
AE test method	18	20	31	7
Optical method	15	23	31	7
Delta Δ of detected cracks	3		0	

In general, one can conclude, that crack events in the upper SiO_x layer after contacting on Cu-pads are accurately detectable using the AE test method with a high correlation rate relative to optical crack inspection methods, such as conventional microscopy, DIC method, and FIB-milled SEM cross-section images.

7.3.4 Comparison of Crack Probability for Oxide and Cu-Pad

Finally, a comparison of the crack probability examined by AE test method for pads of variant 127 and 383 when contacting the SiO_x surface and Cu-pad is given in Fig. 7.39. The respective data and curves were transposed from Fig. 7.31 and Fig. 7.35.

As one can see, the crack robustness is higher when directly contacting the Cu-pad compared to the free SiO_x surface. For pads of variant 383 the characteristic contact force $F_{o,FP10}$ is thereby increased by 54.4mN and that one for pad variant 127 even by 137.8mN. The graphically derived *Weibull* moduli *m* are also increased for both pad types by more than 4 for indenting the

Cu-pad instead of the SiO_x surface, i.e. the data points scatter less. Table 7.8 lists these values inclusively their standard error.

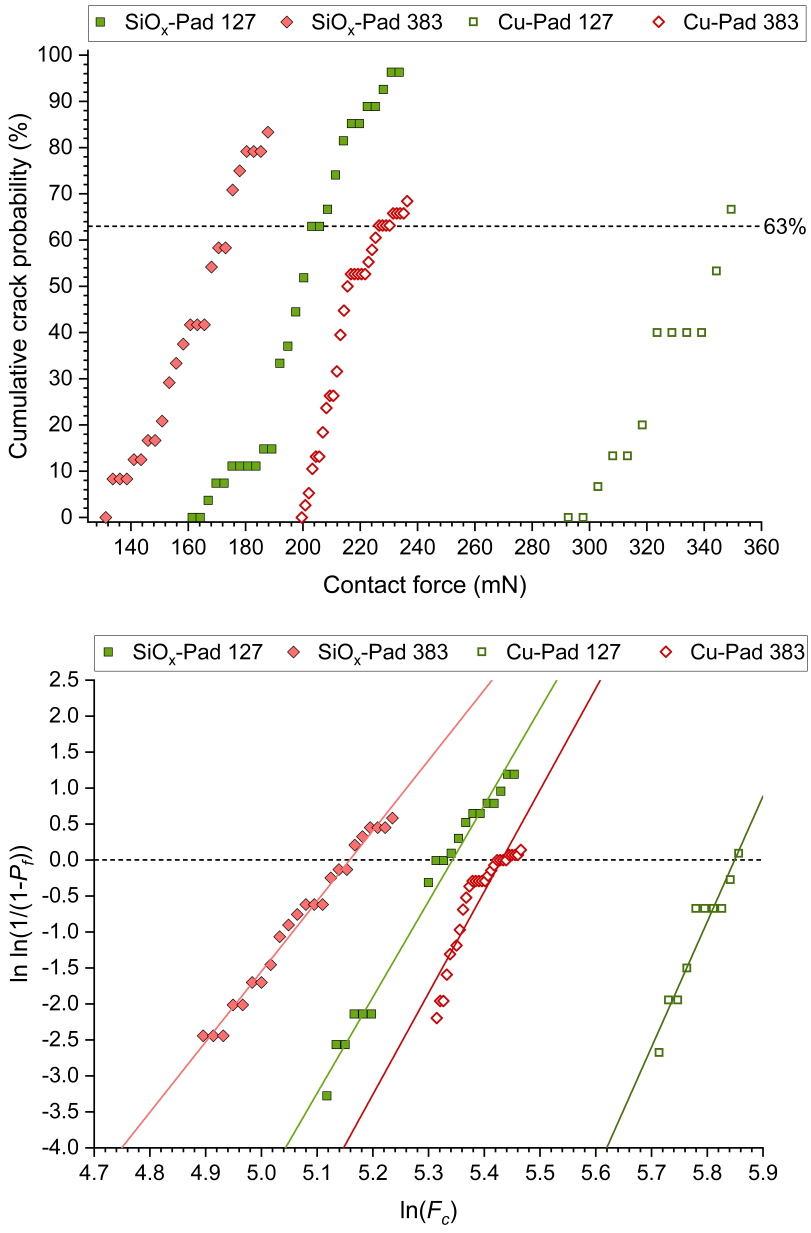

Fig. 7.39. Comparison of crack probability when indenting the SiO_x surface and Cu-pad of pad variants 127 and 383; bin size = no. of indents per pad variant.

Table 7.8. Comparison of SiO_x surface vs. Cu-pad indentation.

Pad ID	m	Δm	$F_{o,FP10}$ **(mN)**	ΔF_{FP10} **(mN)**
SiO_x-Pad 127	13.35 ± 0.49	4.08 ± 2.39	209.1 ± 1.0	137.8 ± 2.0
Cu-Pad 127	17.43 ± 1.90		346.9 ± 1.0	
SiO_x-Pad 383	9.78 ± 0.26	4.33 ± 1.45	173.9 ± 1.0	54.4 ± 2.0
Cu-Pad 383	14.11 ± 1.19		228.3 ± 1.0	

The observations of the experiments in Chap. 7.3 proved, that the design of the metal routing as well as the material of the uppermost layer, which is contacted, have a significant impact on the crack probability, i.e. the mechanical robustness of the BEOL stack against oxide cracks. It has been shown, that the crack probability is lower, when using Cu fill structures instead of Cu stripes in M7 and M6 and keeping the routing density of Cu as small as possible. In contrast, the Cu pad metallization reduces the risk of oxide cracks compared to contacting directly the SiO_x surface. Moreover, Cu-pads improve the BEOL stack robustness of the processed CMOS chips against oxide cracks other than unstructured multi-layer test chips with Al-Cu pads on top (see Sect. 6.3.3). The root cause, which is not yet fully understood, is part of further investigations.

8 Summary, Applications, and Outlook

Complementary to the optical crack inspection method after wet-chemical preparation of the device, the ***A***coustic ***E***mission (AE) test method can from now on be applied to characterize complex layer structures regarding ***P***ad-***O***ver-***A***ctive-***A***rea (POAA) robustness and cracks. Unlike the elaborate and time-consuming creation of cross-section images or optical microscope inspections, the acoustic method offers significant savings in time and cost. Moreover, the new method enables accurate measurements and reliable results with high statistical certainty and efficiency. Hence, it is ideally suited to determine the critical fracture stress in brittle insulation layers and to evaluate the influence of different layer structures on the crack probability.

In the last chapter of this thesis, the different application fields of the modified AE test method for thin layer characterization are explained, starting with a summary of the major achievements of this work. The results enable faster probing qualifications for a wide range of semiconductor technologies and help to develop more robust designs of POAA structures. Finally, an outlook on future work and advanced research fields is given.

8.1 Major Achievements of this Thesis

Within this extensive work, many new findings for a deeper understanding of the POAA failure mechanisms were achieved. Furthermore, various advanced methods were developed to explain, how oxide cracks are generated during contacting with small, rigid tips and how they can be detected in real-time using an optimized AE sensor-indenter system. In the following list, a summary of the most important achievements and developments of this thesis is given:

- Description of challenges and failure mechanisms during probing-over-active-area at semiconductor wafer test
- Overview of failure modes and device fails caused by ***I***nter-***M***etal layer ***D***ielectric (IMD) cracks for most common ***C***omplementary ***M***etal ***O***xide ***S***emiconductor (CMOS) and power semiconductor technologies
- Technical details of conventional microscopy techniques for inspection of pad metal deformation and IMD cracks after probing

- Theoretical description of semiconductor material properties, mechanical contact stress, fracture mechanics, and failure probability function
- Analytical model and ***F***inite ***E***lement ***M***ethod (FEM)-simulation of contact stress, induced by a rigid flat-ended indenter on a monolayer elastic half-space
- Basics of AE testing and related application fields, description of AE test method using an unique test bench with newly developed modifications, and adaption of the innovative concept for thin layer crack detection during indentation
- Modeling, development, and characterization of a resonating sensor-indenter system for crack detection by means of AE test method
- Experimental proof of concept, variance analysis of the modified AE test method on suitable test structures, and validation of the force-dependent crack probability with optical crack inspections
- Explanation of stress concentration in multi-layer structures during indentation by FEM-simulations and correlation with microscopy inspections
- Determination of crack probability with AE test method on unstructured multi-layer test samples and confirmation of crack initiation locations with simulation model
- Experimental parameter studies with different tip diameters and various unstructured test sample designs
- Execution of a case study using the AE test method on processed 40nm CMOS chip with real ***B***ack-***E***nd-***O***f-***L***ine (BEOL) stack to predict the crack probability
- Utilization of new AE test method for advanced POAA qualification process and deriving of BEOL design guidelines for robust probing (see Chap. 8.2 and 8.3)

8.2 Advanced Pad-Over-Active-Area Qualification Process

In Chap. 2, the requirements for today's probing technologies for the wafer test were described in detail. It also discussed the challenges of POAA and the related failure mechanisms for various chip technologies. As stated sev-

eral times in this work, the risk of damage to brittle layers during contacting with sharp tips is always present when the allowable stress is exceeded. Due to the scatter of the crack probability, it is theoretically never 100% avoidable to produce faulty chips after wafer probing on POAA structures. However, the error rates can be reduced to a minimum by an accurate process control during probing. Therefore, the crack probability during operational wafer test must be determined in advance to minimize the quality risk. The AE test method, which was developed in this work and will be introduced near-term as an industrial qualification process, contributes significantly to an improved product quality and reduces the qualification costs and time.

8.2.1 Classical Pad-Over-Active-Area Qualification

Prior to the release of a new probing or wafer technology for the operational wafer test, the probability of cracking must be determined during the POAA qualification. Depending on the customer's quality requirements for the application, a crack rate between 100ppm and 0.1ppm (= number of cracks on 1 million probed pads) is typically specified. A value of 10ppm means, for example, that with 1 million inspected pads a maximum of 10 cracks may occur. As shown in the previous chapters, the crack probability is never assigned to a single specific force value, but scatters according to a *Weibull* distribution. Hence, it is statistically possible, that cracks occur far below the characteristic contact force F_0, even if the applied contact load is correspondingly smaller.

For a real probe card not only the force-related crack probability is still existent, also the mechanical properties and geometry of each needle are varying within a certain range (see Sect. 1.1, Fig. 1.2). That means that the crack probability for every needle is slightly different. In particular, the tip diameter varies in the range of several micrometers and must therefore be regularly checked for quality assurance during wafer test. The contact force, which is another relevant parameter of the crack probability, is mainly influenced by the effective spring deflection (= overdrive) of the needles. The planarity error (= vertical distance between the lowest and highest probe tip) of the probe card, which results in a different overdrive, must hence also be controlled and maintained.

An automatic inspection tool, a so-called *probe card analyser*, can measure the most relevant properties of a probe card. The inspection tool *PRVX-3* manufactured by the company *Applied Precision* (now: *Rudolph Technolo-*

gies), for instance, can be used to evaluate both, the mechanical and electrical condition of probe cards before (i.e. outgoing inspection) and after (i.e. incoming inspection) operational probing as well as during maintenance and repair cycles. With Fig. 8.1 the basic functionality of the *PRVX-3* will be explained [6].

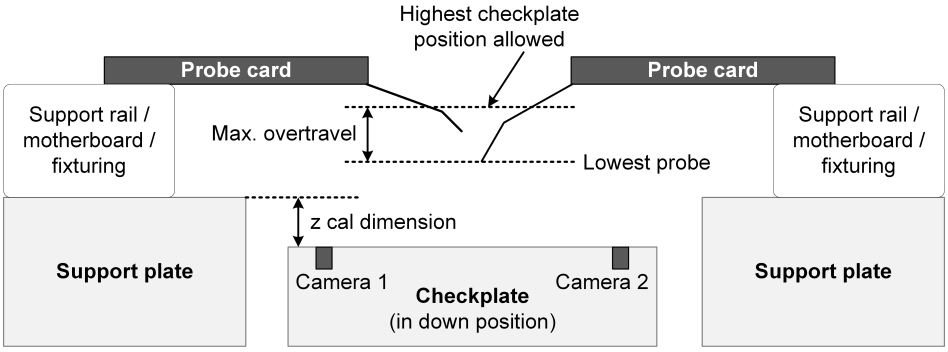

Fig. 8.1. Schematic visualization of the probe card inspection tool.

Its main component is a *x*-*y*-*z* stage on which the checkplate with two embedded cameras is integrated. The two cameras are facing upwards to the probe tips on the probe card, which is fixed above the checkplate. The surface of the checkplate is covered with an electrically conductive, hard, and smooth rhodium layer with openings for the cameras which are covered with glass. To identify the height of the probe tips, the checkplate is moved upwards with a movement resolution of 0.2µm. Each time a probe tip touches the conductive surface, an electric circuit is closed and its vertical position (= *z*-coordinate) is saved. Once all probe tips are found, the median of the *z*-position is calculated. The planarity error is given in form of the measured deviation from the median. Whilst the probe tip is above the camera, the projected diameter of each individual probe tip is optically measured as well [6].

In Fig. 8.2, left, a tip diameter measurement is shown for a 32-DUT probe card with in total 6176 individual probes designed for the 40nm CMOS chip, described in Chap. 7.3. In this example, it is a *vertical* probe card from the manufacturer *Feinmetall GmbH*, type *Buckling Beam* (see Sect. 2.2.2). According to the manufacturer's specification, the maximum contact force per needle of the probe card is F_{max} = 45mN.

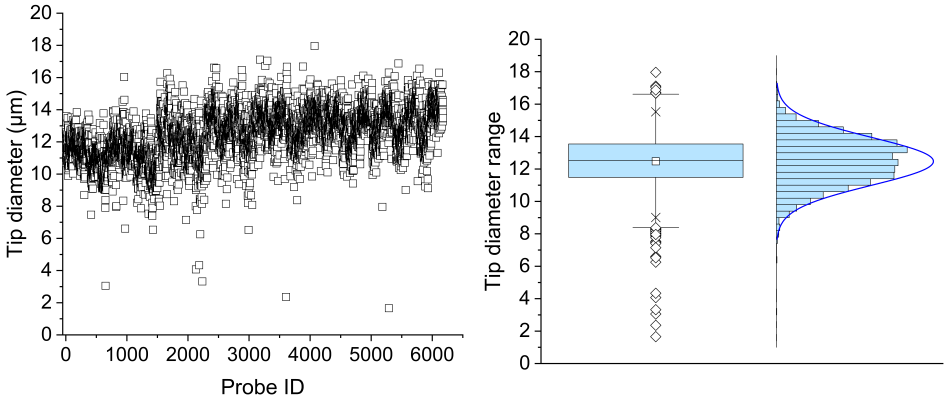

Fig. 8.2. Tip diameter measurement of reference probe card for 40nm CMOS chip.

It can be seen from the box plot and the frequency distribution (see Fig. 8.2, right), that the scattering of the needle diameter is within the range of a minimum of 8.4µm and a maximum of 16.6µm (see horizontal lines outside the box) with a mean value of 12.5µm (see horizontal line in box). The outliers (rhombus symbols) of the measurement below and above the range of dispersion might be caused by measuring errors and are not taken into account here. In addition, it is recognized from the frequency distribution, that the measured values are normally distributed. The probe tips of the probe card are considered to be almost ideally flat, so that the contact stress during wafer test at a particular contact force is comparable to that of the flat diamond tip indentation. The two parameters tip diameter and maximum contact force, apart from the number of repeated contacts on the same chip, significantly influence the risk of oxide cracks in the wafer test and are therefore used as significant factors in the POAA qualification process.

Now briefly the classic POAA qualification process (see Fig. 8.3) will be discussed, which has already been mentioned in Chap. 2.3. Essentially, this process involves four steps:

- Probe card inspection and conditioning
- Wafer probing
- Wet-chemical pad preparation
- Optical crack inspection

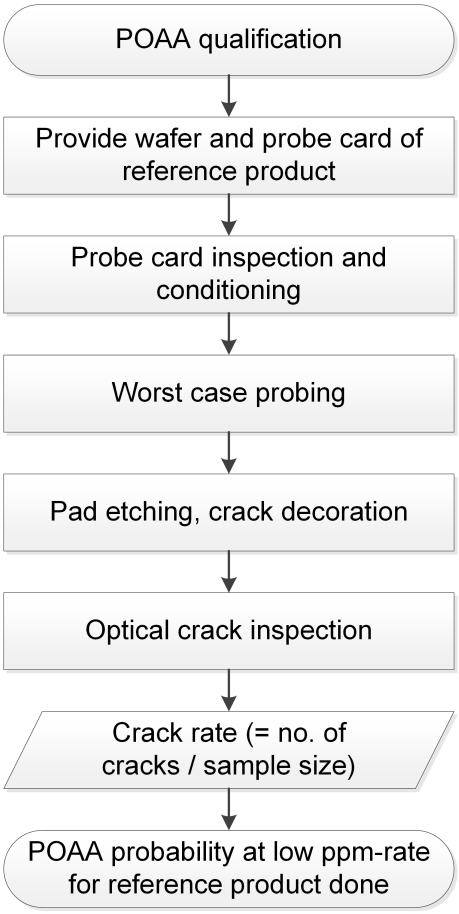

Fig. 8.3. Classical POAA qualification process flow.

The aim of the qualification is to deliberately provoke cracks under the highest possible stress conditions (max. overdrive, low average tip diameter, and increased number of contacts) to determine the failure rate. The probes were previously sharpened, so that the diameter of as many probes as possible is close to the lower specification limit. This process is called "worst case probing", which, however, brings some disadvantages. Even with worst case conditions it is not possible to generate oxide cracks in a sufficiently high number if the crack probability is low. This makes it necessary to partially optically inspect hundreds of thousands or millions of pads, which is a time-consuming work made by humans. Another disadvantage is the susceptibility to error of the chemical preparation method and its unsuitability for some wafer technologies.

As a conclusion, the classical process of POAA qualification is unreliable, sometimes not applicable, lengthy, and causes high labor, material, and equipment costs. Hence, the motivation to find a more efficient qualification process is high.

8.2.2 New Pad-Over-Active-Area Qualification using Acoustic Emission Test Method

The findings and methods that have been achieved in this work help to make the POAA qualification much easier, more accurate, and faster. This section explains how to apply the AE test method to the new POAA qualification process.

As in Sect. 7.2.1 has been demonstrated on various test structures, the diameter of the indenter has a decisive influence on the crack probability, which is defined by the robustness parameters F_0 and m. By determining the crack probability with the aid of the AE test method using flat-punch indenters of different diameters, a so-called ***C**haracteristic **C**ontact **F**orce **F**unction* (*CCFF*), can be experimentally determined. This makes it possible to assign a certain characteristic contact force $F_{0,dtip}$ to any existing tip diameter d_{tip} (see Fig. 8.2) of a probe card and to define a *Weibull* modulus m for a specific pad stack.

The definition of the *CCFF* will be explained in the following example. Fig. 8.4 shows two curves, which are based on the results of the tip diameter variation experiment for LC06 to LC09 from Sect. 7.2.1.

The two dots on the black curve are derived from the AE test results of test structure W01 for the diameters d_{tip} = 10µm for load case LC06 and d_{tip} = 20µm for LC08, which have the respective characteristic contact forces $F_{0,FP10}$ = 192mN and $F_{0,FP20}$ = 571mN. The two dots on the light blue curve are derived from the AE test results of test structure W04 for the diameters d_{tip} = 10µm for load case LC07 and d_{tip} = 20µm for LC09, which have the respective characteristic contact forces $F_{0,FP10}$ = 361mN and $F_{0,FP20}$ = 1069mN. For a diameter d_{tip} = 0µm the characteristic contact force must be zero, because the crack probability gets infinite high

$$\lim_{d_{tip}\to 0} P_f\left(d_{tip}\right) \to \infty. \tag{8.1}$$

So the point of origin of both curves must be at the coordinate (0; 0).

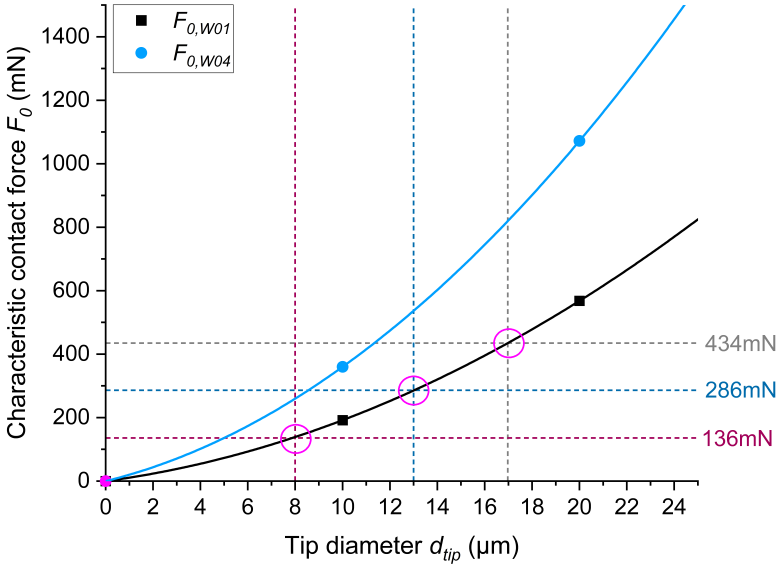

Fig. 8.4. *CCFF* for test samples W01 and W04.

By means of the measured 2 data points and the point of origin at (0; 0), one can fit a curve corresponding to a function for a polynomial of the second order of the form:

$$f(x) = y_0 + B_1 x + B_2 x^2. \tag{8.2}$$

For a diameter d_{tip} = 0µm, y_0 can be set to zero. The coefficients B_1 and B_2 determine the slope of the curve. For the example shown, $B_{1,W01}$ = 10 and $B_{2,W01}$ = 0.92 for W01 and $B_{1,W04}$ = 18.4 and $B_{2,W04}$ = 1.76 for W04 (see Table 8.1).

Table 8.1. Coefficients B_1 and B_2.

	$F_{0,W01}$	$F_{0,W04}$
B_1	10	18.4
B_2	0.92	1.76

Structure W04 is more robust compared to structure W01, as indicated by the larger slope of the orange curve. After defining the coefficients of Eq. (8.2), one can assign to any tip diameter the corresponding characteristic contact force for a specific test structure. The meaning of the dashed lines, circles, and values will be explained further down.

Now, the entire process flow of the new POAA qualification (see Fig. 8.5) will be explained using the AE test method and the previously mentioned *CCFF*.

The specification of the reference probe card and the BEOL stack design are collected analogously to the classical POAA qualification process. Also for the new process the tip diameter of the reference probe card is measured and recorded on the inspection tool. In a parallel process flow, the crack probability is acoustically determined for the reference product. For this purpose, the AE crack checks are performed according to the procedure described in Sect. 7.3.3 for at least 2 different tip diameters. Out of this test one gets the respective characteristic contact force $F_{o,FPdtip}$ and the *Weibull* modulus *m* for the investigated BEOL stack. It should be noted, that the *Weibull* modulus *m* is assumed to be almost identical for different tip diameters (see Sect. 7.2.1), but different for each BEOL stack layout. With these robustness parameters one can fit the *CCFF* graph and determine the tip-specific crack probabilities individually.

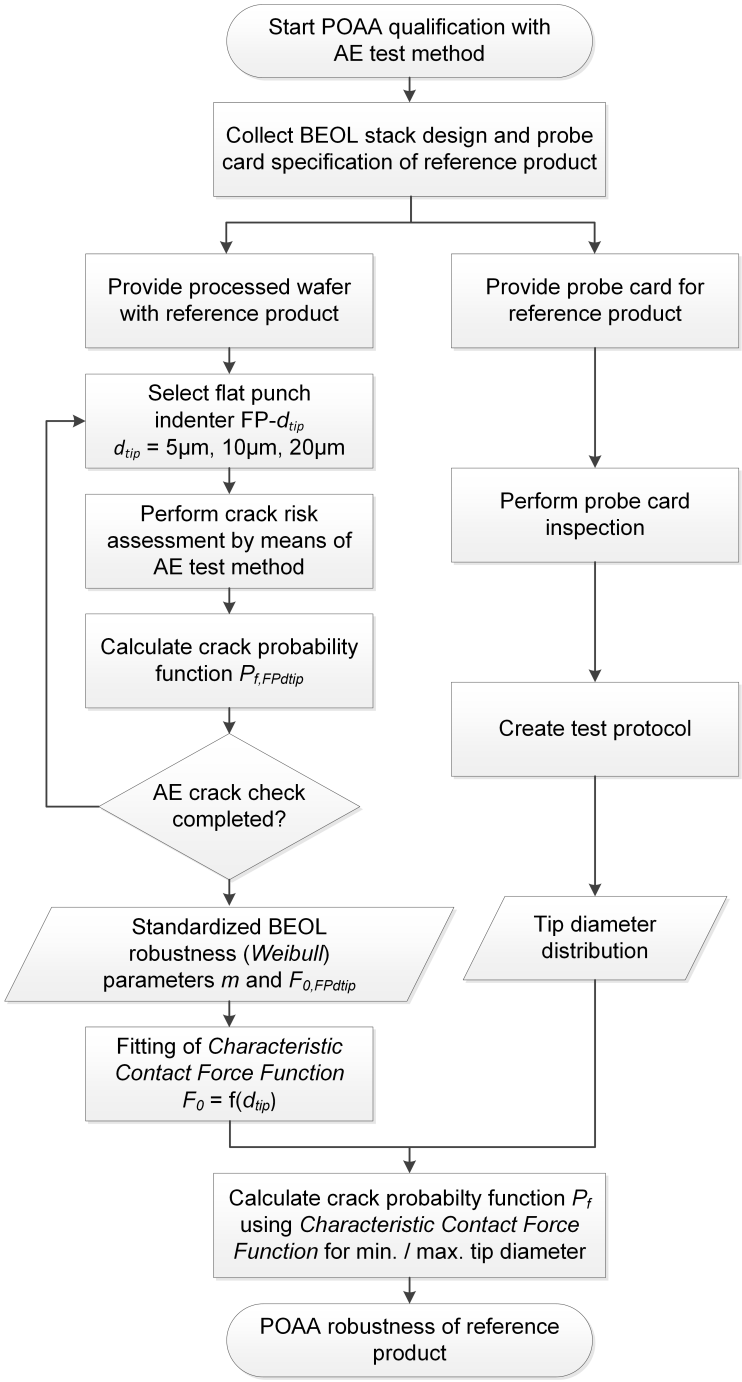

Fig. 8.5. New POAA qualification process flow.

In Fig. 8.6 the crack probability prediction for different tip diameters based on test structure W01 as a function of the contact force according to the new POAA qualification process is shown exemplary for the tip diameters of the inspected probe card of Fig. 8.2. There are three curves shown, which are related to a minimum tip diameter (here: d_{tip} = 8µm, bordeaux curve), a maximum diameter (here: d_{tip} = 17µm, grey curve), and a mean diameter (here: d_{tip} = 13µm, cyan curve).

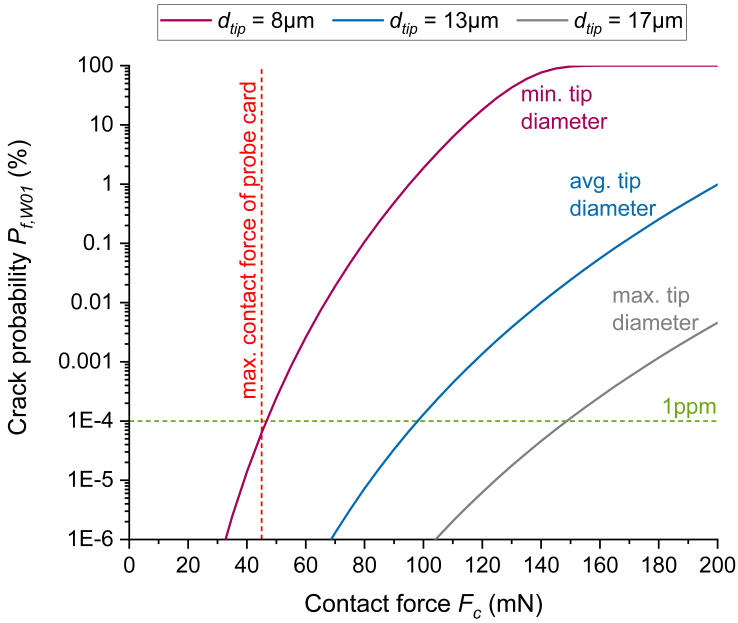

Fig. 8.6. Example of crack probability plot of test sample W01 for reference probe card.

The corresponding contact forces are derived from the results of the *CCFF* graph. In this example, the characteristic contact forces $F_{o,FPdtip}$ (see pink circles in Fig. 8.4) for test structure W01 (*Weibull* modulus m = 12.88, see Table 7.3) are associated to the minimum (d_{tip} = 8µm → $F_{o,FP8}$ = 136mN), average (d_{tip} = 13µm → $F_{o,FP13}$ = 286mN), and maximum (d_{tip} = 17µm → $F_{o,FP17}$ = 434mN) tip diameters of the probe card. Once all robustness parameters are defined, the tip and layer-stack specific crack probability $P_{f,W01}$ can be calculated from Eq. (6.1) as a function of the contact force and graphically displayed. From the graphs in Fig. 8.6 it is now possible to check, assuming a permissible crack probability of 1ppm (green horizontal dashed line) and a maximum specified contact force of the probe card of F_{max} = 45mN (red vertical dashed line), whether the scatter range of the tip

diameter of the probe card is within the allowable specification tolerance. This is true for the given example, because the tip-specific crack probability for a minimum tip diameter d_{tip} = 8µm at a maximum contact force of 45mN is still just below 1ppm. If, as in Chap. 7.3 shown experimentally, BEOL stack variants with different *Weibull* moduli *m* are present the procedure must be done separately for each of the different variants.

The big advantage of the new POAA qualification process is the predictability of the crack probability for any probe tip diameter without the need of time-consuming chemical-optical crack inspection. The AE test method is also applicable to all wafer technologies that have brittle layers and thus produce acoustic signals at fracture. Following this work, the described new process will be correlated with the classical POAA qualification process and applied for POAA qualifications on various new wafer technologies.

8.3 Back-End-Of-Line Stack Design Guidelines

Another application of the AE test method is the optimization of materials, geometries, and manufacturing processes of thin multi-layer semiconductor structures regarding cracks and deformation. This makes it possible to derive guidelines for chip designers and process engineers of the BEOL structure. In this work, important learnings were achieved and further optimizations are possible for the future.

Until today, a lot of work regarding the influence of the BEOL layer design on the IMD layer crack behavior has been carried out (see e.g., [1], [30], [65], or [66]), all revealing its significant impact on the mechanical stack robustness. The AE test method is ideally suited to improve the design robustness for more reliable POAA pad structures.

Some concrete design rules have already been mentioned in Chap. 6 and 7. Fig. 8.7 gives some important guidelines for increasing the BEOL stack robustness based on the findings from the multiple AE crack experiments.

One option is to optimize the pad geometry and material, in order to reduce the stress reaching the underlying oxide structure. Generally, a thicker pad metallization reduces the imprint depth during contacting and so the risk of SiO_x cracking. Furthermore, the stack robustness increases, when using a pad metallization of higher hardness, such as Cu- instead of Al-Cu-pads (see Sect. 6.3.3 and 7.3.3).

As detailed described in Sect. 7.2.2, the thickness of layers below the pad have a significant impact on the mechanical stack robustness. If the bending of the top SiO_x layer, which causes high tensile stress in radial direction

at the tip edge (see Chap. 7.1 and 7.2), is minimized, also the crack probability is lower. Therefore, it is important to prevent the plastic deformation in underlying routing metal layers as much as possible. This can be reached by reducing the thickness of the metal layers in combination with a higher thickness of the brittle oxide layer on top.

According to Chap. 7.3, the crack probability also depends on the layout and area density of the metal routing below the oxide layer. Thus, modifying the metal routing in a suitable manner has a positive influence on the crack risk. One recommendation is to reduce the metal routing density in the pad stack as much as possible and to use metal fill structures, in order to reduce the bending stress on the oxide layer. Since pad stack layouts with metal stripes showed higher crack risk than layouts with fill structures, it is better to avoid metal stripes and reduce the amount of ductile material as much as possible. With these design rules the vertical deflection of the metal layers are lower during contacting and thus the risk of brittle IMD layer cracking is reduced.

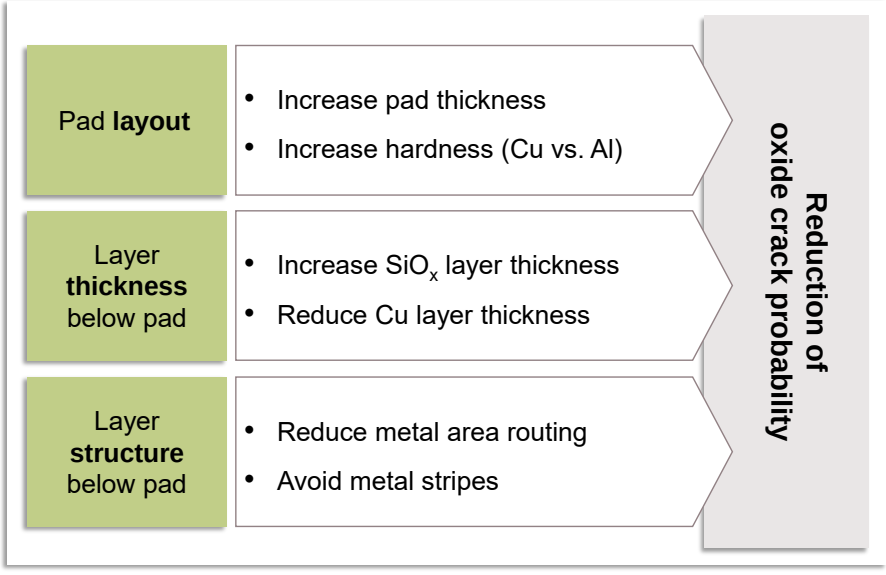

Fig. 8.7. BEOL design guidelines for more reliable POAA pad structures.

Further BEOL design and process studies are planned in combination of the AE test method to reduce the crack risk during POAA, for example on new materials, alternative deposition processes to reduce intrinsic stresses

in the layers, influences of adhesion and diffusion barriers, and design optimizations of vias and wiring levels.

8.4 Further Work and Research Topics

This thesis has made a valuable contribution to the understanding, methodology, and application of the AE test method used for mechanical characterization of thin semiconductor layers. For future work, some topics remain for further development and extension of the scope. The final section of this dissertation will briefly discuss the various research and application areas grouped into three categories.

1. *Approval of AE Test Method for POAA Qualification for Operational Use at Wafer Test:*

The first category is a follow-up to the experiments presented in Chap. 6 and 7 for the operational use of the AE test method for POAA qualification of processed chip technologies. As mentioned several times in this work, the use of a rigid diamond tip with a well-defined surface and shape is an idealization of the real probing process. Therefore, further investigations are necessary to predict the influence of probing parameters on the crack behavior more accurately. For this purpose, the following sub-topics are listed, which are essential for an approval of the new POAA qualification process for industrial use:

- Crack probability correlation of indenter and real probe
- Probe tip geometry and material
- Probing process simulation (lateral scrub, repeated touchdowns, high / low temperature, high strain rate)

A real probe may have an uneven and rough tip surface and often has a non-linear spring characteristic. Hence, acoustic and optical crack inspections with sufficiently high statistics have to be performed, in order to prove the accuracy of the AE test method under more realistic conditions. As shown in this work, the tip geometry probably has the biggest influence. Therefore, further indenter experiments with round rather than flat tip shapes, but also other possible geometries, e.g. truncated pyramid tips, are planned. To what extent the probe material, which in the real application consists of metal instead of diamond, has an influence, needs to be investigated, too.

As explained in Chap. 2, most needles of real probe cards do not only penetrate vertically, but are scrubbing laterally along the pad surface during *cantilever* probing, for instance. Moreover, only single insertions have been performed in the experiments shown here, hence the influence of multiple insertions (so-called repeated touchdowns), which occur frequently in the operational wafer test, must be evaluated to determine the crack probability. Whether the layer stack robustness changes at high or low temperatures or at higher strain rates, is also a part of further investigations.

2. *Acoustic Signal Analysis, Classification, and Simulation*

This category includes the evaluation and analysis of the electrical signals recorded using the AE test method. Relevant are the following sub-topics of further investigations:

- Wave form analysis of acoustic crack events
- AE hit classification by algorithms and machine learning techniques
- AE hit characteristics and burst signal energy relative to imprint depth
- FEM-simulation of mechanical stress and acoustic wave transmission

These topics cover the signal analysis of acoustic events (AE hits) that are detected by the acoustic sensor during contacting (see Chap. 5). The signals, which must be acquired with high sampling rate and resolution, can then be analyzed in the time and frequency domain. Out of the signal characteristics information might be obtained on the nature, propagation, and energy of the cracks as well as deformations of the material.

Another aspect is the classification using algorithms and machine learning techniques to automate the manual filtering and clustering of AE signals. The AE test experiments on the ductile layer shown in Sect. 6.3.3 and 7.3.3 indicate, that the penetration depth of the indenter is related to the burst signal energy and frequency of AE hits. This relation can be used to control the probing process by AE testing. Further research is planned on this topic in the near future.

The FEM-simulations on the vibration analysis of the sensor-indenter system (see Chap. 5.3) and the mechanical stresses in the layer stack during indentation (see Chap. 1 and 7), which were started in this work, will be further refined, in order to improve and accelerate the product and process

development in the future. Within this topic, the main interest is the modeling of crack generation and propagation. In addition, simulations of the propagation and transmission of the acoustic wave are required to improve the understanding of cracks in thin layer stacks.

3. *Further Applications for New AE Test Method*

The third category covers the extension of the presented AE test method to other semiconductor test or manufacturing processes where mechanical loads occur that can lead to cracks or damages of the chip or wafer. The following topics are of interest:

- Semiconductor material and process characterization
- Cracks and deformation during bump probing instead of pads
- Advanced process control at wafer probing
- Crack risk assessment for other assembly applications (e.g. wire bonding, wafer dicing, chip molding, thin wafer handling, etc.)

The presented AE test method is also very well suited to investigate the influence of alternative materials with higher hardness or elasticity. This scope of application is very extensive and can lead to new and improved materials. In the future, it will also be possible to improve the semiconductor processes for the deposition and processing of thin layers, in particular the reduction of temperature-dependent pre-stresses of layers with different thermal expansion coefficients, which can influence the risk of oxide cracks.

An important application of the AE test method is the crack risk assessment during contacting on solder bumps (tin-silver alloys (Sn-Ag), Cu-pillars, etc.) instead of on thin metal layer pads. Both the oxide crack probability of the chip and the deformation of solder bumps itself can be evaluated during contacting.

Another aspect involves the integration of the sensor on a probe card or within the wafer chuck to use the AE test method for advanced process control during wafer test. However, this requires smaller AE sensors, which allow the acoustic signal to be coupled to the probe or to the bottom side of the wafer. Therefore, initial experiments with alternative sensors have been started, which must be further developed.

In addition, there are several other processes in the assembly and interconnection technology of semiconductors where the AE test method can be used to acoustically detect cracks and damage due to mechanical stress.

During wire bonding, like probing, mechanical stress is applied to the pad, whereby the contact force is even higher in comparison. Other processes, such as wafer dicing or chip molding, also generate mechanical forces, which, however, have no impact to the structure in a point-like manner but in a planar manner causing chip bending and vibrations. This leads in part to chip cracks, which can result in a total failure of the ***I***ntegrated ***C***ircuit (IC). Another practical application is the handling of thin wafers (min. thickness < 50µm), which are a problem especially for power semiconductor technologies and can lead to breakage of the wafer. The above-mentioned fields of application are also suitable for the AE test method, but the coupling of the AE sensor is another great challenge here.

Appendix

A) PROFIT Macro and Flow Chart

 # *PROFIT* macro: 10x10 matrix, F_{zmax} = 250mN

```
# ____________________________________________________________
# delete all measured data from memory
cleardatahistory
# delete present filename for date files
clearfilename
# reset touchdown counter to zero
resettdcounter

# set moving velocity of specified axis to value in µm/s
vel z 10
vel x 100
vel y 100

# set HBM lowpass for all channels to 5Hz
hbmlowpass 5
# ____________________________________________________________
# 10 measurement rows
repeat 10
# ____________________________________________________________
# 10 imprints, Fzmax = 250mN
repeat 10

# zero point calibration of HBM channels to present readout
hbmzerocal 1
hbmzerocal 2

# find contact, z-force is limited to 5mN
```

```
# <z-distance in µm><z-step width in µm><z-force limit in mN>
findcontact 10000 0.05 5

# move relative to present position; target z-distance in µm
mvr z -2

# resent timer reference for current touchdown
resettdtimer
# increase counted number of touchdowns by one
inctdcounter
# zero point calibration of HBM channels to present readout
hbmzerocal 1
hbmzerocal 2

# Reduce moving velocity in z-direction to 1µm/s
vel z 1

# perfom full cycle of z-move
# <z-distance in µm><z-step width in µm><z-force limitation value in mN>
# loading: z-force is limited to 250mN
zcycle 25 0.025 250
# hold 2000ms and sample measurement values each 20ms
waitcycle 2000 20
# unload: move -10µm downwards
# <z-distance in µm><z-step width in µm><z-force limitation value in mN>
zcycle -10 -0.025 300

# save data and display graphs of the last contacting
savelasttd
plotlasttd

# move to next contact position, x-, & y-distance between the indents: 500nm
wait 50
```

```
vel z 10
mvr z -5
wait 50
mvr x 500

end repeat
# _____________________________________________________

wait 50
mvr z -500
wait 50
mvr y -500
wait 50
mvr x -5000
wait 50
mvr z 500
wait 50
# _____________________________________________________
end repeat
```

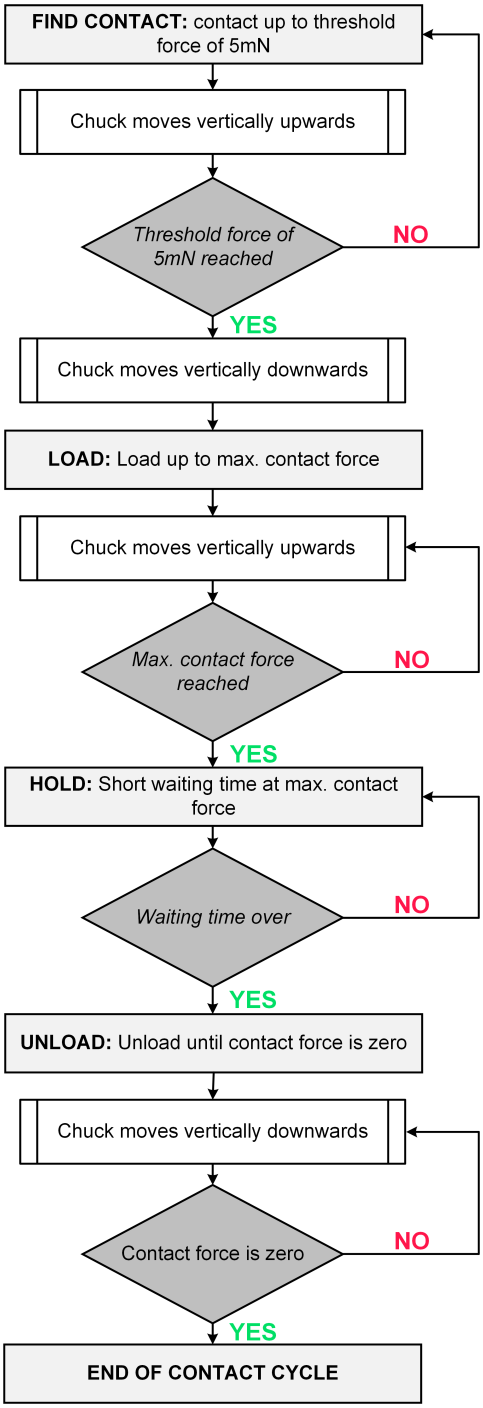

Fig. 0.1. Flow chart for performing a typical contact cycle using the *PROFIT*.

B) Split Plan of Unstructured Test Samples

Jobstep	Recipe	W01	W02	W03	W04
CVD PLASMA SILAN/OXID	500nm 400°C	x	x		
CVD PLASMA SILAN/OXID	800nm 400°C			x	x
CVD PLASMA TEOS	1240nm 400°C	x	x	x	x
SPUTTER LINER COPPER	25nm Ta 28°C + 100nm Cu 12°C	x	x	x	x
ECD METAL COPPER	600nm	x	x		
ECD METAL COPPER	300nm			x	x
CVD PLASMA NITRIDE	50nm 400°C UV SIN	x	x	x	x
CVD PLASMA SILAN/OXID	1000nm 400°C		x		x
CVD PLASMA SILAN/OXID	380nm 400°C	x		x	

Jobstep	Recipe	W05	W06
CVD PLASMA SILAN/OXID	500nm 400°C	x	x
CVD PLASMA TEOS	1240nm 400°C	x	x
SPUTTER LINER COPPER	25nm Ta 28°C + 100nm Cu 12°C	x	
ECD METAL COPPER	600nm	x	
ECD METAL COPPER	No COPPER		x
CVD PLASMA NITRIDE	50nm 400°C UV SIN	x	x
CVD PLASMA SILAN/OXID	3000nm 400°C	x	x
SPUTTER LINER TA	50nm Ta	x	
SPUTTER METAL	40nm Ti/3000nm Al-Cu 350°C	x	
ANNEAL DRY METAL	400°C 30min. (N_2/H_2)	x	
STRIP PLASMA O2-FLASH	10sec. O_2 plasma	x	

C) Layout of 40nm CMOS Chip

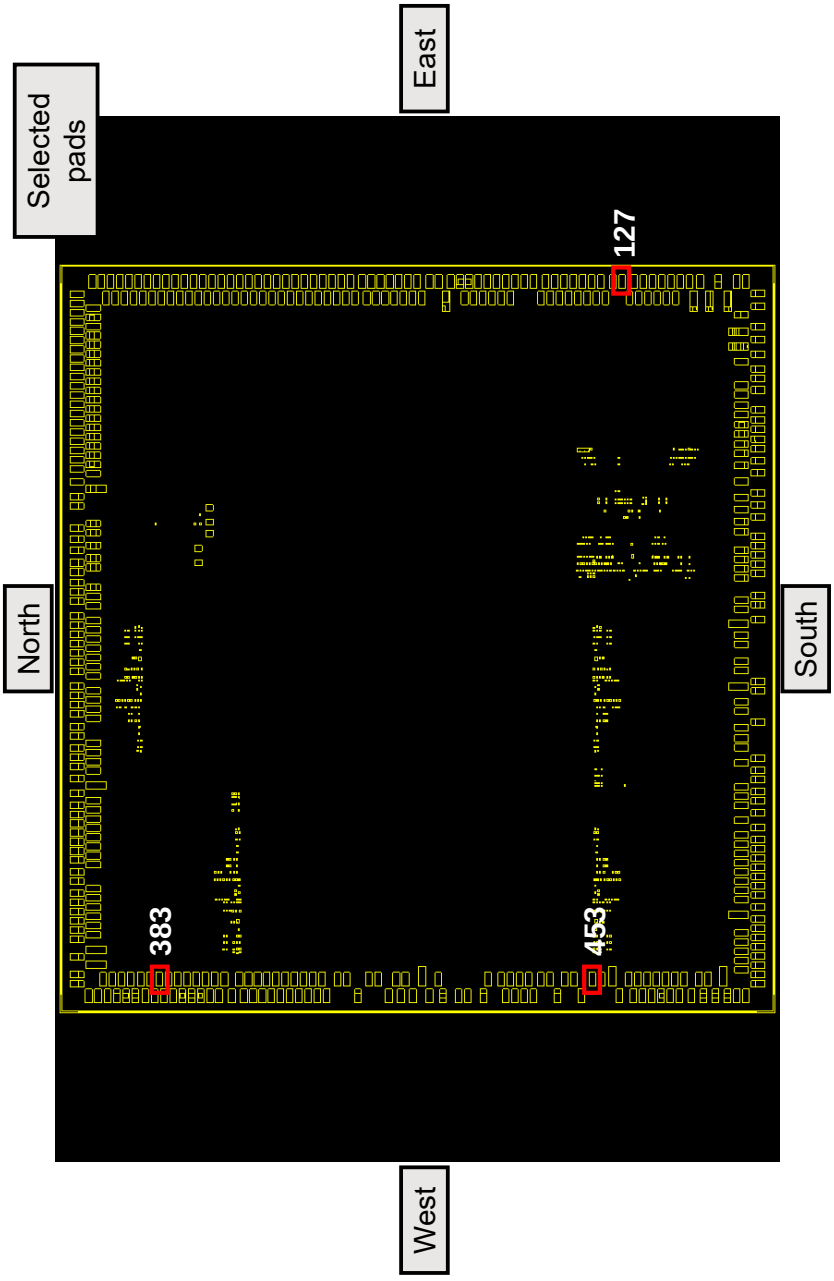

Fig. 0.2. Layout of 40nm CMOS chip.

References

[1] O. Nagler, *Probing-induzierte Defekte bei Halbleitern mit Kontaktpads über aktiven Strukturen*. Doctoral Thesis. Munich: Universitätsbibliothek der Universität der Bundeswehr München, 2009.

[2] U. Hilleringmann, *Silizium-Halbleitertechnologie: Grundlagen mikroelektronischer Integrationstechnik,* 6th ed. Wiesbaden: Springer Vieweg Verlag, 2014.

[3] M. Unterreitmeier, O. Nagler, L. Pfitzner, R. Weigel, and R. Holmer, "An acoustic emission sensor system for thin layer crack detection," *Microelectronics Reliability*, vol. 88-90, pp. 16–21, 2018.

[4] M. B. Read, J. H. Lang, A. H. Slocum, and R. Martens, "Contact resistance in flat thin films," in *Proceedings of the 55th IEEE Holm Conference on Electrical Contacts*, Vancouver, 2009, pp. 303–309.

[5] R. S. Timsit, "Constriction resistance of thin film contacts," *IEEE Transactions on Components and Packaging Technologies*, vol. 33, no. 3, pp. 636–642, 2010.

[6] T. Krebs, *Experimental Evaluation and Statistical Analysis of the Electrical Contact Resistance during Wafer Test*. Master Thesis. Aachen: Universitätsbibliothek RWTH Aachen, 2018.

[7] C. U. Grosse and M. Ohtsu, Eds., *Acoustic Emission Testing: Basics for Research - Applications in Civil Engineering*. Berlin, Heidelberg: Springer Verlag, 2008.

[8] Deutsche Gesellschaft für Zerstörungsfreie Prüfung, "Kompendium Schallemissionsprüfung Acoustic Emission Testing (AT): Grundlagen, Verfahren und praktische Anwendung," 2018. [Online] Available: www.dgzfp.de/Portals/24/PDFs/FA/KompendiumAT.pdf. Accessed on: Jul. 02 2019.

[9] A. Klemmt, *Ablaufplanung in der Halbleiter- und Elektronikproduktion: Hybride Optimierungsverfahren und Dekompositionstechniken*. Wiesbaden: Springer Vieweg Verlag, 2012.

[10] H.-Y. Chang, W.-F. Pan, and S.-M. Lin, "Experimental and theoretical investigation of needle contact behavior of wafer level probing," *Precision Engineering - Journal of the International Societies for Precision Engineering and Nanotechnology*, vol. 35, no. 2, pp. 294–301, 2011.

[11] H.-J. Kwon *et al.*, "Geometry design of vertical probe needle using mechanical testing and finite element analysis," *International Journal of Precision Engineering and Manufacturing*, vol. 15, no. 11, pp. 2335–2342, 2014.

[12] L. Gilg, "Known good die," *Journal of Electronic Testing: Theory and Applications*, vol. 10, pp. 15–25, 1997.

[13] F. Wang, R. Cheng, and X. Li, "MEMS vertical probe cards with ultra densely arrayed metal probes for wafer-level IC testing," *Journal of Microelectromechanical Systems*, vol. 18, no. 4, pp. 933–941, 2009.

[14] R. Doherty and R. Rogers, "Vertical probe alternative for cantilever pad probing," presented at the *IEEE Semiconductor Wafer Test Workshop*, San Diego, 2008. [Online] Available: https://www.swtest.org/swtw_library/2008proc/PDF/S02_02_Doherty_SWTW2008.pdf. Accessed on: Nov. 16 2018.

[15] B. Tunaboylu and A. M. Soydan, "MEMS technologies enabling the future wafer test systems," in *MEMS Sensors - Design and Application*, S. Yellampalli, Ed., London: IntechOpen, 2018, pp. 189–206.

[16] O. Nagler, M. Reinl, F. Kaesen, and I. Eisele, "Advanced characterization of semiconductor wafer probing methodology," in *Proceedings of the 23th International Conference on Electrical Contacts*, Sendai, 2006, pp. 97–102.

[17] R. Holm, *Electric Contacts: Theory and Application,* 4th ed. Berlin, Heidelberg: Springer Verlag, 1967.

[18] M. Gedeon, "The importance of contact force," *Technical Tidbits*, no. 6, 2009.

[19] H. Hofmann and J. Spindler, *Werkstoffe in der Elektrotechnik: Grundlagen - Struktur - Eigenschaften - Prüfung - Anwendung - Technologie,* 7th ed. Munich: Carl Hanser Verlag, 2013.

[20] M. Braunovic, N. K. Myshkin, and V. V. Konchits, *Electrical Contacts: Fundamentals, Applications and Technology*. Boca Raton: CRC Press, 2006.

[21] R. S. Timsit, "Electrical contact resistance: properties of stationary interfaces," *IEEE Transactions on Components and Packaging Technologies*, vol. 22, no. 1, pp. 85–98, 1999.

[22] D. S. Liu, M. K. Shih, and W. H. Huang, "Measurement and analysis of contact resistance in wafer probe testing," *Microelectronics Reliability*, vol. 47, no. 7, pp. 1086–1094, 2007.

[23] Y. Liu, Y. Liu, S. Irving, and T. Luk, "Wafer probing simulation for copper bond pad based BPOA structure," in *Proceedings of the 2007 International Conference on Thermal, Mechanical and Multi-Physics Simulation Experiments in Microelectronics and Micro-Systems.*, London, 2007, pp. 1–5.

[24] P. Laube, "Semiconductor technology from A to Z," [Online] Available: https://www.halbleiter.org/pdf/de/halbleitertechnologie/Halbleitertechnologie%20von%20A%20bis%20Z.pdf. Accessed on: Nov. 16 2018.

[25] Alpha & Omega Semiconductor, "Power MOSFET basics," [Online] Available: http://www.aosmd.com/res/application_notes/mosfets/Power_MOSFET_Basics.pdf. Accessed on: Jan. 10 2019.

[26] A. Wintrich, U. Nicolai, W. Tursky, and T. Reimann, *Applikationshandbuch Leistungshalbleiter,* 2nd ed. Ilmenau: ISLE Verlag, 2015.

[27] B. J. Baliga, *Advanced Power MOSFET Concepts*. New York: Springer Verlag, 2010.

[28] R. Ruffilli *et al.,*"Aluminum metallization and wire bonding aging in power MOSFET modules," *Materials Today: Proceedings*, vol. 5, no. 6, pp. 14641–14651, 2018.

[29] R. Vettori, "General overview on pad damage: probe key parameters and other causes," presented at the *IEEE Semiconductor Wafer Test Workshop*, San Diego, 2016. [Online] Available: https://www.swtest.org/swtw_library/2016proc/PDF/S07_02_Vettori_SWTW2016.pdf. Accessed on: Jan. 10 2019.

[30] S. Hunter, "Recent development work in IC bond pad structure and circuit under pad," *Presentation to International Microelectronics and Packaging Society (IMAPS) Student Chapter*, University Idaho, 2011. [Online] Available: https://docplayer.net/docview/48/24365206/#file=/storage/48/24365206/24365206.pdf. Accessed on: Jan. 10 2019.

[31] J. Lienig and J. Göran, "Elektromigration - Eine neue Herausforderung beim Entwurf elektronischer Baugruppen: Teil 1: Ursachen und Beeinflussungsmoglichkeiten," *F-&-M-Mechatronik*, vol. 110, no. 10, pp. 36–39, 2002.

[32] J. R. Black, "Electromigration - a brief survey and some recent results," *IEEE Transactions on Electron Devices*, vol. 16, no. 4, pp. 338–347, 1969.

[33] R. Wegerhoff, M. Kässens, and R. Reimer, "Mikroskopische Verfahren," in *Romeis - Mikroskopische Technik*, 19th ed., M. Mulisch and U. Welsch, Eds., Berlin, Heidelberg: Springer Verlag, 2015, pp. 1–42.

[34] W. Ockenga, *Differential Interference Contrast (DIC).* [Online] Available: www.leica-microsystems.com/science-lab/differential-interference-contrast-dic/. Accessed on: Jan. 29 2019.

[35] S. W. Paddock, "Principles and practices of laser scanning confocal microscopy," *Molecular Biotechnology*, vol. 16, no. 2, pp. 127–149, 2000.

[36] Thermo Fisher Scientific, *An Introduction to Electron Microscopy: Focused Ion Beam Systems and DualBeam™ Systems.* [Online] Available: www.fei.com/introduction-to-electron-microscopy/fib/. Accessed on: Jan. 30 2019.

[37] A. C. Fischer-Cripps, *Introduction to Contact Mechanics,* 2nd ed. New York: Springer Verlag, 2007.

[38] D. Gross and T. Seelig, *Bruchmechanik: Mit einer Einführung in die Mikromechanik,* 4th ed. Berlin, Heidelberg: Springer Verlag, 2007.

[39] J.-P. Burg, "The causes mechanical aspects of deformation," ETH Zurich, Zurich, 2019. [Online] Available: www.files.ethz.ch/structuralgeology/jpb/files/english/1stress.pdf. Accessed on: Feb. 15 2019.

[40] V. Läpple, *Einführung in die Festigkeitslehre: Lehr- und Übungsbuch,* 3rd ed. Wiesbaden: Springer Vieweg Verlag, 2011.

[41] D. Roylance, "Introduction to fracture mechanics," Massachusetts Institute of Technology, Cambridge, 2001. [Online] Available: http://web.mit.edu/course/3/3.11/www/modules/frac.pdf. Accessed on: Mar. 23 2019.

[42] C. Pagliosa, "Werkstoffpraktikum WS - SS 2003 / 2004: Versuch 5: Mechanisches Verhalten von Keramik," ETH Zurich, Zurich, 2003. [Online] Available: www.nonmet.mat.ethz.ch/education/courses/Ceramic_Laboratory_Practice/6_Mechanische_Eigenschaften.pdf. Accessed on: Mar. 23 2019.

[43] J. B. Wachtman, W. R. Cannon, and M. J. Matthewson, *Mechanical Properties of Ceramics,* 2nd ed. United States: John Wiley & Sons, 2009.

[44] B. Riccardi and R. Montanari, "Indentation of metals by a flat-ended cylindrical punch," *Materials Science and Engineering: A*, vol. 381, no. 1-2, pp. 281–291, 2004.

[45] J. A. Williams and R. S. Dwyer-Joyce, "Contact between solid surfaces," in *Modern Tribology Handbook: Principles of Tribology*, B. Bhushan,

Ed., Boca Raton, London, New York, Washington, D.C.: CRC Press, 2001, pp. 121–162.

[46] R. Mouginot and D. Maugis, "Fracture indentation beneath flat and spherical punches," *Journal of Materials Science*, vol. 20, no. 12, pp. 4354–4376, 1985.

[47] T. Yokohata, K. Kato, T. Miyamoto, and R. Kaneko, "Load-dependency of friction coefficient between silicon-oxides and diamond under ultra-low contact load," *Journal of Tribology*, vol. 120, no. 3, pp. 503–509, 1998.

[48] Vallen Systeme, "Schallemissionsprüfung: Grundlagen - Gerätetechnik - Anwendungen," Munich. [Online] Available: http://www.schallemission.de/zdownload/pdf/sea204.pdf. Accessed on: Jul. 01 2019.

[49] J. Bohse, "Unterscheidung von Quellenmechanismen der Schallemission - Ansätze und Grenzen," in *19. Kolloquium Schallemission - Statusberichte zur Entwicklung und Anwendung der Schallemissionsanalyse*, Augsburg, 2013, pp. 1–10.

[50] G. Gautschi, *Piezoelectric Sensorics: Force Strain Pressure Acceleration and Acoustic Emission Sensors Materials and Amplifiers*. Berlin, Heidelberg: Springer Verlag, 2002.

[51] Vallen Systeme, "Acoustic emission sensors: specification," Munich, 2015. [Online] Available: www.vallen.de/fileadmin/user_up-load/sov.pdf. Accessed on: Mar. 14 2019.

[52] *Standard Guide for Mounting Piezoelectric Acoustic Emission Sensors*, ASTM Standard E650-97, 1997.

[53] P. Theobald, "Guide on acoustic emission sensor couplants," National Physical Laboratory, United Kingdom, 2012. [Online] Available: www.npl.co.uk/acoustics/ultrasonics/research/guide-on-acoustic-emissionsensor-couplants. Accessed on: Oct. 15 2017.

[54] *Zerstörungsfreie Prüfung – Terminologie – Teil 9: Begriffe der Schallemissionsprüfung; Dreisprachige Fassung*, DIN EN 1330-9, 2009.

[55] Vallen Systeme, *Help on Vallen AE Suite, Release: R2016.0811.1*, 2016. [Online] Available: http://www.vallen.de/zdownload/zip/aesuite2016.0811.1.zip. Accessed on: Jul. 12 2019.

[56] A. Nitsch, R. Tilgner, and H. Baumeister, "Method and apparatus for detecting a crack in a semiconductor wafer, and a wafer chuck," US7973547B2, Jul 5, 2011.

[57] K. Magnus, *Schwingungen: Eine Einführung in die theoretische Behandlung von Schwingungsproblemen,* 3rd ed. Stuttgart: Teubner Verlag, 1976.

[58] U. Simon and B. Wieland, "Mathematische Modellierung und Simulation in der Mechanik 2: Dynamik," Ulm University, Ulm, 2011. [Online] Available: www.uni-ulm.de/fileadmin/website_uni_ulmuzwr/mmsm/mmsm2-ss11/Script-MMSM2.pdf. Accessed on: Apr. 17 2019.

[59] D. Kraft, "Kompendium der Maschinendynamik," Fachhochschule München, Munich, 1999. [Online] Available: http://dkraft.userweb.mwn.de/data/mady.pdf. Accessed on: Jul. 03 2019.

[60] S. Kolling and H. Steinhilber, "Technische Schwingungslehre," Technische Hochschule Mittelhessen, Giessen, 2013. [Online] Available: https://www.thm.de/me/images/user/kolling-94/schwingungs-lehre/Schwingungen.pdf. Accessed on: Jul. 03 2019.

[61] D. Gross, W. Hauger, E. A. Werner, and J. Schröder, *Formeln und Aufgaben zur Technischen Mechanik 4: Hydromechanik, Elemente der Höheren Mechanik, Numerische Methoden,* 3rd ed. Berlin: Springer Vieweg Verlag, 2008.

[62] F. Rettenmeier, *Charakterisierung und simulationsgestützte Optimierung des Sensor-Indenter-Systems für die Schallemissionsprüfung beim Wafertest*. Master Thesis. Munich: Bibliothek der Hochschule München, 2017.

[63] F. Tremmel, *FEM Contact Simulation of Cracks during Indentation of Semiconductor Multilayer Structures*. Project Study. Munich: Bibliothek der Hochschule München, 2018.

[64] V. Hatty, H. Kahn, and A. H. Heuer, "Fracture toughness, fracture strength, and stress corrosion cracking of silicon dioxide thin films," *Journal of Microelectromechanical Systems*, vol. 17, no. 4, pp. 943–947, 2008.

[65] K. Hess *et al.,* "Reliability of bond over active pad structures for 0.13-µm CMOS technology," in *Proceedings of the 53th Electronic Components and Technology Conference*, New Orleans, 2003, pp. 1344–1349.

[66] R. Roucou, V. Fiori, K. Inal, and H. Jaouen, "Mechanical issues induced by electrical wafer sort: correlations from actual tests, nanoindentation and 3D dynamic modeling," in *Proceedings of the 3rd Electronics System Integration Technology Conference*, Berlin, 2010, pp. 1–6.

The book provides the reader with a novel, non-destructive test method for mechanical damages in semiconductor structures that can arise when contacting connection pads of integrated circuits during probing on wafer level. Instead of time-consuming and costly failure analyzes using optical and electrical methods, an acoustic emission test method is presented, which was adapted and optimized to the application case wafer test. The system was simulated using suitable models and verified in extensive experiments on suitable test structures. Based on detailed explanations, mathematical derivations of the micromechanical stress and frequency response states, precisely illustrated figures and numerous high-quality optical pictures, a well-founded elaboration of the problem and solution of a newly developed sensor-indenter system for thin layer crack detection is presented. All chapters have an introduction overview and a summary of the main results and conclusions. The work thus makes a significant contribution to reducing development costs and increasing the reliability of complex semiconductor structures of current and future technologies.

ISBN 978-3-96147-305-2

FAU UNIVERSITY PRESS 2020